ISSN 0914-9244
CODEN JSTEEW

Journal of Photopolymer Science and Technology

Volume 34 Number 5

2021

JOURNAL OF PHOTOPOLYMER SCIENCE AND TECHNOLOGY
Home Page http://www.spst-photopolymer.org
https://www.jstage.jst.go.jp/browse/photopolymer

Journal of Photopolymer Science and Technology publishes papers on the scientific progress and the technical development of photopolymers.

The Editorial Office
Assoc. Prof. Hiroyuki MAYAMA
Department of Chemistry, Asahikawa Medical University, 2-1-1-1 Midorigaoka-Higashi, Asahikawa, Hokkaido 078-8510, Japan.
FAX: +81-166-68-2782, e-mail: mayama@asahikawa-med.ac.jp

Information for Contributors

Submit Manuscripts to the SPST Homepage (Journal --> Submission of Papers --> Editorial Manager). Submission is a representation that the manuscript has not been published previously elsewhere. The manuscript should be accompanied by a statement transferring copyright from the authors (or their employers-whoever holds the copyright) to the Society of Photopolymer Science and Technology. A suitable form for copyright transfer is available from the SPST Homepage. This written transfer of copyright, which previously was assumed to be implicit in the act of submitting a manuscript, is necessary under the Japan copyright law. Further information may be obtained from the "Manual for Manuscript Writing" at the SPST Homepage.

Proofs and All Correspondence: Concerning papers in the process of publication should be addressed to the Editorial Office.

Manuscript Preparation: All the papers submitted are reproduced electronically as they were. For this reason, the manuscripts should be prepared according to the Manual for Manuscript Writings shown at the SPST Homepage.

Subscription Price (Airmail Postage included):
¥12,000 (in Japan), US$ 150.00 (for Foreign)

Subscriptions, renewals, and address changes should be addressed to the Editorial Office. For the address changes, please send both old and new addresses and, if possible, include a mailing label from the wrapper of recent issue. Requests from subscribers for missing journal issues will be honored without charge only if received within six months of the issue's actual date of publication; otherwise, the issue may be purchased at the single-copy price.

Publication Charge (Reprint Order): To support a part of the cost of publication of journal pages, the author's institution is requested to pay a page charge of ¥3,000 per page (with a one-page minimum) and an article charge of ¥12,000 per article. The page charge (if honored) entitles the author to 50 free reprints. For Errata the minimum page charge is ¥3,000, with no articles charge and no free reprints.

The cover designed by M. Tsuda and M. Morishita

JOURNAL OF PHOTOPOLYMER SCIENCE AND TECHNOLOGY

Volume 34 Number 5

2021

Published by

THE SOCIETY OF PHOTOPOLYMER SCIENCE AND TECHNOLOGY

THE SOCIETY OF PHOTOPOLYMER SCIENCE AND TECHNOLOGY (SPST)
http://www.spst-photopolymer.org

Office of the Administration
c/o Prof. Takashi KARATSU
Department of Applied Chemistry and Biotechnology,
Chiba University
1-33 Yayoicho, Inage-ku,
Chiba 263-8522, Japan
Phone: +81-43-290-3366
Fax +81-43-290-3401
e-mail:office@spst-photopolymer.org

THE SPST REPRESENTATIVES 2021

Journal of Photopolymer Science and Technology
Volume 34, Number 5 (2021) 423−430 ©2021SPST

Photoluminescence Properties of Copolyimides Containing Naphthalene Core and Analysis of Excitation Energy Transfer between the Dianhydride Moieties

Marina Doi[1], Koichiro Muto[1], Mayuko Nara[1], Naiqiang Liang[1], Kosuke Sano[2], Hiroaki Mori[2], Ryohei Ishige[1], and Shinji Ando[1]*

[1] *Department of Chemical Science and Engineering, Tokyo Institute of Technology, Ookayama, 2-12-1-E4-5, Meguro-ku, Tokyo 152-8552, Japan*
[2] *Chemical Research Laboratory, JFE Chemical Corporation, Kawasaki-cho, 1, Chuo-ku, Chiba-shi, Chiba 260-0835, Japan*
**ando.s.aa@m.titech.ac.jp*

The photoluminescence (PL) properties of semi-aromatic polyimide (PI) films and their model compounds (MCs) prepared from dianhydrides having a rigid naphthalene core were analyzed. The PMMA-dispersed MC and copolymerized PI (CoPI) films derived from 2,3,6,7-naphthalenetetracarboxylic dianhydride (NTDA) exhibited long-lived phosphorescence owing to the suppression of molecular motion by the rigidity of a naphthalene core. Additionally, the PMMA-dispersed MC and the CoPI films derived from 1,5-dibromo derivative of NTDA (DBrNT) exhibited room-temperature phosphorescence due to the enhancement of spin-orbit coupling by bromine atoms. The photophysical processes of the CoPI films prepared from NTDA/DBrNT and 4,4'-oxydiphtalic dianhydride (ODPA) in which the latter absorption band is located at a shorter wavelength than the former were analyzed. After UV irradiation, efficient excitation energy transfer occurs from the ODPA to NTDA/DBrNT moieties, and only the emission from the latter moieties was observed. These results demonstrate that the CoPI films derived from two dianhydrides absorbing different UV wavelengths can be used as spectral conversion films that convert a wide range of UV-light into longer wavelength visible light.

Keywords: Polyimide, Copolymer, Naphthalene, Energy transfer, Spectral conversion

1. Introduction

Polyimides (PIs) are a class of super engineering plastics, and they are widely used for their high thermal, environmental, and radiation stabilities, originating from their rigid repeating unit structures and strong intermolecular interactions [1–2]. Therefore, PIs have been applied in numerous fields, including automotive, microelectronic, photonic, electronic, and aerospace industries. Owing to their characteristic photoluminescence (PL) properties and excellent performance, PI films have been extensively studied as novel thermally stable photoluminescent materials [3–11].

The present authors recently reported a novel white-light emitting PI film by copolymerizing a fluorescent and a phosphorescent PIs [5,12]. Moreover, we have also reported that, by introducing heavy halogens, iodine and bromine, into the dianhydride moiety of PIs, bright phosphorescence (Ph) can be observed at room temperature owing to the heavy atom effect [13,14]. This effect is a phenomenon that introduction of metal or heavy halogen into organic fluorophores enhances the spin-orbit coupling (SOC) interactions and promotes the inter-system crossing (ISC) between the excited singlet and triplet states, which is generally forbidden [15,16]. Room temperature Ph has been expected to be applied to bioimaging [17], document security [18], and wavelength conversion films [19] because it generally exhibits

Received April 7, 2021
Accepted May 6, 2021

an emission at longer wavelengths accompanied by a much longer emission lifetime than fluorescence (Fl) [20,21]. It has been reported that the Ph intensity can be significantly increased at lower temperatures (e.g. 77 K) due to the suppression of local molecular motion [13]. This is because the contribution of non-radiative deactivation induced by local molecular motion is more significant in the Ph processes than in Fl due to the long lifetime of triplet excitons [22–26]. It has been difficult to develop organic compounds that exhibit long-lived Ph at room temperature and in air because Ph is easily quenched by molecular motion at higher temperatures and triplet oxygen in air. In recent years, however, it is strongly in demand to develop organic phosphorescent materials which exhibit long-lived Ph at room temperature, from the perspective of reducing costs and environmental impact. For this reason, the development of organic long-life phosphorescent materials is now being actively pursued [27,28]. In addition, crystalline and multi-crystalline silicon (Si) solar cells, which are mainly used in practical applications, have low absorption coefficients and poor spectral sensitivity to sunlight in the ultraviolet (UV) region [29]. Therefore, phosphorescent materials exhibiting emissions at longer wavelengths than fluorescent materials are expected to be used as spectral conversion films that convert the UV light to the visible light in the longer wavelength range, in which Si solar cells have much higher spectral sensitivity [30].

In this study, we mainly focused on the suppression of molecular motion by introducing a rigid aromatic structure. It is expected that the phosphorescent properties of the PIs derived from dianhydrides having an enlarged π–conjugated system can be improved due to the suppression of molecular motion by strong intermolecular π–π stacking. In that sense, the PIs having a rigid naphthalene core in the dianhydride moiety are expected to undergo restricted molecular motion due to the well-packed π-conjugated system in the solid state. Firstly, we synthesized imide model compounds and PIs using 2,3,6,7-Naphthalenetetracarboxylic dianhydride (NTDA) and evaluated their phosphorescent properties. We also synthesized copolymerized PIs (CoPIs) using NTDA and another dianhydride which absorbs UV light at a different wavelength and investigated the efficiency of energy transfer in the excited states between the dianhydrides.

2. Experimental

2.1. Materials.

2,3,6,7-Naphthalenetetracarboxylic dianhydride (NTDA), 4,4'-(hexafluoroisopropylidene) diphthalic anhydride (6FDA) and 4,4'-oxydiphthalic anhydride (ODPA) were kindly supplied by JFE Chemical Co. (Tokyo, Japan), NTT Advanced Technology Co. (Tokyo, Japan), and MANAC Inc. (Tokyo, Japan) respectively. They were purified by drying at 150 °C for 5 h in vacuo followed by sublimation under reduced pressure. 1,5-Dibromo-2,3,6,7-naphthalene tetracarboxylic dianhydride (DBrNT) was synthesized and supplied by JFE Chemical Co. (Tokyo, Japan). Cyclohexylamine (CHA) purchased from Kanto Chemical Co. (Tokyo, Japan), *N*,*O*-Bis(trimethylsilyl) trifluoroacetamide (BSTFA), polymethyl methacrylate (PMMA), and *N,N*-dimethyl acetamide (anhydrous, 99.8%, DMAc) from Sigma-Aldrich Japan (Tokyo, Japan), chloroform from Wako Pure Chemical Industries,

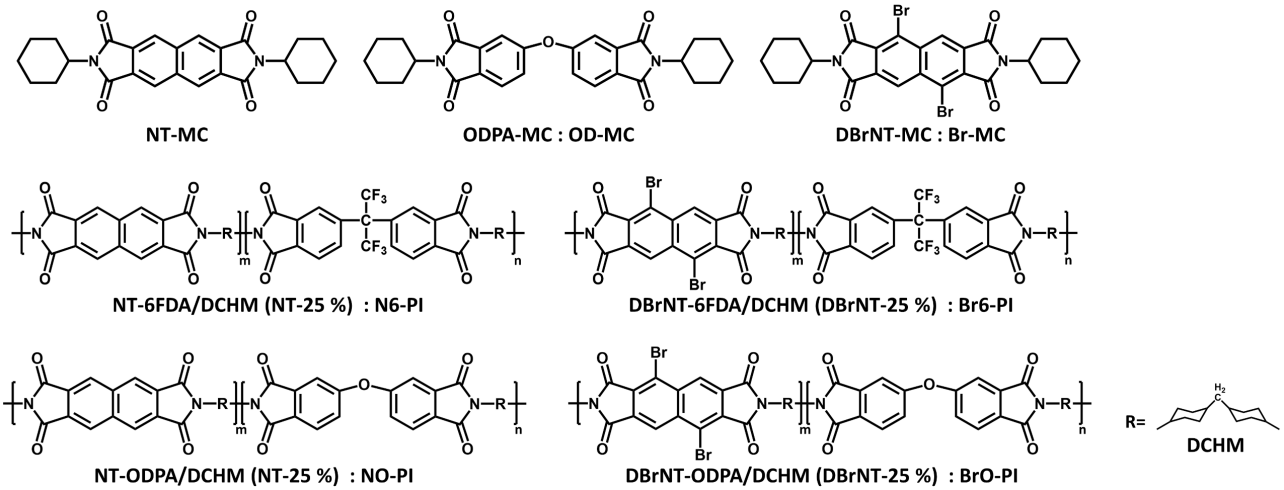

Chart 1. Chemical structures of imide compounds (MCs) and CoPIs.

Ltd. (Osaka, Japan), trifluoroacetic acid (TFA) from Tokyo Kasei Kogyo Co. Ltd. (Tokyo, Japan), and propionic acid from Kanto Chemical Co. (Tokyo, Japan) were used without further purification. Diaminodicyclohexylmethane (DCHM) from Tokyo Kasei Kogyo Co. Ltd. (Tokyo, Japan) was purified by recrystallization from *n*-hexane, followed by sublimation under reduced pressure.

2.2. Synthesis and film preparation of imide model compounds (MCs).

The synthesis scheme of an imide model compound (NT-MC) is shown in Scheme 1. CHA (1.5 g, 15 mmol) and NTDA (1.26 g, 4.7 mmol) were stirred in propionic acid (25 mL) for 30 min. The solution was then refluxed at 150 °C for 10 h under an N_2 flow. After cooling to room temperature, the solid was filtered, washed with ethanol, and then dried at 80 °C in vacuo. A white powder of NT-MC was obtained (1.3 g, 3.0 mmol, 50 % yield) by recrystallization from a mixture of chloroform and TFA. The other two MCs (Br-MC and OD-MC in Chart 1) were prepared in a similar manner by the reaction of DBrNT or ODPA and CHA. The yellowish powder of Br-MC was obtained (0.26 g, 0.44 mmol, 60 % yield). The white powder of OD-MC was obtained (0.43 g, 0.91 mmol, 86 % yield). PMMA (0.071 g) was stirred in chloroform (1 mL) for 3 h, and NT-MC (0.00037 g, 0.00086 mmol) was added to the solution, followed by stirring for 1 day. The resulting colorless and transparent solution was spin-coated onto a fused silica substrate, followed by drying at 100 °C for 1 h. Film of Br-MC and OD-MC dispersed in PMMA were also prepared in a similar manner. The weight fractions of the MCs in these films were 1.0 wt%.

2.3. Preparation of PI films.

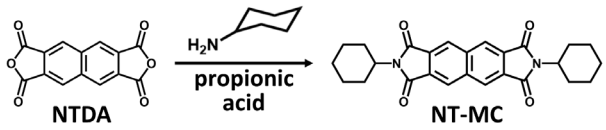

Scheme 1. Synthesis of NT-MC.

The chemical structures of CoPIs, NTDA-6FDA/DCHM (N6-PI), DBrNT-6FDA/ DCHM (Br6-PI), NTDA-ODPA/DCHM (NO-PI), and DBrNT-ODPA/DCHM (BrO-PI), are shown in Chart 1. A synthesis scheme of N6-PI film is shown in Scheme 2. A PI precursor, poly(amic acid)silyl ester (PASE), was prepared using the in situ silylation method [31]. DCHM (0.2 g, 0.95 mmol) and BSTFA (0.26 g, 1.0 mmol) were stirred in DMAc (2.6 mL) for 30 min in an ice bath (solution I). NTDA (0.064 g, 0.24 mmol) was stirred in DMAc (0.5 mL) for 30 min in an ice bath (solution II). Solution II was mixed with solution I and stirred for 10 min in an ice bath. 6FDA (0.32 g, 0.71 mmol) was then added to the solution, followed by stirring for 4 h in an ice bath and 2 days at room temperature. The resulting colorless and transparent solution was spin-coated onto a fused silica substrate, followed by soft-baking at 70 °C for 50 min and subsequent one-step thermal imidization procedure; film was gradually heated from 70 to 220 °C at a heating rate of 3.0 °C/ min, and kept at the final temperature for 1.5 h under an N_2 flow. Thus, N6-PI film was cooled to room temperature. Br6-PI, NO-PI, and BrO-PI films were prepared in the same manner. The CoPI films were prepared using the same molar ratios of NTDA/DBrNT (25 mol%) to 6FDA and ODPA (75 mol%).

2.4. Measurements.

PL excitation/emission spectra were measured with F-7100 luminescence spectrometer (Hitachi Hi-Tech, Japan) equipped with an R928

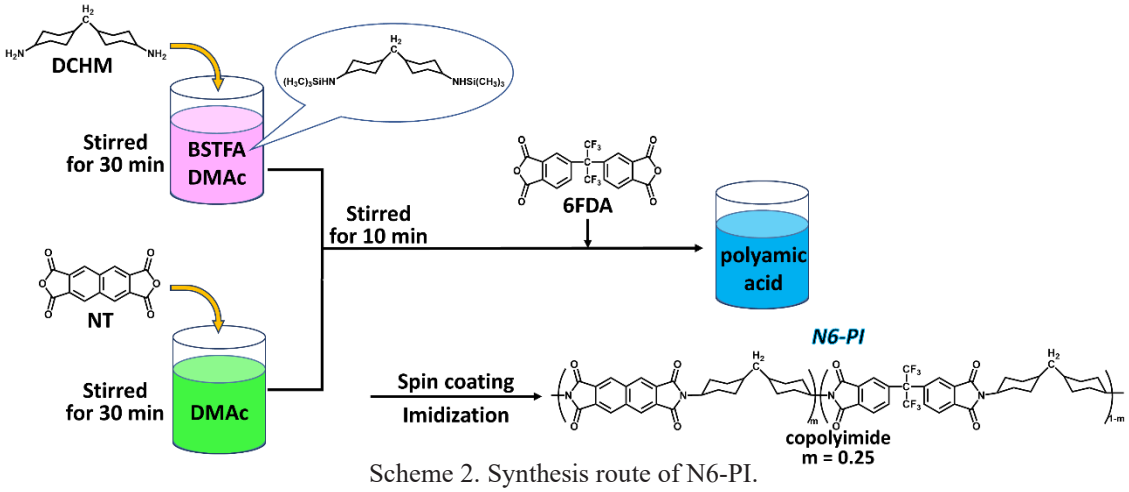

Scheme 2. Synthesis route of N6-PI.

photomultiplier tube (Hamamatsu Photonics, Japan). Photoluminescence spectra under vacuum conditions were measured using a custom-made vacuum chamber (Akada Industry Co., Ltd, Japan) installed in the same luminescence spectrometer. Spectra were measured after pumping the chamber out using a vacuum pump (Xtradry 150-2, Pfeiffer Vacuum GmbH, Germany), and the inside pressure reached around 10 Pa after pumping for 30 min. Photoluminescence spectra at low temperatures were measured by mounting the samples on a temperature controller (CoolSpek UV USP-203-B, Unisoku Co., Ltd, Japan) installed in the same spectrometer. Samples were cooled by liquid nitrogen supplied from the reservoir into the chamber. Photoluminescence quantum efficiency (Φ_{total}) was measured by using a calibrated integrating sphere (C9920-02, Hamamatsu Photonics, Japan) connected to a multichannel analyzer (C7473-36, Hamamatsu Photonics, Japan) via an optical fiber link. Fl lifetime measurements with a time resolution of less than 1 ns were conducted using a PL lifetime measurement system (Quantaurus-Tau, C11367−24, Hamamatsu Photonics, Japan) at room temperature. The decay component was recorded using excitation by applying a flashing light-emitting diode (LED) at wavelengths of 340 nm and 365 nm. Fl decay curves were accumulated until the peak intensity reached 1000 counts. Ph lifetimes were measured using a xenon flash lamp unit (C11567-02, Hamamatsu, Japan). Ph decay curves were recorded under excitation using two bandpass filters (BrightLine 340-12 and 360-12, Semlock Inc., USA) whose transmission ranges were 334-346 nm and 354-366 nm, respectively, and the decay signals were accumulated for 5 min. The emission decay curves were fitted using one to two exponential functions. The average lifetime was calculated as $\langle\tau\rangle = \Sigma A_i\tau_i^2/A_i\tau_i$, where A_i is the pre-exponential factor for a lifetime τ_i.

3. Results and discussion

3.1. Optical properties of PMMA-dispersed MCs.

Figure 1 shows the excitation/emission spectra of NT-MC and Br-MC dispersed in PMMA films measured at room temperature (293 K), where λ_{ex} is the excitation wavelength, and λ_{em} is the monitoring emission wavelength. Table 1 summarizes the peak wavelengths of excitation and emission spectra (λ_{exp}, λ_{emp}), Stokes shifts (ν), and PL quantum yields (Φ_{total}) of the NT-MC and Br-MC films. Figure 2 shows the PL decay curves of the MCs dispersed in

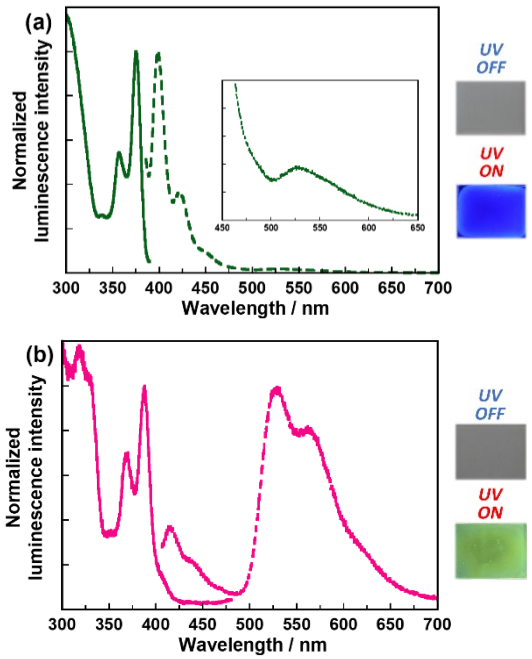

Fig. 1. Excitation (solid line) and emission (dotted line) spectra of (a) NT-MC (Inset: enlarged view of emission spectrum) (λ_{em} = 400, λ_{ex} = 375 nm) and (b) Br-MC (λ_{em} = 528, λ_{ex} = 390 nm).

PMMA films measured at room temperature in the ambient air and under vacuum conditions. NT-MC exhibits two emission peaks at λ_{emp} = 398 and 526 nm. The former peak is readily attributable to the Fl emitted from the locally excited π−π transition because the PL measured at 400 nm decayed exponentially with the longest decay component of 5.42 ns under atmospheric condition with oxygen, and its Stokes shift is relatively small (ν = 1541 cm^{-1}). By contrast, the latter weak peak is attributable to Ph because the PL measured at 525 nm decayed with the longest decay component of 1.52 s under vacuum condition with a very large ν of 7655 cm^{-1}.

Br-MC exhibits three emission peaks at λ_{emp} = 416, 527 and 570 nm. The first one is readily attributable to Fl because of the small ν value of

Table 1. PL properties of MCs dispersed in PMMA and N6-PI/Br6-PI films.

Sample	λ_{exp} (nm)	λ_{emp} (nm)	ν (cm^{-1})	Φ_{total}
NT-MC	375	398 526	1541 7655	0.33
Br-MC	388	416 527	1735 6798	0.10
N6-PI	376	403 508	1781 6910	0.20
Br6-PI	325 386 472	428 542	2542 7388	0.024

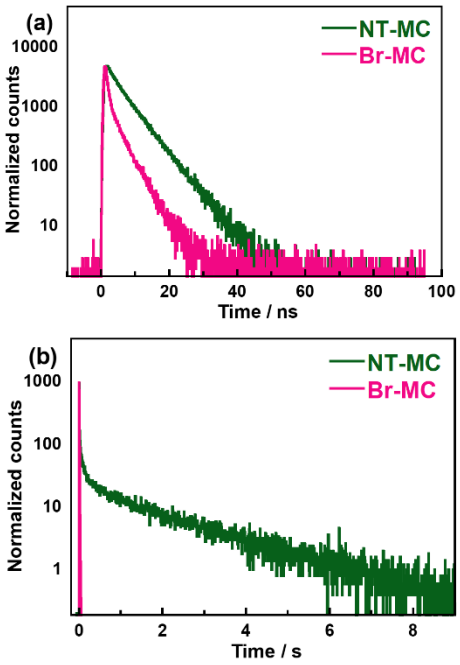

Fig. 2. (a) Fl decay curves under atmospheric condition (NT-MC: (λ_{ex}, λ_{em}) = (365,400 nm), Br-MC: (405, 415 nm) and (b) Ph decay curves under vacuum condition (NT-MC: (λ_{ex}, λ_{em}) = (360, 524 nm), Br-MC: (360, 527 nm).

1735 cm^{-1}, and the PL measured at 415 nm decayed exponentially with the longest decay component of 1.97 ns under vacuum condition. By contrast, the latter two intense peaks are attributable to Ph because of the very large ν value of 7698 cm^{-1} for the second one, and the PL measured at 527 nm decayed with the longest decay component of 4.98 ms under atmospheric condition. The fact that the same decay curves were observed for the second and third peaks indicates that these two peaks originate from the same Ph having different vibration modes. Notably, these are the first observations of the phosphorescence from 2,3,6,7-naphthalene- diimide and its brominated derivative.

The quantum yields of Fl and Ph (Φ_f, Φ_p) of NT-MC and Br-MC were estimated from the Φ_{total} value and the peak areas of the Fl and Ph of NT-MC and Br-MC, and the Φ values thus estimated are listed in Table 2. The Φ_p value of Br-MC is significantly larger than that of NT-MC, which indicates that the efficiency of Ph is drastically increased due to the enhancement of ISC by introducing bromine atoms to the naphthalene core of NTDA.

Table 2. PL quantum yields of MCs.

MCs	Φ_{total}	Φ_f	Φ_p
NT-MC	0.33	0.32	0.01
Br-MC	0.10	0.01	0.09

3.2. Optical properties of N6-PI and Br6-PI films.

Figure 3 shows the PL spectra of N6-PI and Br6-PI films measured at room temperature together with those of the MCs. Table 1 also summarizes the estimated values of λ_{exp}, λ_{emp}, ν, and Φ for N6-PI and Br6-PI films. Note that each of N6-PI and Br6-PI exhibits a similar shape of emission spectrum of the corresponding MC. It indicates that the copolymerization of NTDA or DBrNT with 6FDA can maintain the inherent PL properties of the naphthalene core imide moieties. Intriguingly, 6FDA effectively enhances the solubility of PASEs in polar solvents, but it does not affect the photophysical processes of the CoPIs derived from NTDA/DBrNT.

As shown in Fig. 4(a), the PL measured at 508, 520 nm for N6-PI decayed exponentially with the longest decay component of 1.77 s at 77 K and 0.647 s under vacuum condition at 293 K. The PL measured at 508 nm of NT-MC also decayed exponentially with the longest decay component of 3.63 s at 77 K. In general, typical Ph lifetime (τ_p) of organic compounds are in the order of μs–ms, and τ_p longer than 100 ms is called 'long-lived phosphorescence lifetime'. Thus, the τ_ps of NT-MC and N6-PI are readily categorized as very long-lived Ph [32,33]. The molecular mobility restricted by the rigid structure of NTDA moiety effectively reduces the non-radiative deactivation from the excited triplet state. The fact that the decay components of

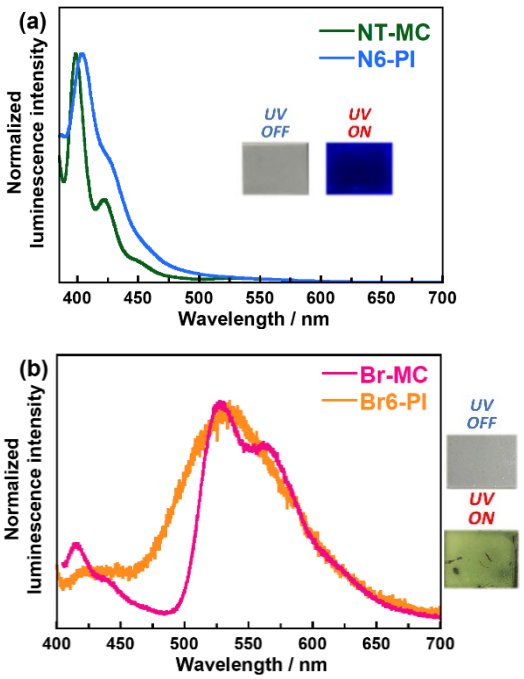

Fig. 3. PL spectra of (a) NT-MC and N6-PI (λ_{ex} = 375 nm), and (b) Br-MC and Br6-PI (λ_{ex} = 390 nm) (Inset: photographs of N6-PI and Br6-PI films).

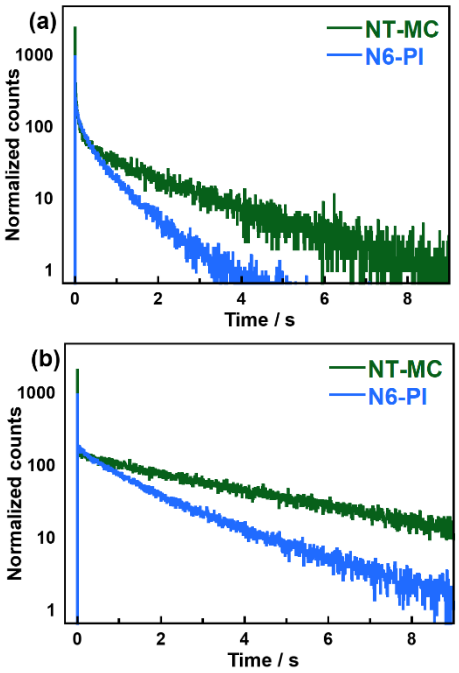

Fig. 4. Ph decay curves (a) measured under vacuum condition at 293 K (λ_{ex} = 360 nm, NT-MC: λ_{em} = 524 nm, N6-PI: λ_{em} = 520 nm) (b) measured at 77 K under nitrogen atmosphere (λ_{ex} = 360 nm, λ_{em} = 508 nm) of NT-MC and N6-PI.

N6-PI are slightly shorter than those of NT-MC suggests that the local motion of NT-MC molecules dispersed in PMMA is more tightly restricted than the NTDA moieties in N6-PI even at 77 K. In other words, the local motion of PI chain is not completely frozen at this temperature.

3.3. Excitation energy transfer between dianhydrides

Figure 5 shows the excitation/emission spectra of OD-MC dispersed in PMMA. OD-MC exhibits an excitation band at 330 nm, which is obviously different from the excitation wavelengths of NT-MC and Br-MC (λ_{exp} = 375 nm for NT-MC, and λ_{exp} = 390 nm for Br-MC) (Fig. 1). This suggests that

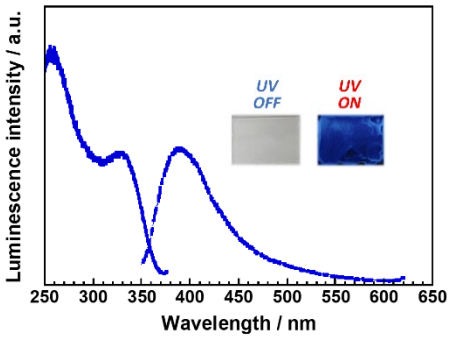

Fig. 5. Excitation (solid line, λ_{em} = 409 nm) and emission (dotted line, λ_{ex} = 340 nm) spectra of OD-MC dispersed in PMMA.

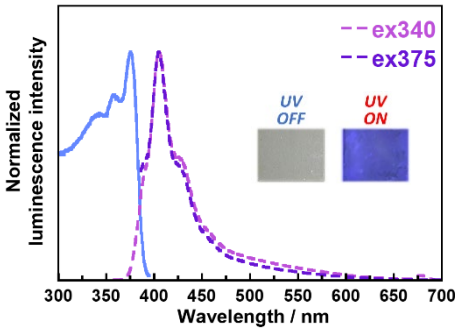

Fig. 6. Excitation (blue solid line, λ_{em} = 404 nm) and emission (purple dotted line) spectra of NO-PI excited at 340 and 375 nm.

each composing dianhydride of CoPIs (NTDA/DBrNT and ODPA) could be selectively excited by adjusting the excitation wavelength of UV irradiation.

Figure 6 shows the emission spectra of NO-PI excited at 340 and 375 nm. NO-PI exhibits two emission peaks at λ_{emp} = 405 and 570 nm regardless of the excitation wavelength. This clearly indicates that the emissions from NTDA and ODPA moieties cannot be separated in NO-PI by changing the excitation wavelength. As mentioned above, OD-MC exhibits an emission peak at around 400 nm which is close to that of NT-MC. Meanwhile, the PL of OD-MC exhibited a Fl lifetime (τ_f) of 5.9 ns and Ph lifetime (τ_p) of 885 ms at 77 K, and these are distinctly different from those of NT-MC (τ_f =5.42 ns, τ_p =3.63 s). Thereby, the emission process of NO-PI could be analyzed from the PL decay curves observed by the excitation of ODPA moiety at 340 nm and that of NTDA moiety at 360 or 365 nm. In case that the PL is only emitted from the NTDA moiety, the decay curve should be fitted by single component, whereas in case that the PL is emitted from both the NTDA and ODPA moieties, the decay curve could be composed of two components having different slopes, which can be used to characterize the major emitting component in the CoPIs.

Figure 7 shows the Fl decay curves of NO-PI excited at 340 and 365 nm and measured at 405 nm, together with the Ph decay curves excited at 340 and 360 nm at 77 K and measured at 570 nm. Both the decay curves show single component decays. Table 3 summarizes the Fl and Ph lifetimes (τ_f, τ_p) of NO-PI. The Fl lifetimes of the dianhydride moiety in the copolymer should be shorter than those of the homopolymers, though the Ph lifetime of NO-PI are significantly longer than those of ODPA-based homopolyimide (τ_f = 7.0 ns, τ_p = 619 ms). These facts suggest that the PL of NO-PI is emitted not

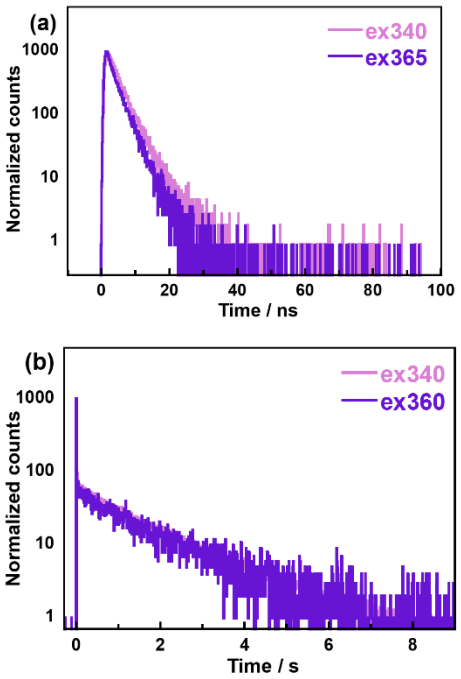

Fig. 7. (a) Fl decay curves at room temperature (λ_{em} = 405 nm) and (b) Ph decay curves at 77 K (λ_{em} = 570 nm) of NO-PI.

from the ODPA moiety but from the NTDA moiety. This is well supported by the fact that the emission lifetimes of NO-PI are close to those of NT-MC. When the ODPA moiety of NO-PI is selectively excited at 340 nm, both the Fl and Ph were emitted only from the NTDA moiety. This result indicates that when the ODPA moiety is irradiated by UV light at 340 nm, efficient excitation energy transfer immediately occurs from the ODPA to NTDA moieties, and then the NTDA moiety emits the PL.

In the same manner, Fig. 8 shows the emission spectra for BrO-PI excited at 340 and 390 nm. BrO-PI exhibits two emission peaks at λ_{emp} = 428 and 548 nm regardless of the excitation wavelength. The emission peaks of BrO-PI can be separated into those from DBrNT and ODPA moieties because OD-MC and Br-MC exhibited emission peaks at different wavelengths (λ_{emp} = 398 nm for OD-MC, and λ_{emp} = 416 and 527 nm for Br-MC). BrO-PI exhibits emission peak not at around 400 nm but at around 420 and 520 nm, which suggests that the ODPA moiety in BrO-PI does not emit the major part of PL but the DBrNT moiety emits. When the ODPA moiety of BrO-PI is selectively excited at 340 nm, the Fl and Ph of BrO-PI were emitted only from the DBrNT moiety. These facts also indicate that when the ODPA moiety is irradiated at 340 nm, efficient excitation energy transfer immediately occurs from the ODPA to DBrNT moieties, and then the DBrNT moiety emits the PL.

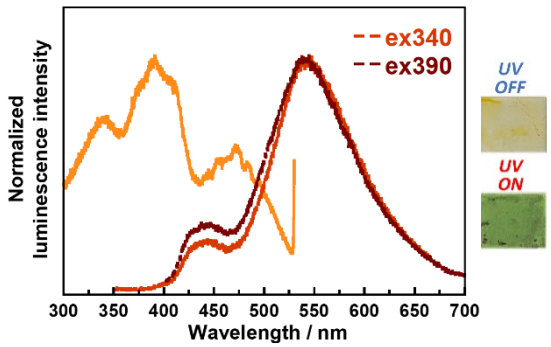

Fig. 8. Excitation (orange solid line, λ_{em} = 540 nm) and emission (brown dotted line) spectra of BrO-PI excited at 340 and 390 nm.

Accordingly, these results clearly demonstrate that the copolymerization of NTDA and DBrNT with ODPA having different excitation wavelengths is a facile and versatile method to incorporate and enhance the energy transfer mechanisms in the excited states, which enables to absorb a wide wavelength range of UV light and convert to the useful visible light in the longer wavelength region with desirable efficiency. Moreover, it is

Table 3. Fl and Ph lifetimes of NO-PI film.

NO-PI	τ_f [ns]	τ_p [s]
ex340	3.64	1.88
ex360/365	3.50	1.87

demonstrated that NO-PI can convert a wide wavelengths range of UV light to long-lived phosphorescence emission through excitation energy transfer, and BrO-PI can convert UV light to room temperature phosphorescence at a longer wavelength of 520 nm. This green light emission is well suited for the spectral response of conventional crystalline Si-type solar cells.

4. Conclusion

The optical absorption and PL properties of three kinds of MCs dispersed in PMMA and four kinds of CoPIs prepared using two dianhydrides containing a rigid naphthalene core (NTDA/DBrNT) were analyzed. It was clarified that copolymerization with 6FDA can maintain the inherent luminescence properties of NTDA/DBrNT moieties. 6FDA endows precursors (PASEs) with excellent solubility without interference in the photophysical processes of NTDA/DBrNT moieties. It was clarified that the restricted molecular mobility by the rigid and planar structures of NTDA and DBrNT moiety reduces the non-radiative deactivation from

the excited states. It was also demonstrated that the CoPIs of NTDA and DBrNT with ODPA having a different excitation wavelength can absorb UV light in a wide wavelength range. When the ODPA moiety in the CoPIs is irradiated at a shorter wavelength of 340 nm, efficient excitation energy transfer occurs from the ODPA to the NTDA/DBrNT moieties, and then bright PL is emitted from the NTDA/DBrNT moieties. In particular, BrO-PI shows Ph emission at a longer wavelength (520 nm) than ODPA-PI. Accordingly, this CoPI film is expected to be applied to wavelength conversion films which absorb a wide range of UV light and readily emit useful and valuable visible light at longer wavelengths which is well suited for the spectral response of crystalline and multi-crystalline Si solar cells.

References

1. C.E. Sroog, *J. Polym. Sci., Part D Macromol. Rev.*, **11** (1976) 161.
2. D. Creed, C. E. Hoyle, J. W. Jordan, C. A. Pandey, R. Nagarajan, and S. Pankasem, *Macromol. Symp.*, **116** (1997) 1.
3. J. Wakita, H. Sekino, K. Sakai, Y. Urano, and S. Ando, *J. Phys. Chem. B*, **113** (2009) 15212.
4. M. Hasegawa and K. Horie, *Prog. Polym. Sci.*, **26** (2001) 259.
5. K. Takizawa, J. Wakita, K. Sekiguchi, and S. Ando, *Macromolecules*, **45** (2012) 4764.
6. K. Kanosue, T. Shimosaka, J. Wakita, and S. Ando, *Macromolecules*, **48** (2015) 1777.
7. K. Kanosue, R. Augulis, D. Peckus, R. Karpicz, T. Tamulevičius, S. Tamulevičius, V. Gulbinas, and S. Ando, *Macromolecules*, **49** (2016) 1848.
8. K. Kanosue and S. Ando, *Phys. Chem. Chem. Phys.*, **17** (2015) 30659.
9. R. Orita, M. Franckevičius, A. Vyšniauskas, V. Gulbinas, H. Sugiyama, H. Uekusa, K. Kanosue, R. Ishige, and S. Ando, *Phys. Chem. Chem. Phys.*, **20** (2018) 16033.
10. N. Liang, E. Fujiwara, M. Nara, R. Ishige, and S. Ando, *J. Photopolym. Sci. Technol.*, **32** (2019) 449.
11. E. Fujiwara, R. Orita, A. Vyšniauskas, M. Franckevičius, R. Ishige, V. Gulbinas, and S. Ando, *J. Phys. Chem. B*, **125** (2021) 2425.
12. M. Nara, R. Orita, R. Ishige, and S. Ando, *ACS Omega*, **5** (2020) 14831.
13. K. Kanosue, S. Hirata, M. Vacha, R. Augulis, V. Gulbinas, R. Ishige, and S. Ando, *Mater. Chem. Front.*, **3** (2019) 39.
14. K. Kanosue and S. Ando, *ACS Macro Lett.*, **5** (2016) 1301.
15. N. J. Turro, V.Ramamurthy, and J. C. Scaiano, *Angew. Chemie Int. Ed.*, **49** (2009) 6709.
16. H. Shi, Z. An, P.Z. Li, J. Yin, G. Xing, T. He, H. Chen, J. Wang, H. Sun, W. Huang, and Y. Zhao, *Cryst. Growth Des.*, **16** (2016) 808.
17. J. Mei, Y. Huang, and H. Tian, *ACS Appl. Mater. Interfaces*, **10** (2018) 12217.
18. Z. Yang, Z. Mao, X. Zhang, D. Ou, Y. Mu, Y. Zhang, C. Zhao, S. Liu, Z. Chi, J. Xu, Y. C. Wu, P. Y. Lu, A. Lien, and M. R. Bryce, *Angew. Chemie Int. Ed.*, **55** (2016) 2181.
19. R. Reisfeld, *Opt. Mater.*, **32** (2010) 850.
20. S. Hirata, *Adv. Opt. Mater.*, **5** (2017) 1.
21. L. Xiao, Z. Chen, B. Qu, J. Luo, S. Kong, and Q. Gong, *Adv. Mater.*, **23** (2011) 926.
22. V. Gray, D. Dzebo, M. Abrahamsson, B. Albinsson, and K. Moth-Poulsen, *Phys. Chem. Chem. Phys.*, **16** (2014) 10345.
23. Y. Shang, S. Hao, C. Yang, and G. Chen, *Nanomaterials*, **5** (2015) 1782.
24. P. Duan, D. Asthana, T. Nakashima, T. Kawai, N. Yanai, and N. Kimizuka, *Faraday Discuss.*, **196** (2017) 305.
25. S. Guha, M. Chandrasekhar, U. Scherf, and M. Knaapila, *Phys. Status Solidi Basic Res.*, **248** (2011) 1083.
26. S. Guha and M. Chandrasekhar, *Phys. Status Solidi Basic Res.*, **241** (2004) 3318.
27. H. Ma, Q. Peng, Z. An, W. Huang and Z. Shuai, *J. Am. Chem. Soc.*, **141** (2019) 1010.
28. S. Mukherjee and P. Thilagar, *Chem. Commun.*, **51** (2015) 10988.
29. A. Amillo, T. Huld, P. Vourlioti, R. Müller and M. Norton, *Energies*, **8** (2015) 3455.
30. D. Yang, H. Liang, Y. Liu, M. Hou, L. Kan, Y. Yang, and Z. Zang, *Dalt. Trans.*, **49** (2020) 4725.
31. Y. Oishi, K. Ogasawara, H. Hirahara, and K. Mori, *J. Photopolym. Sci. Technol.*, **14** (2001) 37.
32. K. Narushima, Y. Kiyota, T. Mori, S. Hirata, and M. Vacha, *Adv. Mater.*, **31** (2019) 1807268.
33. Y. Su, S.Z.F. Phua, Y. Li, X. Zhou, D. Jana, G. Liu, W.Q. Lim, W.K. Ong, C. Yang, and Y. Zhao, *Sci. Adv.*, **4** (2018) 9732.

Journal of Photopolymer Science and Technology
Volume 34, Number 5 (2021) 431−437 ©2021SPST

Self-assembly of Crosslinked Polyimides Templated by Block Copolymers for Fabrication of Porous Films

Takahiro Komamura[1], Yuta Nabae[1], and Teruaki Hayakawa[1*]

[1] Department of Materials Science and Engineering, School of Materials and Chemical Technology, Tokyo Institute of Technology, 2-12-1-S8-36, Ookayama, Meguro-ku, Tokyo, 152-8552, Japan
**hayakawa.t.ac@m.titech.ac.jp*

Crosslinked porous polyimide films were fabricated by a soft-template method using the microphase-separated structure based on a template block copolymer. A trifunctional amine, 1,3,5-tris(4-aminophenyl)benzene (TAPB), was used as a crosslinkable monomer of the poly(amic acid) (PAA) to achieve the well-ordered and flexible films. The crosslinking by TAPB improved the thermal stability of the nanostructures of the PAA/polystyrene-*b*-poly(2-vinyl pyridine) composite films without reduction of the ratio of polyimide. A porous polyimide film was successfully fabricated by thermal treatment of a PAA composite film that has porous lamella structures and disordered porous structures with approximately 50 nm gaps based on the nanostructure of the PAA composite films before thermal treatment.
Keywords: Polyimide, Block copolymer template, Self-assembly, Porous polyimide, Crosslinked polyimide

1. Introduction

Polyimides have outstanding mechanical strength, heat resistance, and chemical stability and are applied to aerospace materials and electronic material fields [1]. Among them, porous polyimides have both excellent properties of polyimides as well as features of porous polymers. Therefore, they are expected to advance the development of functional materials such as gas separation membranes, low dielectric materials, thermal insulators, and separators for fuel cells [2–7]. Well-defined porous polyimides especially have gathered attention because of their excellent properties and controlled pore structure. The fabrication of the well-defined porous polyimides has been reported using the breath figure method [3,8–12], silica-particle template method [13–15], and covalent organic frameworks [16–18]. In the mesoporous range, only a few cases have been reported by the silica sphere template method, which uses hydrofluoric acid to remove the silica template for the pore-forming, and is associated with chemical hazards. Therefore, a much simpler method was strongly desired to fabricate well-defined mesoporous polyimide films.

Based on such background, the fabrication of ordered mesoporous polyimide films by the soft-template method has been reported [19–26]. In this method, an amphiphilic block copolymer with a narrow polydispersity and a well-defined composition ratio is used as a template to form ordered microphase-separated structures. The hydrophilic domain of the block copolymer is miscible with poly(amic acid) (PAA) selectively. The PAA/block copolymer composite co-assembles and forms into an ordered microphase-separated structure. The imidization of PAA is carried out by heating. Subsequently, the composite film is processed by thermal treatment, reactive ion etching, or ozonolysis to decompose the template block copolymer selectively and create an ordered mesoporous structure. This method allows the fabrication of ordered mesoporous polyimide films by facile and safe processes. Furthermore, this method has potential to form various morphologies such as spheres, cylinders, lamellae, and bicontinuous structures by controlling the volume fractions. In those previous works, however, decomposing the template block copolymer at high temperatures (~380 °C) resulted in the collapse of the nanostructure. Although the addition of resol

Received April 1, 2021
Accepted May 5, 2021

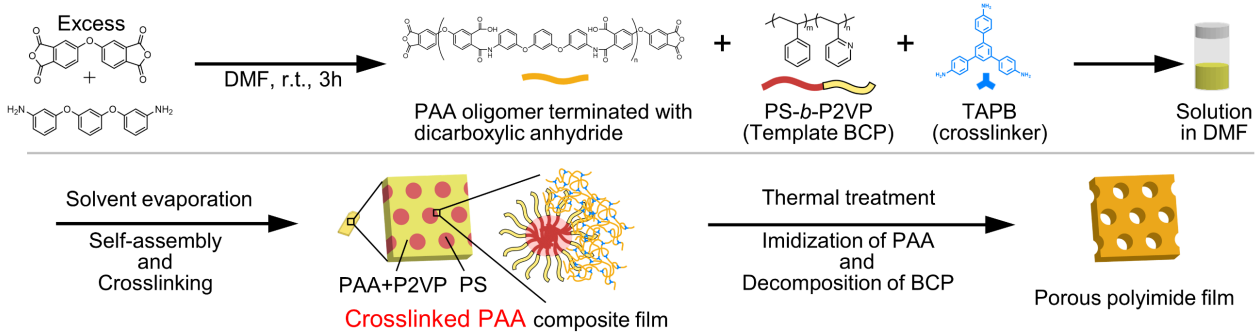

Fig. 1. Schematic image of the fabrication of the porous polyimide.

improved the thermal stability of the nanostructure, the use of excess amounts of resol might cause less flexibility of the film. Therefore, the fabrication of mesoporous polyimide films with both of well-ordered pores and flexibility is still challenging.

In this context, we hereby a novel fabrication method of mesoporous polyimide films using a soft template and crosslinkable polyimide instead of the use of crosslinkers such as resol (Fig. 1). A trifunctional amine, 1,3,5-tris(4-aminophenyl)benzene (TAPB), was used as a crosslinkable monomer of the PAA to achieve both order and flexibility of the films. The use of TAPB allows crosslinking of the polyimide without other crosslinkers such as resol. Polystyrene-*b*-poly(2-vinyl pyridine) (PS-*b*-P2VP) was used as a template block copolymer. Well-ordered microphase-separated structures are expected to be formed by strong segregation between the hydrophobic domain: PS and the hydrophilic domain: P2VP. The microphase-separated structures of the composite films were characterized by small-angle X-ray scattering (SAXS) and Transmission electron microscopy (TEM). Furthermore, promising PAA composite films were treated in sequential processes, thermal imidization of PAA, and the thermal degradation of PS-*b*-P2VP. The successful fabrication of the mesoporous polyimide film was demonstrated by SAXS, field emission scanning electron microscopy (FE-SEM), and Fourier Transform-Infrared spectroscopy (FT-IR).

2. Experimental

2.1. Materials

Oxydiphthalic anhydride (ODPA), 1,3-bis(3-aminophenoxy)benzene (BAPB), 1,3,5-Tris(4-aminophenyl)benzene (TAPB), styrene, 2-vinylpyridine (2VP), were purchased from Tokyo Chemical Industry Co., Ltd (Tokyo, Japan). ODPA and BAPB were purified by sublimation at 270 °C and recrystallization from water/methanol = 1/1 (v/v), respectively. TAPB was used as received. *N*,*N*-dimethylformamide(DMF) was purchased from FUJIFILM Wako Pure Chemical Corporation (Osaka, Japan) and was stirred over calcium hydride (CaH_2, Nacalai Tesque) overnight then distilled under reduced pressure. Styrene and 2VP were stirred with CaH_2 overnight and distilled under reduced pressure. The monomers were redistilled immediately prior to use over a small amount of di-*n*-butylMagnesium (Aldrich) and CaH_2, respectively, respectively. *Sec*-Butyllithium (*sec*-BuLi, 0.99 M in 95 % cyclohexane and 5 % *n*-hexane), tetrahydrofuran (THF, >99.5 %, dehydrated and stabilizer free), *n*-hexane, ethanol, and methanol were purchased from Kanto Chemical Co., Inc. (Tokyo, Japan), and used as received.

2.2. Characterization

The inherent viscosity of the PAA was measured using an Ostwald viscometer with 0.5 g dL^{-1} of *N*,*N*-Dimethylacetamide solutions at 30 °C. Nuclear magnetic resonance (NMR) was acquired on a JEOL JNM-ECS 400 spectrometer (JEOL, Tokyo, Japan) at 400 MHz for ^{1}H and 100 MHz for ^{13}C. The number-average molecular weight (M_n) and dispersity (M_w/M_n) were measured on a ShodexGPC-101 with a ShodexLF804 column using THF as an eluent. Thermogravimetric analysis (TGA) was performed with an EXSTAR TG/DTA 7300 (Seiko Instrument Inc., Tokyo, Japan) at a heating rate of 3 °C min^{-1}. SAXS were measured with a Bruker NanoSTAR (Bruker AXSK.K., Kanagawa, Japan, 50 kV per 50 mA, CuKα radiation) with a 2D-PSPC detector (camera length 1055 mm). TEM was performed using an H-7650 Zero A (Hitachi, Ltd., Tokyo, Japan) microscope at an accelerating voltage of 100 kV. The TEM specimens with 80 nm thickness were prepared with an ultramicrotome (EM UC7, Leica, Wetzlar, Germany) and stained by iodine. FE-SEM was performed on an SU-9000 microscope (Hitachi High-Technologies Corporation, Tokyo, Japan) at 3 kV accelerating voltage. The cross-section of FE-

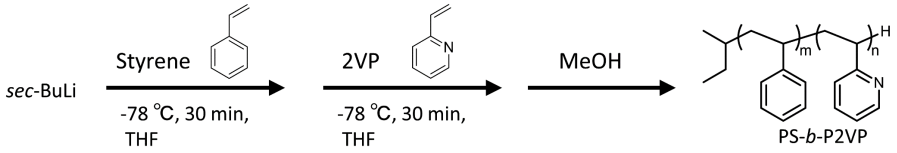

Fig. 2. Synthesis of PS-*b*-P2VP.

SEM specimens was prepared by breaking a bulk sample in liquid nitrogen. FT-IR was measured with a JASCO FT/IR-4100 plus spectrophotometer by the KBr pellet method.

2.3 Synthesis of PS-*b*-P2VP

PS-*b*-P2VP was synthesized via living anionic polymerization (Fig. 2). 80 mL of dehydrated THF was transferred to a 100 mL Schlenk flask and cooled to -78 °C in a cool bath. Approximately 0.8 ml of sec-BuLi was added and the solution turned yellow. After 10 min, the Schlenk flask was returned to room temperature and the solution became colorless. The Schlenk flask was cooled to -78 °C in a cool bath again. Subsequently, 110 μL of *sec*-BuLi solution (118 μmol) and 2.65 mL of styrene (23.0 mmol) were added immediately, which turned the solution reddish-brown. After 30 min of stirring, 1.64 mL (15.2 mmol) of 2VP was added to the solution and the color turned to a deep red. After 30 min of stirring, 10 mL of dry methanol was added to quench the reaction and the solution became colorless. The obtained proton-terminated polymer was precipitated in hexane, vacuum filtered, then dried in a vacuum oven at 40 °C for 24 h to obtain a white powder of PS-*b*-P2VP (3.29 g, 82 % yield, $M_{n,SEC}$ = 17,500 g mol^{-1}, M_w/M_n = 1.25, PS_{91}-$P2VP_{77}$). ^{1}H NMR ($CDCl_3$, 400) δ (ppm): 1.42-2.05 (br, **CH_2**, 4H), 2.32 (br, **CH** P2VP, 1H), 2.88 (br, **CH** PS, 1H), 6.35-7.07 (br, **Ar** PS, **Ar** P2VP, 8H), 8.08-8.40 (br, **Ar** P2VP, 1H). ^{13}C NMR ($CDCl_3$, 100 MHz) δ (ppm): 40.3, 42.9, 120.6, 125.6, 127.9, 135.3, 145.1, 148.6, 164.3.

2.4. Preparation of crosslinked PAA composite films

The synthesis of crosslinked PAAs and the fabrication of PAA/PS-*b*-P2VP composite films were performed continuously as follows. PAA oligomer terminated with dicarboxylic anhydride was prepared by mixing BAPB and an excess amount of ODPA in DMF for 3 h at 25 °C. The solution was mixed with PS-*b*-P2VP and stoichiometric TAPB and was stirred for 5 min to obtain a homogeneous solution. The crosslinked PAA composite film was cast on a silicone mold from the solution of 10 wt% polymer mixture through a membrane filter (pore diameter: 0.2 μm), followed by solvent evaporation and crosslinking of PAA at 50 °C for 24 h.

2.5. Preparation of porous polyimide films

Porous polyimide composite films were fabricated by thermal treatment of the crosslinked PAA composite films at 380 °C for 3 h under nitrogen flow (50 mL/min). The imidization of PAA and decomposition of PS-*b*-P2VP were confirmed by TGA and FT-IR. The resulting porous polyimide films were characterized by SAXS and FE-SEM.

Table 1. Preparation conditions and characterization of the PAA composite films and porous polyimide films.

	Preparation ratio of PAA monomers			Weight fraction of PAA composite films		Phase separated structure of PAA composite films		Porous structure of polyimide films	
Sample	ODPA	BAPB	TAPB	PAA [%]	PS-*b*-P2VP [%]	d_0 [a] [nm]	Morphology [b]	d_0 [a] [nm]	Morphology [c]
1	-	-	-	0	100	21.0	Lamella	N/A	N/A
2	1.00	0.95	0.03	25	75	33.0	Cylinder	N/A	N/A
3	1.00	0.95	0.03	50	50	25.4	Sphere	N/A	N/A
4	1.00	0.95	0.03	75	25	31.1	Sphere	N/A	N/A
5	1.00	0.95	0.03	25	75	33.0	Cylinder	-	-
6	1.00	0.70	0.20	25	75	37.8	Cylinder	-	-
7	1.00	0.30	0.47	25	75	29.3	Lamella/Disordered	28.2	Slit/Disordered

[a] The domain spacings (d_0) were estimated by SAXS.
[b] The morphologies were estimated by SAXS and TEM.
[c] The morphologies were estimated by SAXS and SEM.

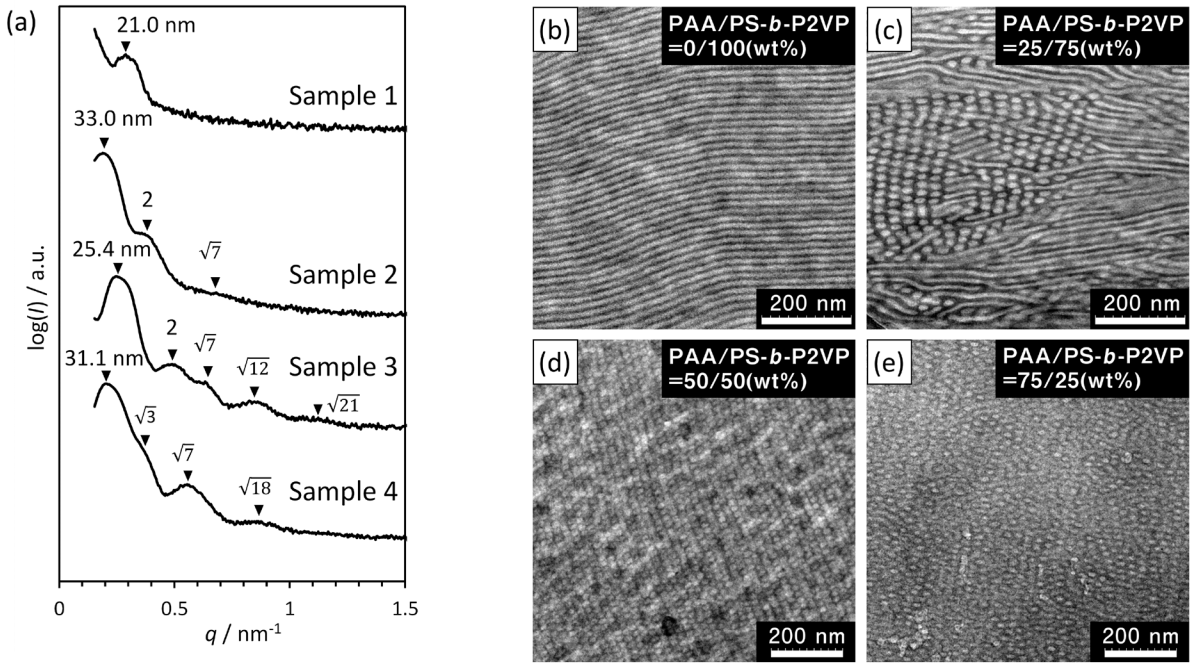

Fig. 3. (a) SAXS profiles and (b-e) TEM images of the PAA/PS-*b*-P2VP composite films (Sample1~4). (b) Sample 1, (c) Sample 2, (d) Sample3, (e) Sample 4. TEM specimens were stained with iodine.

3. Results and discussion

3.1. Self-assembly of crosslinked PAA composite films

The nanostructure of the PAA/PS-*b*-P2VP composite films was studied by investigating several PAA composite films with different composition ratios using SAXS and TEM. The composite films were prepared by solution casting as follows (Fig. 1 and Table 1). A solution of polymers in DMF/THF co-solvent was cast on a polytetrafluoroethylene (PTFE) block, and then the solvent was slowly evaporated at 50 °C for 24 h. The obtained film was dried under reduced pressure at 50 °C for 24 h.

The SAXS profile of pristine PS-*b*-P2VP film Sample 1 (Fig. 3 (a)) showed the first scattering peak, indicating the formation of a microphase-separated structure with domain spacing of 21.0 nm. The TEM image (Fig. 3 (b)) showed darker and brighter linear patterns, suggesting the formation of a well-ordered lamellar structure. The average center-to-center distance of the brighter lines was 16 nm.

The SAXS profile of PAA/PS-*b*-P2VP composite film Sample 2 (Fig. 3 (a)) showed higher-order scattering peaks with q/q^* ratio of 1:2:√7, indicating the formation of ordered nanostructures with domain spacing of 33.0 nm, where q^* was the position of the first-order scattering peak. The TEM image (Fig. 3 (c)) showed a pattern of brighter dots and lines in a darker matrix which corresponds to a PS cylinder domain in a P2VP+PAA matrix.

The SAXS profile of PAA/PS-*b*-P2VP composite film Sample 3 (Fig. 3 (a)) showed higher-order scattering peaks with q/q^* ratio of 1:2:√7:√12: √21, indicating the formation of an ordered nanostructure with domain spacing of 25.4 nm. The TEM image (Fig. 3 (d)) showed a pattern of brighter dots in a darker matrix which corresponds to a PS sphere domain in a P2VP+PAA matrix.

The changing of morphology from the lamella structure of the pristine PS-*b*-P2VP film to PS cylinder or sphere structures of the PAA/PS-*b*-P2VP composite film indicates an increase in the volume fraction of the hydrophilic domain because PAA is miscible with the P2VP segments selectively.

3.2. Self-assembly of PAA composite films

The effect of crosslinking by TAPB on the nanostructure of the composite films was studied by investigating three kinds of samples with different TAPB molar ratios: Sample 5, Sample 6, and Sample 7 (Table 1) with SAXS and TEM. The composition ratio for all the samples was (PAA/PS-*b*-P2VP = 75/25 wt%), which is the same as that of Sample 2.

The SAXS profiles of Sample 5 and Sample 6 (Fig. 4 (a) top and middle) showed higher-order scattering peaks with q/q^* ratio of 1: 2: √7 with domain spacing of 37.8 nm and 1: √3: √7 with domain spacing of 33.0 nm, respectively. This result indicates that cylinder structures were formed. The TEM images (Fig. 4 (b) and (c)) showed PS cylinder structures that were similar to Sample 2.

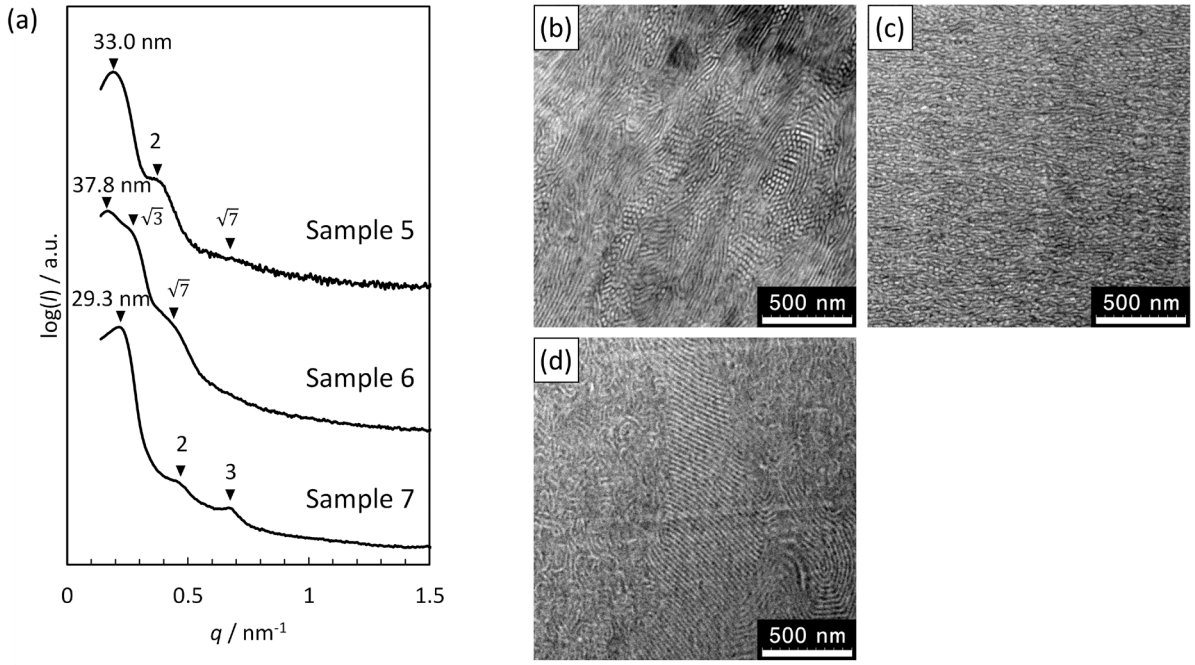

Fig. 4. (a) SAXS profiles and (b-d) TEM images of composite films, (b) Sample 5, (c) Sample 6, and (d) Sample 7. The TEM specimens were stained with iodine.

The SAXS profile of Sample 7 (Fig. 4 (a) bottom) showed higher-order scattering peaks with q/q^* ratio of 1:2:3, indicating the formation of a lamella structure with domain spacing of 29.3 nm. The TEM image (Fig. 4 (d)) indicated a mixture of areas where brighter and darker lines form clear stripes (near the center of the image) and areas where short line-shaped brighter areas are distributed in the darker area matrix (left and upper right of the image).

Compared Fig. 4 (b) with Fig. 4 (c), a less ordered cylinder structure was obtained in Fig. 4 (c). Also, partly less ordered lamellar areas were observed in Fig. 4 (d). These could be attributed to the rearrangement of the polymer chains being limited by many crosslinking points because Sample 6 and Sample 7 had relatively higher TAPB contents. These results suggest that the nanostructures based on the self-assembly of the template block copolymer could be retained even with relatively high TAPB contents.

3.3. Thermal treatment of PAA composite films

Porous crosslinked polyimide films were fabricated by the thermal treatment of crosslinked PAA films at 380 °C for 3 h under a nitrogen flow. The imidization of PAA and degradation of PS-*b*-P2VP were confirmed by TGA and FT-IR.

The TGA profile of the PAA/PS-*b*-P2VP composite film Sample 7 is shown in Fig. 5. The TGA curve showed 15.6 % of weight loss at 250 °C, corresponding to the dehydration of the PAA during imidization and evaporation of the residual solvent.

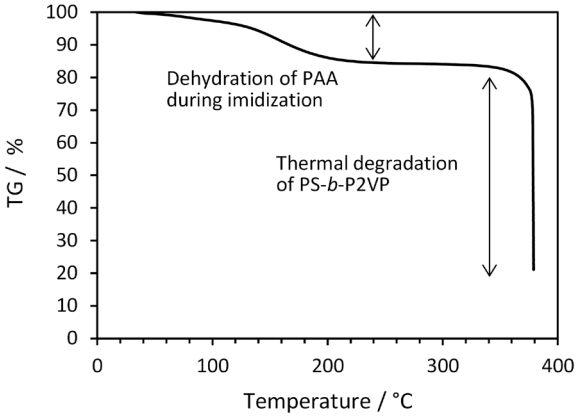

Fig. 5. TGA profile of the PAA/PS-*b*-P2VP composite film (Sample 7).

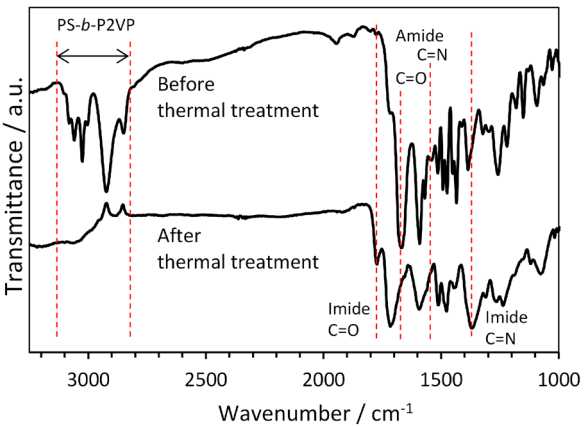

Fig. 6. IR spectra of the PAA/PS-*b*-P2VP composite film (Sample 7), before and after thermal treatment.

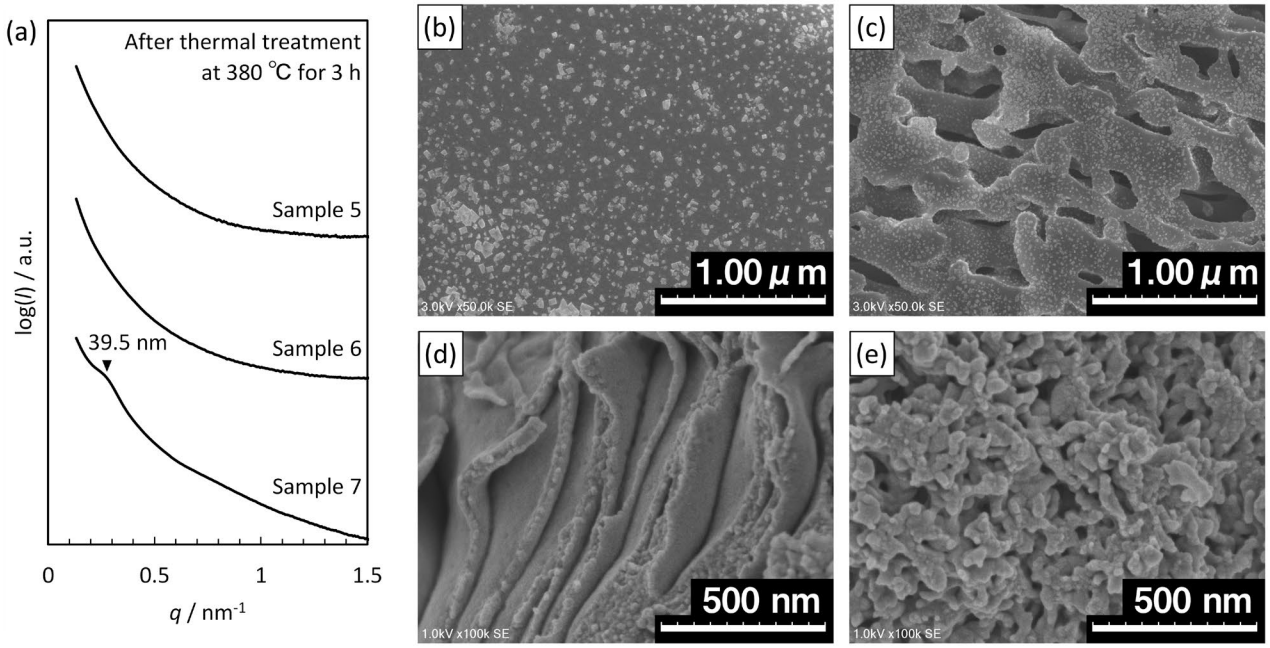

Fig. 7. (a) SAXS profiles and (b-e) SEM images of porous polyimide films after thermal treatment at 380 °C for 3 h. (b,c) Sample 6 and (d,e) Sample 7.

Also, the weight loss corresponding to the degradation of the template block copolymer began at approximately 350 °C. The final weight of the sample was 21.1 % after heating at 380 °C for 3 h, indicating that the degradation of the template block copolymer successfully completed.

The FT-IR spectra of Sample 7 before and after the thermal treatment are shown in Fig.6. On the FR-IR spectra, the peaks at 1779 cm^{-1}(C=O) and 1371 cm^{-1}(C-N) due to polyimide appeared, and the peaks at 1670 cm^{-1} (C=O) and 1542 cm^{-1} (C-N) due to PAA disappeared, which indicate that the complete imidization of the PAA. Moreover, the peaks from 2800 cm^{-1} to 3100 cm^{-1} disappeared, suggesting the degradation of PS-*b*-P2VP.

3.4. Fabrication and characterization of porous crosslinked polyimide film

The effect of crosslinking on the thermal stability of the nanostructure of PAA composite films was studied by investigating three kinds of porous polyimide film: Sample 5, Sample 6, and Sample 7 using SAXS and FE-SEM.

The SAXS profiles of the porous polyimide films are shown in Fig. 7 (a). Sample 5 and 6 (Fig. 7 (a) top and middle) showed no scattering peaks, indicating the collapse of the ordered nanostructures in the PAA composite films. Sample 7 showed only the first peak, indicating that the nanostructures still remained after the thermal treatment.

The FE-SEM images of Sample 6 (Fig. 7 (b) and (c)) showed both the areas with no pores (Fig. 7 (b)) and the area with pores with several hundred nm of diameter (Fig. 7 (c)). This result indicates that the ordered cylindrical nanostructure collapsed, probably due to some fluidity of the polyimide because of lack of crosslinking.

The FE-SEM images of Sample 7 showed that porous lamella structures (Fig. 7 (d)) and disordered porous structures (Fig. 7 (e)) with approximately 50 nm gaps. These porous structures are likely derived from the lamella structures and disordered structures of the PAA composite film, Sample 7 (Fig. 4 (d)).

Thus, it could be concluded that crosslinked mesoporous polyimide films have been successfully obtained via the soft template method using a crosslinkable monomer, TAPB. The porous polyimide films have both well-ordered nanostructures and flexibility.

4. Conclusion

Porous polyimide films were fabricated via the soft-template method using co-assembly of PAA and PS-*b*-P2VP and crosslinking by a trifunctional amine, TAPB. The resulting films exhibit both flexibility and thermally stable nanostructures. The crosslinked PAA composite films formed various microphase-separated structures such as lamella, cylinder, and sphere, depending on the composition ratio of PAA and PS-*b*-P2VP, and the TAPB content. The thermal treatment of the PAA composite films gave porous polyimide films based on the microphase-separated structures. Further studies will be done to expand this methodology to develop various porous and high-performance polymer films.

Acknowledgement

We are grateful to Ryohei Kikuchi (Open Facility Center, Materials Analysis Division, Tokyo Institute of Technology) for the TEM and FE-SEM observations. This study was financially supported by NEDO and JSPS KAKENHI Grant 20H02785.

References

1. D.-J. Liaw, K.-L. Wang, Y.-C. Huang, K.-R. Lee, J.-Y. Lai, and C.-S. Ha, *Prog. Polym. Sci.*, **37** (2012) 907.
2. J. L. Hedrick, R. D. Miller, C. J. Hawker, K. R. Carter, W. Volksen, D. Y. Yoon, and M. Trollsås, *Adv. Mater.*, **10** (1998) 1049.
3. H. Yabu, M. Tanaka, K. Ijiro, and M. Shimomura, *Langmuir*, **19** (2003) 6297.
4. S. Shishatskiy, C. Nistor, M. Popa, S. P. Nunes, and K. V. Peinemann, *Adv. Eng. Mater.*, **8** (2006) 390.
5. G. Li and Z. Wang, *Macromolecules*, **46** (2013) 3058.
6. E. Aram, and S. Mehdipour-Ataei, *Int. J. Polym. Mater. Polym. Biomater.*, **65** (2016) 358.
7. X. M. Tan and D. Rodrigue, *Polymers (Basel).*, **11** (2019) 1310.
8. Y. Tian, S. Liu, H. Ding, L. Wang, B. Liu, and Y. Shi, *Polymer (Guildf).*, **48** (2007) 2338.
9. X. Han, Y. Tian, L. Wang, C. Xiao, and B. Liu, **43** (2007) 4382.
10. A. Martínez-Gómez, C. Alvarez, J. de Abajo, A. del Campo, A. L. Cortajarena, and J. Rodriguez-Hernandez, *ACS Appl. Mater. Interfaces*, **7** (2015) 9716.
11. F. W. Lin, X. L. Xu, L. S. Wan, J. Wu, and Z. K. Xu, *RSC Adv.*, **5** (2015) 30472.
12. L. Xu, Y. Ma, J. Xie, W. Zhang, Z. Wu, and Z. He, *J. Mater. Sci.*, **54** (2019) 5952.
13. H. Munakata, D. Yamamoto, and K. Kanamura, *Chem. Commun.*, **0** (2005) 3986.
14. L. Jiang, J. Liu, D. Wu, H. Li, and R. Jin, *Thin Solid Films*, **510** (2006) 241.
15. H. Munakata, D. Yamamoto, and K. Kanamura, *J. Power Sources*, **178** (2008) 596.
16. Q. Fang, Z. Zhuang, S. Gu, R. B. Kaspar, J. Zheng, J. Wang, S. Qiu, and Y. Yan, *Nat. Commun.*, **5** (2014) 4503.
17. Q. Fang, J. Wang, S. Gu, R. B. Kaspar, Z. Zhuang, J. Zheng, H. Guo, S. Qiu, and Y. Yan, *J. Am. Chem. Soc.*, **137** (2015) 8352.
18. X. Yuan, Y. Wang, G. Deng, X. Zong, C. Zhang, and S. Xue, *Polym. Adv. Technol.*, **30** (2019) 417.
19. C. Wang, T. M. Wang, and Q. H. Wang, *Express Polym. Lett.*, **7** (2013) 667.
20. Y. Liu, K. Ohnishi, S. Sugimoto, K. Okuhara, R. Maeda, Y. Nabae, M. Kakimoto, X. Wang, and T. Hayakawa, *Polym. Chem.*, **5** (2014) 6452.
21. L. Gao, K. Azuma, Y. Kushima, K. Okuhara, A. Chandra, and T. Hayakawa, *J. Photopolym. Sci. Technol.*, **29** (2016) 247.
22. Y. Nabae, S. Nagata, K. Ohnishi, Y. Liu, L. Sheng, X. Wang, and T. Hayakawa, *J. Polym. Sci. Part A Polym. Chem.*, **55** (2017) 464.
23. T. Komamura and T. Hayakawa, *J. Photopolym. Sci. Technol.*, **30** (2017) 173.
24. L. Gao, A. Chandra, Y. Nabae, and T. Hayakawa, *Polym. J.*, (2018) 389.
25. T. Komamura, K. Okuhara, S. Horiuchi, Y. Nabae, and T. Hayakawa, *ACS Appl. Polym. Mater.*, **1** (2019) 1209.
26. T. Komamura, K. Azuma, Y. Nabae, and T. Hayakawa, *J. Photopolym. Sci. Technol.*, **33** (2020) 573.

Journal of Photopolymer Science and Technology
Volume 34, Number 5 (2021) 439−448 ©2021SPST

Orientation Control of the Microphase-separated Nanostructures of Block Copolymers on Polyimide Substrates

Hayato Maeda, Yuta Nabae, and Teruaki Hayakawa*

Department of Materials Science and Engineering, School of Materials and Chemical Technology, Tokyo Institute of Technology,
2-12-1-S8-36, Ookayama, Meguro-ku, Tokyo 152-8552, Japan
**hayakawa.t.ac@m.titech.ac.jp*

This study aimed to form a perpendicularly orientated lamellar structure with polystyrene-*block*-poly(methyl methacrylate) (PS-*b*-PMMA) by its microphase separation on a polyimide substrate. Eight types of polyimides were prepared from different combinations of monomers and tested as the bottom layer for the microphase separation of PS-*b*-PMMA. The surface free energies of those polyimide substrates were evaluated by the Owens-Wendt method. Thin films of PS-*b*-PMMA were prepared on the polyimide substrates and the self-assembly was induced by thermal annealing, and the surface architecture was observed by atomic force microscopy. In the tested polyimide substrates, only one from 2,2-bis[4-(3,4-dicarboxyphenoxy) phenyl]propane dianhydride (tetracarboxylic dianhydride) and 1,12-bis (4-aminophenoxy) dodecane (diamine) showed a perpendicularly oriented lamellar structure. This polyimide substrate shows one of the smallest polar components in its surface free energy. Relatively large domain size and long correlation length in the PS-*b*-PMMA layer were obtained by optimizing the conditions for fabrication of the polyimide substrate, which were prepared by casting the polyimide onto a silicon wafer, followed by thermal annealing. These results suggest that the combination of one monomer with relatively large molecular weight, which will result in a low density of imide groups, and the other monomer with long alkyl chains, which will reduce the polarity of the resulting polyimide, contributes to providing a perpendicular orientation.

Keywords: Block copolymer, Polyimide, Microphase-separated nanostructure, Thin films, Orientation control

1. Introduction

Block copolymer (BCP) lithography is considered to be one of the promising technologies for the next-generation lithography [1–4] In the BCP lithography, line and dot resist patterns are required to be fabricated by the microphase separation of BCPs, to draw circuit patterns on silicon substrates. For this purpose, the microphase separated lamellar structures are required to be perpendicularly oriented against their substrates, whereas many of BCPs tend to form parallelly oriented lamellae reflecting the interfacial free energy of the interfaces consisting of the BCP domains, the bottom surface, and the top surface (typically air) [5]. In the case of a typical polymer for the BCP lithography, polystyrene-*block*-poly(methyl methacrylate) (PS-*b*-PMMA), the strong affinity of the PMMA domain and the silicon substrate results in a parallel orientation [6]. There have been several ways to induce perpendicular orientation as follows: solvent annealing [7], application of an electric field [8], and modification of the substrate by neutral layers [9–20]. The most common method is to cast a random copolymer (RCP) mainly consisting of PS and PMMA, as a neutral layer to balance the interfacial free energies of the PS/substrate and PMMA/substrate interfaces.

On the other hand, the development of flexible devices has recently received a great deal of attention [21]. For this purpose, polyimides (PIs)

Received April 2, 2021
Accepted May 5, 2021

have been considered to be suitable for the flexible substrate due to their mechanical, chemical, and thermal strength. Furthermore, PIs have been proven to be biocompatible [22] and are expected to be applied in the biomedical field recently [23,24]. In this context, technologies for fabricating fine circuit patterns onto PI substrates have been extensively studied [25,26]. The application of the BCP lithography on flexible substrates has also been attempted [13,27–32]. In the typical BCP lithography on flexible substrates, the perpendicular orientation has been achieved by fabricating a neutral layer between the substrate and BCP, which is a similar approach to those on silicon substrates. If the neutral layer becomes unnecessary for the BCP lithography on flexible substrates, these technologies will be more attractive.

In this context, our research group has been motivated to achieve the direct fabrication of perpendicularly oriented lamellae of PS-*b*-PMMA onto PI substrates without any neutral layers. We assume that this could be achieved if the interfacial free energies of the PS/PI and PMMA/PI interfaces are balanced, and the molecular structure of PI needs to be carefully designed. Considering the fact that PIs can be easily synthesized by polycondensation of tetracarboxylic dianhydrides and diamines [33], an adequate design could be achieved by carefully selecting the molecular structures of the monomers.

The objective of this study is to demonstrate a perpendicularly oriented lamella of PS-*b*-PMMA on a PI substrate as illustrated in Fig. 1. Eight types of PIs listed in Table 1 were tested as the substrate for PS-*b*-PMMA. The chemical structures of the monomers for these PIs are shown in Fig. 2. The PI layers were fabricated by casting the solutions of poly(amic acid)s (PAAs) and heating the layers on a silicon wafer for imidization. The surface free energies of the substrates with PIs were evaluated by the Owens-Wendt method for the contact angles [34]. Thin films of PS-*b*-PMMA were prepared on the PI substrates and thermally annealed to induce the self-assembly. The surface architecture of the obtained films was characterized by atomic force microscopy (AFM). The correlation among the monomer structure for PI, the surface free energy of PI, and the resulting surface architecture of PS-*b*-PMMA is discussed in terms of comparison against the self-assembly of PS-*b*-PMMA on a typical neutral layer, a RCP of PS, PMMA, and poly(glycidyl methacrylate) (PS-*r*-PMMA-*r*-PGMA).

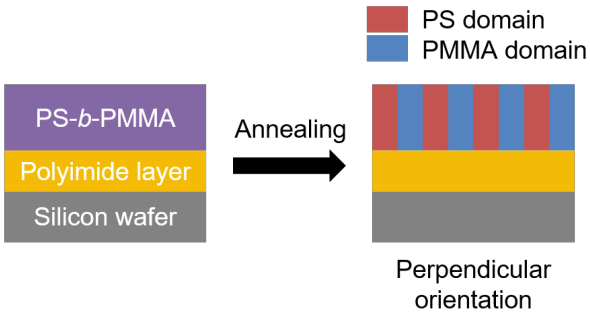

Fig. 1. Schematic illustration for orientation control of the microphase-separated lamellar nanostructures of block copolymers on a substrate with PI.

Table 1. Combination of the monomers and polymerization conditions

Label	Tetracarboxylic dianhydride	Diamine	Solvent	Reaction period (h)	η_{inh} (dL g^{-1})
PI1	PMDA	ODA	DMAc	3	1.27
PI2	6FDA	*m*-Tolidine	-	-	-
PI3	6FDA	TFMB	DMF	24	0.65
PI4	6FDA	DA5MG	-	-	-
PI5	BPDA	*m*-Tolidine	-	-	-
PI6	TAHQ	DA10MG	NMP	24	0.91
PI7	TAHQ	DA12MG	NMP	24	0.98
PI8	BPADA	DA12MG	NMP	3	0.70

2. Experimental

2.1. Materials

Styrene, methyl methacrylate (MMA) and glycidyl methacrylate (GMA) were distilled over calcium hydride. The purified styrene and MMA for living anionic polymerization were further distilled over di-*n*-butylmagnesium and tri-*n*-octylaluminium, respectively. 1,1-Diphenylethylene was distilled over *n*-butyllithium. 2,2'-Azobis (isobutyronitrile) was recrystallized from methanol (MeOH). PMDA was recrystallized from acetic anhydride. 4,4'-(Hexafluoroisopropylidene) diphthalic anhydride (6FDA) was recrystallized from a solution of acetic acid and acetic anhydride. 1,4-Phenylene bis (1,3-dioxo-1,3-dihydroisobenzofuran-5-carboxylate) (TAHQ) was recrystallized from 1,4-dioxane. 2,2-Bis [4-(3,4-dicarboxyphenoxy) phenyl] propane dianhydride (tetracarboxylic dianhydride) (BPADA) was recrystallized from a solution of toluene and acetic anhydride. ODA was recrystallized from ethanol. 2,2'-Bis (trifluoromethyl) benzidine (TFMB) was recrystallized from MeOH. 1,10-Bis (4-aminophenoxy) decane (DA10MG), 1,12-bis (4-aminophenoxy) dodecane (DA12MG), and all the

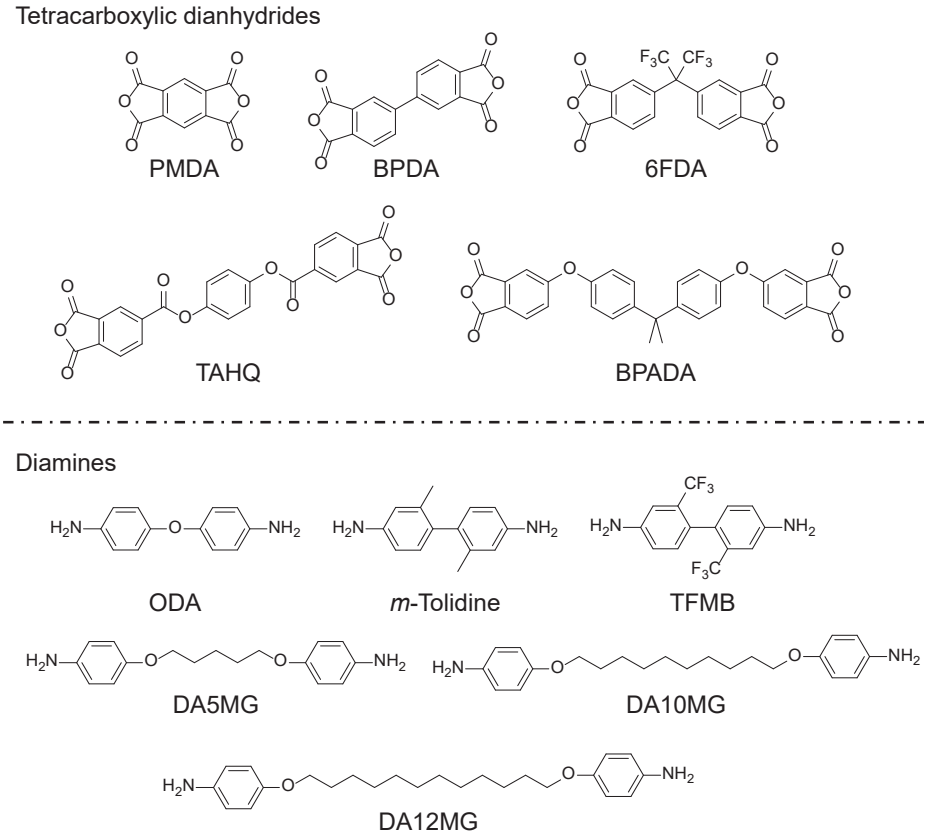

Fig. 2. Molecular structures and abbreviations of monomers used.

other chemicals were used as received without further purification. The substrates with PI2, PI4 and PI5 represent the PI using 4,4'-biphthalic anhydride (BPDA), *m*-tolidine and 1,5-bis (4-aminophenoxy) pentane (DA5MG), respectively, as shown in Table 1. The substrates coated with these PIs were supplied by a chemical company, and used as received.

2.2. Measurements

^{1}H nuclear magnetic resonance (^{1}H-NMR) for PS-*b*-PMMA and PS-*r*-PMMA-*r*-PGMA were performed at room temperature on a JEOL ECS400 spectrometer. The number-average and weight-average molecular weights (M_n and M_w) were determined by the size exclusion chromatography (SEC) using a Shodex GPC-101 system equipped with a refractive index detector and a LF-804 column (Showa Denko) with tetrahydrofuran (THF) as the eluent. Small angle X-ray scattering (SAXS) for the bulk polymer sample was performed using a Bruker NanoSTAR (50 kV/50 mA) with a 2D-PSPC detector (camera length of 1055 mm). The inherent viscosities of the PAAs were determiend by the viscometry for 0.5 g dL^{-1} of polymer solutions in *N*,*N*-dimethylacetamide (DMAc), *N*,*N*-dimethylformamide (DMF), or *N*-methyl-2-pyrrolidone (NMP) at 30 °C using an Ostwald viscometer. The thickness of the polymer films was measured by a FILMETRICS F20-EXR. Contact angles of water and diiodomethane on the PI substrates were measured using a Kyowa DM-501YH. AFM was performed using a JPK NanoWizard Ultra Speed AFM system.

2.3. Polymer synthesis

2.3.1 PS-*b*-PMMA

PS-*b*-PMMA was synthesized *via* living anionic polymerization. All the polymerization procedures were performed under an argon purge. THF (50 mL) and lithium chloride (11.0 mg, 0.26 mmol) were transferred to a 100 mL schlenk flask and then cooled to −78 °C. *sec*-Butyllithium for drying THF was added until the color changed to light yellow. After treating the flask at room temperature to deactivate the *sec*-butyllithium for drying, the flask was cooled again to −78 °C, and *sec*-butyllithium solution in *n*-hexane (50 μL, 0.05 mmol) was added as the initiator. Styrene (1.82 mL, 15.9 mmol) was added and stirred for 30 min, until the color changed to bright orange, followed by the addition of 1,1-diphenylethylene (45 μL, 0.26 mmol), resulting in a

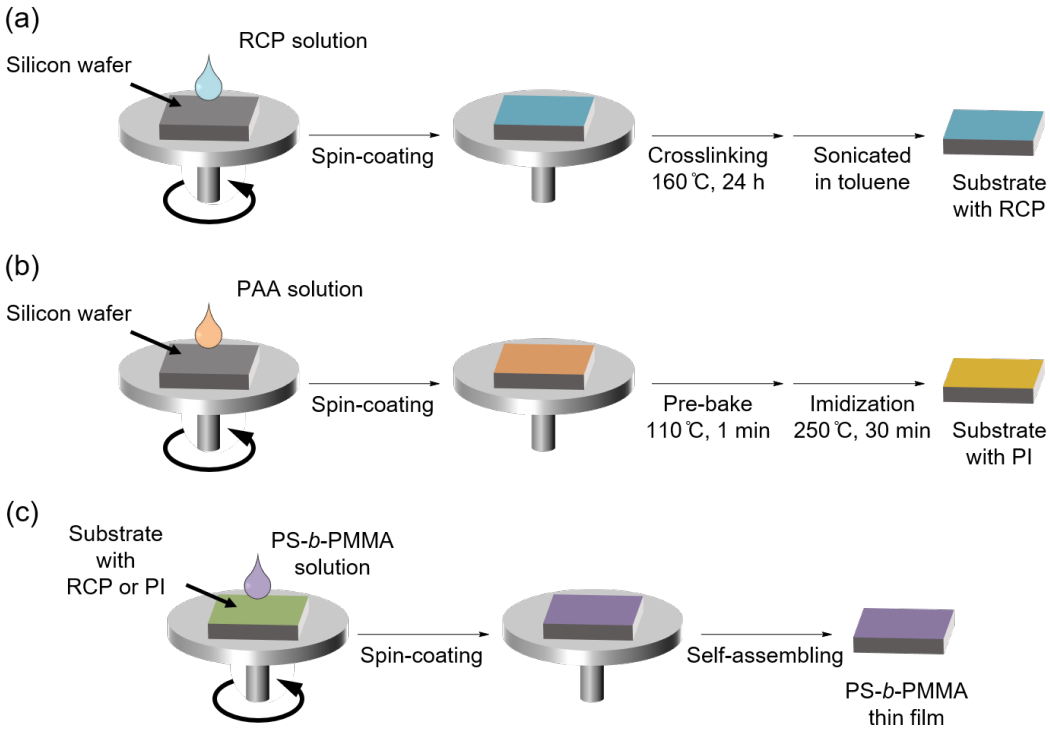

Fig. 3. Preparation of (a) RCP substrate, (b) PI substrates, and (c) PS-*b*-PMMA thin film on each of the substrates.

deep red color. After 30 min of stirring, MMA (2.00 mL, 18.8 mmol) was added and further stirred for 30 min, until the solution became colorless. Then, 5 mL of MeOH (excess amount) purged with argon was added to the flask for termination. The polymer was precipitated into an excessive amount of MeOH and filtered. The residue was dried under a reduced pressure overnight to yield whitish powder (2.76 g, 78% yield). M_n: 46.3 kDa. M_w/M_n: 1.13. ^{1}H-NMR (400 MHz, $CDCl_3$, δ, ppm): 0.70-1.05 (br, 3H, C*H*$_3$), 1.20-1.55 (br, 2H, back bone C*H*$_2$CH), 1.70-2.23 (br, 3H, back bone CH$_2$C*H*, back bone C*H*$_2$C), 3.40-3.84 (br, 3H, C*H*$_3$O), 6.33-6.91 (br, 2H, aromatic ortho), 6.92-7.24 (br, 3H, aromatic meta and para).

2.3.2. PS-*r*-PMMA-*r*-PGMA

PS-*r*-PMMA-*r*-PGMA was synthesized *via* free radical polymerization. 2,2'-Azobis(isobutyronitrile) (0.016 g, 0.1 mmol), styrene (1.145 mL, 10 mmol), MMA (1.04 mL, 9.8 mmol), and GMA (0.021 mL, 0.2 mmol) were added to a 20 mL schlenk tube, and the solution was degassed by three freeze-pump-thaw cycles and backfilled with argon gas. The solution was stirred at 80 °C for 2 h. The polymerization was quenched by rapid cooling in liquid nitrogen. The crude product was diluted with THF, precipitated into an excessive amount of MeOH, and filtered. The residue was dried under a reduced pressure overnight to yield whitish powder (1.59 g, 77 % yield). M_n: 54 kDa. M_w/M_n: 2.29. ^{1}H-NMR(400 MHz, $CDCl_3$, δ, ppm): 0.24–1.08, 1.10–1.36, 1.37–2.08, 2.09–2.50, 2.62–3.04, 3.10–3.70, 6.40–7.40.

2.3.3 PAAs

All PAAs were synthesized *via* polyaddition of tetracarboxylic dianhydride and diamines. The synthetic scheme, combinations of the monomers, polymerization conditions, and inherent viscosities were presented in Scheme 1 and Table 1. An example of the synthesis is as follows. In a 100 mL three-necked flask purged with nitrogen, ODA (1.00 g, 5.0 mmol) was dissolved in 10 mL of DMAc at room temperature with a mechanical stirrer. Next, PMDA (1.09 g, 5.0 mmol) was added to the solution, and the mixture was left to be stirred for 3 h. Subsequently, the solution was diluted with 30 mL of DMAc and the solution was reprecipitated into an excessive amount of MeOH and filtered. The residue was dried under a reduced pressure at 40 °C overnight to yield yellowish solid.

2.4. Preparation of the bulk sample of PS-*b*-PMMA

The bulk sample for the morphology study was prepared by slowly evaporating a dilute solution of PS-*b*-PMMA in chloroform at room temperature, followed by drying under reduced pressure at 170 °C for 24 h.

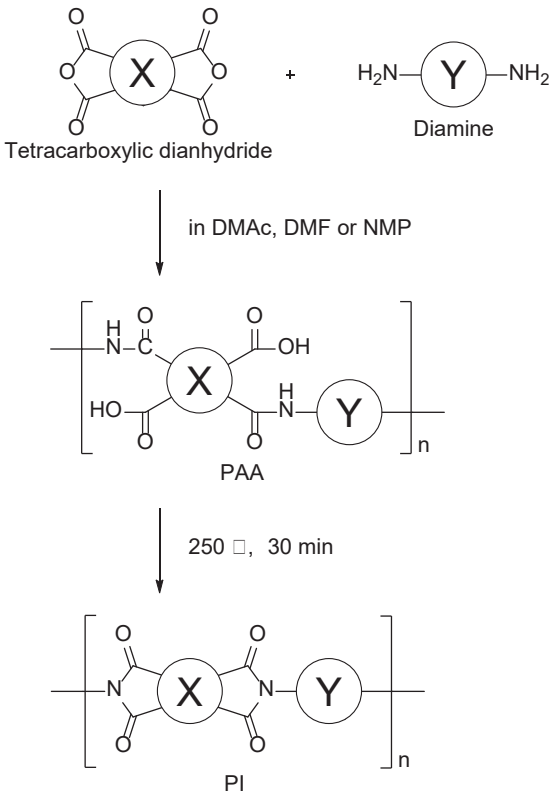

Scheme 1. Synthetic scheme of PAA and PI.

2.5. Preparation of the substrates

2.5.1. Substrate with a RCP

Silicon wafer was cut into 1 cm^2 piece, and sonicated in acetone, chloroform, and isopropyl alcohol for 30 min each., and then rinsed with ethanol. Next, the wafer was treated with a mixture of H_2O_2 (30%) and H_2SO_4 (70%) (v/v) at 100 °C for 2 h, and rinsed with water and ethanol. As shown in Fig. 3(a), the RCP layer was fabricated by spin-coating a PS-*r*-PMMA-*r*-PGMA solution in toluene (1 wt%) onto the cleaned silicon substrate at 3000 rpm for 30 s using a MIKASA spin coater IH-D7. The spin-coated substrate was treated at 160 °C for 24 h for cross-linking, and the unreacted polymer was removed by sonicating the substrate in toluene.

2.5.2. Substrates with PI layers

An example of preparation is as follows. Silicon wafer was cut and treated in the above-mentioned manner. As shown in Fig. 3(b), a layer was fabricated by spin-coating a 1.5 wt% PAA solution in NMP at 3000 rpm for 30 s, and drying it at 110 °C for 1 min under a nitrogen flow. And then the substrate was treated at 250 °C for 30 min under a reduced pressure for imidization as shown in Scheme 1.

2.6. Preparation of PS-*b*-PMMA thin films on the substrates

As shown in Fig. 3(c), a PS-*b*-PMMA thin film was fabricated by spin-coating a 1.2 wt% PS-*b*-PMMA solution in toluene at 3000 rpm for 30 s onto the substrate prepared in the above-mentioned manner. This condition provided *ca*. 1.3 L_0 of thickness (1 L_0 is a period of the lamellar domain). The fabricated thin films were annealed under the conditions listed in Table 2.

Table 2. The surface free energies of the substrates and annealing condition for PS-*b*-PMMA thin films

Substrate	Total surface free energy (mJ m^{-2})	Polar component (mJ m^{-2})	Dispersion component (mJ m^{-2})	Annealing condition of PS-*b*-PMMA thin film
RCP(PS-*r*-PMMA-*r*-PGMA)	43.1	0.5	42.6	230 ℃, 1 h
RCP(PS-*r*-PMMA-*r*-PGMA)				170 ℃, 24 h
PI1(PMDA/ODA)	46.5	1.2	45.3	230 ℃, 1 h
PI1(PMDA/ODA)				170 ℃, 24 h
PI2(6FDA/*m*-Tolidine)	39.3	1.1	38.2	170 ℃, 24 h
PI3(6FDA/TFMB)	39.0	0.3	38.7	170 ℃, 24 h
PI4(6FDA/DA5MG)	41.5	0.5	41.0	170 ℃, 24 h
PI5(BPDA/*m*-Tolidine)	45.9	1.7	44.2	170 ℃, 24 h
PI6(TAHQ/DA10MG)	46.7	1.7	45.0	170 ℃, 24 h
PI7(TAHQ/DA12MG)	43.6	1.6	42.0	170 ℃, 24 h
PI8(BPADA/DA12MG)	47.1	0.3	46.8	170 ℃, 24 h

3. Results and discussion

3.1. Characterization of PS-*b*-PMMA

PS-*b*-PMMA was synthesized *via* living anionic polymerization. The volume fraction of the PS block was determined as 51 vol% based on the ^{1}H NMR spectrum and the polymer densities (PS: 1.05 g cm^{-3}, PMMA: 1.18 g cm^{-3}) [35].

The microphase-separated morphology of the bulk sample was analyzed by SAXS as shown in Fig 4. The scattering pattern clearly suggests the formation of a lamellar structure, and the *d*-spacing was determined as 33 nm based on the first-order scattering peak. Thus, L_0 of this polymer was considered to be 33 nm in the following study.

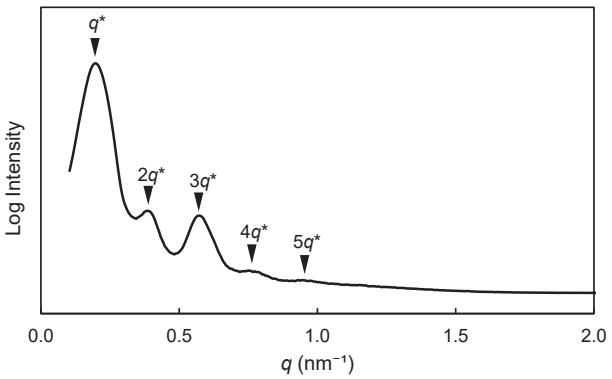

Fig. 4. SAXS 1D profile of a PS-*b*-PMMA bulk annealed at 170 ℃ for 24 h.

3.2. Orientation property of PS-*b*-PMMA thin films on the substrates

The surface free energy of each substrate was evaluated *via* the water and diiodomethane contact angle measurements based on the Owens–Wendt method, and the results are summarized in Table 2. In comparison against RCP, the polar components of the surface free energies with PI surfaces tend to be higher, but some PI surfaces showed similar values to that with RCP. The correlation between the surface free energy and the resulting microphase separation of PS-*b*-PMMA is discussed in the following sections.

The AFM images of thin films on the RCP and PI1 substrates are shown in Fig. 5(a-h). The images with the RCP substrate clearly showed fingerprint patterns, suggesting the perpendicular orientation of PS-*b*-PMMA (Fig. 5(d)). In contrast, the images with the PI1 substrate annealed at 170 °C for 24 h (Fig. 5(e)) showed a hole pattern with 1 L_0 depth, which was confirmed by the cross-sectional profile (Fig. 5(i)). This hole pattern is probably derived from the segregation of the PMMA domain on the PI1 substrate, as illustrated in Fig. 5(j) [36–38]. This suggests that the polarity of PI1 is too high to achieve the perpendicular orientation, and PI substrates with less polarity will be of interest.

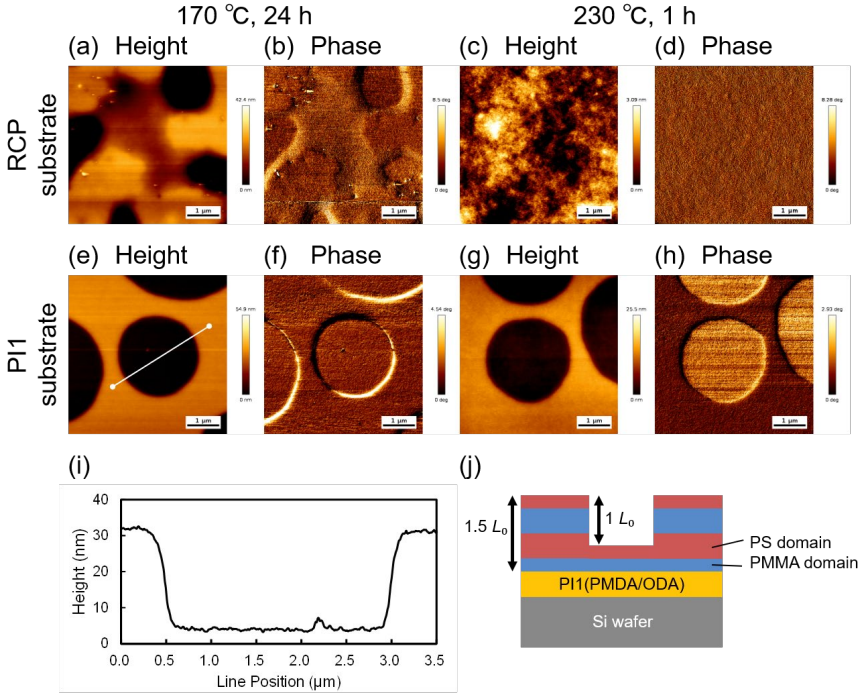

Fig. 5. AFM (a) height and (b) phase images (scale: 5 μm × 5 μm) of the PS-*b*-PMMA thin film on the substrate with RCP annealed at 170 °C for 24 h. AFM (c) height and (d) phase images (scale: 5 μm × 5 μm) of the film on RCP annealed at 230 °C for 1 h. AFM (e) height and (f) phase images (scale: 5 μm × 5 μm) of the PS-*b*-PMMA thin film on the substrate with PI1 annealed at 170 °C for 24 h. AFM (g) height and (h) phase images (scale: 5 μm × 5 μm) of the film on PI1 annealed at 230 °C for 1 h. (i) The cross-sectional profile of the white line in the image e. (j) Illustration of showing the orientation of e. PS-*b*-PMMA concentration: 1.2 wt%.

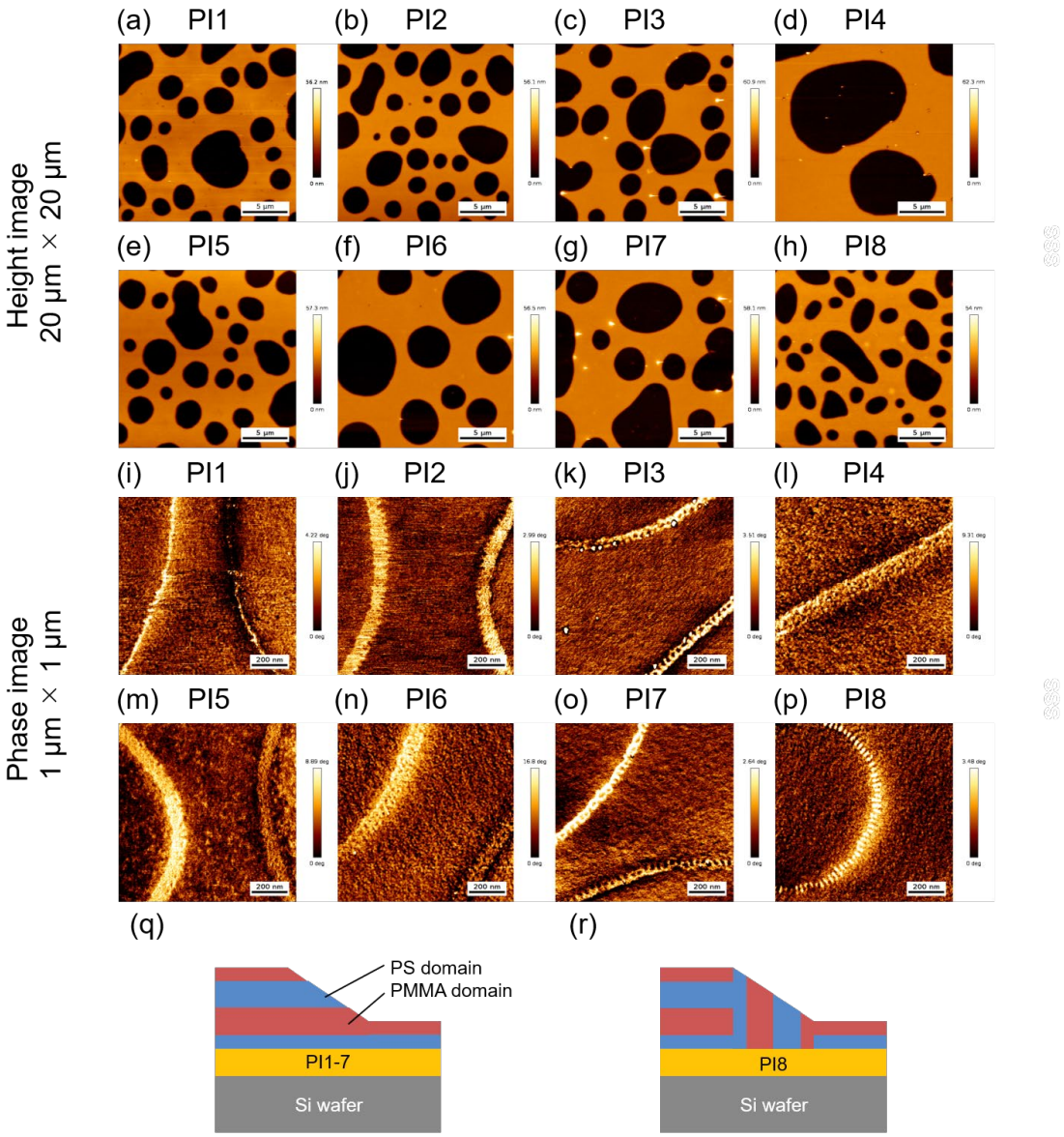

Fig. 6. AFM height images (scale: 20 μm × 20 μm) of the PS-*b*-PMMA thin films on the substrates with (a) PI1, (b) PI2, (c) PI3, (d) PI4, (e) PI5, (f) PI6, (g) PI7, and (h) PI8 annealed at 170 °C for 24 h. AFM phase images (scale: 1 μm × 1 μm) of the PS-*b*-PMMA thin films on the substrates with (i) PI1, (j) PI2, (k) PI3, (l) PI4, (m) PI5, (n) PI6, (o) PI7, and (p) PI8 annealed at 170 °C for 24 h. Illustrations showing the orientation of the PS-*b*-PMMA thin films on the substrates with (q) PI1-7 and (r) PI8. PS-*b*-PMMA concentration: 1.2 wt%.

The AFM images of thin films on the PI substrates are shown in Fig. 6(a-p). The film thickness of each thin film was approximately 1.3 L_0 before annealing. While all the PI substrates showed hole patterns of PS-*b*-PMMA, the edges of the holes seem to be different among the samples. While the images in Fig. 6(i-o) show smooth edges for the holes, Fig. 6(p) shows a dotted fringe pattern. This difference could be explained as follows. The PI substrates for Fig. 6(i-o) probably formed lamellar structures as illustrated in Fig. 6(q), and such edges could be quite smooth without any discontinuous dots. In contrast, if the edge region was perpendicularly oriented as illustrated in Fig. 6(r), the AFM image could show some discontinuous dots as seen in Fig. 6(p). This phenomenon is reasonable if one considers that PI8 has shown one of the lowest polar components in Table 2. Introducing a long alkyl chain in the amine monomer, and selecting a relatively large molecular unit for the tetracarboxylic dianhydride monomer might have contributed to lowering the polarity of the resulting polyimide, and provided a suitable interfacial energy for the PS-*b*-PMMA/substrate interface.

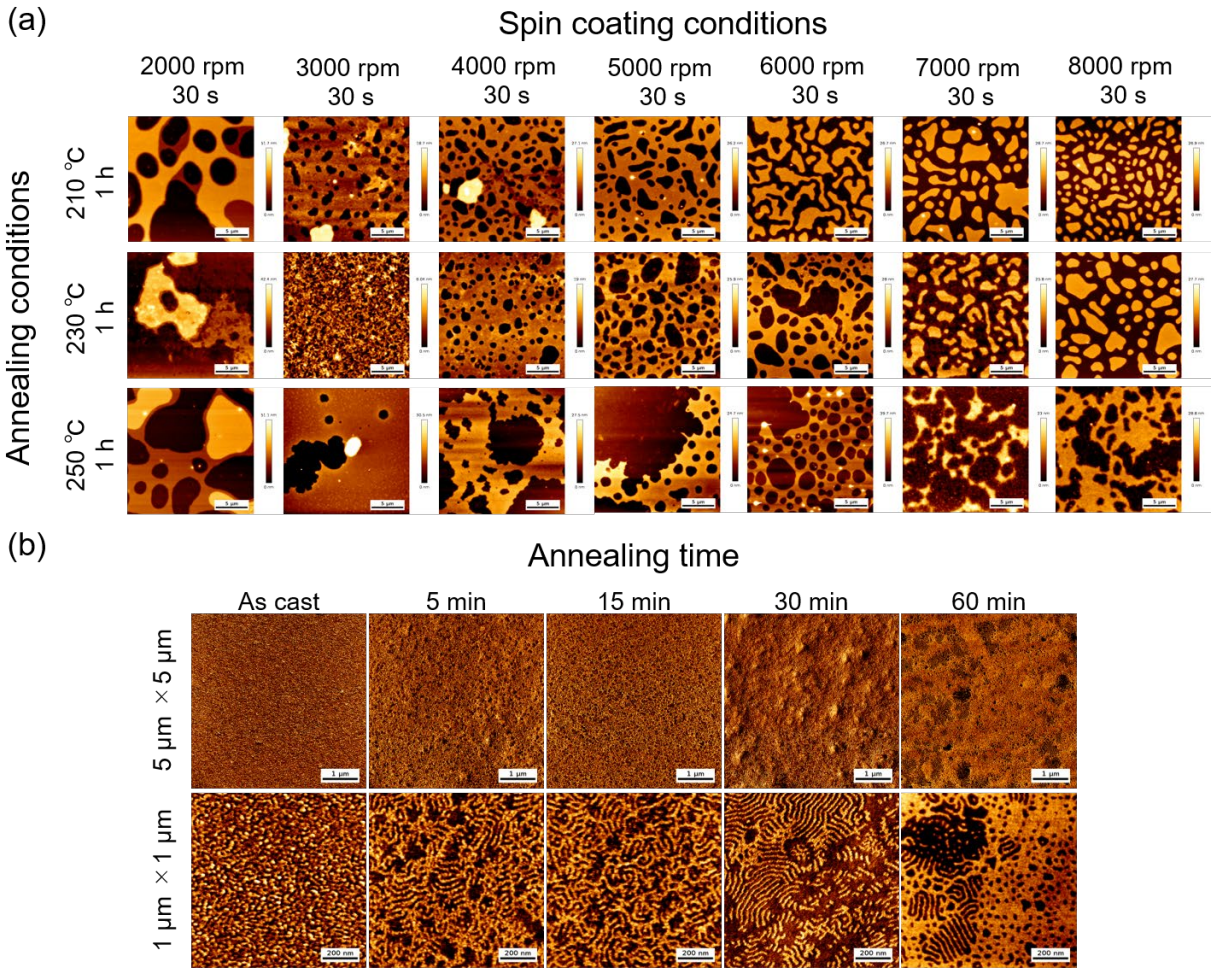

Fig. 7. (a) AFM height images (scale: 20 μm × 20 μm) of the PS-*b*-PMMA thin films on the substrates with PI8 which were annealed at 210 °C, 230 °C, or 250 °C for 1 h, and spin-coated at that the rotation speed were to 2000 rpm, 3000 rpm, 4000 rpm, 5000 rpm, 6000 rpm, 7000 rpm, or 8000 rpm for 30 min. (b) AFM phase images (scale: 5 μm × 5 μm and 1 μm × 1 μm) of the PS-*b*-PMMA thin films on the substrates with PI8 which were annealed at 230 °C for 0 min, 5 min, 15 min, 30 min, or 60 min. PS-*b*-PMMA concentration: 1.0 wt%.

3.3. Investigation of optimal conditions for perpendicular orientation of microdomains in PS-*b*-PMMA thin films on PI8 (BPADA/DA12MG)

Since PI8 showed the perpendicular orientation in a quite limited area, the conditions for the film fabrication on the PI8 substrate were further optimized. At first, the rotation speed and the annealing temperature were optimized as shown in Fig. 7(a). Among the tested conditions, 3000 rpm and 230 °C provided the smoothest surface, whereas other conditions resulted in island and hole structures. This rotation speed provided a film thickness of 0.9 L_0. And then, the annealing time was varied to determine the optimized condition, as shown in Fig. 7(b). In the tested annealing lengths, 30 min provided the best result, showing a clear fingerprint pattern, although its correlation length needs to be further improved.

To the best of our knowledge, this is the first report to demonstrate a direct fabrication of perpendicularly oriented lamellae of PS-*b*-PMMA onto a PI substrate without any neutral layers. We believe that the present findings are quite promising for the development of various flexible devices in the near future.

4. Conclusion

Aiming for direct fabrication of perpendicularly oriented lamellae of PS-*b*-PMMA onto a PI substrate, eight types of polyimides were prepared from different combinations of monomers, and tested as the bottom layer for the microphase separation of PS-*b*-PMMA. Among the tested PI substrates, only the PI substrate prepared from BPADA/DA12MG showed a perpendicular orientation. This PI showed one of the smallest

polar components of the surface free energy, probably owing to the long alkyl chain in the amine monomer and a large molecular unit in the tetracarboxylic dianhydride monomer. Further studies require to be done for obtaining more large domains of the self-assemble structure, and expand this methodology for future applications.

Acknowledgements

Part of this work was supported by the JSPS KAKENHI Grant 20H02785 and the New Energy and Industrial Technology Development Organization (NEDO).

References

1. H. C. Kim, S. M. Park, W. D. Hinsberg, and I. R. Division, *Chem. Rev.*, **110** (2010) 146.
2. C. M. Bates, M. J. Maher, D. W. Janes, C. J. Ellison, and C. G. Willson, *Macromolecules*, **47** (2014) 2.
3. G. Jeong, D. M. Yu, J. K. D. Mapas, Z. Sun, J. Rzayev, and T. P. Russell, *Macromolecules*, **50** (2017) 7148.
4. J. K. D. Mapas, T. Thomay, A. N. Cartwright, J. Ilavsky, and J. Rzayev, *Macromolecules*, **49** (2016) 3733.
5. G. Coulon, T. P. Russell, V. R. Deline, and P. F. Green, *Macromolecules*, **22** (1989) 2581.
6. B. H. Sohn and S. H. Yun, *Polymer (Guildf).*, **43** (2002) 2507.
7. J. Bang, S. H. Kim, E. Drockenmuller, M. J. Misner, T. P. Russell, and C. J. Hawker, *J. Am. Chem. Soc.*, **128** (2006) 7622.
8. T. L. Morkved, M. Lu, A. M. Urbas, E. E. Ehrichs, H. M. Jaeger, P. Mansky, and T. P. Russell, *Science.*, **273** (1996) 931.
9. P. Mansky, Y. Liu, E. Huang, T. P. Russell, and C. Hawker, *Science.*, **275** (1997) 1458.
10. E. Huang, L. Rockford, T. P. Russell, and C. J. Hawker, *Nature*, **395** (1998) 757.
11. R. D. Peters, X. M. Yang, T. K. Kim, B. H. Sohn, and P. F. Nealey, *Langmuir*, **16** (2000) 4625.
12. S. O. Kim, H. H. Solak, M. P. Stoykovich, N. J. Ferrier, J. J. De Pablo, and P. F. Nealey, *Nature*, **424** (2003) 411.
13. D. Y. Ryu, K. Shin, E. Drockenmuller, C. J. Hawker, and T. P. Russell, *Science.*, **308** (2005) 236.
14. I. In, Y. H. La, S. M. Park, P. F. Nealey, and P. Gopalan, *Langmuir*, **22** (2006) 7855.
15. E. Han, K. O. Stuen, Y. H. La, P. F. Nealey, and P. Gopalan, *Macromolecules*, **41** (2008) 9090.
16. S. Ham, C. Shin, E. Kim, D. Y. Ryu, U. Jeong, T. P. Russell, and C. J. Hawker, *Macromolecules*, **41** (2008) 6431.
17. R. Guo, E. Kim, J. Gong, S. Choi, S. Ham, and D. Y. Ryu, *Soft Matter*, **7** (2011) 6920.
18. W. Lee, S. Park, Y. Kim, V. Sethuraman, N. Rebello, V. Ganesan, and D. Y. Ryu, *Macromolecules*, **50** (2017) 5858.
19. Z. Jiang, M. M. Alam, H. H. Cheng, I. Blakey, and A. K. Whittaker, *Nanoscale Adv.*, **1** (2019) 3078.
20. J. Zhao, F. J. McCallum, Z. Jiang, J. A. Kaitz, J. F. Cameron, P. Trefonas, I. Blakey, H. Peng, and A. K. Whittaker, in *Advances in Patterning Materials and Processes XXXVIII*, eds. D. Guerrero and D. P. Sanders, SPIE, **11612** (2021) 29.
21. Z. Bao and X. Chen, *Adv. Mater.*, **28** (2016) 4177.
22. R. R. Richardson, J. A. Miller, and W. M. Reichert, *Biomaterials*, **14** (1993) 627.
23. P. J. Rousche, D. S. Pellinen, D. P. Pivin, J. C. Williams, R. J. Vetter, and D. R. Kipke, *IEEE Trans. Biomed. Eng.*, **48** (2001) 361.
24. J. L. Charest, L. E. Bryant, A. J. Garcia, and W. P. King, *Biomaterials*, **25** (2004) 4767.
25. B. Cui, Y. Cortot, and T. Veres, *Microelectron. Eng.*, **83** (2006) 906.
26. C. Y. Chiu and Y. C. Lee, *J. Micromechanics Microengineering*, **19** (2009) 105001.
27. S. Park, D. H. Lee, and T. P. Russell, *Adv. Mater.*, **22** (2010) 1882.
28. G. Singh, K. G. Yager, D. M. Smilgies, M. M. Kulkarni, D. G. Bucknall, and A. Karim, *Macromolecules*, **45** (2012) 7107.
29. J. Y. Kim, B. H. Kim, J. O. Hwang, S.-J. Jeong, D. O. Shin, J. H. Mun, Y. J. Choi, H. M. Jin, and S. O. Kim, *Adv. Mater.*, **25** (2013) 1331.
30. J. H. Kim, S. S. Kim, and B. H. Sohn, *J. Mater. Chem. C*, **3** (2015) 1507.
31. J. H. Cho, R. Katsumata, S. X. Zhou, C. Bin Kim, A. R. Dulaney, D. W. Janes, and C. J. Ellison, *ACS Appl. Mater. Interfaces*, **8** (2016) 7456.
32. A. Hayirlioglu, M. Kulkarni, G. Singh, A. M. Al-Enizi, I. Zvonkina, and A. Karim, *Emergent Mater.*, **2** (2019) 11.
33. C. E. Sroog, *Prog. Polym. Sci.*,**16** (1991) 561.
34. D. K. Owens and R. C. Wendt, *J. Appl. Polym. Sci.*, **13** (1969) 1741.
35. R. Hiorns, *Polym. Int.*, **49** (2000) 807.
36. M. J. Maher, J. L. Self, P. Stasiak, G. Blachut, C. J. Ellison, M. W. Matsen, C. M. Bates, and C. G. Willson, *ACS Nano*, **10** (2016) 10152.

37. J. Doise, B. T. Chan, M. Hori, and R. Gronheid, *J. Micro/Nanolithography, MEMS, MOEMS*, **16** (2017) 1.

38. M. Dolejsi and P. Nealey, *J. Micro/Nanolithography, MEMS, MOEMS*, **17** (2018) 1.

Journal of Photopolymer Science and Technology
Volume 34, Number 5 (2021) 449−456 ©2021SPST

Effect of Phase Separation due to Solvent Evaporation on Particle Aggregation in the Skin Layer of the Gas Separation Membrane

Shiori Higashi[1], Masafumi Yamato[1], and Hiroyoshi Kawakami[1*]

[1] Department of Applied Chemistry, Graduate School of Urban Environment Sciences, Tokyo Metropolitan University, 1-1 Minamiohsawa, Hachioji, Tokyo 192-0397, Japan
**kawakami-hiroyoshi@tmu.ac.jp*

The asymmetric mixed matrix membrane (MMM) composed of fluorinated polyimide and the surface-modified silica nanoparticles were fabricated using the dry-wet phase inversion method. The thinning of the skin layer of the asymmetric MMM led to a significant improvement in gas permeability and a decrease in gas selectivity. The decrease in gas selectivity originated in particle coarsening before vitrification caused by immersion in the coagulation bath. In addition, particle aggregation, that was caused by liquid-liquid phase separation due to evaporation of good solvent, occurred even before immersion in the coagulation bath. The composition of the mixed solvent, which allow suppression of particle aggregation during both dry and wet processes, is important to produce defect-less asymmetric MMMs.

Keywords: Mixed matrix membrane, Asymmetric membrane, Silica particle, Fluorinated polyimide, Phase separation,

1. Introduction

Polyimide is one of polymer with excellent performance in mechanical and thermal properties. Fluorinated polyimides having CF_3 group are the polymer that show excellent gas separation performance because bulky CF_3 group suppress the rotation of the polymer chain and function as spacers that form a free volume [1–3]. However, due to the trade-off between gas permeability and selectivity, a neat polymer membrane does not reach the performance required by industrial use such as carbon dioxide capture, utilization and storage (CCUS) [4]. In recent years, performance improvement has been carried out by mixed matrix membrane (MMM) composed of inorganic particles and polymer matrix [5].

The addition of porous inorganic materials such as zeolite and MOF to the polymer matrix provide improvement of the characteristics of gas permeability and selectivity, and the development of MMM containing porous inorganic particle is one of the useful techniques for the development of a gas separation membrane [6,7]. On the other hand, we have succeeded in developing MMM with excellent gas permeation coefficient by loading polymer matrix with bulky organic moiety modified non-porous silica nanoparticles [8–10].

Even in MMMs with excellent gas permeation characteristics, thinning is indispensable for practical use as gas separation membranes. However, since the toughness of the membrane decreases in the MMM, thinning the MMM has become a major challenge [7,11].

A dry-wet phase inversion method, which is one of the membrane formation methods, provides fabrication of an asymmetric membrane consisting of a thin selective layer on a support layer [12,13]. Therefore, we tried to apply this method to the production of MMM. In this study, fluorinated polyimide, which has a proven track record in the dry-wet phase inversion method [14,15], was used as the polymer matrix and the effect of phase separation on skin layer formation during membrane production was studied.

2. Experimental

2.1. Materials

All reagents were purchased from commercial sources and used as received without any mention. 2,2-bis(3,4-anhydrodiccarboxyphenyl) hexafluoropropene) (6FDA) and 2,2-bis(3-amino-4-hydroxyphenyl) (6FAP) were

Received March 22, 2021
Accepted April 30, 2021

purchased from Central Glass Co., Ltd. (Tokyo, Japan). 6FDA was purification by sublimation and 6FAP was purified by recrystallization in ethanol.

Non-porous pearl-necklace-like silica nanoparticle (SNOWTEX® ST-PS-SO) was provided from Nissan Chemical Corporation (Tokyo, Japan). (3-aminopropyl)triethoxysilane (APTES), 3,5-diaminobenzoic acid (DABA), and 1H-benzotriazol-1-yloxytris(dimethylamino) phosphonium hexafluorophosphate (BOP) were purchased from Sigma-Aldrich Co. (St. Louis, MO, United States). Dimethylacetamide (DMAc), Acetic anhydride, dichloromethane (DCM), trichloroethane (TCE), butanol (BuOH), potassium carbonate, triethylamine (TEA), anhydrous *N*,*N*-dimethylformamide (DMF), anhydrous *N*-methyl-2-pyrrolidone (NMP), isopropanol, tetrahydrofuran (THF), 1,4-dioxane, chloroform, and acetone were purchased from Kanto Chemical Co. (Tokyo, Japan). Deionized and distilled water was obtained by a water purifier (WG250, Yamato Scientific Co., Tokyo, Japan).

2.2. Synthesis and characterization of fluorinated polyimide (FPI)

The fluorinated polyimide, FPI, was synthesized by chemical imidization of the poly (amic acid) precursors as reported in the literature (Scheme 1) [16]. The synthesized FPI had the weight-average molecular weight of 1.1×10^5 with a polydispersity index of 3.6 estimated by gel permeation chromatography (GPC, LC-2000Plus series, JASCO, Tokyo, Japan) with THF as the solvent.

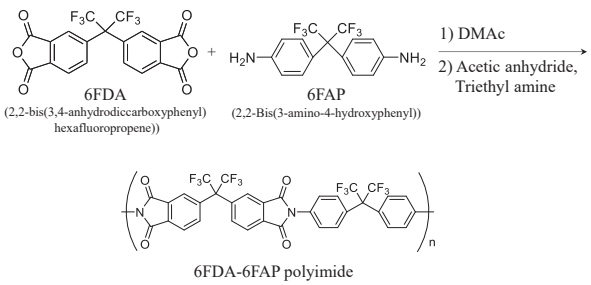

Scheme 1. Polymerization of fluorinated polyimide.

2.3. Synthesis and characterization of surface-modified silica nanoparticles

Surface-modified silica nanoparticles were prepared by APTES modification step and DABA modification steps (Scheme 2) as previously reported [10].

The surface-modified silica nanoparticles were characterized by thermogravimetric analysis (TGA, STA7000, Hitachi High-Tech Science, Tokyo, Japan) and Fourier transform infrared spectroscopy (FT-IR, 6100V, JASCO, Tokyo, Japan).

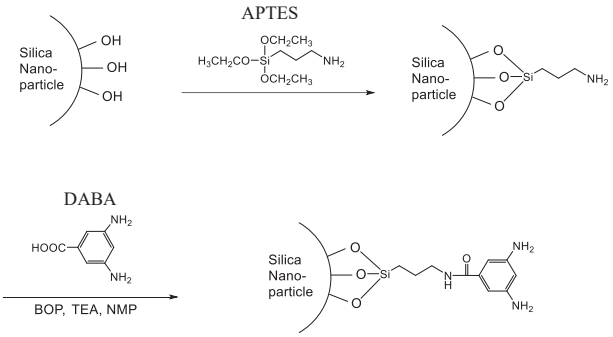

Scheme 2. Synthesis of surface-modified silica nanoparticles.

2.4. Fabrication and characterization of MMM

Asymmetric Membranes were fabricated by a dry-wet phase inversion method. A schematic diagram of the method for producing an asymmetric membrane is shown in Scheme 3. A mixed solvent of DCM, TCE, and BuOH was used as the solvent. The composition ratio of polymer, DCM, TCE, and BuOH was 11:59:23:7 [14,15]. Methanol was used the coagulation solvent. The thickness of the skin layer of the asymmetric membrane formed was achieved by varying the standing time in the atmosphere. Dense membranes were also prepared without immersing in a coagulation bath. The obtained membranes were dried in the atmosphere and then dried in vacuum.

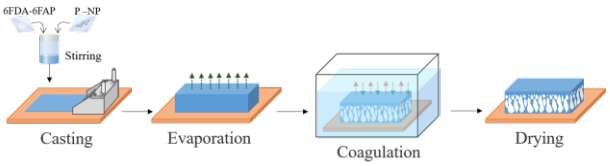

Scheme 3. Schematic drawing of a dry-wet phase inversion method for producing an asymmetric membrane.

To investigate the morphology of the MMMs, cross-section of the membranes was observed by scanning electron microscope (SEM, JXP-6100P, JEOL, Tokyo, Japan).

The gas permeance of the membranes were measured with pure gasses (N_2, CO_2) at 35°C and 76 cmHg using a differential pressure type high vacuum apparatus (Rika Seiki, Inc., K-315-H, Tokyo, Japan), where the membrane was set between upper and lower chambers.

Gas permeance was calculated based on pressure increment (dp/ dt) at steady state according to the following equation:

$$Q = \frac{273 \times 10^{10}}{760} \frac{V}{Ap_0T} \frac{dp}{dt} \quad (1)$$

where Q is the gas permeance of the membrane in GPU (1 GPU = 1×10^{-6}cm^3 (STP) / (cm^2 s cmHg)), V is the volume of downstream reservoir (cm^3), A is the membrane area (cm^2), T is the operating temperature (K) and p_0 is the upstream pressure (cmHg). The gas permeability P in Barrer (1 Barrer = 1×10^{-10}cm^3 (STP) cm/ (cm^2 s cmHg)) was evaluated using the relationship of $P = Q\ L$, where L is the membrane thickness(cm).

3. Results and discussion

3.1. Characterization of surface-modified silica nanoparticles

Fig. 1 shows the TGA curves of original particle and the precursor particles which surface was modified with APTES and the surface modified particle as final product. The weight loss ratios of the original particle and the precursor particle and the surface modified particle after heating to 1000°C were 2.48, 3.34 and 8.91 wt%, respectively.

The particle weight loss measured by TGA and the correction ratios ([APTES] / [OH], [DABA] / [APTES]) estimated by the TGA results are summarized in Table 1. The modification rate was slightly lower than that of the previously prepared nanoparticles [10].

The surface modification on silica nanoparticles was confirmed using FT-IR spectroscopy. The FT-IR spectrum of the surface modified silica nanoparticles shown in Fig. 2 was similar to those reported previously [10,17]. The insert in Fig. 2 shows an enlarged spectrum of the part where the change due to modification can be most clearly confirmed. The peak at 1547 cm^{-1} and the shoulder observed around 1600 cm^{-1} suggest the presence of a phenylamine group or an aromatic ring [18]. This spectrum strongly suggested successful DABA modification to silica nanoparticles.

3.2. Fabrication of MMMs

Fig. 3(a) shows photo images of the membranes formed by the dry-wet phase inversion method. The MMM was colored. The color is attributed to surface-modified nanoparticles [10]. Both the neat FPI membrane and the MMM became opaque. The formation of voids that greatly scatter light was suggested. Fig. 3 (b) shows the surface SEM image of the asymmetric MMM. Although surface irregularities due to the inclusion of particles were observed on the front side, no defects were observed.

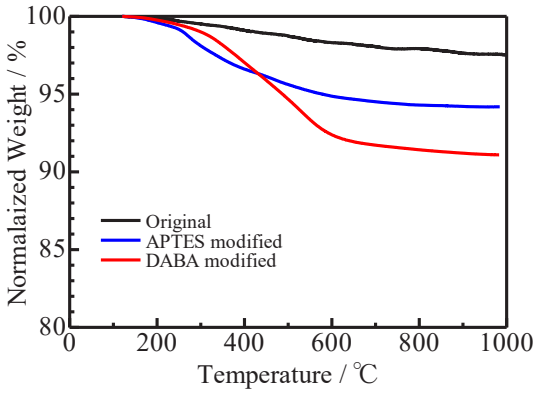

Fig. 1. TGA curves of original particle (black lines), APTES modified nano-particle as precursor (blue line), and DABA modified nano-particle (red line).

Table 1. Weight loss of the particles measured by TGA and modification molar ratios ([APTES]/[OH], [DABA]/[APTES]) estimated by TGA results.

	Weight loss / %	[APTES] / [OH]	[DABA] / [APTES]
Original	2.48	-	-
Precursor	3.34	0.36	-
Surface modified	8.91	-	0.43

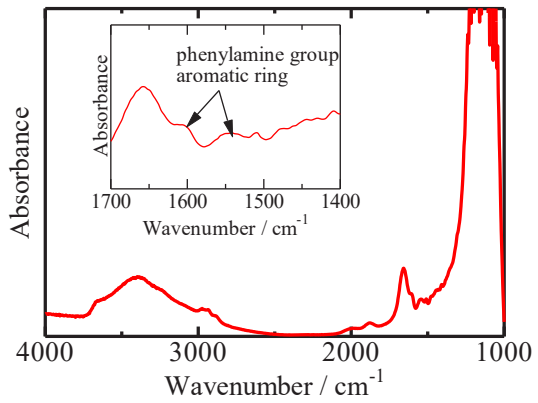

Fig. 2. FT-IR of DABA modified nano-particle. The insert shows an enlarged spectrum of the part where the change due to modification can be most clearly confirmed.

On the other hand, many voids were observed on the back side. The dry-wet phase inversion method could introduce asymmetric structure into the MMM.

3.3. Gas permeation properties of MMMs

Fig. 4 shows the permeance of carbon dioxide and

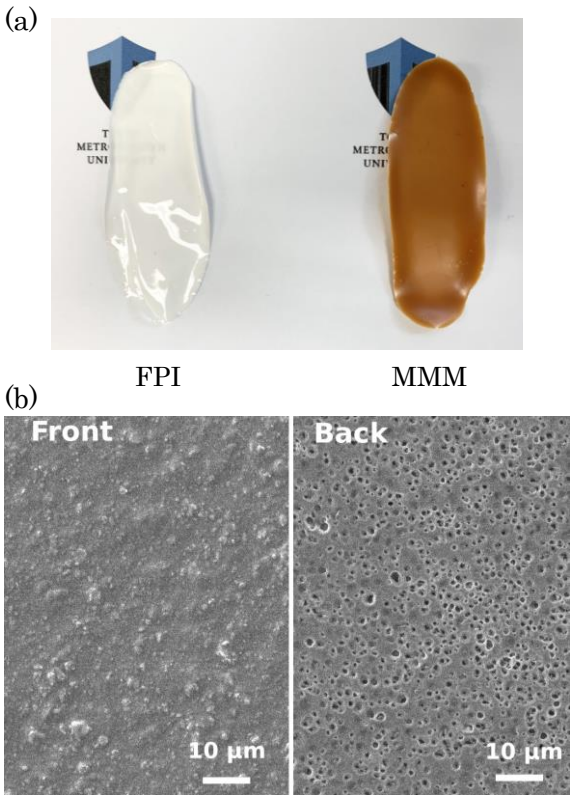

Fig. 3. Photo of asymmetric membranes of the neat FPI and the MMM (a) and SEM images of front and back side of the asymmetric MMM prepared by the standing time of 300 s (b).

the gas selectivity of carbon dioxide and nitrogen as a function of standing time in the asymmetric membrane formation process and the values of the permeance and the gas selectivity were summarized in Table 2.

The gas permeance of MMM was larger than that of neat FPI membrane at any standing time, suggesting the effect of surface-modified particles addition [8–10]. The gas permeance of both neat FPI membrane and MMM decreased as the standing time increased up to 300 seconds. After the standing time of 300 seconds, the change in permeance of the membranes with increasing in the standing time became very gradual.

On the other hand, regarding the gas selectivity, which is the ratio of the permeance of carbon dioxide to the permeance of nitrogen, the tendency in the MMM was significantly different compared to the neat FPI membrane. With respect to the neat FPI membrane, no significant change in the gas selectivity was observed with the standing time, and the gas selectivity was similar to that of the dense membrane shown in Table 3. The apparent thickness of the skin layer of the neat FPI membrane obtained in this study was 1.6 μm at the thinnest (Table 2). Generally, defects can be formed in a process of thin

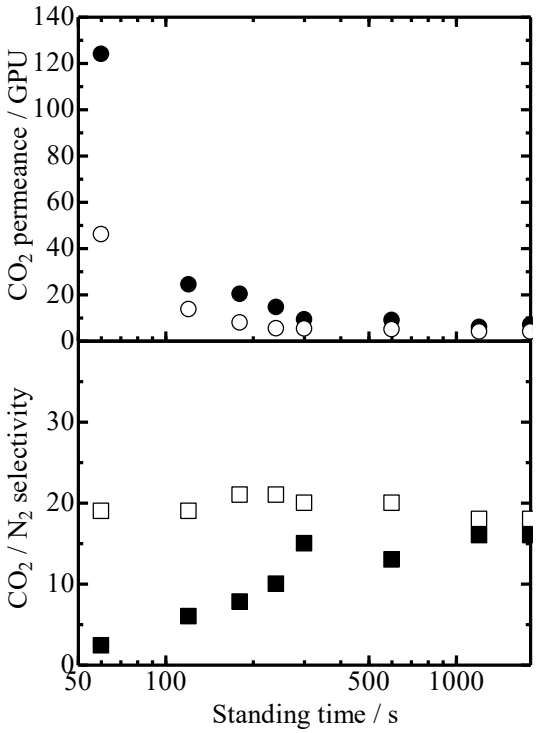

Fig. 4. Effect of standing time on gas permeance and gas selectivity of the asymmetric membranes. The open and closed symbols represent the neat FPI and the MMM, respectively.

films, resulting in reduction of gas selectivity. It seems that no defects were generated in the skin layer of the asymmetric membrane of the neat FPI under the film formation conditions in this study.

On the other hand, in the asymmetric membrane of the MMM, the gas selectivity largely depended on the standing time in the membrane formation process. The gas selectivity of the MMM which was produced more than 300 seconds remained the constant value that was similar to the selectivity obtained with the dense membrane.

However, a significant decrease in the gas selectivity was observed as the standing time became shorter than 300 seconds. The gas selectivity decreased to 2.4 in the MMM prepared by standing for 60 seconds. In general, a large decrease in gas selectivity means the formation of defects which has not a gas selectivity. In other words, it was suggested that in the asymmetric membrane containing the particles, the surface skin layer had a structure that reduced gas selectivity.

3.4. Structure of surface skin layer

To clarify the cause of the significant decrease in gas selectivity, we evaluated the thickness of the skin layer of the asymmetric membranes and observed the aggregation of particles in the skin layer using cross-sectional SEM images. Fig. 5 shows cross-sectional SEM images of various asymmetric

membranes.

The thickness of the skin layer was calculated using image analysis software (Image J). The analysis was performed at arbitrary 50 points, and the average value was used as the thickness of the skin layer. The interface between the skin layer and the support layer was very vague, and the effective pore size for gas separation is smaller than the SEM resolution. Therefore, the skin layer thickness was analyzed from the membrane surface to the region with clear holes that can be observed by SEM. As mentioned in other reports, the skin layer thickness may be overestimated than the original thickness [19].

If the skin layer of the asymmetric membrane exhibits the same characteristics as the dense membrane, we could estimate the apparent skin layer thickness using the gas permeability of the dense membrane (Table 2). Although the skin layer thickness obtained from cross-sectional SEM image tended to be larger than the apparent thickness estimated from the gas permeation that was summarized in Table 2, they showed almost the same thickness. In other words, it would be reasonable to evaluate the thickness of the skin layer by SEM in this study.

Fig. 6 shows the standing time dependence of the skin layer thickness of the asymmetric membrane obtained from the cross-sectional SEM image. The skin layer thickness increased with the standing time up to 300 seconds regardless of the presence or absence of particles and remained almost constant thereafter.

The thickness of the skin layer of the MMM was thicker than that of the neat FPI in all standing time.

Table 2. Summary of the gas permeation properties of the asymmetric membranes and the apparent skin layer thickness evaluated from the gas permeability of the dense membrane.

Standing time / s	Loading / wt%	Q_{CO2} / GPU	Q_{N2} / GPU	Q_{CO2}/Q_{N2}	Thickness / μm
60	0	46.1	2.39	19	1.6∓0.1
	30	124	51.9	2.4	0.6∓0.5
120	0	13.7	0.728	19	5.4∓0.3
	30	24.4	4.07	6.0	3.7∓1.7
180	0	7.92	0.379	21	9.9∓0.5
	30	20.3	2.59	7.8	4.7∓2.2
240	0	5.40	0.256	21	14.7∓0.6
	30	14.6	1.43	10	7.9∓1.6
300	0	5.32	0.262	20	16.6∓4.0
	30	9.30	0.638	15	15.7∓1.0
600	0	5	0.2	20	16.9±0.8
	30	9	0.7	13	14.2±1.0
1200	0	4	0.2	18	17.9±1.4
	30	6	0.4	16	25.6±1.1
1800	0	4	0.2	18	20.5±2.2
	30	7	0.4	16	22.7±1.0

1 GPU = 1×10^{-6}cm^3 (STP) / (cm^2 s cmHg)

Table 3. Gas permeation properties of the dense membranes.

Loading / wt%	Q_{CO2} / GPU	Q_{N2} / GPU	Q_{CO2}/Q_{N2}	P_{CO2} / Barrer	P_{N2} / Barrer	P_{O2} / Barrer	P_{CO2}/P_{N2}	Thickness / μm
0	3.60	0.169	21	77.4	3.63	16.1	21	21.5
30	5.08	0.320	16	152	9.56	33.3	16	29.9

1 Barrer = 1×10^{-10}cm^3 (STP) cm/ (cm^2 s cmHg), 1 GPU = 1×10^{-6}cm^3 (STP) / (cm^2 s cmHg)

As shown in Table 3, the thickness of MMM increased by about 40% compared to that of the neat FPI in the dense membrane. The thickness of the skin layer increased by about 50% in the asymmetric membrane formed more than 300 seconds of the standing time. Considering that the thickness of the skin layer was evaluated by SEM, the particle dispersion in the skin layer of the asymmetric membrane would be the same as that of the dense membrane.

On the other hand, when the standing time was less than 300 seconds, the skin layer thickness of the asymmetric membrane tended to double by the addition of particles. It is suggested that the particle dispersion changes significantly during the skin layer formation process when immersed in a coagulation bath before the standing time of 300 seconds.

The average size of particle aggregates in MMM was also calculated from the cross-sectional SEM image. The average particle size of particle aggregates was calculated for 50 aggregates considered to be in the skin layer using image analysis software (Image J). Fig. 7 shows the standing time dependence of the average size of particle aggregates in the MMM. The particle aggregate size decreased with the increase of the standing time until the standing time of 300 seconds and became almost constant of 1.4 μm thereafter.

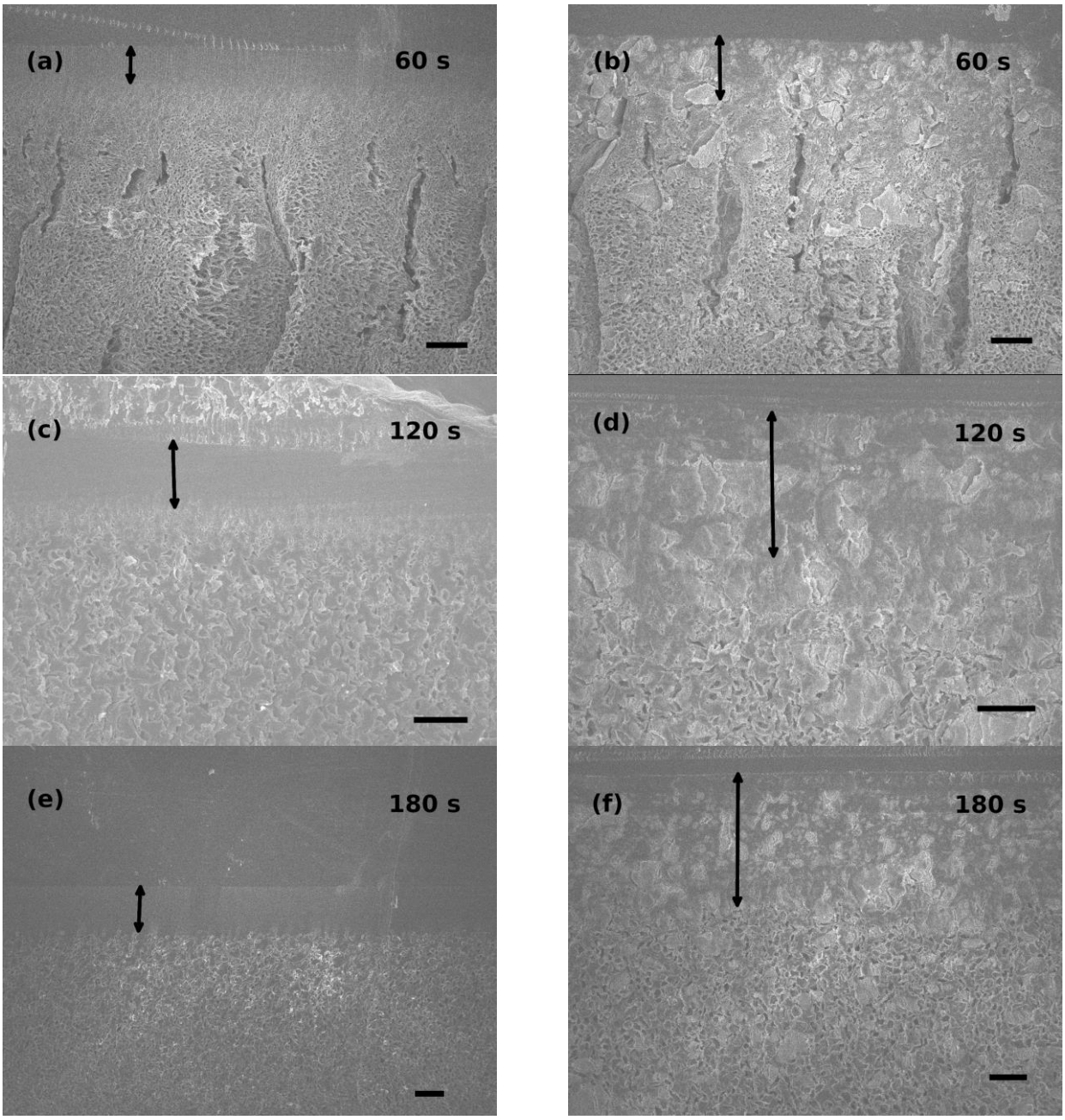

Fig. 5. Cross-sectional SEM images of the asymmetric membranes of the neat FPI(a), (c), (e) and the MMM (b), (d), (f). The standing time during film formation is shown in the figure. Black lines are a scale bar of 10 μm. Arrows indicate the skin layer.

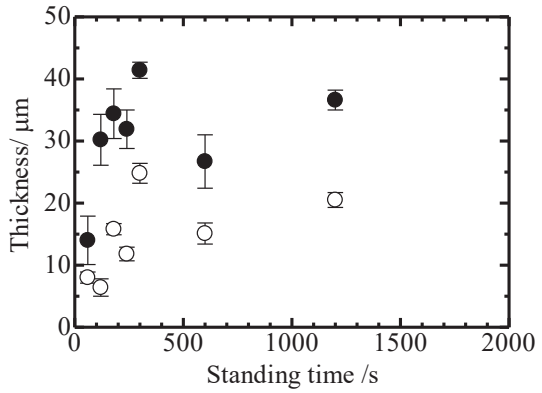

Fig. 6. Dependence of the skin layer thickness of the asymmetric membranes on standing time. The skin layer thickness was estimated from cross-sectional SEM images. The open circles represent the neat FPI membrane, and the filled circles represent the MMM.

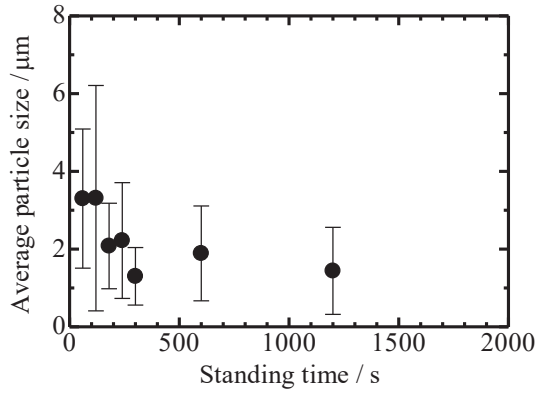

Fig. 7. Dependence of particle aggregate size in the MMMs on standing time. The size of the particle aggregation was calculated from the results of SEM observation.

While the size of the particle agglomerates in the dense MMM which was dried without being immersed in the coagulation bath was 1.51 ± 0.89 μm. The tendency that the particle agglutination size did not change after the standing time of 300 seconds was similar to the skin layer thickness.

3.5. Effect of solvent evaporation on skin layer formation

Fig. 8 shows the time dependence of weight of the neat FPI solution due to solvent evaporation at 25 °C. A rapid weight loss was confirmed immediately after casting and the rate of weight loss gradually decreased. This reflects the difference in the evaporation rate of each component in the mixed solvent. Initially, DCM, a low boiling point solvent, is the main component of the weight loss. While TCE and BuOH, which have higher boiling points, evaporate slower than DCM. The solution weight decreased to 43% of the initial weight after standing for 300 seconds, resulting in almost completely evaporation of DCM.

When immersed in a coagulation bath after DCM evaporation, vitrification would be rapidly induced at the surface having enough polymer concentration, resulting in formation of skin layer maintaining particle dispersion in the polymer solution. If the amount of evaporation of DCM was insufficient, the polymer concentration nearby the surface would be not sufficient for vitrification. Therefore, the coagulation-solvent inversion process caused particle coarsening in the polymer solution prior to vitrification. The particle coarsening increase non-uniformity in the skin layer, leading to the formation of defects in the skin layer and the increase in skin layer thickness.

3.6. Effect of solvent evaporation on particle aggregation

As discussed in the previous section, when the standing time was short, the immersion in a coagulation bath effected on the particle coarsening

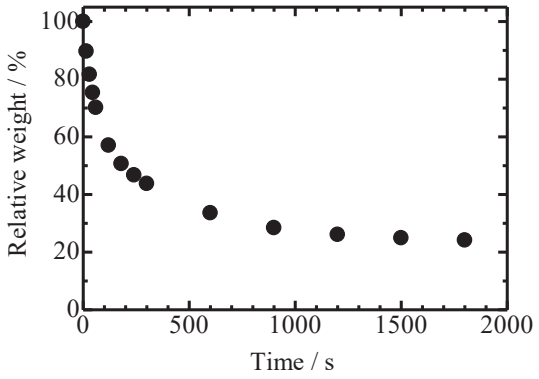

Fig. 8. Time dependence of weight of the neat FPI solution during solvent evaporation process at 25 °C.

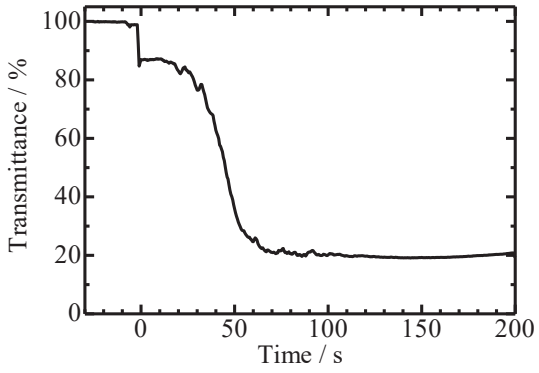

Fig. 9. Temporal change of light transmittance through the polymer solution containing the particles.

in the skin layer. However, even when the standing time was long enough, the particles in the skin layer were much larger than the original particle size less than 100 nm [10].

A mixture composed of good solvent and poor solvent is used as the solvent used for production of an asymmetric membrane. The composition of the mixed solvent is very important for both the formation of the skin layer by vitrification and the formation of the support layer by liquid-liquid phase separation [20]. DCM is a good solvent and TCE and BuOH are poor solvents for the FPI used.

Fig. 9 shows the temporal change of light transmittance after casting of the polymer solution containing the particles. The transmittance decreased immediately after casting and became constant after 70 seconds. The change in transmittance originated in the phase separation in the polymer solution cause by the evaporation of the DCM. This liquid-liquid phase separation would also result in the aggregation of the surface-modified silica nanoparticles in polymer solution. The mixed solvent used this time was suitable for formation of an asymmetric membrane for the neat FPI. However, in order to fabricate an asymmetric MMM, a solvent composition that allows suppression of particle aggregation in polymer solution during solvent evaporation will be required.

4. Conclusion

The asymmetric MMM composed of FPI and the surface-modified silica nanoparticles were produced using the dry-wet phase inversion method. The thinning of the skin layer of the MMM, which depended on the standing time, led to a significant improvement in gas permeability. While the gas selectivity was significantly reduced by thinning of the skin layer. The significant decrease in gas selectivity originated in particle coarsening caused by immersion in the coagulation bath before vitrification. The particle coarsening before vitrification introduced defects without gas selectivity in the skin layer. In addition, particle aggregation, that was caused by phase separation due to evaporation of good solvent, occurred even before immersion in the coagulation bath. The composition of a mixed solvent suppressing particle aggregation will be important for the fabrication of asymmetric MMM.

Acknowledgement

This work was partially supported by a grant (P14004) from NEDO and JSPS KAKENHI Grant Number JP25281040.

Reference

1. T. H. Kim, W.J. Koros, G. R. Husk, and K. C. O'Brien, *J. Appl. Polym. Sci.*, **34** (1987) 1767.
2. T. H. Kim, W. J. Koros, G. R. Husk, and K. C. O'Brien, *J. Memb. Sci.*, **37** (1988) 45.
3. S. A. Stern, Y. Mi, H. Yamamoto, and A. K. S. Clair, *J. Polym. Sci. Part B Polym. Phys.*, **27** (1989) 1887.
4. L. M. Robeson, *J. Memb. Sci.*, **320** (2008) 390.
5. A. Sabetghadam, X. Liu, A.F. Orsi, M.M. Lozinska, T. Johnson, K. M. B. Jansen, P.A. Wright, M. Carta, N. B. McKeown, F. Kapteijn, and J. Gascon, *Chem. - A Eur. J.*, **24** (2018) 12796.
6. Y. Cheng, Y. Ying, S. Japip, S.-D. Jiang, T.-S. Chung, S. Zhang, and D. Zhao, *Adv. Mater.*, **30** (2018) 1802401.
7. M. Galizia, W. S. Chi, Z. P. Smith, T. C. Merkel, R.W. Baker, and B. D. Freeman, *Macromolecules*, **50** (2017) 7809.
8. S. Hasebe, S. Aoyama, M. Tanaka, and H. Kawakami, *J. Memb. Sci.*, **536** (2017) 148.
9. N. Sakaguchi, M. Tanaka, M. Yamato, and H. Kawakami, *ACS Appl. Polym. Mater.*, **1** (2019) 2516.
10. Y. Kudo, H. Mikami, M. Tanaka, T. Isaji, K. Odaka, M. Yamato, and H. Kawakami, *J. Memb. Sci.*, **597** (2020) 117627.
11. G. Dong, H. Li, and V. Chen, *J. Mater. Chem. A*, **1** (2013) 4610.
12. I. Pinnau and W.J. Koros, *J. Appl. Polym. Sci.*, **43** (1991) 1491.
13. H. Kawakami, M. Mikawa, and S. Nagaoka, *J. Memb. Sci.*, **137** (1997) 241.
14. M. Mikawa, N. Seki, S. Nagaoka, and H. Kawakami, *J. Polym. Sci. Part B Polym. Phys.*, **45** (2007) 2739.
15. N. Seki, S. Nagaoka, and H. Kawakami, *J. Appl. Polym. Sci.*, **118** (2010) 105.
16. H. Kawakami, M. Mikawa, and S. Nagaoka, *J. Appl. Polym. Sci.*, **62** (1996) 965.
17. H. Mikami, S. Higashi, T. Muramoto, M. Tanaka, M. Yamato, and H. Kawakami, *J. Photopolym. Sci. Technol.*, **33** (2020) 313.
18. Z. Rzaczynska, R. Mrozek, J. Lenik, M. Sikorska, and T. Glowiak, *J. Chem. Crystallogr.*, **30** (2000) 519.
19. M.L. Jue, V. Breedveld, and R.P. Lively, *J. Memb. Sci.*, **530** (2017) 33.
20. D. Wang, K. Li, and W.K. Teo, *J. Memb. Sci.*, **115** (1996) 85.

Journal of Photopolymer Science and Technology
Volume 34, Number 5 (2021) 457−462 ©2021SPST

Thermal Conversion of Polyamic Acid Gel to Polyimide Solution Having Amino Group Sidechains

Yoshikatsu Shiina, Shohta Ohnuki, and Atsushi Morikawa*

Department of Biomolecular Functional Engineering,
Ibaraki University,4-12-1, Nakanarusawa, Hitachi, Ibaraki, 316-8511, Japan
**atsushi.morikawa.reg@vc.ibaraki.ac.jp*

Deformation of a polyamic acid gel was observed upon heating. The gel prepared from 1,1-bis[4-(aminophenoxy) phenyl]-1-[4-(4-amino-2-trifluoromethylphenoxy) phenyl] ethane (triamine-CF_3), 4,4'-oxydianiline (ODA) and benzohenonetetracarboxylic dianhydride (BTDA) in *N*-methyl-2-pyrrolidone (NMP) at 20 °C was heated to 180 °C. The swelling became weak upon increasing the temperature, and the gel turned into a solution that could be stirred easily above 80 °C. The solution heated to 180 °C did not returned to the gel state even upon cooling to 20 °C. IR measurements of the heated gel showed that the deformation was due to an amide exchange reaction, which proceeded through scission of the amide linkage into anhydride and amine end groups. The viscosity barely changed upon heating. The amide exchange and imidation reactions proceeded simultaneously upon heating the polyamic acid gel, and formed a soluble polyimide containing amino sidechains.

Keywords: Deformation of polyamic acid gel, Amino group sidechains, Triamine-CF_3, Amide exchange, Imidation reaction

1. Introduction

Polyimide-silica hybrid materials have been prepared by a sol-gel process involving tetraethoxysilane in a polyamic acid solution, followed by thermal treatment [1-3]. Transparent and tough hybrid films with high silica contents were prepared using polyamic acid by conjugation to silica [4-5]. We prepared the polyamic acid containing amino group sidechains from BTDA, 4,4'-ODA, and triamine-CF_3. The amino group reacted with 3-(triethoxysilyl)propyl succinic anhydride (TESSA) to introduce ethoxysilyl moieties that allowed for the conjugation to silica. The polyimide-silica hybrid films were prepared by sol-gel reaction with tetraethoxysilane in the polyamic acid solution, and thermal imidation. These hybrid films were more transparent than those prepared without TESSA [6]. In the preparation of polyamic acid, the 4-amino-2-trifluoromethylphenoxy group in triamine-CF_3 was expected to react slower with the anhydride than the 4-aminophenoxy group in triamine-CF_3 due to the electron-withdrawing effect of the trifluoromethyl group. This would lead to a polyamic acid containing amino group sidechains [6]. However, gelation was also observed. The gel became a solution upon heating and could be reacted with TESSA to introduce the ethoxysilyl moiety.

In this study, the change of the chemical structure during heating of the polyamic acid gel as it changed into a solution was evaluated.

2. Experimental

2.1. Preparation of polyamic acid gel from triamine -CF_3

In a three-necked flask, 1.128 g (3.5 mmol) of BTDA was added to a solution of 0.324g (0.5 mmol) of triamine-CF_3 and 0.601 g (3.0 mmol) of ODA in 30.0 mL of NMP at 20 °C. The mixture was stirred at 20 °C under nitrogen. The solution became more viscous as BTDA was dissolved and formed a gel.

The gel was heated at a rate 2 °C/min to 180 °C. It became a solution above 80 °C. Upon cooling to 20 °C, this sample remained in the solution state.

Received March 7, 2021
Accepted April 30, 2021

2.2. Preparation of polyamic acid gel from 2,4,4'-triaminodiphenyl ether [7]

In a three-necked flask, 1.128 g (3.5 mmol) of BTDA was added to a solution of 0.108g (0.5 mmol) of 2,4,4'-triaminodiphenyl ether and 0.601 g (3.0 mmol) of ODA in 30.0 mL of NMP at 20 ° C. The mixture was stirred at 20 ° C under nitrogen. The solution became more viscous as BTDA was dissolved and gelation occurred.

The gel was heated at a rate 2 ° C/min to 180 ° C. It did not become a solution even at 180 ° C.

2.3. Measurements

IR measurements were carried out using a SHIMADZU IR 435 spectro-photometer with the films prepared by drying the gel or solution at 70 ° C. Viscosity measurements were carried out at a concentration of 0.5 g dL $^{-1}$ in NMP at 30 ° C using an Ostwald viscometer.

3. Results and discussion

3.1. Deformation of polyamic acid gel and imidation

Deformation of polyamic acid gel was observed by heating. The gel prepared from triamine-CF_3, ODA and BTDA in NMP at 20 ° C was heated to 180 ° C. The gel changed as shown in Fig. 1. The swelling became weak with increasing temperature, and the gel became a solution which could be stirred easily above 80 ° C. The solution heated to 180 ° C did not return to a gel even if cooled to 20 ° C.

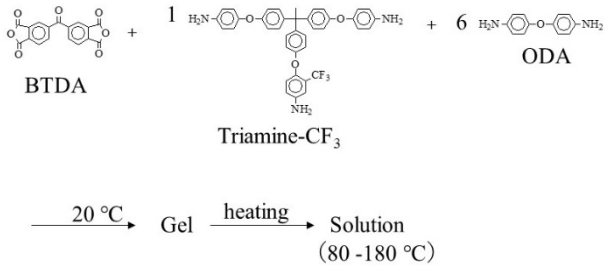

Fig. 1. Reaction between BTDA, ODA and triamine-CF_3, and the change by heating.

The formation of a polyamic acid is an exothermic reaction, which involves an equilibrium [8-10]. The equilibrium constant K is very large, and the concentration of amic acid is very high in the equilibrium. When the polyamic acid solution is heated, the reverse reaction, which is caused by chain scission into amine and anhydride groups, proceeded at an early stage. However, the forward reaction, reformation of polyamic acid, proceeds later since the concentration of amic acid is lower due to thermal imidation during heating of polyamic acid solution [11-12].

Figure 2 shows IR spectra of the films prepared from the gel at 20 ° C, and the solutions at 80 ° C, 150 ° C, and 180 ° C. The IR absorption peak due to carbonyl stretching of the amide group appeared at about 1650 cm $^{-1}$ in the film from the gel at 20 ° C. Additional absorption peaks appeared at 1850 cm $^{-1}$ (↑), 1780 cm $^{-1}$, 1720 cm $^{-1}$, and 730 cm $^{-1}$ in the film formed from the solution at 80 ° C. The 1850 cm $^{-1}$ band is attributed to asymmetric stretching of the carbonyl groups in the anhydride moiety [13], 1780 cm $^{-1}$ and 1720 cm $^{-1}$ bands are attributed to the symmetric and asymmetric stretching of the carbonyl groups in the imide group, respectively, and the 730 cm $^{-1}$ band is attributed to deformation of the imide ring [13-14]. The anhydride peak at 1850 cm $^{-1}$ suggests that chain scission into amine and anhydride groups occurred. The intensity of the imide peaks at 1780 cm $^{-1}$, 1720 cm $^{-1}$ and 730 cm $^{-1}$ were higher in the films formed from the solution at higher temperatures and reached a maximum in the film from the solution at 180 ° C at 3 h. The percent imidation [13,15] calculated from the absorbance ratio of the characteristic absorption due to imide groups at 1720 cm $^{-1}$ to that due to aromatic groups at 1500 cm $^{-1}$ was 95%. As for the calculation, a value of the previously prepared polyimide film produced by heating the polyamic acid film at 100 ° C for 1 h, 200 ° C for 1 h, and finally 300 ° C for 1 h under vacuum was performed as 100% [6]. The polyimide was not precipitated during heating in spite of the high percent imidation. Polyimide was reported to be prepared by heating anhydride-terminated amic acid oligomer, 2, 4-diaminotoluene, and 3,3',4,4'-biphenyltetracarboxylic dianhydride in NMP at 180 ° C for 3 h [16].

The relationship between the inherent viscosity (η_{inh}) and temperature of the heating solution is shown in Fig. 3. An initial decrease followed by an increase in the viscosity were observed at 80-120 ° C and 140-180 ° C, respectively. The decrease at 80-120 ° C is thought to be correlated with the generation of anhydrides by chain scission, and the increase at 140-180 ° C is thought to be correlated with the reformation of polyamic acid and the imidation reaction. η_{inh} barely changed during heating, nor did water formed during the imidation have a great influence on η_{inh} due to the small amount present.

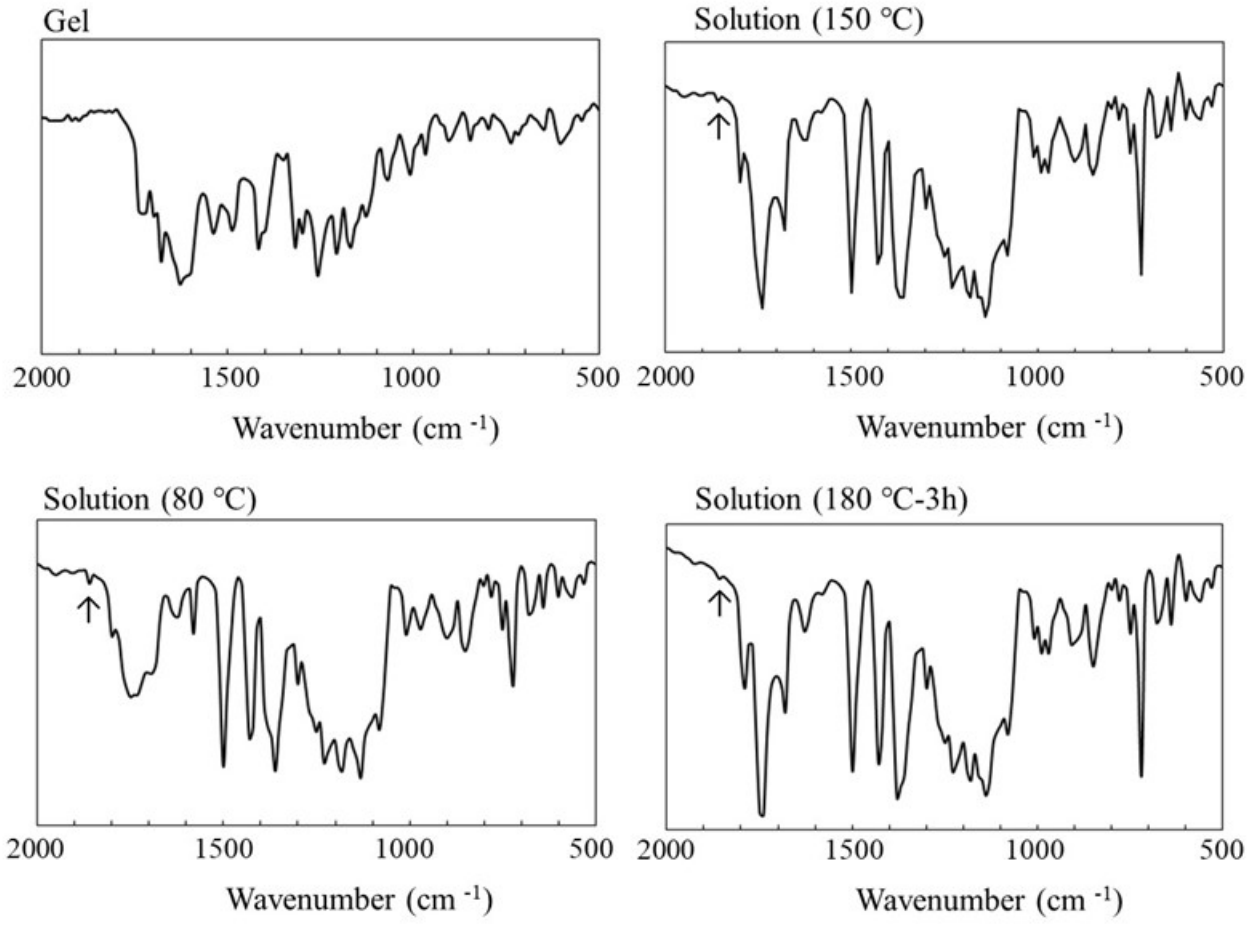

Fig. 2. IR spectra of films prepared after heating the polyamic acid gel.

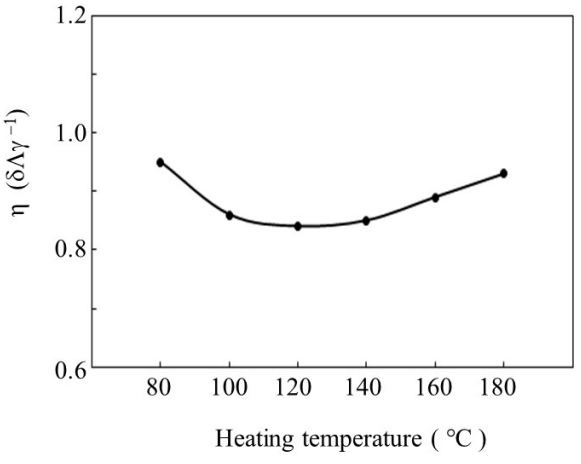

Fig. 3. Inherent viscosity as function of heating temperature.

Crosslinking to form a gel occurred by the reaction of all amino groups in triamine-CF_3 with anhydride groups. The transformation of the gel to a solution is proposed to occur as shown in Fig. 4. The crosslinking is broken by the scission of amic acid into amine and anhydride groups. Next, a reaction causing reformation of the amic acid is followed by imidation. In the reformation of amic acid, the 4-aminophenoxy group (○) and the 4-amino-2-trifluoromethylphenoxy group (×) could both react with anhydride groups. The 4-amino-2-trifluoromethylphenoxy group (×) was expected to react slower than the 4-aminophenoxy group (○) due to the electron-withdrawing effect of the trifluoromethyl group. Since the equilibrium process of scission and recombination (amide exchange reaction) [17-18] occurred sufficiently, the number of crosslinking sites was reduced.

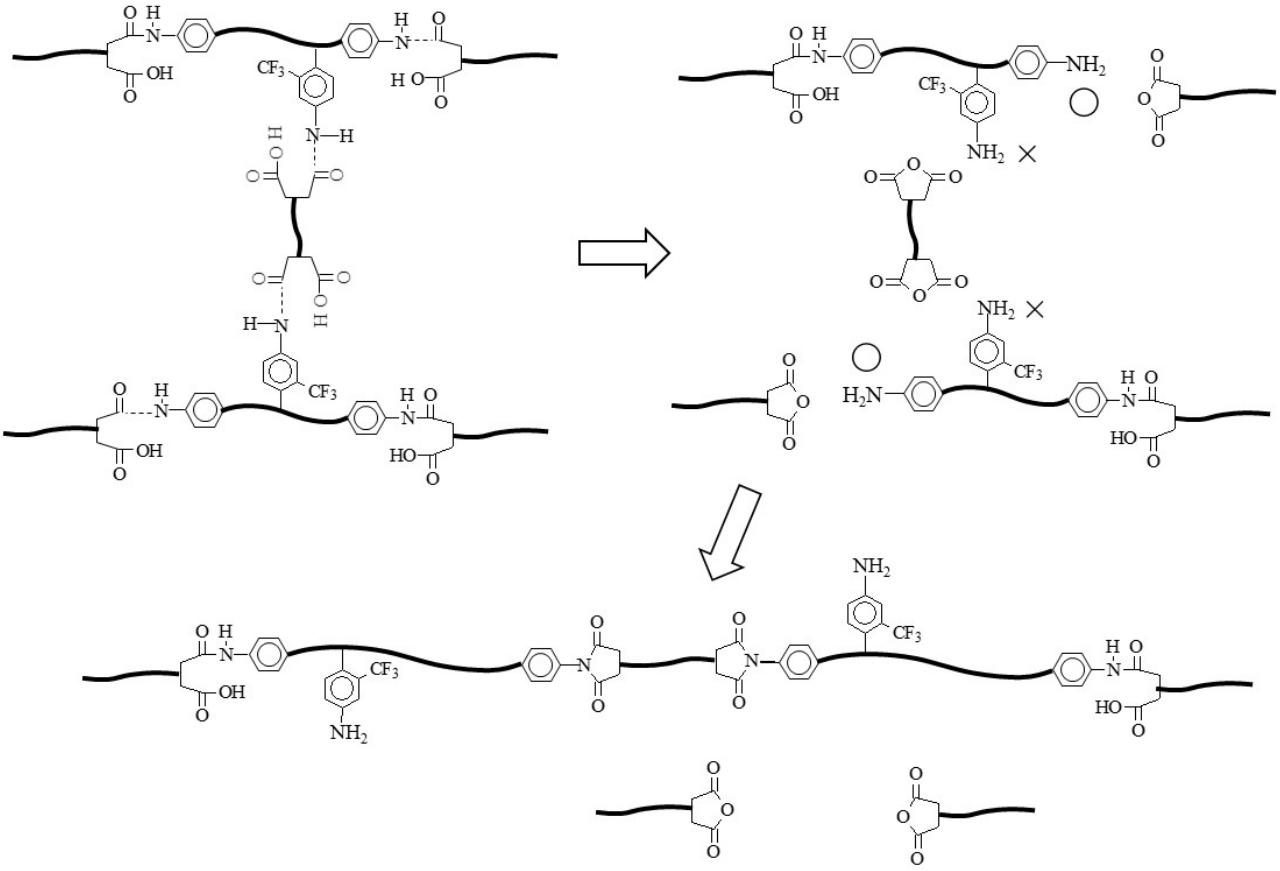

Fig. 4. Structual change of the gel by heating.

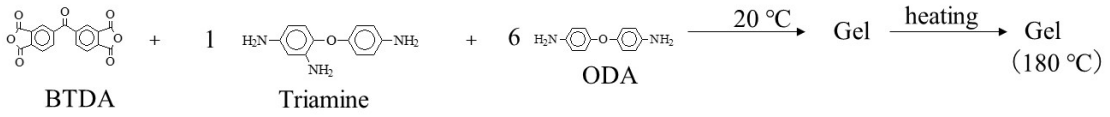

Fig. 5. Reaction between BTDA, ODA and 2,4,4'-triaminodiphenyl ether, and the result of heating.

Such reactivity of amino group was reported to influence the storage time of polyamic acid / polyamic acid solutions before becoming random copolyimide [19]. For example, the storage time of the pyromellitic dianhydride (PMDA)-*p*-phenylenediamine (PPD)/ PMDA-2,2-bis(4-aminophenyl) hexafluoropropane (6F) blend was much longer than that of PMDA-PPD/ PMDA-ODA due to the electron-withdrawing character of the hexafluoroisopropylidene group in 6F. The gel prepared from 2,4,4'-triaminodiphenyl ether without a trifluoromethyl group, ODA and BTDA in NMP did not became a solution even upon heating to 180 °C but remained in the gel state (Fig. 5) [20].

3.2. Preparation of polyimide-silica hybrid films from polyimide solution having amino group sidechain

The polyamic acid gel prepared from triamine-CF_3 changed to a soluble polyimide containing amino sidechains by heating to 180 °C. The amino group could then be reacted with TESSA to introduce ethoxysilyl moieties that allow for conjugation to silica. The sol-gel reaction of tetraethoxysilane was carried out in the polyimide solution, followed by thermal imidation of the amic acid generated from TESSA, and polyimide-silica hybrid films were prepared as shown in Fig. 6. For comparison, the polyimide-silica hybrid film was also prepared without TESSA (Fig 7). The fractured surfaces of the hybrid films containing 20 wt% silica were observed by SEM (Fig. 8). The fractured morohology of the hybrid film prepared using TESSA showed smooth surface. On the other hand, silica particles were clearly observed as beads having diamwter 1.0-2.0 μm in the hybrid film

prepare without TESSA. It was suggested that TESSA acted as conjugation between the polyimide and silica.

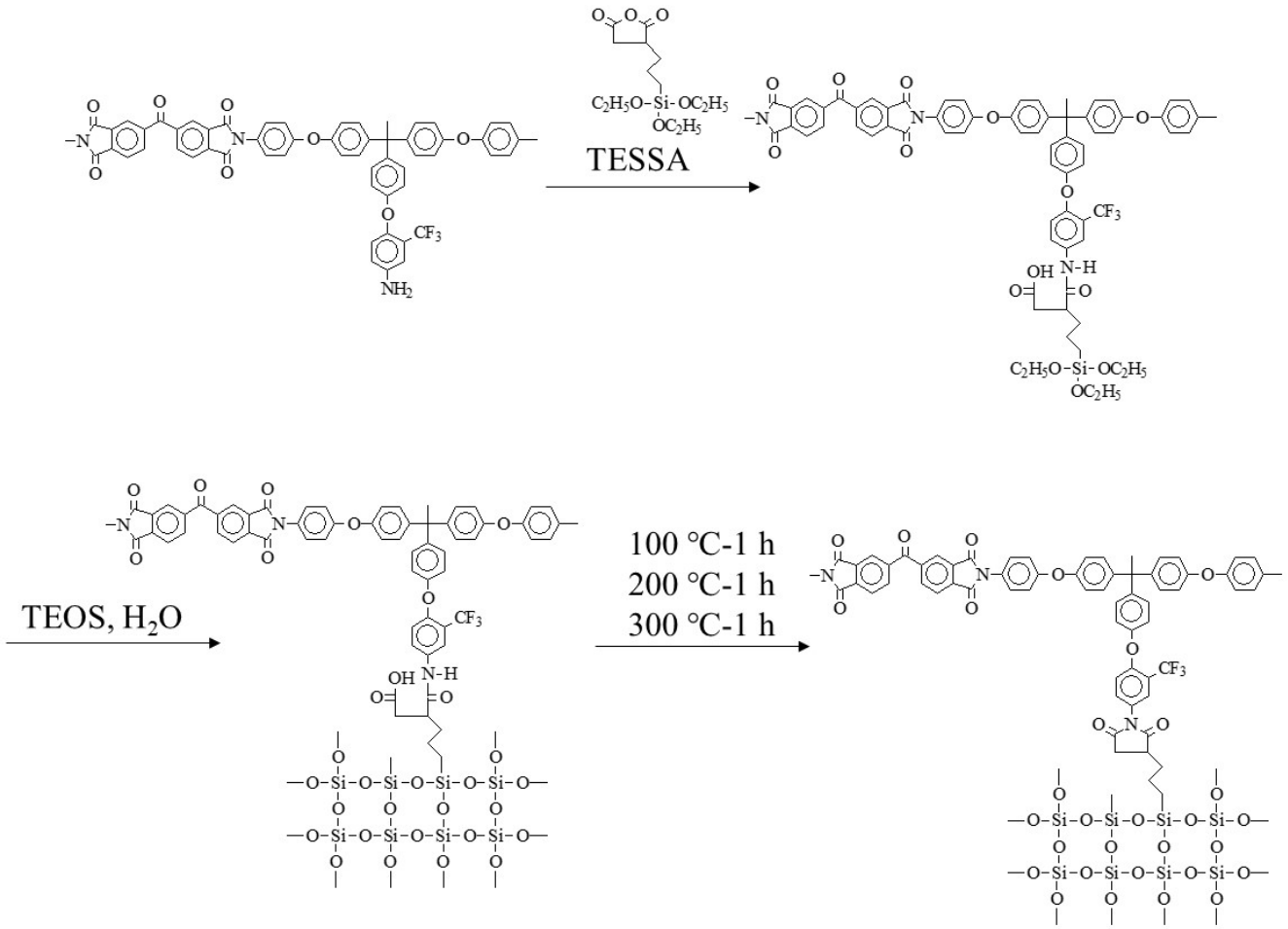

Fig. 6. Preparation of polyimide-silica hybrid film from polyimide solution using TESSA.

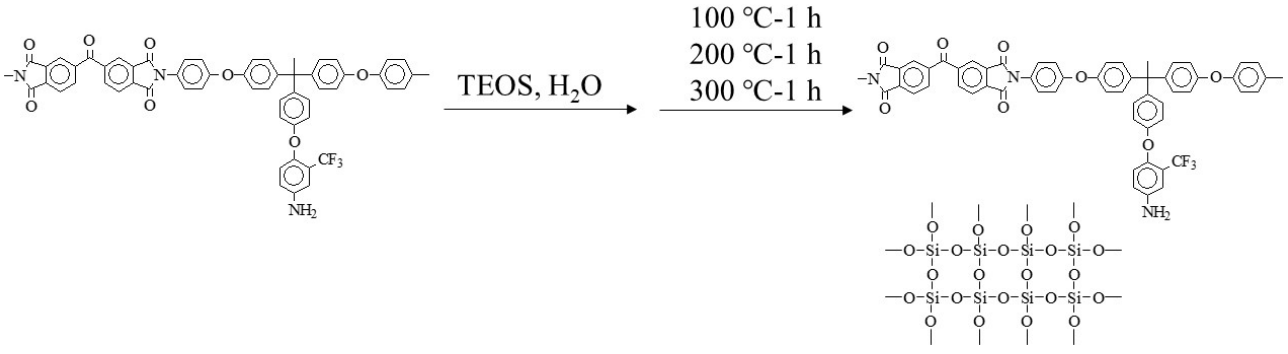

Fig. 7. Preparation of polyimide-silica hybrid film from polyimide solution without TESSA.

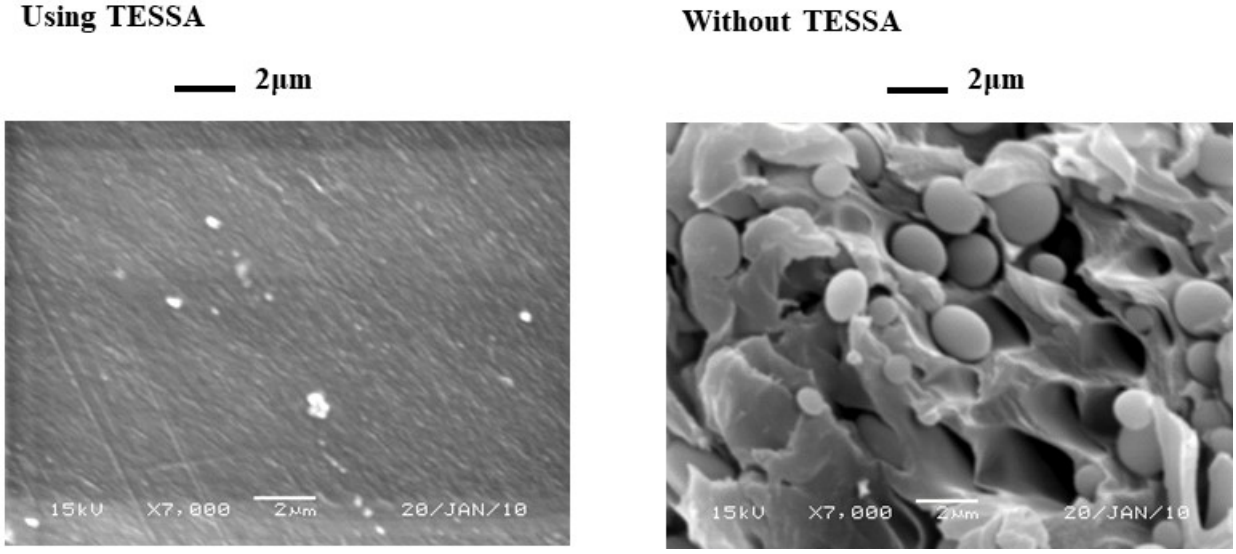

Fig. 8. SEM micrographs of polyimide-silica hybrid films containing 20 wt% silica.

4. Conclusion

During heating of a polyamic acid gel to 180 °C, equilibrium processes involving the scission and recombination of amic acid occurred, followed by imidation, which change the gel into a soluble polyimide containing amino group sidechains.

References

1. A. Morikawa, Y. Iyoku, M. Kakimoto, and Y. Imai, *Polym. J.*, **24** (1992) 107.
2. A. Morikawa, K. Suzuki, and K. Asano, *J. Photopolym. Sci. and Technol.*, **28**(2015)151.
3. A. Morikawa, K. Suzuki, and K. Asano, *J. Photopolym. Sci. and Technol.*, **29**(2016)231.
4. A. Morikawa, Y. Iyoku, M. Kakimoto, and Y. Imai, *J. Mater. Chem*, **2** (1992) 679.
5. T. Suzuki and Y. Yamada, *High Perform. Polym.*, **19** (2007) 553.
6. Y. Shiina and A. Morikawa, *Reactive and Functional Polymers*, **71** (2011) 85.
7. K. Wang, M. Kakimoto, and M. Jikei, *High Perform. Polym.*, **17** (2005) 225.
8. P. M. Kass, *J. Polym. Sci: Polym. Chem.* **19** (1981)2255.
9. P. R. Young, J. J. Davis, A. C. Chang, and J. N. Richardson, *J. Polym. Sci., Part A: Polym. Chem.* **28** (1990)3107.
10. M-J. Brekner and C. Feger, *J. Polym. Sci., Part A: Polym. Chem.*, **25** (1987) 2479.
11. R. Ishige, T. Masuda, Y. Kozaki, E. Fujiwara, T. Okada, and S. Ando, *Macromolecules*, 50 (2017) 2112.
12. H. Sugitani and Y. Nakamura, *J. Thermosetting Plastics, Japan,* **15** (1994) 125.
13. C. A, Pryde, *J. Polym. Sci., Part A: Polym. Chem.*, **27** (1989) 711.
14. T. Matsuura, Y. Hasuda, S. Nishi, and N. Yamada, *Macromolecules*, 2**4** (1991) 5001.
15. H. Inoue, Y. Sasaki, and T. Ogawa, *J. Appl. Polym. Sci*., **60** (1996) 123.
16. Y. Shirai, T. Kawauchi, T. Takeich, and H. Itatani, *J. Photopolm. Sci. Technol.*, **24** (2011) 283.
17. M. Hasegawa, Y. Shindo, T. Sugimura, K. Horie, R. Yokota, and I. Mita, *J. Polym. Sci., Part A: Polym. Chem.,* **29** (1991) 1515.
18. P. M. Cotts, W. Volksen, and S. Ferline, *J. Polym. Sci., Part B: Polym. Phys.,* **30** (1992)373.
19. M. Ree, D. Y. Yoon, and W. Volksen, *J. Polym. Sci., Part B: Polym. Phys.*, **29** (1991) 1203.
20. A. Morikawa and S. Ohnuki, *Japan Polyimide and Aromatic Polymers Study Group 2020*, (2020) 48.

Communication

Journal of Photopolymer Science and Technology
Volume 34, Number 5 (2021) 463−468 ©2021SPST

Fabrication and Characterizations of Polymer Electrolyte Composite Membranes Consisted of Polymer Nanofiber Framework Bearing Connected Proton Conductive Pathways

Takahiro Ogura, Kazuto Suzuki, Manabu Tanaka, and Hiroyoshi Kawakami*

Department of Applied Chemistry, Tokyo Metropolitan University,
1-1, Minami-osawa, Hachioji, Tokyo 192-0397, Japan
** kawakami-hiroyshi@tmu.ac.jp*

Nanofiber Framework (NfF)-based polymer electrolyte membranes were investigated for polymer electrolyte fuel cells. New processes, including the hot-pressing and vapor-welding, were attempted to the polybenzimidazole nanofibers (PBINfs) to increase the fractions and connectivity of the Nfs. The phytic acid (Phy)-doping to the Nfs and the followed composition with Nafion gave hot-pressed NfF (HPNfF)/Nafion and vapor-welded NfF (VWNfF)/Nafion composite membranes. These new composite membranes showed higher proton conductivity than a conventional NfF composite membrane by forming connected effective proton conductive pathways at the interface of the three-dimensionally connected Nfs and the matrix polymer electrolyte. The mechanical and gas barrier properties were also evaluated to reveal the effectiveness of the new processes.

Keywords: Composite Membrane, Electrospinning, Nanofiber, Polymer Electrolyte Fuel Cell, Proton conductivity

1. Introduction

Polymer Electrolyte Fuel Cell (PEFC), which generates electricity using hydrogen and oxygen without the carbon dioxide emission, is one of the key technologies for the carbon-neutral society [1]. For further popularization of PEFCs, higher efficiency, more extended durability, and lower cost of the PEFC components and system are required [2, 3]. The fuel cell operating at high temperatures (120°C or above) without humidification is the promising approach to improve the catalyst activity, leading to higher efficiency and lower cost [4, 5]. However, high temperatures and low- or non-humidification are severe conditions for polymer electrolyte membranes (PEMs). In conventional PEMs, protons can dissociate from sulfonic acid groups and diffuse by hydration in the membranes. In addition, other essential characteristics, including gas barrier properties and membrane stability, generally decrease at high temperatures. Therefore, novel PEMs that achieve high proton conductivity at low relative humidity, low gas permeability, and sufficient membrane stability are strongly desired.

Over the past decades, there have been enormous numbers of reports on PEMs to achieve higher proton conductivity and better electrolyte characteristics. In addition to the optimization of chemical structures of proton conductive polymers, the composition of polymer electrolytes with functional additives is an expected approach to achieve high-performance PEMs [6-8]. One of the promising materials for composite membranes includes polymer nanofibers (Nfs) prepared from an electrospinning method [9-13]. In particular, proton conductive Nfs fabricated from sulfonated polymers, such as Nafion, sulfonated poly (ether sulfone), and sulfonated polyimide, can enhance proton conductivity along with the improvement of gas barrier properties and membrane stabilities [14-20]. Instead of sulfonated polymer Nfs, we focused on acid-doped Nfs, in which polybenzimidazole (PBI) and phytic acid (Phy) that has six phosphoric acid groups were selected as a polymer for Nfs and a doped acid, respectively. The nanofiber framework

Received March 30, 2021
Accepted April 28, 2021

(NfF) was combined with matrix polymer electrolytes, such as Nafion, to give composite membranes[21, 22]. The NfF/Nafion composite membrane showed improved electrolyte characteristics and fuel cell performances, especially at low humidity [21]. Based on our previously proposed concept, in which the combination of sulfonic acid and phosphoric acid realized efficient proton conduction at low humidity [23], the Phy-doped PBINfs formed sulfonic and phosphoric acids-concentrated areas at the interfaces between the Nfs and the matrix electrolyte.

Most recently, we revealed that the compression of Nfs is a practical approach to achieve higher proton conductivity and other properties by increasing nanofiber fractions and connectivity among Nfs in the composite membranes [24]. In this study, we proceed this idea to further improve the electrolyte characteristics by the hot-pressing and the followed vapor-welding (Fig. 1). Pressing the Nfs under heating conditions is expected to make tigheter the Nfs than the previous pressing at room temperature. Also, exposure to good solvent vapor can soften and swollen the Nfs, and then the Nfs weld to each other after cooling and drying. The construction of connected proton conductive pathways is expected to enhance the proton conductive characteristics. The influence of these processes was investigated by forming three types of NfF composite membranes and evaluating their mechanical strength, proton conductivity, and gas barrier properties.

2. Experimental

All the commercially available chemicals, such as phytic acid (50wt% aqueous solution, TCI Co., Tokyo Japan) and Nafion DE 520 dispersion (Sigma-Aldrich Co., St. Louis, USA), were used without purification. Polybenzimidazole nanofibers (PBINfs) fabricated by an electrospinning method were supplied from Japan Vilene Company, Ltd. The fiber diameters, fibrous membrane thickness, and porosity were *ca.* 200 nm, 15 μm, and 90%, respectively.

Hot Pressed Nanofiber Framework (HPNfF) was prepared by pressing the pristine PBINf with 10 MPa at 120°C for 1 hour. Vapor Welded Nanofiber Framework (VWNfF) was obtained by exposing the HPNfF in *N*, *N*-dimethylformamide (DMF) vapor at 60°C for 10 min, and then dried under vacuum. All the NfFs, including conventional pristine PBINFs, were doped with Phy by immersing the NfFs in 50wt% Phy aqueous solution at room temperature for 1 hour. The Phy-doped NfFs were repeatedly washed in hot water at 80ºC for total 24 hours to remove unreacted Phy that was not chemically doped on NfFs. Then, each Phy-doped NfF was put in a petri dish, and an appropriate volume of Nafion dispersion was poured. The volume of Nafion dispersion was calculated to fill the voids among the Nfs with Nafion after slowly evaporating the

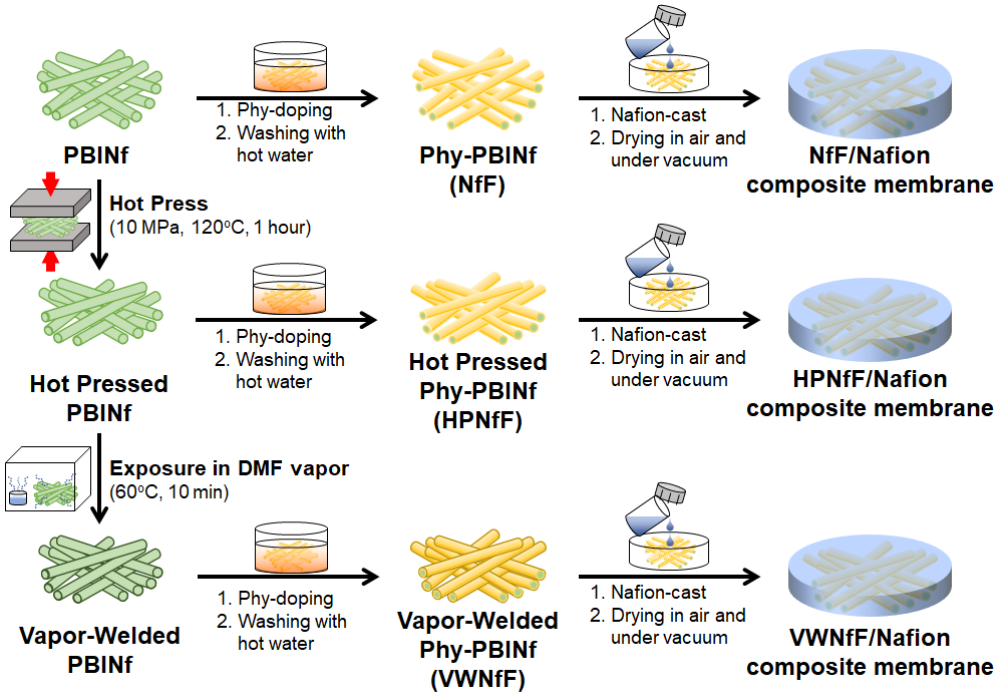

Fig. 1. Fabrication procedure of three types of NfF composite membranes.

solvent in air. Three types of obtained Phy-PBINf composite membranes, including conventional NfF/Nafion, HPNfF/Nafion, and VWNfF/Nafion, were dried under vacuum at 80°C for 24 hours.

The nanofiber and membrane morphologies were observed by JEOL JXP-6100P scanning electron microscopy (SEM). The mechanicl strength of the NfFs and membranes were measured by a tensile testing machine (AGS-X5kN, Shimadzu Co., Tokyo, Japan). The proton conductivity of the electrolyte membranes was evaluated by the electrochemical impedance analyzer (3532-50, Hioki Co., Tokyo, Japan) in a temperature- and humidity-controlled chamber. Proton conductivity σ (S cm^{-1}) was determined from the equation: $\sigma = d / (R A)$, where d, R, and A represent the distance between two platinum electrodes (cm), impedance value (Ω) in measured by the analyzer, and cross-sectional area of the membrane (cm^2), respectively. Water uptake was evaluated by the thickness change after immersing a membrane in hot water at 80°C for 24 hours. Oxygen gas permeability coefficients P_{O2} and water vapor permeance Q_{H2O} were measured according to our previous study [21,24] using a gas permeability apparatus (RGP-3000Z, Round Science Inc., Kyoto, Japan).

3. Results and discussion

3.1. NfF fabrication

Three types of NfFs were fabricated according to the procedures shown in Fig. 1. The hot-pressed PBINf was obtained by pressing the pristine PBINf with 10 MPa at 120°C for 1 hour. The thickness of the nanofibrous mat reduced from 30 μm to 24 μm after the process (Fig. 2). Although the nanofiber diameters maintained their original values (200±20 nm), the porosity also reduced from 90% to 85% by the compression. The vapor welded PBINf was prepared by exposing the hot-pressed PBINf in DMF vapor at 60°C for 10 min. Since DMF is a good solvent for the PBI, the PBINfs softened and swollen with DMF and welded each other after evaporating DMF from the Nfs. The average fiber diameter estimated by SEM slightly increased from 200±20 nm to 220±30 nm after the welding. The thickness and porosity also reduced to 19 μm and 82%, respectively. Then, each Nf, including conventional PBINf, hot-pressed PNINf, and vaper-welded PBINf, was doped with Phy and was washed with hot water to yield NfF, HPNfF, and VWNfF, respectively. Finally, pouring the Nafion dispersion onto each NfF and the followed evaporating solvent provided the NfF/Nafion, HPNfF/Nafion, and VWNf/Nafion composite membranes.

3.2. Mechanical property

Fig. 3(a) shows the mechanical strength of the three types of NfFs. In this figure, the tensile force

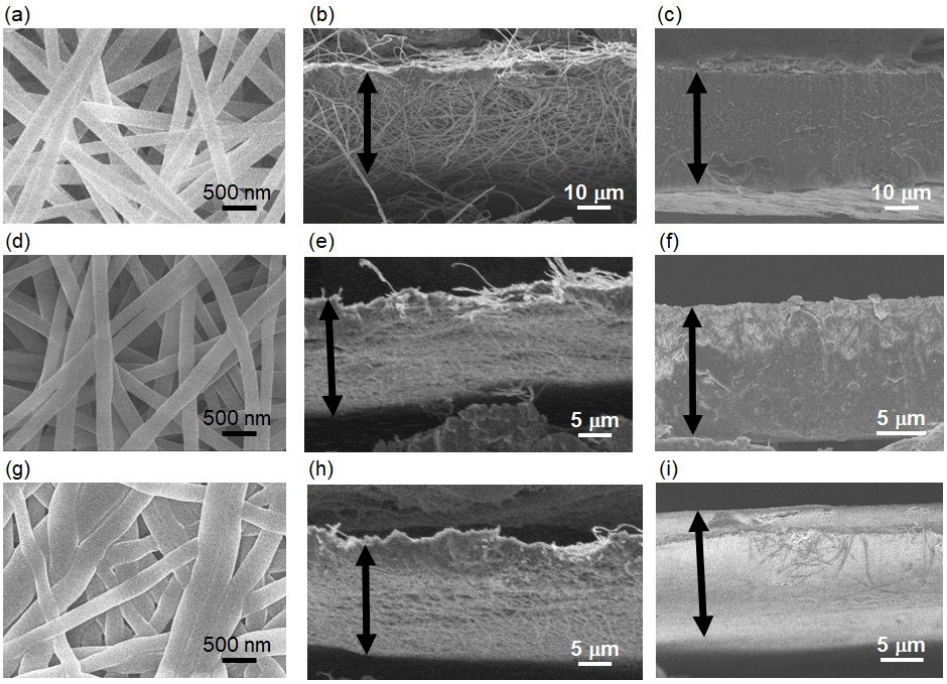

Fig. 2. Surface and cross-sectional SEM images of (a), (b) NfF (pristine PBINf), (c) NfF/Nafion composite membrane, (d), (e) HPNfF, (f) HPNfF/Nafion composite membrane, (g), (h) VWNfF, and (i) VWNfF/Naafion composite membrane.

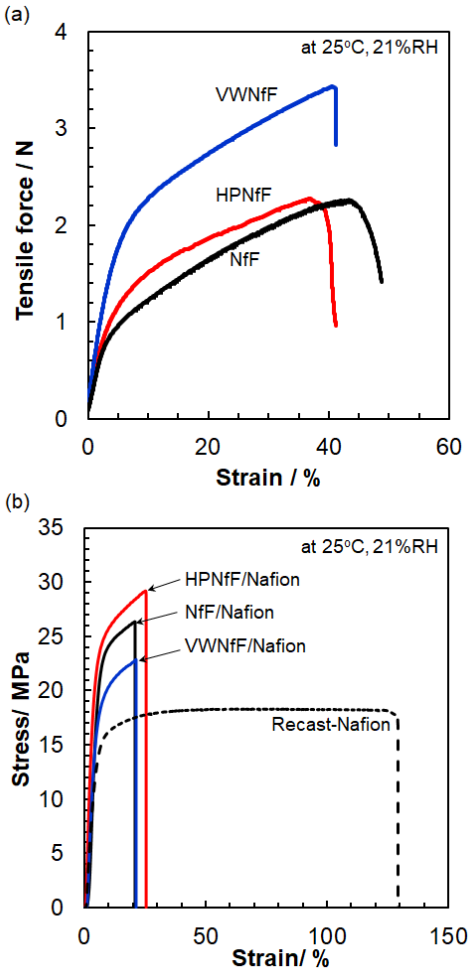

Fig. 3. Mechanical strength of (a) three types of NfFs and (b) the corresponding NfF composite membranes and the recast-Nafion membrane.

(N) was used as a Y-axis instead of stress (MPa) because the cross-sectional area of the NfFs was unclear due to the porous nanofibrous mat structures. As expected, the HPNfF and VWNfF showed higher tensile force than the conventional NfF. It indicates the hot-pressing and vapor-welding processes are effective ways to increase the mechanical strength of the NfFs. The mechanical strengths of a series of NfF/Nafion composite membranes were also depicted in Fig.3(b). The HPNfF/Nafion composite membrane indicated higher maximum stress (29.2 MPa) and elastic modulus (0.42 GPa) than those of the NfF/Nafion composite membrane (26.4 MPa and 0.39 GPa) and the recast-Nafion membrane (17.8 MPa and 0.34 GPa), respectively. However, the mechanical strength of the VWNfF/Nafion composite membrane was slightly inferior to that of the NfF/Nafion composite membrane. It may result from the insufficient densification of the VWNfF/Nafion composite membrane. As shown in Fig. 2 (g) and (h), The VWNfF formed densely welded structures that could patricianly inhibit the filling of Nafion to the void space of the nanofibrous mat. Future study for denser composite membranes from the VWNfF has the potential to achieve higher mechanical strength.

3.3. Proton conductivity

Proton conductivity is an essential characteristics of polymer electrolyte membranes. In particular, high proton conductive characteristics at low relative humidity are desired. Fig. 4 demonstrates the relative humidity and temperature dependency

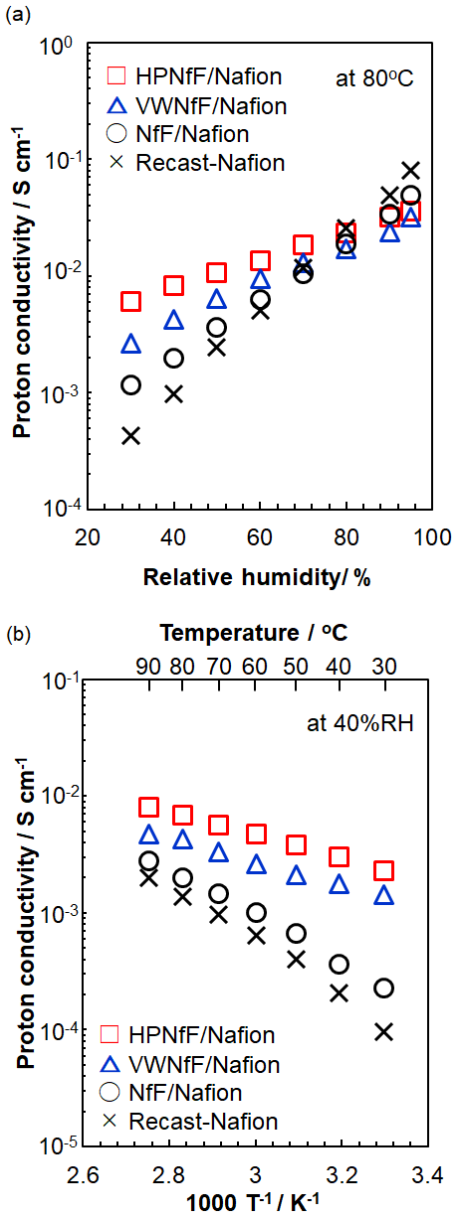

Fig. 4. Proton conductivity of the NfF composite membranes and the recast-Nafion membrane: (a) Relative humidity dependency at 80°C. (b) Temperature dependency at 40%RH.

of the proton conductivity on the NfF composite membranes. The HPNfF/Nafion and VWNfF/Nafion composite membranes showed higher proton conductivity than the conventional NfF composite membrane using pristine PBINfs and the recast-Nafion membrane without Nfs. Besides, the activation energy (E_a) of the proton conductivity at 40%RH on the HPNfF/Nafion and VWNfF/Nafion composite membranes were both 19 kJ mol^{-1}, which were much lower than those of the NfF/Nafion composite (E_a = 39 kJ mol^{-1}) and the recast-Nafion (E_a = 45 kJ mol^{-1}) membranes. These results mean that increase of the Nf fraction and the connectivity in the composite membranes is significantly effective for proton conduction, especially at low relative humidity. As is the case with mechanical strength, the VWNfF/Nafion composite membrane showed lower proton conductivity than the HPNfF/Nafion composite membrane. One possible reason is insufficient densification of the VWNfF/Nafion composite membrane, as described before. Another reason includes the difference in water uptake between the two composite membranes. After water uptake (in water at 80°C for 24 hours), a thickness change of the VWNfF/Nafion composite membrane was only 2%. In contrast, the HPNfF/Nafion and NfF/Nafion composite membrane showed their thickness change of 4.1 and 9.4% under the same conditions, respectively. The three-dimensionally connected VWNfF prevented the water swelling which may lead to lower proton conductivity of the VWNfF/Nafion composite membrane than the HPNfF/Nafion composite membrane.

3.4. Gas and water vapor permeability

High gas barrier property, that is to say low gas permeability, is required to polymer electrolyte membranes. In the fuel cell operation, gas crossover through the membrane is problematic because such gas crossover decreases the open circuit potential and the power generation efficiency. Besides, gas crossover increases the risk of decomposition of the membrane and the catalyst electrodes by forming hydrogen peroxide and radical spices from the permeated hydrogen and oxygen on the precious metal catalyst. On the other hand, sufficient water vapor permeability is required for membranes to utilize generated water by the oxygen reduction reaction effectively. As shown in Fig. 5 (a), the NfF composite membranes, especially the HPNfF/Nafion composite membrane, showed significantly lower oxygen gas permeability than

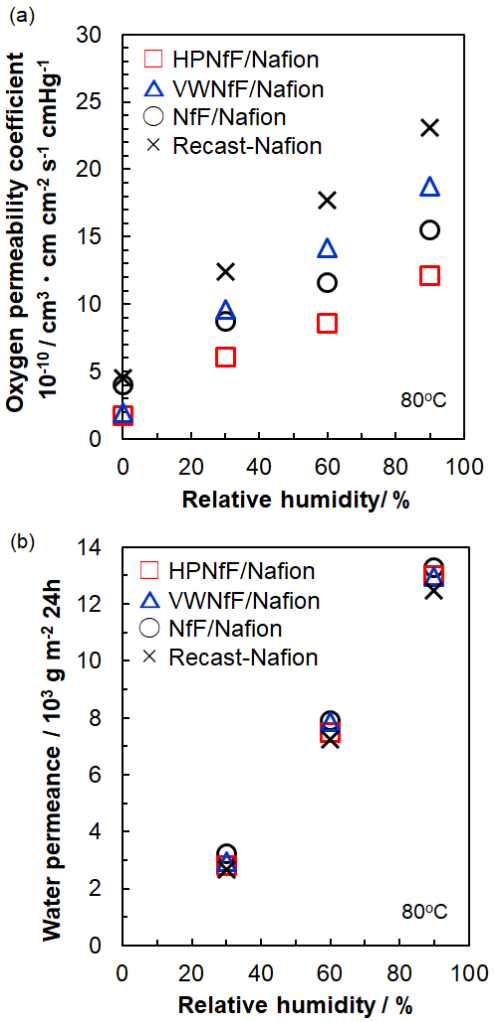

Fig. 5. Oxygen gas permeability coefficient and water vapor permeance of the NfF composite membranes and the recast-Nafion membranes.

the recast-Nafion membrane. The low gas permeable PBINfs can reduce gas diffusion in the composite membranes. By contrast, all the NfF composite membranes indicated similar water vapor permeance to the recast-Nafion membrane without nanofibers (Fig. 5 (b)). At this moment, the water vapor diffusion pathways are not clearly understood. However, based on our previous study [21], it is considered that adequate water vapor diffusion pathways were constructed at the interface between the Phy-doped PBINfs and the matrix electrolyte.

4. Conclusion

The new NfF-based polymer electrolyte membranes were developed for future PEFC applications operated under high temperatures and low- or non-humidity conditions. The hot-pressing and vapor-welding processes on PBINfs increased the nanofiber fractions and connectivity among the

Nfs. The HPNfF/Nafion and VWNfF/Nafion composite membranes showed higher proton conductivity than a conventional NfF/Nafion composite membrane. It indicates that the construction of three-dimensionally connected NfF is a promising approach to form effective proton conductive pathways in PEMs. Furthermore, mechanical strength and gas barrier property were also improved by the new NfFs. Although the VWNfF/Nafion composite membrane did not reach the expected performances due to its insufficient densification, further study on compacted and connected NfFs will promise to achieve significant characteristics to apply to future PEFCs.

Acknowledgments

This work was partially supported by a grant (Platform for Technology and Industry) from Tokyo Metropolitan Government and JSPS KAKENHI Grant No. 17K06002.

References

1. T. E. Lipman and A. Z. Weber, "*Fuel Cells and Hydrogen Production"*, Springer, New York, USA (2018).
2. Y. Manoharan, S. E. Hosseini, B. Butler, H. Alzhahrani, B. T. F. Senior, T. Ashuri, and J. Krohn, *Appl. Sci.*, **9** (2019) 2296.
3. Y. Wang, D. F. R. Diaz, K. S. Chen, Z. Wang, and X. C. Adroher, *Mater. Today*, **32** (2020) 178.
4. J. Marcinkoski, B. D. James, J. A. Kalinoski, W. Podolski, T. Benjamin, and J. Kopasz, *J. Power Sources*, **196** (2011) 5282.
5. T. Lochner, R. M. Kluge, J. Fichtner, H. A. El-Sayed, B. Garlyyev, and A. S. Bandarenka, *ChemElectroChem*, **7** (2020) 3545.
6. A. Kusoglu and A. Z. Weber, *Chem. Rev.*, **117** (2017) 987.
7. J. Miyake and K. Miyatake, *Polym. J.*, **49** (2017) 487.
8. G. G. Gagliardi, A. Ibrahim, D. Borello, and A. El-Kharouf, *Molecules*, **25** (2020) 171.
9. Y. Karube and H. Kawakami, *Polym. Adv. Technol.*, **21** (2010) 861.
10. T. Tamura and H. Kawakami, *Nano Lett.*, **10**, (2010) 1324.
11. M. Tanaka, *Polym. J.*, **48** (2016) 51.
12. P. Kallem, N. Yanar, and H. Choi, *ACS Sustain. Chem. Eng.*, **7** (2019) 1808.
13. N. Shaari and S. K. Kamarudin, *Int. J. Energy Res.*, **43** (2019) 2756.
14. B. Dong, L. Gwee, D. Salas-de la Cruz, K. I. Winey, and Y. A. Elabd, *Nano Lett.*, **10** (2010) 3785.
15. R. Takemori, G. Ito, M. Tanaka, and H. Kawakami, *RSC Adv.*, **4** (2014) 20005.
16. R. Sood, S. Cavaliere, D. J. Jones, and J. Rozière, *Nano Energy*, **26** (2016) 729.
17. H. Wang, C. Tang, X. Zhuang, B. Cheng, W. Wang, W. Kang, and H. Li, *J. Power Sources*, **365** (2017) 92.
18. T. Makinouchi, M. Tanaka, and H. Kawakami, *J. Memb. Sci.*, **530** (2017) 65.
19. G. Ito, M. Tanaka, and H. Kawakami, *Solid State Ionics*, **317** (2018) 244.
20. K. Vezzù, G. Nawn, E. Negro, G. Crivellaro, J. W. Park, R. Wycisk, and P. N. Pintauro, *J. Am. Chem. Soc.*, **142** (2020) 801.
21. M. Tanaka, Y. Takeda, T. Wakiya, Y. Wakamoto, K. Harigaya, T. Ito, T. Tarao, and H. Kawakami, *J. Power Sources*, **342** (2017) 125.
22. T. Ibaraki, M. Tanaka, and H. Kawakami, *Electrochim. Acta*, **296** (2019) 1042.
23. K. Suzuki, Y. Iizuka, M. Tanaka, and H. Kawakami, *J. Mater. Chem.*, **22** (2012) 23767.
24. T. Wakiya, M. Tanaka, and H. Kawakami, *Membranes*, **11** (2021) 90.

Journal of Photopolymer Science and Technology
Volume 34, Number 5 (2021) 469−478 ©2021SPST

Temporal Variations of Optical Emission Spectra in Microwave-Excited Plasma in Saturated Water Vapor under Reduced Pressure during Photoresist Removal

Takuya Kitano[1], Takeshi Aizawa[1,2], Tatsuo Ishijima[1*], Hiroaki Suzuki[1], Arufua Shiota[1], Yasunori Tanaka[1] and Yoshihiko Uesugi[1]

[1] Faculty of Electrical Engineering and Computer Science, Kanazawa University, Kakuma, Kanazawa, Ishikawa 920–1192, JAPAN
[2] Yonekura Mfg. Co., Ltd., Kawaasa Bldg. 2F, 2–11–5, Shin-Yokohama, Kohoku, Yokohama, Kanagawa 222–0033, JAPAN
**ishijima@ec.t.kanazawa-u.ac.jp*

Mechanisms of photoresist removal were investigated using microwave-excited plasma in saturated water vapor under a reduced pressure condition (approx. 6 kPa). A few seconds of white emission were observed at the beginning of photoresist removal. To ascertain the species of spectra, optical emission spectroscopy was used for photoresist removal from a Si wafer. Emission spectra of OH ($A^2\Sigma - X^2\Pi$), H_α (656 nm), and O (777 nm) derived from dissociation of water molecules were observed. Other emission spectra attributed to CO molecules were also detected and identified as the Ångström system ($B^1\Sigma - A^1\Pi$). This result indicates CO molecule generation during photoresist removal. The CO molecule emission intensity reached a maximum value at 1.1 s after plasma ignition, whereas those of OH, H_α, and O reached a minimum value at almost identical time. Furthermore, normalized emission spectra shape from CO molecules during photoresist removal were almost identical for Δv = +1, 0, -1, -2, -3, and -4. Rotational and vibrational temperatures of the CO molecules during photoresist removal were found to be almost constant and to be 1500 and 2500 K, respectively. These results suggest increased CO molecular density above the Si wafer at 1.1 s.

Keywords: Microwave, Optical emission spectroscopy, Photoresist removing, Water vapor plasma, CO molecular band spectra

1. Introduction

A photoresist is used for manufacturing semiconductor devices such as integrated circuits (IC) and large-scale integrated circuits (LSI). Photoresist patterns are made using three processes: spin coating, exposure, and development. Later, etching and ion implantation processes are conducted using the photoresist as a mask. For positive-tone photoresist films, an unexposed photoresist film keeps a patterned structure but an exposed photoresist is removed during development. Finally, the photoresist film mask is removed using a conventional photoresist removal technique. A mixture of sulfuric acid and hydrogen peroxide mixture (SPM) and/or O_2 plasma is used for photoresist removal [1–10]. When using the SPM, large amounts of environmentally unfriendly chemicals are used. Additionally, reuse of the chemicals is expensive. Furthermore, using SPM makes it difficult to remove hardened photoresists by ion implantation. Alternatively, if using O_2 plasma, photoresist removal rates are typically low; poor uniformity over large areas presents other difficulties. To increase photoresist removal rates, the Si wafer is usually heated to temperatures higher than 250 °C to enhance chemical reactivities on the photoresist film. This heating might degrade the efficiency of the semiconductor devices and increase defect rates. Reportedly, H_2O addition to the O_2 plasma was applied to photoresist removal. This addition might reduce the activation energy of the ashing reaction and raise photoresist removal rates in microwave-excited O_2 downstream plasma at a 2.45 GHz frequency and at 107 Pa [3]. Reportedly, photoresist

Received March 30, 2021
Accepted April 22, 2021

removal rates doubled to about 1 mm/min when the water vapor mixing ratio was increased from 0% to 10%. However, the operating temperature range was 140–200 °C. The photoresist removal rates showed strong dependence on the temperature. Moreover, particles were emitted during removal of the ion-implanted photoresist from the O_2 plasma.

Recently, photoresist removal using wet ozone instead of the conventional methods described above has been proposed. This low-temperature (approx. 100 °C) process is environmentally friendly. Wet ozone is produced by mixing ozone gas with a small amount of water vapor. However, using wet ozone entails some reported difficulties for removing ion-implanted photoresists [6–10]. Some other methods have been reported for photoresist removal, such as using CO_2 plasma [11]. The CO_2 plasma method has been evaluated for its economy and safety. Recent reports revealed its potential, compared to using O_2 plasma, for reducing low-k damage during photoresist removal. However, CO_2 ions can damage the Si wafer at chamber pressures as low as 6.7 Pa.

Using a slot antenna, we developed microwave-excited plasma produced in water bubbles under a reduced saturated vapor pressure condition [12–15] and applied it to photoresist removal [16]. Using this method, ultrapure water is used as a source gas for the microwave-excited plasma. A scroll pump was used to achieve saturated vapor pressure of approx. 6 kPa in the chamber. A Si wafer is cooled directly by water during photoresist removal. Results showed that an environmentally friendly and low-temperature photoresist removal was realized using this method. The 6 kPa operating pressure is about two orders higher than that using conventional O_2 plasma ashing. Furthermore, microwave plasma is generated in a narrow region of a few millimeters between the Si wafer and the slot antenna, which is expected to expose high radical flux density. To date, we have confirmed photoresist removal rates higher than 1 μm/min using this method, even for a positive-tone Novolak photoresist film stiffened by ion-implantation [16]. Application of this method using the slot-antenna-excited microwave plasma to a large-area process appears to be possible by customizing a suitable microwave frequency, a slot length, and slot patterns [17–22]. In such a case, clarification of photoresist removal using this method is important for application to practical industrial semiconductor manufacturing processes.

This study investigated temporal variations of optical emission images and spectra during photoresist removal using microwave-excited plasma with video camera observation and optical emission spectroscopy. The results were discussed to elucidate the mechanisms of photoresist removal using microwave-excited plasma.

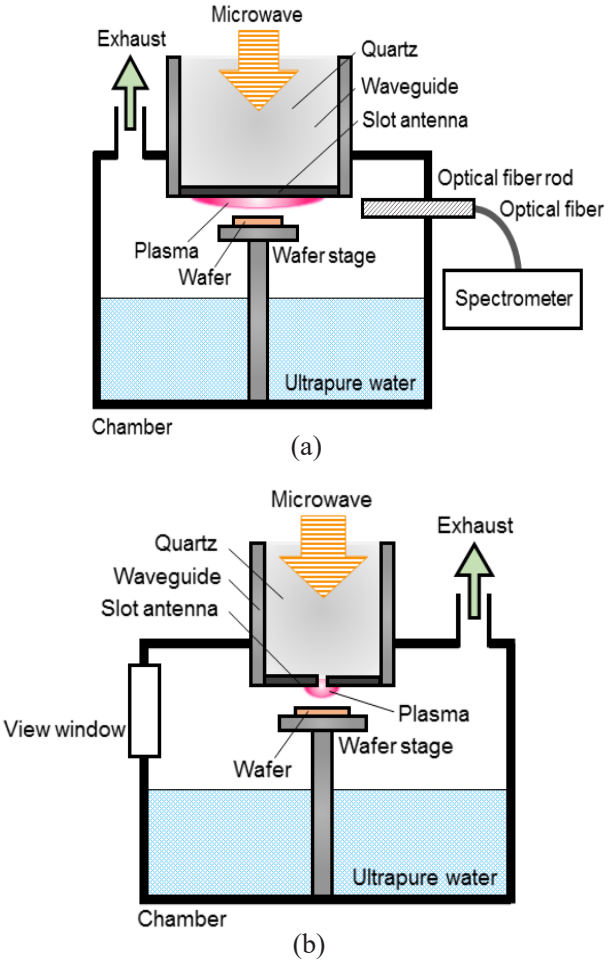

Figure 1. Experiment setup of microwave excited plasma for the photoresist removal process in saturated water vapor under the reduced pressure condition: (a) front view and (b) side view.

2. Experiment setup to assess microwave-excited plasma for photoresist removal and to diagnose its spectral

Figure 1 portrays the setup of a microwave-excited plasma experiment to elucidate photoresist removal under conditions of saturated water vapor with reduced pressure. A quartz-filled rectangular waveguide was equipped in the stainless steel chamber (V = 2 L). A silicon slot antenna [23–25] was set at the end of the waveguide. A stainless steel wafer stage was installed at the bottom of the chamber. The distance between the bottom of the 0.5 mm wide and 20 mm long slot antenna and the wafer surface was fixed at 2 mm. The chamber was

partially filled with 1 L of ultrapure water. The slot antenna was maintained under saturated water vapor during photoresist removal to avoid optical emission scattering because of bubbles. The chamber internal pressure reduced to approx. 6 kPa using a scroll pump.

A half-inch Si wafer (ϕ = 12.5 mm) for a Minimal Fab System [26, 27] was used for this study. Using a minimal coater (Litho Tech Japan Corp.), a positive-tone Novolak photoresist (OFPR-5000; Tokyo Oka Kogyo Co., Ltd.) for g/i line lithography was spin-coated onto the wafer at 800 rpm for 3 s and at 4000 rpm for 65 s. The photoresist film thickness was 1.0 μm. The wafer was baked at 90 °C for 60 s after spin-coating.

A magnetron-oscillation type microwave generator (MMG-213VPT; Micro Denshi Co., Ltd.) was used as a plasma source. A water-cooled dummy load was equipped between the microwave generator and the plasma to protect the magnetron from damage [25]. Non-modulated 2.45 GHz microwaves were injected into the water vapor through the slot antenna [12–15]. Forward and reflected microwave powers were measured using a mean-responding power detector that had been set for use in high-frequency receiver and transmitter signal chains up to 2.5 GHz (MMO-220HP; Ohta Electronics Co. Ltd.). We adjusted the impedance matching using an E-H tuner to reduce the reflected microwave power. For this experiment, the net microwave power was set at 200 W. Plasma was generated for 30 s after plasma ignition.

Video camera measurements and optical emission spectroscopy were conducted simultaneously during photoresist removal. Optical emission images were obtained from a viewing window equipped on the chamber. The video camera frame rate was set at 30 fps. Optical emission spectra were measured using a compact spectrometer (USB2000+ UV-VIS; Ocean Optics Inc.) with a grating of 600 lines/mm, slit width of 25 mm, and optical resolution of 1.5 nm for full width at half maximum. An optical fiber rod (ϕ = 6 mm, SOG-70S; Sumita Optical Glass Inc.) was connected in series to an optical fiber (ϕ = 50±5 μm, UV-VIS High OH content; Ocean Optics Inc.) and a spectrometer. The optical fiber rod was installed at a viewing port on the chamber side wall. The distance between the edge of the optical fiber rod and the center of the slot antenna was set at 17 mm. Optical emission spectra were recorded at every 100 ms with integration time of 10 ms.

3. Temporal variations of optical emission images and spectra during photoresist removal using microwave-excited plasma

White emission was observed at the moment of a microwave-excited plasma ignition (t = 0 s) when a Si wafer with photoresist was located below the slot antenna. Figure 2 presents temporal variations of optical emission images of the plasma during photoresist removal at t = 0, 1.0, and 5.0 s. From visual observation, we inferred that the white emission intensity reached its maximum at around t = 1 s. The white emission immediately turned to red-purple color in a few seconds, which was the same color as that observed in the case of a bare Si wafer. The red-purple emission derived from H_α (656 nm)

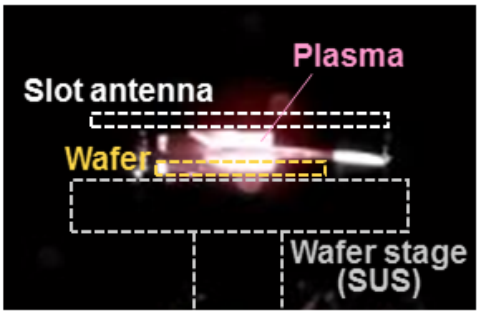

(a)

(b)

(c)

Figure 2. Optical emission images of microwave excited plasma during photoresist removal at (a) t = 0 s, (b) 1.0 s, and (c) 5.0 s. They were reflected optical emission images observed on the Si surface and stainless steel holder.

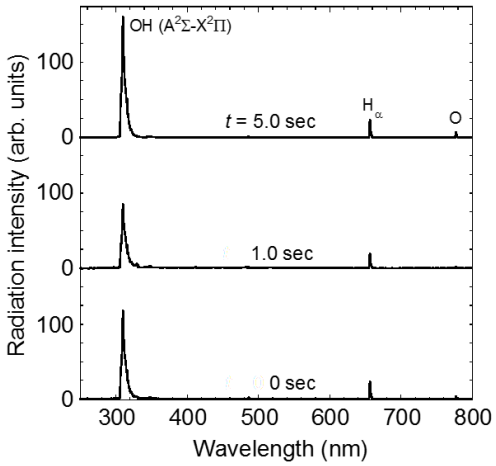

Figure 3. Spectra of microwave-excited plasma during photoresist removal at t = 0, 1.0, and 5.0 s.

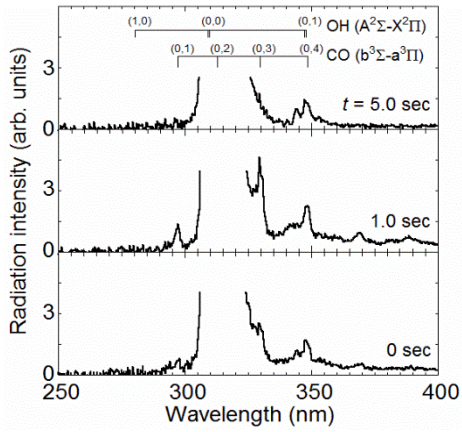

(a)

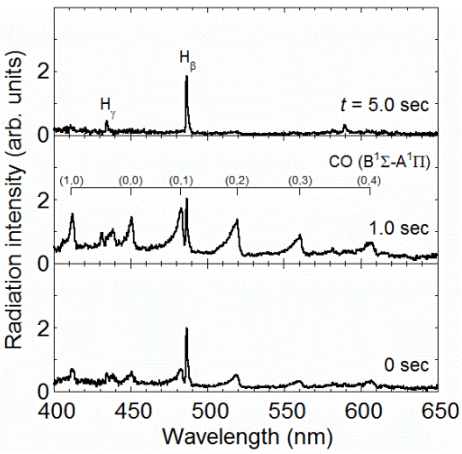

(b)

Figure 4. Optical emission spectra from (a) OH ($A^2\Sigma - X^2\Pi$) and CO ($b^3\Sigma - a^3\Pi$) in the 250 – 500 nm range and (b) H_β, H_γ, and CO ($B^1\Sigma - A^1\Pi$) in the 400–650 nm range, respectively, during photoresist removal at t = 0, 1.0, and 5.0 s.

of the hydrogen atomic line spectrum. This drastic color change suggests that the compositions of radicals, chemical species, and their densities in the plasma changed considerably in a few seconds.

Figure 3 shows widely various spectra in 250–800 nm at t = 0, 1.0, and 5.0 s. The emission spectra of OH ($A^2S - X^2P$, $\Delta v = 0$), H_α, and O (777 nm) derived from dissociation of water molecules were observed clearly [12, 28–31]. The OH band spectrum of 309 nm was the strongest among the observed spectra. OH radicals are produced mainly by electron-impact dissociation of water molecules [28] as

$$e + H_2O \rightarrow H + OH + e \qquad (1).$$

Therein, OH ($A^2\Sigma - X^2\Pi$) is a spontaneous emission observed when electrons in an excited state ($A^2\Sigma$) return to the ground state ($X^2\Pi$) [31]. Because OH radicals have high oxidation potential [30], OH radicals decompose the photoresist [16].

Emission spectra of CO (third positive system, $b^3\Sigma - a^3\Pi$) [1, 2, 32–35] and another CO (Ångström system, $B^1\Sigma - A^1\Pi$) [1, 2, 32–40] are presented respectively in Tables 1(a) and 1(b) [35]. These spectra are readily apparent. The same is also true for spectra of H_β (486 nm) and H_γ (434 nm) in the 250–650 nm range at around t = 1.0 s, as shown in Figs. 4(a) and 4(b).

Figure 5 shows temporal variations of emission intensity of OH ($A^2\Sigma - X^2\Pi$, $\Delta v = 0$), H_α, O, and CO ($B^1\Sigma - A^1\Pi$, Δv = -1, 484 nm). The CO emission intensity of Δv = -1 increased and reached a

Table 1. List of the band-heads of (a) CO (third positive system, $b^3\Sigma - a^3\Pi$) and (b) CO (Ångström system, $B^1\Sigma - A^1\Pi$) [35]

(a)

Wavelength (nm)	Sequence $\Delta v = (v'\text{-}v'')$	Transition (v', v'')
297.74	-1	(0,1)
313.44	-2	(0,2)
330.57	-3	(0,3)
349.33	-4	(0,4)

(b)

Wavelength (nm)	Sequence $\Delta v = (v'\text{-}v'')$	Transition (v', v'')
412.36	+1	(1,0)
451.09	0	(0,0)
483.53	-1	(0,1)
519.82	-2	(0,2)
561.02	-3	(0,3)
607.99	-4	(0,4)

maximum value at t = 1.1 s. Subsequently, the CO emission intensity of Δv = -1 decreased monotonically for 10 s until it became undetectable. However, the emission intensities of OH, H_α, and O respectively reached minimum values at t = 1.1 s, in contrast to the results found for CO.

Figure 6 portrays the CO molecular band spectra obtained using the Ångström system ($B^1\Sigma - A^1\Pi$) for 470–570 nm, which will be used for deeper investigation of the temporal variation of the CO band spectra shape. The CO emission spectra at t = 0, 1.0, and 2.0 s are shown. The continuum compositions [41, 42] in these spectra were subtracted and normalized at 484 nm (Δv = -1). The CO molecular spectra shapes almost all mutually overlapped even though these CO molecular intensities varied greatly, as portrayed in Fig. 4(b).

4. Evaluating CO molecule rotational and vibrational temperatures

Rotational and vibrational temperatures of CO molecules were ascertained from calculations of optical emission spectra of $B^1\Sigma - A^1\Pi$ electronic transitions of the CO molecule. The electronic transitions take place from the rotational levels of the various levels of one electronic state to the rotational and vibrational levels of another electronic state. The energy of a molecule is calculated using the sum of electronic energy T_e, vibrational energy $G(v)$, and rotational energy $F_v(J)$, as shown below.

$$E = T_e + G(v) + F_v(J) \tag{2}$$

Therein, v represents a vibrational state; J denotes a rotational state. The energy difference ΔE from an upper state to a lower state is presented below.

$$\begin{aligned}\Delta E &= \Delta T_e + \Delta G(v) + \Delta F_v(J) \\ &= T_{e'} - T_{e''} + G(v') - G(v'') + F_{v'}(J') - \\ &\quad F_{v''}(J'')\end{aligned} \tag{3}$$

Therein, the upper state and the lower state are represented respectively by apostrophes and double quotation marks. Each molecular band emission spectrum depends on the rotational and vibrational states according to the rotational and vibrational temperatures. Assuming that the number density of excited molecules in the upper state follows a Boltzmann distribution, the spectrum is calculated using spectrum emission coefficients. The spectrum emission coefficients of diatomic molecules are calculated using the following equations [38, 43].

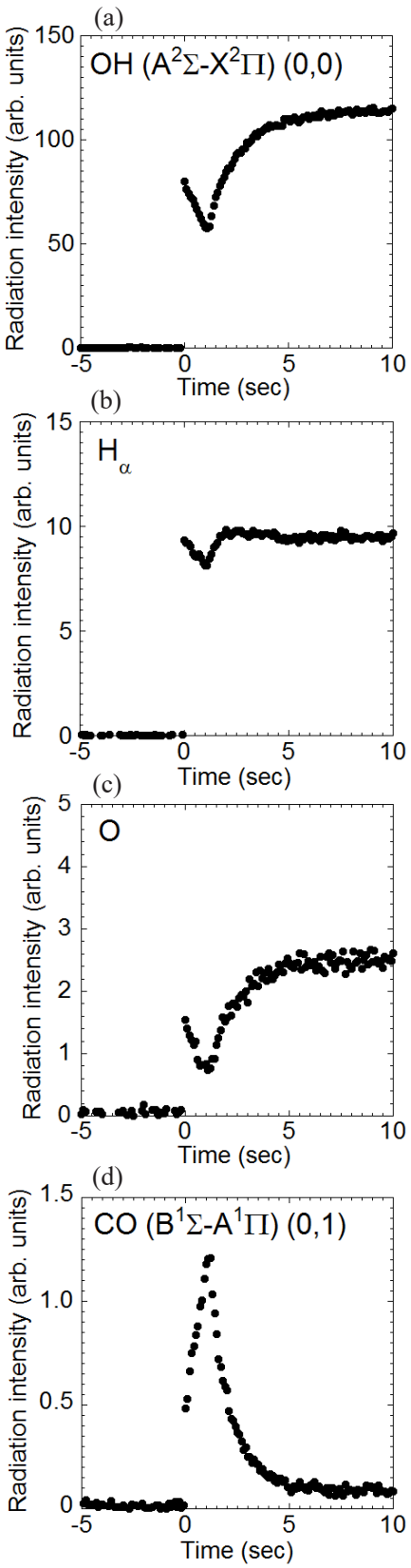

Figure 5 Temporal variations of emission intensities of (a) OH, (b) H_α, (c) O, and (d) CO ($B^1\Sigma - A^1\Pi$, Δv = -1, 484 nm) before and during photoresist removal.

Emission coefficient:

$$\varepsilon_{n'n''v'v''J'J''} = \frac{1}{4\pi}\frac{hc}{\lambda_{n'n''v'v''J'J''}} N_{n'v'J'} A_{n'n''v'v''J'J''} \quad (4)$$

Therein, $N_{n'v'J'}$ denotes the number density of molecules in an upper state, $A_{n'n''v'v''J'J''}$ denotes a transition probability from an upper state to a lower state, n', n'', v', v'', J', and J'' respectively denote an electronic state, a vibrational quantum number, and rotational quantum numbers of upper and lower states.

Number density in the upper state:

$$N_{n'v'J'} = \frac{N(T_{ex},T_{vib},T_{rot})}{Z(T_{ex},T_{vib},T_{rot})}(2J'+1)\cdot\exp\left(-\frac{hcT_{e'}}{kT_{ex}}\right)\cdot \exp\left(-\frac{hcF_{v'}(J')}{kT_{rot}}\right)\cdot\exp\left(-\frac{hcG(v')}{kT_{vib}}\right) \quad (5)$$

Transition probability:

$$A_{n'n''v'v''J'J''} = A_{n'n''}q_{v'v''}\frac{S_{J'}}{2J'+1} \quad (6)$$

$$A_{n'n''} = \frac{64\pi^4 e^2}{3hc^3\lambda_{n'n''}^3}\left|R_e^{n'n''}\right|^2 \quad (7)$$

Hönl–London Factors for P, Q, and R branches:

$$S_{J'}^P = \frac{(J'+1+\Lambda')(J'+1-\Lambda')}{J'+1} \quad (8)$$

$$S_{J'}^Q = \frac{(2J'+1)\Lambda'^2}{J'(J'+1)} \quad (9)$$

$$S_{J'}^R = \frac{(J'+\Lambda')(J'-\Lambda')}{J'} \quad (10)$$

Rotational energy:

$$F_v(J) = B_vJ(J+1) - D_vJ^2(J+1)^2 \quad (11)$$

Vibrational energy:

$$G(v) = \omega_e\left(v+\frac{1}{2}\right) - \omega_e x_e\left(v+\frac{1}{2}\right)^2 \quad (12)$$

In those equations, N represents the total number density of molecules, Z stands for the internal state sum of molecules, $q_{v'v''}$ are Franck–Condon factors, $S_{J'}$ is the intensity factor, $|R_e^{n'n''}|$ denotes the electronic transition moment deduced from the average radiative lifetimes of the $B^1\Sigma$ states of CO [37], h is Planck's constant, k is Boltzmann's constant, c represents the velocity of light, T_{ex} stands for the excitation temperature, T_{vib} denotes the vibrational temperature, T_{rot} expresses the rotational temperature, ω_e and $\omega_e x_e$ are vibrational constants, L represents the total orbital angular momentum. Also,

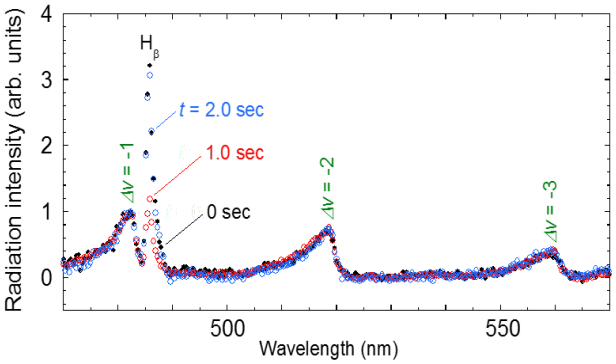

Figure 6. Spectral shapes of CO ($B^1\Sigma$ – $A^1\Pi$) normalized at Δv = -1 (484 nm) for t = 0, 1.0, and 2.0 s in the 470–570 nm range.

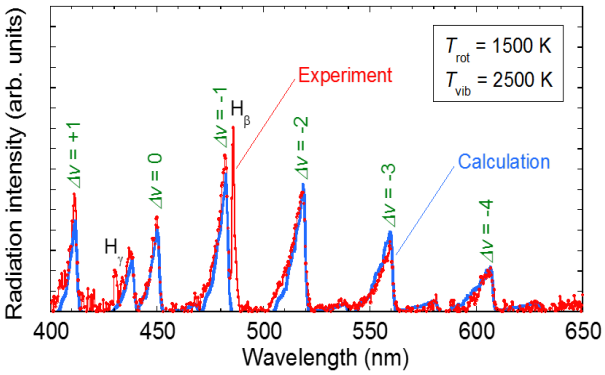

Figure 7. Spectra of CO ($B^1\Sigma$ – $A^1\Pi$): experiment and calculated results in the 400–650 nm range.

B_v and D_v are the rotational constants, which are defined as

$$B_v = B_e - \alpha_e\left(v+\frac{1}{2}\right) \text{ and } \quad (13)$$

$$D_v = D_e + \beta_e\left(v+\frac{1}{2}\right), \quad (14)$$

where B_e is the rotational constant for the equilibrium position, D_e is the value of the constant for the equilibrium position, and α_e and β_e are correction factors [43]. These molecular constants of electronic states, which are adopted for calculations, are presented in Table 2 [34, 38, 39]. β_e is calculated using an approximate formula shown in [38].

When we represent ΔE using an energy unit of centimeter^{-1}, which is the wavenumber of transition spectra from upper to lower state, ΔE is expressed as

$$\Delta E = \frac{1}{\lambda_{n'n''v'v''J'J''}}, \quad (15)$$

where $\lambda_{n'n''v'v''J'J''}$ (cm) represents the wavelength of

Table 2. Molecular constants of electronic states for CO (Ångström system, $B^1\Sigma - A^1\Pi$) [34, 38, 39]

State	T_e (cm^{-1})	ω_e (cm^{-1})	$\omega_e x_e$ (cm^{-1})	B_e (cm^{-1})	α_e (cm^{-1})	D_e (cm^{-1})
$B^1\Sigma$	86948	2150.41	34.09	1.961	0.027	6.48×10^{-6}
$A^1\Pi$	65075	1515.61	17.25	1.612	0.022	6.45×10^{-6}

transition spectra from an upper to lower state. For this study, we measure the emission spectra of the CO molecule band (Ångström system, $B^1\Sigma - A^1\Pi$, which is presented in Table 1(b)). Figure 7 portrays calculated spectra with experimentally obtained spectra at t = 1.0 s during photoresist removal in the 400–650 nm range. A continuum light component [41, 42] in the experimental spectra was subtracted. Fitting the calculated theoretical spectra as functions of rotational and vibrational temperatures with experimentally obtained spectra, the respective rotational and vibrational temperatures were found to be 1500 and 2500 K.

5. Discussion

For this study, we performed a spectroscopic diagnosis during photoresist removal using microwave plasma in saturated water vapor. The characteristic band spectra were found. These band spectra appeared especially at the beginning of photoresist removal in the 250–650 nm range, although they were much weaker than the emission spectra of OH ($A^2\Sigma - X^2\Pi$), O, and H, as depicted in Fig. 3. By comparing the observed band spectra with reference spectra of CO (Ångström system, $B^1\Sigma - A^1\Pi$) [1, 2, 32–40], CO (third positive system, $b^3\Sigma - a^3\Pi$) [1, 2, 32–35], CO (Herzberg system, $C^1\Sigma - A^1\Pi$) [35], CO (Asundi bands, $a'^3\Sigma - a^3\Pi$) [35, 40], CO (Triplet bands, $d^3\Delta - a^3\Pi$) [35, 40], CO_2 (carbon monoxide flame bands, $^1B_2 - X^1\Sigma$) [35], CO_2^+ (Fox, Duffendack, and Barker's system, $A^2\Pi - X^2\Pi$) [11, 35, 40], C_2 (Swan system, $A^3\Pi - X'^3\Pi$) [35, 43], CH (4300Å system, $A^2\Delta - X^2\Pi$) [35], and CH (3900Å system, $B^2\Sigma - X^2\Pi$) [35] including carbon component, we identified the measured spectra as CO molecule bands of the Ångström system ($B^1\Sigma - A^1\Pi$) and the third positive system ($b^3\Sigma - a^3\Pi$) [1, 2, 32–40], as shown in Figs. 4(a) and 4(b).

Results show that the Ångström system ($B^1\Sigma - A^1\Pi$) was spectrally isolated from the other systems, although the third positive system was partially overlapped with the OH ($A^2\Sigma - X^2\Pi$) band system. The electronic energy of the upper state of CO ($B^1\Sigma$) and CO ($b^3\Sigma$) is lower than that of H_α, H_β, H_γ, and O [32, 33, 36, 45, 46], suggesting that there might be sufficient electrons with high energy to excite CO molecules to the states of ($B^1\Sigma$, $b^3\Sigma$) in microwave-excited plasma. Observation of the CO molecular band system indicates clearly that CO arises from plasma-induced oxidation of the polymeric photoresist material.

The CO band spectra were also observed in radiofrequency (rf) O_2 plasma during photoresist removal [1, 2]. The plasma is produced using rf coils at rf frequency of 13.56 MHz, pressure of 27 Pa, power of 300 W, and an O_2 flow rate of 55 sccm. The photoresist (SC-180; Fujifilum Hunt Chemicals USA Inc.) was coated onto a 2-inch Si wafer. The photoresist thickness was 3 mm. For O_2 plasma ashing, excited oxygen atoms decompose the photoresist film and produce excited-state CO molecules as well as hydrogen atoms. The measured CO molecular band intensity was almost comparable with the OH band spectral intensity [1, 2]. However, from this study, we observed intense OH band spectra and H-and-O atomic lines, whereas the intensity of CO band spectra is much weaker than that of other spectra. This finding suggests that the reactive radical densities of, for example OH, H, and O supplied from water molecules, are much greater than the CO molecular density from the photoresist film compared with the O_2 plasma ashing case.

Regarding the existence of CO_2 ions, the emission spectra of CO_2 ions (288 nm) were confirmed only in CO_2 plasma under the condition of higher CO_2 gas composition [11]. The CO_2 plasma was produced at an rf frequency of 2.0 and 13.56 MHz, 6.7 Pa pressure, 300 W power, and a CO_2 gas flow rates of 40 to 500 sccm. The energies for dissociation and ionization of CO_2 molecules are presented below.

$$CO_2 + e \rightarrow CO + O^* + e \quad 5.4\,eV \quad \text{(dissociation)} \tag{16}$$

$$CO_2 + e \rightarrow {CO_2}^+ + 2e \quad 13.8\,eV \quad \text{(ionization)} \tag{17}$$

When the plasma is generated using an rf

generator with a lower frequency, the electron energy presumably increases because the electrons are likely to be accelerated by the electric field in such a low pressure condition of 6.7 Pa. The emission spectra of CO_2 ions are also observed at low pressure [35]. The emission intensity of CO_2 ions (288 nm) was higher than that of the oxygen line of 777 nm in CO_2 plasma ashing [11]. The CO_2 ion emission intensity was too low to be measured in this study, indicating that the CO_2 molecular density was sufficiently low during the ashing process.

In addition, a broad continuum emission was observed in the 250–650 nm range, especially at t = 1.0 s, as shown in Figs. 4(a) and 4(b). Because the operating pressure is as high as 6 kPa and because the microwave-excited plasma was produced in the narrow region, high-density plasma might be generated above the Si wafer including high-density neutral molecules. The broad continuum emission might be attributed to Bremsstrahlung [41, 42]. It is noteworthy that, N_2 second positive system ($C^3\Pi$ – $B^3\Pi$) [35] was not observed clearly in this study, but it was observed in the O_2 ashing plasma [1, 2] as shown in Figs. 4(a) and 4(b). This result suggests that the presence of negligibly small molecular nitrogen in the system accounts for the observable emission bands.

The emission intensity of CO ($B^1\Sigma$ – $A^1\Pi$, Δv = -1, 484 nm) reached a maximum value at 1.1 s after plasma ignition, whereas that of OH ($A^2\Sigma$ – $X^2\Pi$, Δv = 0), H_α, and O reached a minimum value simultaneously, as presented in Fig. 5. The temporal variations of other CO ($B^1\Sigma$ – $A^1\Pi$, Δv = +1, 0, -2, -3, and -4) as well as CO ($b^3\Sigma$ – $a^3\Pi$, Δv = -1, 298 nm) band spectra intensity followed an almost identical tendency as that of CO ($B^1\Sigma$ – $A^1\Pi$, Δv = -1) (not shown here). These results indicate that the compositions of radicals and chemical species, and their densities in the plasma, were changed drastically during a few seconds after plasma ignition, which suggests that the photoresist on the half-inch Si wafer, where the optical rod was located, has been removed completely in a few seconds. Consequently, monitoring the emission intensity of CO molecules becomes a matter of endpoint detection. This endpoint detection technique will be useful to control damage to the Si wafer during manufacturing. Temporal variations of CO ($b^3\Sigma$ – $a^3\Pi$, 297.7 nm), CO ($B^1\Sigma$ – $A^1\Pi$, 519.8 nm), H_α, and O (615.6 nm) were reported when using O_2 plasma ashing [1, 2]. As one earlier study found [2], the emission intensity of CO ($B^1\Sigma$ – $A^1\Pi$, 519.8 nm) reached a maximum value at around 6.3 min after plasma ignition (t = 0 s). The H_α emission intensity also increased concomitantly with increasing treatment time [2]. By contrast, this study demonstrated that the H_α emission intensity decreased slightly and reached a minimum value, in contrast to results obtained for O_2 plasma ashing, when CO band spectra reached a maximum value during photoresist ashing. Furthermore, the H_α intensity increased and became saturated rapidly after the CO band spectra started to decrease, suggesting abstraction of H atom from the photoresist film [2]. The emission intensity of O decreased when CO overlapped with OH, and CO intensities (283.0, and 308.9 nm) increased in O_2 plasma ashing. However, OH and O intensities decreased and increased gradually when CO ($B^1\Sigma$ – $A^1\Pi$, $b^3\Sigma$ – $a^3\Pi$) band spectra increased in this study. Temporal variations of OH, O, and H show clearly that the origins of H atom differ greatly from that of OH and O species, supporting the hypothesis of the H abstraction reaction on the photoresist film surface. It is noteworthy that rapid variations of OH and O radicals show an excess amount of radical species derived from water vapor, resulting in enhancement of surface reaction on the photoresist film and a high-speed ashing process.

To investigate the temporal variation of the rotational and the vibrational temperatures of CO molecules, measured CO band spectra were compared at t = 0, 1.0, and 2.0 s, as depicted in Fig. 6. These spectra are overlapped almost completely for 2 s after plasma ignition, indicating that the rotational and vibrational temperatures of the CO molecules were stable and almost constant during photoresist removal, even though the CO, O, and H_α intensities were altered dramatically. Therefore, the increase of emission intensity of CO molecules, as presented in Fig. 5(d), showed a rapid increase of CO molecule density above the Si wafer.

The following scenario is proposed for a photoresist removal mechanism in the case of using microwave-excited plasma in saturated water vapor under the reduced pressure condition. First, radicals such as OH, H, and O derived from water vapor are produced by microwave plasma. Then these reactive species react with the photoresist film and cause desorption of carbon-including molecules such as CO_x and C_yH_z. Subsequently, the molecules which contain desorbed carbon increase in number. Electron impacts oxidize and excite them. They are de-excited above the Si wafer because of the increased CO emission intensity. Finally, the CO emission intensity decreases when the photoresist

film is removed by the plasma.

For the 400–650 nm range, we conducted calculations of C_2 swan band spectra [44] to elucidate the possibility of appearance and overlap. In doing so, we found out that the C_2 swan spectra intensity would be negligibly small. Carbon-containing species would most likely be CO molecules, although we were unable to detect unexcited radical species. In this study, the calculated CO spectra show very good agreement with experimentally obtained spectra for obtained CO rotational and vibrational temperatures, respectively, of 1500 and 2500 K.

6. Conclusions

Optical emission images and optical emission spectra during photoresist removal were investigated using microwave-excited plasma. In this study, the microwave plasma was generated at a power of 200 W, and at a water vapor pressure of approx. 6 kPa. The distance between the bottom of the slot antenna and the wafer surface was fixed at 2 mm. A film thickness of positive-tone Novolak photoresist was 1.0 μm. White emission was observed at the moment of microwave-excited plasma ignition (t = 0 s). After a few seconds, the white emission turned to a red-purple color. The emission spectra of OH ($A^2\Sigma$ – $X^2\Pi$, Δv = 0), H_α (656 nm), H_β (486 nm), H_γ (434 nm), and O (777 nm) derived from dissociation of water molecules were observed clearly during photoresist removal. The emission spectra of CO (third positive system, $b^3\Sigma - a^3\Pi$) and CO (Ångström system, $B^1\Sigma - A^1\Pi$) were also observed at around t = 1.0 s. The emission intensity of CO ($B^1\Sigma - A^1\Pi$, Δv = -1, 484 nm) reached a maximum value at t = 1.1 s, whereas those of OH, H_α, and O reached their respective minimum values at t = 1.1 s. The CO molecular spectra shapes almost overlapped during photoresist removal. These results indicate the occurrence of a high-speed ashing process. Rotational and vibrational temperatures of the CO molecules during photoresist removal were found, respectively, to be 1500 and 2500 K.

Acknowledgments

The authors thank Dr. Shiro Hara and Dr. Sommawan Khumpuang, Minimal Fab Development Association, The National Institute of Advanced Industrial Science and Technology, for preparing the photoresist-coated Si wafer. Mr. Naoto Kodama, Faculty of Electrical Engineering and Computer Science, Kanazawa University, and Dr. Eugen Stamate, Department of Energy Conversion and Storage, Technical University of Denmark, are also acknowledged for fundamental assistance with optical emission spectroscopy. This work was partially supported by Strategic Core Technology Advancement Program (Grant No. 2730807053) by Ministry of Economy, Trade and Industry.

References

1. E. O. Degenkolb, C. J. Mogab, M. R. Goldrick, and J. E. Griffiths, *Appl. Spectrosc*., **30** (1976) 520.
2. J. E. Griffiths and E. O. Degenkolb, *Appl. Spectrosc*., **31** (1977) 134.
3. S. Fujimura, K. Shinagawa, M. T. Suzuki, and M. Nakamura, *J. Vac. Sci. Technol*., *B* **9** (1991) 357.
4. K. Taniguchi, K. Tanaka, T. Inomata, and M. Kogoma, *J. Photopolym. Sci. Technol*., **10** (1997) 113.
5. K. Tanaka, T. Inomata, and M. Kogoma, *Plasmas Polym*., **4** (1999) 269.
6. H. Horibe, M. Yamamoto, T. Ichikawa, T. Kamimura, and S. Tagawa, *J. Photopolym. Sci. Tech*., **20** (2007) 315.
7. H. Horibe, M. Yamamoto, Y. Goto, T. Miura, and S. Tagawa, *Jpn. J. Appl. Phys*., **48** (2009) 026505.
8. Y. Goto, Y. Angata, M. Igarashi, M. Yamamoto, T. Nobuta, T. Iida, A. Kono, and H. Horibe, *Jpn. J. Appl. Phys*., **51** (2014) 026504.
9. M. Takahashi, H. Ishikawa, T. Asano, and H. Horibe, *J. Phys. Chem. C*, **116** (2012) 12578.
10. Y. Goto, Y. Angata, E. Tsukazaki, S. Takahashi, K. Koike, T. Yamagishi, and H. Horibe, *Jpn. J. Appl. Phys*., **53** (2014) 02BB04.
11. Y. Susa, H. Ohtake, Z. Jianping, L. Chen, and T. Nozawa, *J. Vac. Sci. Technol*. A **33** (2015) 061307.
12. T. Ishijima, H. Hotta, and H. Sugai, *Appl. Phys. Lett*., **91** (2007) 121501.
13. T. Ishijima, H. Sugiura, R. Saito, H. Toyoda, and H. Sugai, *Plasma Sources Sci. Technol*., **19** (2010) 015010.
14. R. Saito, H. Sugiura, T. Ishijima, and H. Toyoda, *Curr. Appl. Phys*., **11** (2011) S195.
15. T. Takahashi, N. Takada, and H. Toyoda, *Jpn. J. Appl. Phys*., **53** (2014) 07KE01.
16. T. Ishijima, K. Nosaka, Y. Tanaka, Y. Uesugi, Y. Goto, and H. Horibe, *Appl. Phys. Lett.,* **103** (2013) 142101.
17. N. Sato, S. Iizuka, Y. Nakagawa, and T. Tsukada, *Appl. Phys. Lett*., **62** (1993) 1469.
18. T. Ikushima, Y. Okuno, and H. Fujita, *Appl. Phys. Lett*., **64** (1994) 25.
19. D. Korzec, F. Werner, R. Winter, and J.

Engemann, *Plasma Sources Sci. Technol.,* **5** (1996) 216.
20. R. Winter, D. Korzec, and J. Engemann, *Surf. Coat. Tech*., **93** (1997) 134.
21. C. Tian, T. Nozawa, K. Ishibashi, H. Kameyama, and T. Morimoto, *J. Vac. Sci. Technol*., A **24** (2006) 1421.
22. H. Suzuki, S. Nakano, H. Itoh, M. Sekine, N. Hori, and H. Toyoda, *Jpn. J. Appl. Phys.,* **55** (2016) 01AH09.
23. H. G. Booker, *J. IEE III A* **93** (1946) 620.
24. W. H. Watson, The physical principles of waveguide transmission and antenna systems, Oxford University Press, Clarendon, pp.137 (1947).
25. F. Werner, D. Korzec, and J. Engemann, *Plasma Sources Sci. Technol*., **3** (1994) 473.
26. S. Khumpuang, H. Maekawa, and S. Hara, *IEEJ Trans. Sensors Micromachines*, **133** (2013) 272.
27. S. Khumpuang and S. Hara, *IEEE. T. Semiconduct. M*., **28** (2015) 393.
28. A. A. Joshi, B. R. Locke, P. Arce, and W. C. Finney, *J. Hazard. Mater*., **41** (1995) 3.
29. J. S. Clements, M. Sato, and R. H. Davis, *IEEE Trans. Ind. Appl*., **32** (1) (1996) 106.
30. P. Sunka, V. Babicky, M. Clupek, P. Lukes, M. Simek, J. Schmidt, and M. Cernak, *Plasma Sources Sci. Technol.,* **8** (1999) 258.
31. P. Bruggeman, D. C. Schram, M. G. Kong, and C. Leys, *Plasma Process. Polym.,* **6** (2009) 751.
32. Raymond T. Birge, *Phys. Rev.,* **28** (1926) 1157.
33. O. S. Duffendack, and G. W. Fox, *Astrophys. J.,* **65** (1927) 214.
34. P. H. Krupenie, The Band Spectrum of Carbon Monoxide, Institute for Basic Standards National Bureau of Standards, Washington D.C. (1966).
35. G. Herzberg, The Identification of Molecular Spectra, Chapman and Hall, London (1976).
36. I. Tobias, R. J. Fallon, and J. T. Vanderslice, *J. Chem. Phys.,* **33** (1960) 1638.
37. J. Rogers, and R. Anderson, *J. Opt. Soc. Am.,* **60** (1970) 278.
38. G. Herzberg, Molecular Spectra & Molecular Structure Vol. 1, Chapman and Hall, London (1975).
39. R. Kepa and M. Rytel, J. Phys. B: *At. Mol. Opt. Phys*., **26** (1993) 3355.
40. C. Rond, A. Bultel, P. Boubert, and B. G. Cheron, *Chem. Phys*., **354** (2008) 16.
41. H. R. Griem, Principle of Plasma Spectroscopy, Cambridge University Press, Edinburgh (1997).
42. S. Park, W. Choe, H. Kim, and J. Y. Park, *Plasma Sources Sci. Technol.,* **24** (2015) 034003.
43. G. Herzberg, The spectra and structures of simple free radicals, Dover Publications, New York (1975).
44. Y. Haruta, K. Fujimoto, S. Horita, Y. Tanaka, Y. Uesugi, and T. Ishijima, *J. Phys. Conf. Ser*., **441** (2013) 012017.
45. R. J. Fallon, I. Tobias, and J. T. Vanderslice, *J. Chem. Phys*., **34** (1961) 167.
46. Atomic Spectra Database NIST, https://www.nist.gov/pml/atomic-spectra-database.

Journal of Photopolymer Science and Technology
Volume 34, Number 5 (2021) 479−484 ©2021SPST

Improved Uniformity of Photoresist Ashing for a Half-Inch Wafer with Double U-shaped Antenna Structure in a Microwave-Excited Water Vapor Plasma

Takeshi Aizawa[1,2*], Taishin Shimada[1], Tasuku Sakurai[1], Yusuke Nakano[1] Yasunori Tanaka[1], Yoshihiko Uesugi[1] and Tatsuo Ishijima[1]

[1] Electrical Engineering and Computer Science, Graduate School of Natural Science & Technology, Kanazawa University, Kakuma-machi, Kanazawa, Ishikawa 920-1192, Japan
[2] Yonekura MFG Co., Ltd. 2-11-5 Shin-yokohama, Kohoku, Yokohama 222-0033, Japan
**t-aizawa@stu.kanazawa-u.ac.jp, ishijima@ec.t.kanazawa-u.ac.jp*

In this study, the uniformity of a photoresist ashing for a half-inch wafer was improved by a developed antenna structure, a double U-shaped antenna, in microwave-excited water vapor plasma. The optimized double U-shaped antenna structure, obtained by simulating an electric field, generated a spread distribution microwave plasma. Experimentally obtained results demonstrate that the observed optical emission distribution image from the microwave plasma resembles the electric field distribution obtained from the simulation under the present water vapor plasma generation condition. The double U-shaped antenna showed a higher ashing rate and better uniformity than the conventional slot antenna.
Keywords: Double U-shaped antenna, Electromagnetic field simulation, Microwave-excited plasma, Water vapor

1. Introduction

Lithography processes of semiconductor manufacturing commonly use a photoresist. It functions as a mask on the substrate surface during ion implantation or etching. It must be removed after these processes. For photoresist removal, chemical solution treatment (sulfuric acid hydrogen peroxide mixture, SPM) [1] or oxygen plasma treatment [2–4] is generally used. Actually, SPM processing requires transportation and chemical storage, which entails operational costs. Furthermore, sulfuric acid recycling is difficult. It is not environmentally friendly. However, oxygen plasma treatment requires a higher substrate temperature for a higher ashing rate, which can exacerbate oxidation of metal wiring. Moreover, earlier reports have described that the device performance is degraded by damage on to a dielectric material with low-k during the oxygen plasma ashing process. Therefore, several ashing techniques have been studied for this purpose [5–9]. These ashing techniques are expected to reduce damage, but at with a reduced ashing rate, which is approximately 1 μm/min.

Among the various ashing techniques, water–plasma–asher (WPA) is expected to realize a very effective process that produces little damage. Microwave excited plasma is generated with a slot antenna using only ultrapure water as the material gas [10]. Moreover, WPA has a higher ashing rate. It is effective for photoresists hardened by ion implantation [11]. Furthermore, the substrate can be cooled directly with ultrapure water. Actually, slot antennas are often used with microwave-excited plasmas [12]. However, microwave plasma processes using a slot antenna often have difficulties such as poor uniformity and small processing size. Therefore, various antennas and microwave plasma-generation methods such as the spoke antenna [13], ring slot antenna [14], multislotted planar antenna [15], radial-line antenna [16,17], slotted waveguide antennas [18], long-line shaped antenna [19–21], using a dielectric material embedded multi-hollow structures under a slot antenna [22], among others [23–30] have been proposed to improve uniformity and to increase the

Received March 29, 2021
Accepted April 23, 2021

process size. The approaches associated with these antennas for improving the uniformity and increasing the processing size include changing the antenna arrangement and the shape. For instance, arranging many slots radially in a radial-line slot antenna increases the processing area considerably. Minimal Fab [31], which uses a half-inch wafer, has been developed to provide an optimal system for semiconductor devices having low and medium volume markets. Because placing multiple slots in a small area is difficult, this study specifically examines the antenna shape. Our earlier work assessed an antenna used in the WPA: a slot antenna with a single slit [10]. Plasma was generated in an elliptical shape along this slit. Therefore, the photoresist removal shape in WPA was observed as an elliptical shape resembling the plasma emission shape. Previous studies show that the ashing rate of a photoresist of OFPR5000 at the center of a half-inch wafer was 12 μm/min, but the rate outside of the wafer was only 4 μm/min when the wafer was placed on a stage at 3.5 mm below the antenna. Plasma irradiation is performed excessively on the substrate surface at the wafer center. Therefore, the ashing rate uniformity on the wafer surface must be improved.

For this study, we simulated the electric field distribution of antenna with various shapes using electromagnetic simulation to investigate the ashing rate uniformity of the substrate. The experimental study was also conducted to confirm improvement of the uniformity with the new type of antenna developed for this study.

2. Antenna Model Simulation

2.1. Calculation model

The slot antenna structure was modified to generate uniform plasma and thereby improve the ashing rate uniformity. The antenna structure was designed using commercially available electromagnetic wave simulation software: CST Microwave Studio© [10,32]. Figure 1 presents a simplified model based on which the simulation was performed. Simulation was conducted at frequencies of 2.2–2.7 GHz using a time domain solver. The electric field distribution was evaluated assuming that the microwave input power was 1 W because the plasma was not considered in this simulation. Microwaves were applied to the antenna through quartz with relative permittivity ε_r of 3.75 inserted into the R22 standard rectangular waveguide with size set to 56 × 28 mm^2. The quartz was loss-free. Free space boundary conditions were

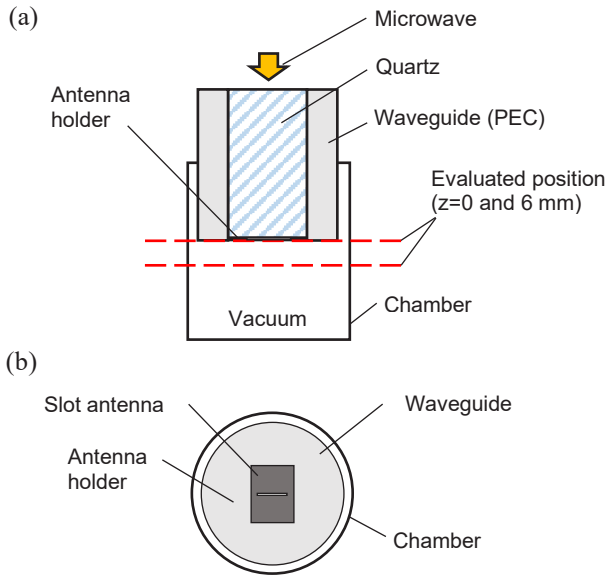

Fig. 1. Simulation model for electromagnetic waves in WPA: (a) side view and (b) bottom view.

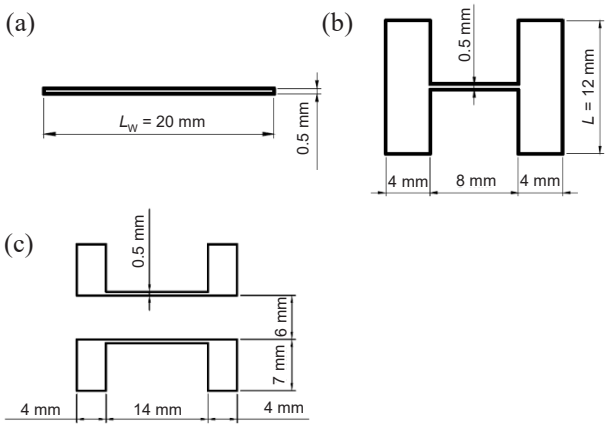

Fig. 2. Simulated antenna structure: (a) slot antenna, (b) H-shaped antenna, and (c) double U-shaped antenna.

applied at the top of the quartz waveguide. The chamber was assumed to be a polytetrafluoroethylene. The waveguide was assumed to be a perfect conductor. The antenna material, low-resistance Si, had electrical conductivity of 1000 S/m in electric field calculations. The chamber interior space was regarded as vacuum. Water was not introduced into the chamber because the calculation time was higher with water even though the calculation result underwent no significant change. The antenna surface on the chamber side was set as z = 0 mm. The electric field distribution was evaluated at z = 0 mm and z = 6.0 mm.

Fig. 2 portrays the antenna structure in this simulation model. This simulation investigated a slot antenna with a single slit (Fig. 2(a)), an H-

shaped antenna used in our earlier study with rectangular space at both ends of the slit (Fig. 2(b)), and a double U-shaped antenna with a separated H-shaped structure (Fig. 2(c)).

2.2. Simulation of Electric Field Distribution

Fig. 3 presents the electric field intensity at the center of the antenna surface $z = 0$ mm as a function of vertical length L for the H-shaped antenna presented in Fig. 2(b). The electric field intensity increases with length L. It takes the maximum value at $L = 13$ mm after which it decreases as L increases further. The antenna is considered to have a resonant structure when the outer circumference length of the slit approaches the microwave wavelength in the quartz λ_ε. We experimentally applied the TE_{10} mode in the R22 standard waveguide at 2.45 GHz excitation. Therefore, the guided microwave wavelength in the quartz λ_ε is equal to $\lambda_g/\sqrt{\varepsilon_r} \approx 76$ mm, where λ_g represents the guided microwave wavelength in vacuum. For this study, an H-shaped antenna with vertical length $L = 12$ mm was chosen. The outer circumference length was 79 mm, which approaches the calculated value of λ_ε. For the double U-shaped antenna, the outer circumference length of a single slit was set to 71 mm, which is also close to the value of λ_ε. For the slot antenna, the antenna with slit length $L_W = 37$ mm has maximum electric field intensity at total circumference of 75 mm. However, the slot antenna was manufactured with $L_W = 20$ mm for an earlier study because of device size restrictions.

Fig. 4 presents simulation results of the electric field distribution at $z = 6.0$ mm. The electric field distribution of the slot antenna in Fig. 4(a) is elliptical. This distribution matches well with the appearance of the plasma light emission and the ashing shape of the photoresist in an earlier study. Moreover, results show that the electric field intensity decreased greatly as the distance increased from the center of the slot antenna, where the electric field intensity had a maximum value of about 100 V/m. Uniformity of the electric field intensity was defined as $(E_{max}\text{-}E_{min})/2 \times E_{avg}$, where E_{max}, E_{min}, and E_{avg} respectively represent the maximum, minimum, and average electric field intensity at 14,641 points in a ± 6 mm square area at 0.1 mm intervals. The slot antenna uniformity was 34.2%. However, for the H-shaped antenna presented in Fig. 4(b), the electric field distribution is circular instead of an elliptical shape. Also, E_{max} increased by one digit compared to the slot antenna. The H-shaped antenna uniformity was 36.4%. It is

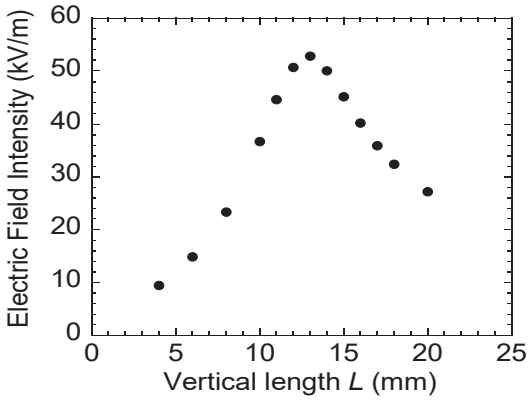

Fig. 3. Central electric field intensity at $z = 0$ as a function of vertical length L of the H-shaped antenna.

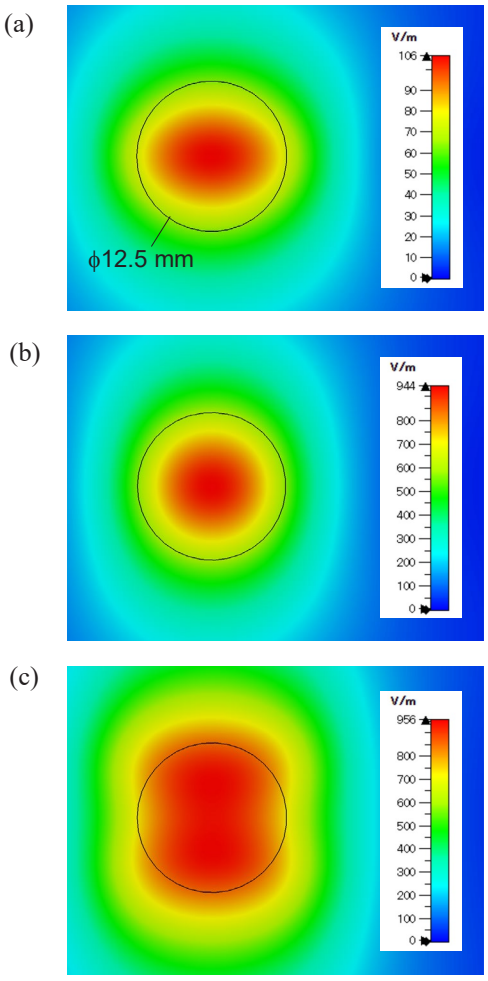

Fig. 4. Electric field distribution at $z = 6.0$ mm: (a) slot antenna, (b) H-shaped antenna, and (c) double U-shaped antenna.

expected that the ashing uniformity will not differ much, but the ashing rate is expected to be higher because plasma is generated easily in a high electric field. For the double U-shaped antenna presented in Fig. 4(c), the electric field distribution was much greater over the 0.5 inch wafer size. The uniformity

was 13.7%. The uniformity is expected to be improved considerably.

3. Experiment Results and Discussion

3.1. Experiment setup

Fig. 5 presents a schematic diagram of the experimental apparatus for WPA. Ultrapure water was introduced into the chamber up to 30 mm height under the antenna. The chamber pressure was reduced using a scroll pump. It was fixed at about 1.8 kPa. Consequently, the chamber was filled with saturated vapor of ultrapure water. Microwaves were guided along the TE_{10} mode of a quartz-filled rectangular waveguide, and propagated to the antenna installed at the waveguide end. This experiment used the slot antenna, the H-shaped antenna with L = 12 mm, and the double U-shaped antenna. These antenna were cut out from a Si wafer with a resistivity of less than 1.2×10^{-3} Ω · cm. The input microwave was modulated using a 100 Hz square wave. The peak power was 200 W. The on-time duty factor was 30%. Plasma emission images were obtained from the chamber bottom using a digital camera. Ashing was performed on the photoresist using these antennas to assess the ashing rate uniformity. The ashing target was an image reversal photoresist (AZ5214) spin-coated onto a half-inch p-type Si wafer. After the wafer was placed on an alumina stage at 6.3 mm below the antenna, the plasma was irradiated for 1 min. The film thickness before and after ashing was measured using an interference thickness meter (HORIBA STEC). The film thickness before ashing was about 1.4 μm. The ashing rate and its uniformity were evaluated by measuring the film thickness before and after ashing at 81 points in a circular area of 10 mm diameter.

3.2. Results and Discussion

Fig. 6 portrays emission images of plasma observed using the antennas of three types. Elliptical plasma was observed with the slot antenna. For the H-shaped antenna, an enlarged plasma was observed in the vertical direction of the slit. For the double U-shaped antenna, results showed that the plasma was generated in each slit. These plasmas mutually interfered and became one large plasma body. This interference was observed only with high peak power based on high-speed camera observations (emission images are not shown here). These findings suggest that the antenna structure and modulated microwave power can enlarge the plasma shape.

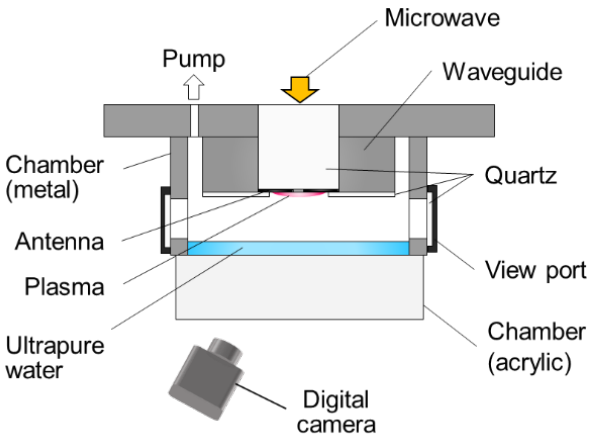

Fig. 5. Schematic of the experimental setup.

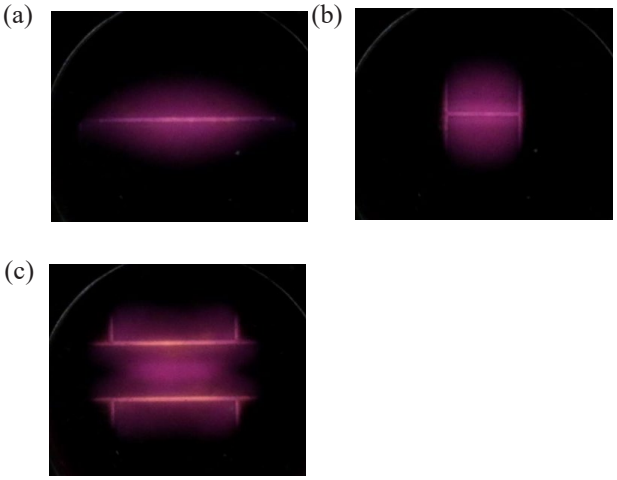

Fig. 6. Emission images of microwave excited plasma at P_{avg} = 60 W, p = 1.8 kPa: (a) slot antenna, (b) H-shaped antenna, and (c) double U-shaped antenna.

Fig. 7 shows the ashing rate distribution found for each antenna. The maximum value of the color map is the same as the maximum value of the ashing rate. For the slot antenna, the photoresist was removed with an elliptical shape under influence by the elliptical plasma shape. However, with the H-shaped antenna, the photoresist was removed with a circular shape influenced by the circular plasma shape. These distribution results are similar to the electric field distribution but the maximum ashing rate did not correlate with the electric field intensity. By the double U-shaped antenna, the photoresist was removed more uniformly over the entire wafer surface than other antennas, indicating improved uniformity. However, the ashing rate was highest at the wafer center, which was slightly different from the electric field distribution. The electron density at the center of the antenna increased, probably because of integration of the two plasmas generated at the double U-shaped antenna. When uniformity is

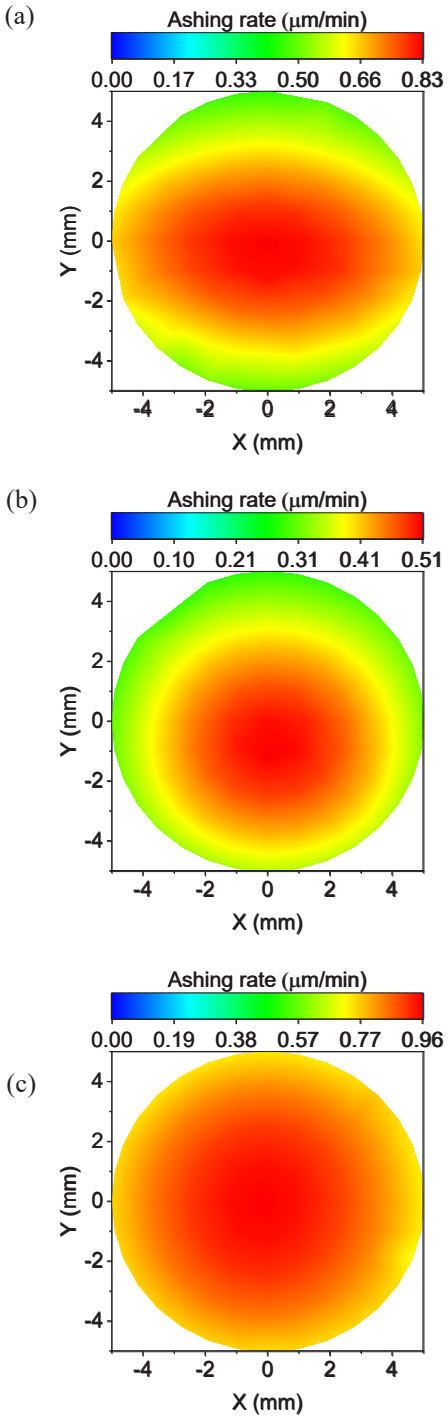

Fig. 7. Photoresist ashing rate distribution at P_{avg} = 60 W, p = 1.8 kPa, and d = 6.3 mm: (a) slot antenna, (b) H-shaped antenna, and (c) double U-shaped antenna.

defined as $(R_{max}\text{-}R_{min})/2 \times R_{avg}$, the slot antenna was 28.4%, the H-shaped antenna was 30.0%, and the double U-shaped antenna was 14.7%, where R_{max}, R_{min}, and R_{avg} respectively represent the maximum, minimum, and average ashing rates for results of Fig. 7. These distribution results are similar to the electric field distribution but the maximum ashing rate did not correlate with the electric field intensity. It is assumed that the highest ashing rate achieved by the double U-shaped antenna is attributable to plasma integration and the increased electron density and radical density near the substrate. Laser-induced fluorescence measurement of the H-shaped antenna revealed that the OH radical density at d = 5.5 mm was about 2×10^{14} cm^{-3}[33], so the double U-shaped antenna is also regarded as having density on the order of 10^{14} cm^{-3} or more. The OH radical density as well as electron density measurements are the future work to understand the ashing rate difference between the H-shaped antenna and double U-shaped antenna.

4. Conclusion

Electromagnetic field simulation of the antenna structure was performed to improve the ashing rate and the uniformity. The H-shaped antenna changed the plasma spread from elliptical to circular. The ashed photoresist shape also became circular, but the uniformity was the same as that for the slot antenna. However, for the double U-shaped antenna, the uniformity was improved greatly. The maximum ashing rate was increased. The ashing rate distribution result was similar to the distribution of the electric field intensity at 6 mm from the antenna, suggesting that the ashing shape can be estimated from the simulation. The double U-shaped antenna can not only improve the uniformity; it can also increase the electric field intensity. The electric field intensity obtained using the antenna with the optimal shape parameter was 10 times greater than that obtained using a conventional slot antenna. Results show that the microwave-excited plasma was generated efficiently and that the ashing rate was higher when using the double U-shaped antenna.

Acknowledgments

The authors thank Mr. Y. Onishi from Yonekura Mfg. Co., Ltd. and Mr. T. Hitobo from Tateyama Machine Co., Ltd. for supporting development of microwave excited plasma system used for this study.

References

1. W. Kern, *J. Electrochem. Soc.,* **137** (1990) 1887.
2. S. Fujimura, J. Konno, K. Hikazutani, and H. Yano, *Jpn. J. Appl. Phys.,* **28** (1989) 2130.
3. K. Taniguchi, K. Tanaka, T. Inomata, and M. Kogoma, *J. Photopolym. Sci. Technol.,* **10** (1997) 113.

4. S. Fujimura, K. Shinagawa, M.T. Suzuki, and M. Nakamura, *J. Vac. Sci. Technol. B Microelectron. Nanom. Struct.,* **9** (1991) 357.
5. Y. Susa, H. Ohtake, Z. Jianping, L. Chen, and T. Nozawa, *J. Vac. Sci. Technol. A Vacuum, Surfaces, Film*, **33** (2015) 061307.
6. H. Horibe, M. Yamamoto, T. Maruoka, Y. Goto, A. Kono, I. Nishiyama, and S. Tagawa, *Thin Solid Films*, **519** (2011) 4578.
7. M. Yamamoto, Y. Goto, T. Maruoka, H. Horibe, T. Miura, E. Kusano, and S. Tagawa, *J. Electrochem. Soc.,* **156** (2009) H505.
8. H. Horibe, M. Yamamoto, E. Kusano, T. Ichikawa, and S. Tagawa, *J. Photopolym. Sci. Technol.,* **21** (2008) 293.
9. T. Miura, M. Kekura, H. Horibe, and M. Yamamoto, *J. Photopolym. Sci. Technol.,* **21** (2008) 311.
10. T. Ishijima, H. Sugiura, R. Saito, H. Toyoda, and H. Sugai, *Plasma Sources Sci. Technol.,* **19** (2010) 6.
11. T. Ishijima, K. Nosaka, Y. Tanaka, Y. Uesugi, Y. Goto, and H. Horibe, *Appl. Phys. Lett.,* **103** (2013) 142101.
12. F. Werner, D. Korzec, and J. Engemann, *Plasma Sources Sci. Technol.,* **3** (1994) 473.
13. H. Shirai, K. Yoshino, G. Ohkawara, and H. Ueyama, *Jpn. J. Appl. Phys.,* **40** (2001) L701.
14. K. Shimatani, T. Okamoto, and Y. Okamoto, *Vacuum*. **66** (2002) 359.
15. Y. Yasaka, D. Nozaki, K. Koga, M. Ando, T. Yamamoto, N. Goto, N. Ishii, and T. Morimoto, *Jpn. J. Appl. Phys.,* **38** (1999) 4309.
16. C. Tian, T. Nozawa, K. Ishibashi, H. Kameyama, and T. Morimoto, *J. Vac. Sci. Technol. A Vacuum, Surfaces, Film*, **24** (2006) 1421.
17. T. Goto, M. Hirayama, H. Yamauchi, M. Moriguchi, S. Sugawa, and T. Ohmi, *Jpn. J. Appl. Phys.,* **42** (2003) 1887.
18. T. Ishijima, H. Toyoda, Y. Takanishi, and H. Sugai, *Jpn. J. Appl. Phys.,* **50** (2011) 036002.
19. Y. Kimura, H. Kawaguchi, S. Kagami, M. Furukawa, and H. Shindo, *Appl. Phys. Express*, **2** (2009) 126002.
20. H. Suzuki, S. Nakano, H. Itoh, M. Sekine, M. Hori, and H. Toyoda, *Appl. Phys. Express*, **8** (2015) 036001.
21. T. Fukasawa, S. Fujii, and H. Shindo, *Jpn. J. Appl. Phys.,* **44** (2005) 1945.
22. S. Nakao and H. Sugai, *Jpn. J. Appl. Phys., Part 2 Lett.*, **46** (2007) 1039.
23. H. Kousaka, K. Ono, N. Umehara, I. Sawada, and K. Ishibashi, *Thin Solid Films*, **506–507** (2006) 503.
24. T. Ishijima, Y. Nojiri, H. Toyoda, and H. Sugai, *Jpn. J. Appl. Phys.,* **49** (2010) 086002.
25. M. Kanoh, K. Aoki, T. Yamauchi, and Y. Kataoka, *Japanese J. Appl. Physics, Part 1 Regul. Pap. Short Notes Rev. Pap.*, **39** (2000) 5292.
26. M. Nagatsu, S. Morita, I. Ghanashev, A. Ito, N. Toyoda, and H. Sugai, *J. Phys. D. Appl. Phys.,* **33** (2000) 1143.
27. H. Kousaka, J. Xu, and N. Umehara, *Jpn. J. Appl. Phys.,* **44** (2005) L1052.
28. K. Sasai, H. Suzuki, and H. Toyoda, *Jpn. J. Appl. Phys.,* **55** (2016) 016203.
29. M. Hotta, Y. Hasegawa, K. Nakamura, D. Lubomirsky, S. Park, S. Kobayashi, and H. Sugai, *Jpn. J. Appl. Phys.,* **56** (2017) 116002.
30. J.-D. Gu and P.-L. Chen, *Thin Solid Films*, **498** (2006) 14.
31. S. Khumpuang, H. Maekawa, and S. Hara, *IEEJ Trans. Sensors Micromachines*, **133** (2013) 272.
32. CST Microwave Studio, 2018, www.cst.com.
33. I. Inoue, T. Aizawa, T. Ishijima and R. Ono, *J. Phys. D. Appl. Phys.,* **54** (2021)195201.

Journal of Photopolymer Science and Technology
Volume 34, Number 5 (2021) 485−489 ©2021SPST

Effect of pH on Decomposition of Organic Compounds Using Ozone Microbubble Water

Kazuki Tsujimoto and Hideo Horibe*

Graduate School of Engineering, Osaka City University,
3-3-138 Sugimoto, Sumiyoshi-ku, Osaka 558-8585, Japan
**hhoribe @a-chem. eng. osaka-cu.ac.jp*

Microbubbles are tiny bubbles with a particle size of 1 - 100 μm. Microbubbles have been reported that the gas dissolving ability is excellent and hydroxyl radical generates when microbubbles collapse in water. On the other hand, ozone is a gas with high oxidation power and eventually decomposes into oxygen. So, ozone is environmentally friendly. Therefore, we thought that ozone microbubbles water, in which ozone is dissolved in microbubbles water, could be used to efficiently decompose persistent organic compounds while being environmentally friendly. In this study, we evaluated the decomposition of phenol, an object subject to wastewater regulation, by ozone water and ozone microbubbles water. At a constant dissolved ozone concentration, we could not confirm the effect of microbubbles in decomposing phenol. Also, under the same conditions, when the pH was changed, the effect of microbubbles could not be confirmed. However, under basic conditions, phenol was decomposed the most because of self-decomposition reaction of ozone. Therefore, the effect of microbubbles could not be confirmed in the phenol degradation by ozone microbubbles in this experiment.

Keywords: Microbubble, Ozone, Resist removal, Environmentally friendly Cleaning technique

1. Introduction

Microbubbles are tiny bubbles with a diameter of 1-100 μm and possess remarkable properties differing from those of normal bubbles. Firstly, rising speed of microbubbles in the water is slow, which follow scheme (1).

$$u_B = \frac{{d_B}^2(\rho_L - \rho_G)\, g}{18\, \mu_L} \qquad (1)$$

Rising speed of microbubbles is given as (1), where u_B is the rising speed and d_B is the diameter. In addition, ρ_L and ρ_G are liquid and gas density, μ_L is liquid viscosity coefficient and g is gravitational acceleration. Due to the large diameter of normal bubbles, they float quickly in water, reach the gas-liquid interface, and disappear after a few seconds. On the other hand, since the microbubbles have a small diameter, the rising speed is small, and the bubble collapses while shrinking. And, microbubbles can efficiently dissolve internal gas with surrounding liquid because internal gas pressure is increased by surface tension at the gas-liquid interface [1,2]. The size of bubble affects the pressure difference between the inside and outside of the bubble. The equation (Young-Laplace equation, (2)) is shown below.

$$\Delta p = \frac{4\sigma}{d_B} \qquad (2)$$

Interfacial tension between gas phase and liquid phase is given as (2), where Δp is pressure difference between inside and outside, σ is the surface tension between water and air and d_B is the

Received April 2, 2021
Accepted April 22, 2021

diameter of the bubble. From this equation, the smaller the diameter, the larger the pressure difference. Since microbubbles shrink over time, the pressure difference becomes larger. This effect is called the self-pressurization effect. The most interesting property of microbubbles is their ability to generate hydroxyl radicals. Due to the self-pressurization effect, microbubbles shrink and release very strong energy upon collapsing, which reacts with some of the surrounding water to produce hydroxyl radicals (Figure 1). The standard redox potential of hydroxyl radicals is much higher than that of oxidants such as ozone and hydrogen peroxide. The hydroxyl radicals non-selectively decompose organic compounds. Therefore, it is thought that microbubbles are useful for decomposing persistent organic compounds [3,4].

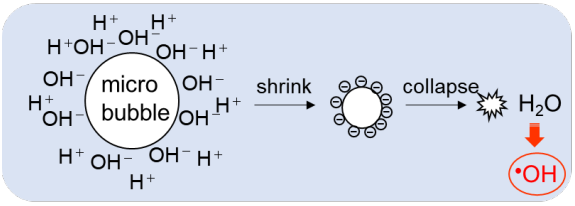

Fig. 1. Mechanism of hydroxyl radical generated from microbubbles.

On the other hand, ozone is applied to environmentally friendly cleaning techniques for water and semiconductor manufacturing [5-13]. Ozone water degrades compounds with C=C bond to ketone and carboxylic acid [14,15]. Additionally, ozone generates reactive oxygen species through self-decomposition in water. Reactive oxygen species can degrade organic compounds because of its extremely strong oxidation power.

Therefore, we thought that ozone microbubbles water, in which ozone is dissolved in microbubbles water, could be used to efficiently decompose persistent organic compounds while being environmentally friendly [16-18].

In this study, we confirmed the effect of microbubbles by decomposing phenol, an object of wastewater regulation, by ozone microbubbles [19]. In order to focus on the behavior of the electric double layer of microbubbles, we changed the pH in the aqueous solution and decomposed phenol.

2. Experimental

2.1. Ozone microbubbles generation systems

Figure 2 shows a schematic diagram of the ozone microbubbles generator. Microbubbles were generated using pressurized dissolution method. Ozone gas was dissolved by pressurizing with 0.5 MPa using a bellows pump (ΣP - 15 D - V, Sigma Technology Co.). An ozone aqueous solution in a supersaturated state was generated and opened to the atmosphere through a dispersion nozzle (Resource Development Co., Ltd.) to generate microbubbles. The presence or absence of microbubbles was switched depending on this nozzle. Dissolved ozone concentration was measured using the ozone monitor (Ebara Kogyo Co., Ltd.). A low-pressure mercury lamp with an emission wavelength of 253.7 nm was used as the light source. Ozone water was supplied to the detection part, and the dissolved ozone concentration was measured by measuring the ultraviolet absorption amount.

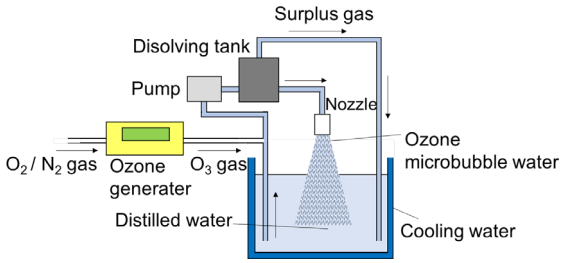

Fig. 2. Schematic illustration of ozone microbubbles generation system.

2.2. Decomposition treatment of phenol by ozone microbubbles

Ozone microbubbles were generated in 3 L of ion exchanged water. Dissolved ozone concentration was stabilized at 30 and 60 mg/L at 15 ± 1 ° C water temperature. 3mmol of phenol (Wako Pure Chemical Industries) was dissolved in ozone microbubbles and ozone water and stirred for 5-60 minutes. The decomposition rate and decomposition products of phenol were measured using HPLC. The total organic carbon (TOC) content of the treated samples was measured using the combustion catalytic oxidation method. The pH of the aqueous phenol solution was adjusted by using hydrochloric acid (Wako Pure Chemical Industries) and sodium hydroxide (Wako Pure Chemical Industries).

3. Results and Discussion

3.1. Relationship between supplied ozone gas concentration and dissolved ozone concentration with and without microbubbles

Fig. 3 shows relationship between supplied ozone gas concentration and dissolved ozone concentration with and without microbubbles. The dissolved ozone concentration increased in proportion to the ozone gas supply. When the ozone gas supply was kept constant, the dissolved ozone concentration of ozone microbubbles water was higher than that of ozone water. This result suggests that microbubbles have a large specific surface area and dissolved a lot of gas.

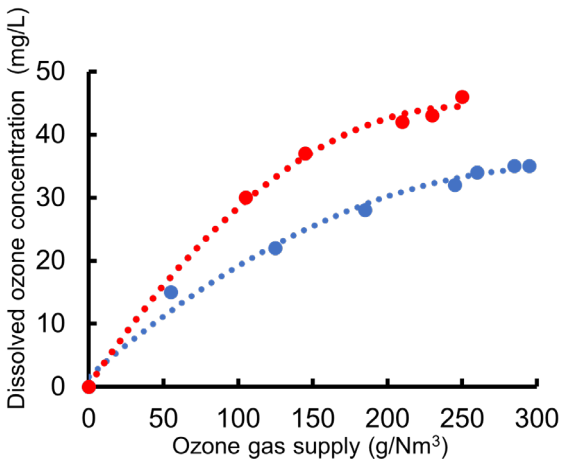

Fig. 3. Relationship between dissolved ozone concentration of ozone water with (●) or without (●) microbubbles and ozone gas supply.

3.2. Decomposition of phenol by using ozone microbubbles

Phenol was decomposed by circulating ozone microbubbles water and ozone water for 5 min, and the HPLC chromatogram of the aqueous solution is shown in Fig. 4. It was found that the phenol was decomposed by 70-90% by ozone water and ozone microbubbles water treatment for 5 min. Divalent phenol was also observed as a decomposition product [20,21]. When the concentration of the ozone gas supply was kept constant at 120 g/Nm3, the phenol was decomposed better by treatment with ozone microbubbles water than with ozone water. This could be attributed to the increase in dissolved ozone concentration by using microbubbles. On the other hand, when the dissolved ozone concentration was kept constant at 30 mg/L, there was no dominant difference in phenol degradation between ozone microbubbles water and ozone water. From these results, the direct reaction by ozone was the main reaction for the decomposition of phenol, and the effect of OH radicals, which are thought to be generated from the collapsing of microbubbles, could not be confirmed. Therefore, hydrogen peroxide, one of the decomposition products, which is considered to be due to OH radicals generated by the self-decomposition of ozone.

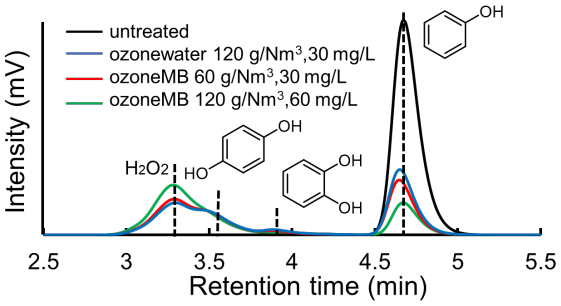

Fig. 4. HPLC chromatogram of untreated (black) and treated phenol aqueous solution. In addition, these treated solutions were prepared by ozone water (blue) and ozone microbubbles (red, green) for 5min, respectively.

3.3. Relationship between decomposition of phenol by treatment of ozone microbubbles and pH

The residual rate of phenol treated with ozone water and ozone microbubbles water for 5 min is shown in Fig 5. In all conditions, phenol was found to be decomposed by 80-90%. Although the superiority of microbubbles could not be confirmed in all conditions, phenol was decomposed the most under basic conditions. This is thought to be due to the reaction of ozone and hydroxyl ions, which produced a large number of reactive oxygen species (scheme 3.).

Fig. 6 shows the time course of TOC of phenol solution treated by ozone microbubbles and ozone water. The 60-minute treatment resulted in a 40-60% reduction in TOC. The decrease in TOC was not observed under acidic conditions than under neutral or basic conditions. It is thought that this is because under acidic conditions, it is difficult for ozone to cause self-decomposition reaction and generate

reactive oxygen species. This suggests that changes in pH affect ozone, but not microbubbles.

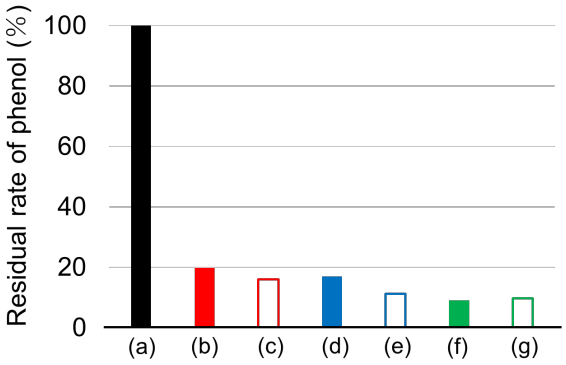

Fig. 5. Decomposition rate of phenol before the treatment (a), after the treatment by ozone water in the ((b), (d) and (f)) presence or ((c), (e) and (g)) absence of microbubbles at various pH (—: pH = 6, — pH = 2.2, —: pH = 10).

$$O_3 + OH^- \rightarrow HO_2^\bullet + O_2^-$$

$$O_3 + HO_2^\bullet \rightarrow 2O_2 + {}^\bullet OH$$

$$O_3 + {}^\bullet OH \rightarrow O_2 + HO_2^\bullet$$

$$2HO_2^\bullet \rightarrow O_3 + H_2O$$

$$HO_2^\bullet + {}^\bullet OH \rightarrow O_2 + H_2O$$

Scheme 3. Self-decomposition reactions of ozone.

4. Conclusion

At the same ozone gas supply, the dissolved ozone concentration was higher in the ozone microbubble water than in the ozone water. Therefore, phenol was treated at the same dissolved ozone concentration to investigate the degradation effect of microbubbles. As a result, no significant difference in decomposition of phenol could be confirmed in ozone water and ozone microbubble water treatment. The same experiment was also conducted by varying the pH. As a result, the effect of microbubbles could not be confirmed at any pH. At pH = 2.2, the mineralization of phenol did not progress as much as at pH = 6 or 10. This is thought to be due to the difficulty of self-decomposition of ozone to progress. It is assumed that the decomposition of phenol is not caused by microbubbles, but caused by ozone.

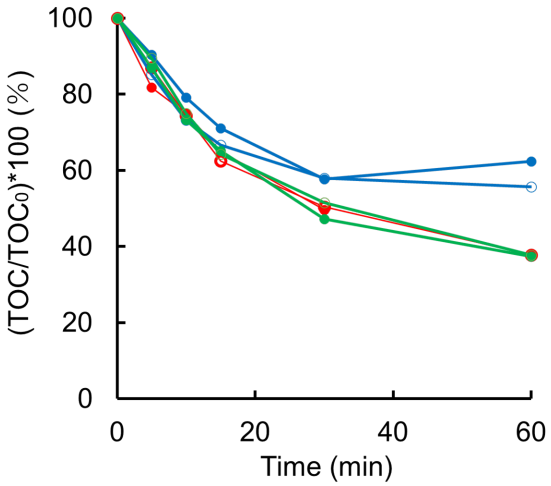

Fig. 6. TOC of aqueous solution of phenol after the treatment by ozone water in the (closed symbol) presence or (open symbol) absence of microbubbles at various pH (—: pH = 6, — pH = 2.2, —: pH = 10).

5. References

1. M. Takahashi, K. Chiba, and P. Li, *J. Phys. Chem. B*, **111** (2007) 1343.
2. P. Li, H. Tsuge, and K. Itoh, *Ind. Eng. Chem. Res.*, **48** (2009) 8048.
3. H. Tsuge, "*The Latest Technology on Microbubbles and Nanobubbles*", CMC Publishing Co., Tokyo, (2007, p 109.
4. J. S. Park and K. Kurata, *Hort. Tech.*, **19** (2009) 212.
5. F. De Smedt, S. De Gendt, M. Heyns, and C. Vinckier, *J. Electrochem. Soc.*, **148** (2001) G487.
6. H. Vankerckhoven, F. De Smedt, B. Van Herp, M. Claes, S. De Gendt, M. M. Heyns, and C. Vinckier, *Ozone: Sci. Eng.*, **24** (2002) 391.
7. H. Vankerckhoven, F. De Smedt, M. Claes, S. De Gendt, M. M. Heyns, and C. Vinckier, *Solid State Phenom.*, **92** (2003) 101.
8. D. M. Knotter, M. Marsman, P. Meeusen, G. Gogg, and S. Nelson, *Solid State Phenom.*, **92** (2003) 223.
9. S. Noda, M. Miyamoto, H. Horibe, I. Oya, M. Kuzumoto, and T. Kataoka, *J. Electrochem. Soc.*, **150** (9) (2003) G537.

10. M. N. Kawaguchi, J. S. Papanu, B. Su, M. Castle, and A. Ai-Bayati, *J. Vac. Sci. Technol*. B, **24** (2006) 657.
11. H. Horibe, M. Yamamoto, T. Ichikawa, T. Kamimura, and S. Tagawa, *J. Photopolym. Sci. Technol*., **20** (2007) 315.
12. H. Horibe, M. Yamamoto, Y. Goto, T. Miura, and S. Tagawa, *Jpn. J. Appl. Phys.*, **48** (2009) 026505.
13. Q. Wang, T. Shen and S. Tong, *Ind. Eng. Chem. Res.,* **55** (2016) 10513.
14. Y. Abe, A. Kaneko, T. Yagi, H. Hamada, M. Ike, T. Asano, Y. Kato, and K. Fujimori, *KAGAKU KOGAKU RONBUNSHU*, **36** (2010), 41.
15. L. G. Wade Jr, "*Organic-chemistry 6th ed*", Prentice Hall, 2006, p. 360.
16. K. Matsuura, T. Nishiyama, E. Sato, M. Yamamoto, T. Kamimura, M. Takahashi, K. Koike, and H. Horibe, *J. Photopolym. Sci. Technol.*, **29** (2016) 623.
17. T. Nishiyama, K. Matsuura, E. Sato, N. Kometani, and H. Horibe, *J. Photopolym. Sci. Technol.*, **30** (2017) 285.
18. T. Miyazaki, E. Sato, and H. Horibe, *J. Photopolym. Sci. Technol.*, **31** (2018) 409.
19. G. H. Kelsall, S. Tang, A. L. Smith, and S. Yudakul., *J. Chem. Soc., Faraday Trans,* **92** (1996) 3879.
20. Pan Li, *Chemosphere*, **75** (2009) 1371.
21. Pan Li, *Chemosphere*, **77** (2009) 1157.

Journal of Photopolymer Science and Technology
Volume 34, Number 5 (2021) 491−494 ©2021SPST

Improvement of Resist Characteristics by Synthesis of a Novel Dissolution Inhibitor for Chemically Amplified Three-Component Novolac Resist

Shinya Akechi and Hideo Horibe

Department of Applied Chemistry and Bioengineering, Graduate School of Engineering, Osaka City University, 3-3-138 Sugimoto, Sumiyoshi-ku, Osaka 558-8585, Japan
hhoribe@a-chem.eng.osaka-cu.ac.jp

A photosensitive polymer called photoresist is used to create fine circuit patterns on the surface of semiconductors. The aim of this study was to improve the resist function by incorporating a chemical amplification mechanism into the base polymer, novolac resin. The resist is composed of three components: base polymer, dissolution inhibitor (DI), and photoacid generator. The ability to inhibit the dissolution of resist polymer in the unexposed area was improved by increasing the molecular size of DI. The high acidity of deprotected DI with carboxyl groups improved the ability to promote dissolution of resist polymer in the exposed area. The resists containing DIs with large molecular size and high acidity showed improved resolution.

Keywords: Novolac resist, Dissolution inhibitor, Positive tone resist, Chemically amplified system

1. Introduction

Semiconductors are used in a variety of electronic devices. In order to achieve high performance and miniaturization of these electronic devices, semiconductors must be made finer and denser [1-6]. A photosensitive polymer material called photoresist is used to form circuit patterns on the surface of semiconductors. When the resist is exposed, a chemical reaction occurs, which changes its solubility in alkaline developing solution. The procedure for forming the circuit pattern is shown below. After the formation of the oxide film on the Si substrate, resist is applied to its surface. The resist pattern is then formed on the substrate surface by exposure and development. The formed resist pattern serves as a mask in the etching process. After etching, the resist is removed and the electronic circuit is fabricated on the substrate.

In this study, we developed a three-component resist by applying the chemical amplification mechanism to novolac resin [7, 8]. A three-component resist consists of a novolac resin as the base polymer, a photoacid generator (PAG) that generates protons when exposed, and a dissolution inhibitor (DI) that controls the resist's solubility. Before exposure, the interaction between the novolac resin and DI, such as intermolecular forces and hydrogen bonds, prevents the resist film from dissolving into the developing solution [9-11]. First, exposure releases protons from the PAG, which cause the dissolution inhibitor to undergo a deprotection reaction and decompose into a dissolution accelerator (DA). Since DA is soluble in the developing solution, the resist film in the exposed area dissolves into the developing solution. When the dissolution inhibitor decomposes, protons are generated again. This generated proton repeatedly works for the dissolution reaction of the dissolution inhibitor, and the proton functions as a catalyst, which is the chemical amplification mechanism [12-14]. The chemical amplification mechanism is expected to improve sensitivity and resolution over conventional novolac positive resists, which consist of two components: a novolac resin and a diazonaphthoquinone (DNQ) derivative [15-17]. In addition, dissolution of the novolac resin

Received March 31, 2021
Accepted April 22, 2021

can be promoted by making the molecular weight distribution of the novolac resin wider. This is because if the novolac resin has a wide molecular weight distribution, the resin with the smaller molecular weight will dissolve in the developing solution, and the contact area between the resin with the larger molecular weight and the developing solution will increase. Therefore, the dissolution rate is faster than that of novolac resin with a narrow molecular weight distribution. Since DA is a low molecular weight compound compared to the resin, it is thought to function in the same way as a resin with a small molecular weight. Therefore, the addition of DI is expected to improve the dissolution promotion capability over normal resists.

We improved the dissolution inhibition ability of DI and the dissolution enhancement ability of DA for novolac resin by designing the molecules of DI. The dissolution inhibitor was designed to have different numbers of benzene rings in the molecule, and the molecular size was varied [18]. In addition, by increasing the acidity after decomposition, DA dissolves in the developing solution in a shorter time, and the contact between the resin and the developing solution occurs faster. Thinking that this would improve the dissolution promotion ability, we synthesized two types of DI: the phenol type, in which the decomposition product becomes phenol, and the carboxylic acid type, in which the decomposition product becomes carboxylic acid. In order to evaluate only the effect of acidity after degradation, the molecular sizes of phenolic and carboxylic acid type DIs were designed to be almost equal. These DIs made it possible to incorporate acid-catalyzed chemical amplification mechanism into the resists by protecting the dissolution promoters with tBoc and tBu groups that can be degraded by acid. Using the DIs synthesized by the above molecular design, we aimed to improve the sensitivity and resolution of three-component positive resists.

2. Experimental

Novolac resin (M_w 9000) were used as a base polymer. Propylene glycol monomethylether acetate (PGMEA) was used as a solvent for base resin. 2-Methyl-α-[2-[[(propylsulfonyl)oxy]imino]-3(2H)-thienylidene]benzeneacetonitrile (product name : Irgacure PAG103) was obtained from BASF and used as a photo acid generater (PAG). 2.38% of tetramethylammonium hydroxide (TMAH) aqueous solution was used as a developer. Hydroquinone (DA1), 4,4'-[1-[4-[1-(4-hydroxyphenyl)-1-methylethyl]phenyl]ethylidenee]bis[phenol] (DA2), 4,4'-((2-hydroxyphenyl)methylene)bis(2,6-dimethylphenol) (DA3) and 4,4'-methylenebis(2-(4-hydroxybenzyl)-3,6-dimethylphenol) (DA4) were used as DA. tBoc-DI1, tBoc-DI2, tBoc-DI3, and tBoc-DI4 were synthesized by the reaction of DA1-4 with Di-t-butyl Dicarbonate in the presence of 4-Dimethylaminopyridine (DMAP) [19]. di-tert-butyl 2,2'-(((1-(4-(2-(4-(2-(tert-butoxy)-2-oxoethoxy)phenyl)propan-2-yl)phenyl)ethane-1,1-diyl)bis(4,1-phenylene))bis(oxy))diacetate (tBu-DI2) and di-tert-butyl 2,2'-((((2-(2-(tert-butoxy)-2-oxoethoxy)phenyl)methylene)bis(2,6-dimethyl-4,1-phenylene))bis(oxy))diacetate (tBu-DI3) were synthesized as follows: DA2, DA3 and *t*-butyl bromoacetate were reacted in DMF in the presence of potassium carbonate and heated and stirred in an oil bath at 90 °C for 24 h while refluxing [20]. The chemical structure of the synthesized DI is shown in Scheme 1.

The polymer solution was prepared by dissolving novolak resin in PGMEA and the concentration of was 30 wt%. DIs was added at 0.10, 0.20, and 0.30

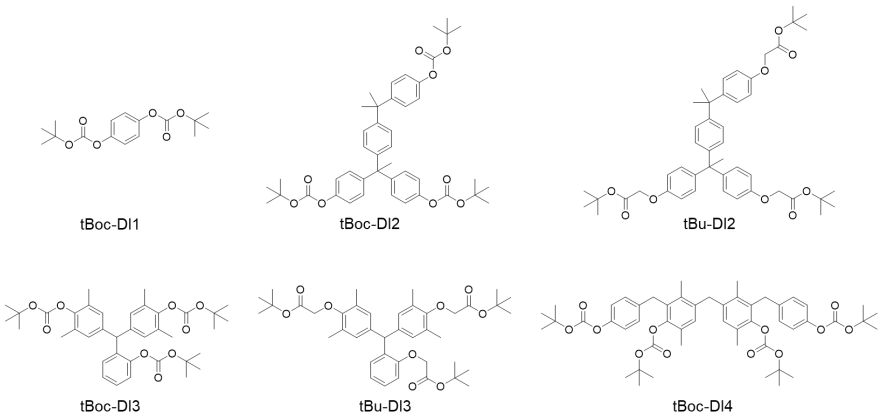

Scheme 1. Chemical structure of DIs.

mmol/g of the novolac resin unit mass into the novolac resin solution. The resist solution was prepared by adding 3 wt% of photoacid generator to the novolac resin. The resist solution was prepared by stirring at 80°C when tBoc-DI2 and tBoc-DI3 was added, and at room temperature when other DIs were added.

The prepared solution was spin-coated on a three inches silicon wafer. Silicon wafers were treated with 1,1,1,3,3,3-Hexamethyldisilazane (HMDS). After spin-coating, the wafer was prebaked on a hot plate at 100 °C for 5 min, and the film thickness was measured using stylus surface profilometer (Bruker Co., Ltd., Dektak XT). The prebaked resist was then exposed and baked again at 100 °C for 2 min. All films were developed with 2.38% of TMAH aqueous solution for 1 min. The film thickness remained after development was measured. The exposure conducted using M-1S (Mikasa Co., Ltd.).

3. Results and discussion

To evaluate the dissolution inhibition ability of the synthesized dissolution inhibitors against novolac resin, resist films with various amount of DI were prepared and its Alkali dissolution rate (ADR) was measured. The correlation between the ADR of the resist film and the amount of DI per gram of polymer was shown in Figure 1. Without the dissolution inhibitor, the ADR of the polymer solution was 2700 nm/min. The ADR of the resist films with tBu-DI2 was the smallest, followed by tBoc-DI4, tBoc-DI2, tBu-DI3, tBoc-DI3, and tBoc-DI1 added films. Comparing the ADRs of the resist films with the same substituent DIs, the ADRs of the resist films became smaller in the order of tBoc-DI1, tBoc-DI3, tBoc-DI2, and tBoc-DI4 (tBoc-DI1 < tBoc-DI3 < tBoc-DI2 < tBoc-DI4). From these results, it was found that the dissolution inhibition ability increased as the molecular size of DI increased. When the ADRs of the resist films were compared by DI of the same structure, the ADRs of the films containing tBu-DI2 were smaller than those of tBoc-DI2 and those of the films containing tBu-DI3 were smaller than those of tBoc-DI3 (tBu-DI2, 3 < tBoc-DI2, 3). Therefore, it was found that the dissolution inhibition ability of DI protected by tBu group was larger than that of tBoc group.

The effect of DI on resist properties was evaluated using tBoc-DI2, 3 and tBu-DI2, 3 with different acidity after deprotection. The sensitivity curve is shown in Figure 2 and 3. Exposure dose at which the resist film began to dissolve was smaller for the tBoc group-protected resist than for the tBu

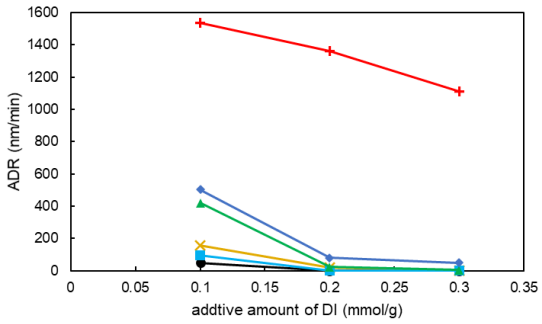

Fig. 1. ADR of polymer films containing tBoc-DI1(+), tBoc-DI3(◆), tBu-DI3(▲), tBoc-DI2(×), tBoc-DI4(■) and tBu-DI2(●).

group-protected resist. This may be attributed to the fact that tBoc groups are more easily decomposed than tBu groups. The sensitivity was 70, 85, 200, and 220 mJ/cm2 for tBoc-DI2, tBoc-DI3, tBu-DI2, and tBuDI3 added resists, respectively, and resists including tBoc-protected DI had higher sensitivity. Since tBoc group-protected DI becomes phenol after decomposition and tBu group-protected DI becomes carboxylic acid after decomposition, we expected that tBu-DI2, 3 added resists with higher acidity after decomposition would have higher sensitivity, but the actual result was the opposite. Next, the γ value was calculated according to Equation 1.

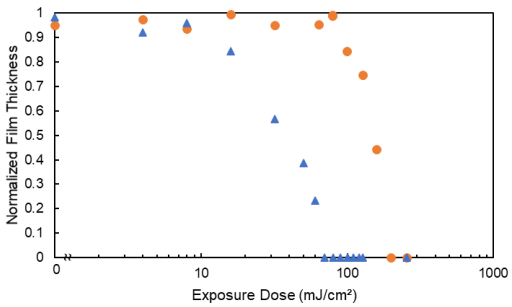

Fig. 2. Sensitivity curves of Novolac resist including tBoc-DI2 (▲) and tBu-DI2 (●)).

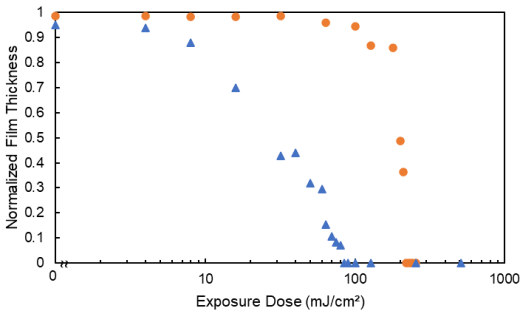

Fig. 3. Sensitivity curves of Novolac resist including tBoc-DI3 (▲) and tBu-DI3 (●).

$$\gamma = 0.5[\log(D_0/D_{50})]^{-1} \quad (1)$$

The exposure amount when the residual film ratio is 0% is "D_0" and the exposure amount when the residual film ratio is 50% is "D_{50}". The γ values are 1.18, 0.87, 2.02, and 2.92 for the tBoc-DI2, tBoc-DI3, tBu-DI2, and tBuDI3 added resists, respectively, and the tBu group protected resist is expected to have better pattern resolution.

The shapes of the patterns created using tBoc-DI2 and tBu-DI2 added resists were observed using SEM to evaluate the pattern resolution. Each pattern image is shown in Figure 4. For patterning, a mask with L/S = 3 μm was used. The resist including tBoc-DI2 was exposed at 85 mJ/cm^2 and the resist including tBu-DI2 was exposed at 660 mJ/cm^2. Comparing the shapes of the patterns produced, it was found that the tBu-DI2 doped resist produced better shaped patterns. Therefore, it was found that the improvement in pattern resolution was achieved by using a carboxylic acid type DI.

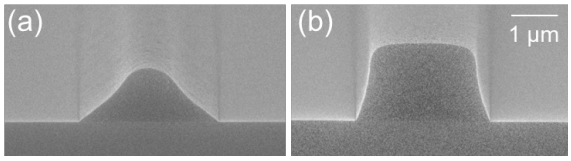

Figure 4. SEM images of the patterns prepared by resist containing (a) tBoc-DI2 and (b) tBu-DI2.

4. Conclusion

A three-component resist was developed by applying the chemical amplification mechanism to novolac resin. By increasing the molecular size of DI, the inhibitory ability of DI to dissolve the polymer was improved. In the case of the tBoc group-protected DI added resist, the sensitivity was improved compared to the tBu group-protected resist. Resists added with tBu group-protected DI, which have a higher acidity after decomposition, have improved contrast; when resists added with tBu-DI2 were used, 3 μm patterns could be formed.

References

1. R. Haruta, *J. Inst. Electri. Electron. Eng.*, **10** (2007) 353.
2. G. Mago, *J. Surf. Finish. Soc. Jpn.*, **65** (2014) 349.
3. K. Sakai, K. Nakahira, M. Umeda, and K. Kitami, *J. JSPE.,* **83** (2017) 125.
4. K. Takagi, *J. Surf. Finish. Soc. Jpn.*, **61** (2010) 350.
5. K. Toriyama, K. Okamoto, S. Kohara, and Y. Orii. *Trans JIEP.*, **14** (2011) 372.
6. R. Schaller, *IEEE Spectrum.*, **34** (1997) 52.
7. D. R. McKean, S. A. MacDonald, R. D. Johnson, N. J. Clecak, and C. G. Willson, *Chem. Mater.*, **2** (1990) 619.
8. L. Schlegel, T. Ueno, H. Shiraishi, N. Hayashi and T. Iwayanagi, *Chem. Mater.*, **2** (1990) 299.
9. H. Y. Shih and A. Reiser, *Macromolecules*, **28** (1995) 5595.
10. M. Endo, M. Sasago, and K. Ogawa, *Kobunshi Ronbunshu*, **45** (1988) 771.
11. K. Honda, B.T. Seauchemin, Jr., R.J. Hurditch, A. J. Blakeney, Y. Kawabe, and T. Kokubo, *Proc. SPIE*, **1262** (1990) 492.
12. H. Ito and G.G. Willson, *Polym. Eng. Sci.*, **23** (1983) 1012.
13. E. Reichmanis, F. M. Houlihan, O. Nalamasu and T. X. Neenan, *Chem. Mater.*, **3** (1991) 394.
14. S. A. MacDonald, C. G. Willson and J. M. J. Frechet, *Acc. Chem. Res.*, **27** (1994) 151.
15. K. Doki, H. Miyamoto, A. Tsuji, A. Matsumoto, K. Hasegawa and A. Fukuda, *Kobunshi Ronbunshu*, **53** (1996) 231.
16. M. Hanabata and A. Furuta, *Kobunshi Ronbunshu*, **45** (1988) 803.
17. A.Yokota, M. Nishida, M. Furuta, and S. Asaumi, *Kobunshi Ronbunshu*, **51** (1994) 309.
18. Hiroshi Ito, Tomonari Nakayama, Mark Sherwood, Dolores Miller, and Mitsuru Ueda, *Chem. Mater*, **20** (2008) 341.
19. H. Horibe, T. Kumada, and S. Kubota, *Kobunshi Ronbunshu*, **53** (1996) 133.
20. Honshu Kagaku Kougyo, "*Trisphenols such as trioxymethylcarboxylic acid and tertiary cyclopentyl ester*", Japan Patent JP4125263, 2008-05-16.

Journal of Photopolymer Science and Technology
Volume 34, Number 5 (2021) 495−498 ©2021SPST

Influence of Glycerol in Developer on Novolak-Type Positive-Tone Resist Solubility

Shunpei Kajita[1*], Yukiko Miyaji[1], and Hideo Horibe[2]

[1] Sakamoto Yakuhin Kogyo Co., Ltd., 3-1-62, Ayumino, Izumi, Osaka 594-1157, Japan
[2] Department of Applied Chemistry and Bioengineering, Osaka City University. 3-3-138 Sugimoto, Sumiyoshi, Osaka 558-8585, Japan
**kajita@sy-kogyo.co.jp*

Photoresist is used for circuit fabrication in semiconductor devices. The material generally used for manufacturing semiconductor devices is the novolak-type positive-tone resist; however, it is necessary to minimize its line width while improving the resolution. To improve the resolution of novolak-type positive-tone resist, in this study, developers containing water-soluble organic solvents or surface-activating agents have been designed for controlling the resist solubility. The addition of glycerol, as a water-soluble organic solvent in the developer, inhibits the dissolution of the novolak resist, particularly in the unexposed area. The developer containing glycerol improves the novolak resist resolution, thereby developing a fine pattern.

Keywords: Developer, Novolak-type resist, Positive-tone resist, Developer additive

1. Introduction

To improve the performance of electronic devices such as smartphones, lithography technology has been developed to improve the density and integration of semiconductor devices. Lithography pattern scaling has improved the resolution by implementing a short-wavelength light source for lithography. In the development of photoresists specific to each wavelength, such as g-line (426 nm), i-line (365 nm), KrF (248 nm), ArF (193 nm), and EUV (13.5 nm), it is necessary to select suitable polymer to ensure wavelength transmittance. Generally, a novolak-type resist is used in g-line and i-line lithography, polyhydroxy styrene-type resist in KrF, and polymethacryl-type resist in ArF [1–5].

Furthermore, tetramethyl ammonium hydroxide (TMAH) aqueous solution has been widely applied to an alkali developer without metallic ions during the lithography process [6–9]. In addition to the transition of the resist following a shorter wavelength, the alkali developer was also improved. To improve the resolution of the resist pattern, the molecular structure of the organic alkali in the developer was reconstructed to inhibit the swelling of the resist pattern, and a water-soluble organic solvent or surface activating agent was added to the developer to control the developer wettability to the resist and substrate, as reported in several patented studies [10–12]. However, how these additives control the swelling of resist and the wettability of the developer to the resist has not been described in detail. To reveal the effect of water-soluble organic solvent on the developer, it is necessary to thoroughly examine the lithography process, especially the resist solubility.

Therefore, this study evaluates the effect of adding a water-soluble organic solvent in an alkali developer, particularly glycerol. The lithography performance of a novolak-type positive-tone resist in developer TMAH aqueous solution with or without glycerol is observed and compared based on a sensitivity curve and exposure dose vs. solubility curve [13–16]. Furthermore, we compared the resolution of the novolak resist with the developed TMAH aqueous solution with or without glycerol by the lithography simulation system (PROLITH) and direct observation of the resist pattern profile using scanning electron microscopy (SEM) images [17–20].

Received March 30, 2021
Accepted April 22, 2021

2. Experimental

2. 1. Evaluation of novolak resist solubility

OFPR-800LB 23cp (Tokyo Ohka Kogyo), for a novolak-type positive-tone resist, was coated on a 3-inch silicon wafer hydrophobized with hexa-methyl disilazane (HDMS) using a spin-coater (Opticoat MS-100A, Mikasa) at 2000 rpm for 30 s. After coating, the wafer was pre-baked on a hot plate (HHP-4030, Azone) at 90 °C for 1 min, and the film thickness was measured using a stylus surface profilometer (Dektak 6M, Bruker). Thereafter, the resists were exposed to 365 nm in the mask aligner M-1S (Mikasa Co., Ltd.) through a bandpass filter (MX0365, Asahi Spectra); the resists were baked again on a hot plate at 90 °C for 1 min. Thereafter, novolak resist were developed for 2 min by hand stirring at 23 °C with 2.38% TMAH aqueous solution, 2.38% TMAH and 2.00% glycerol aqueous solution (TMAH 2.38%/Gly 2% aq.), and 2.38% TMAH and 4.00% glycerol aqueous solution (TMAH 2.38%/Gly 4% aq.). Developers were diluted from 25% TMAH aqueous solution with water and glycerol, maintaining the concentration of TMAH constant at 2.38%. The remaining film thickness after the development was measured using a stylus surface profilometer (Dektak 6M).

2.2. Simulation of pattern profile

The performance of the novolak resist in the prepared developer was evaluated using a resist development analyzer (RDA-790, Litho Tech Japan). After resist formation in the process described in 2-1, novolak resist were developed for 3 min with each developer in the RDA at 23 °C. Subsequently, the maximum and minimum solubility rates of the novolak resist in each developer were calculated. The resist pattern profile after development can be readily obtained by providing several parameters as input to the profile simulator as follows: Novolak resist ABC parameter input to 1.0 μm^{-1} as A Parameter, 0.1 μm^{-1} as B Parameter, and 0.015 cm^2/mJ as C Parameter. The exposure parameter inputs were the wavelength of 365 nm, N.A. as 0.50, and σ as 0.50. Resist formation condition was ensured through appropriate input to the 2-1 process. The maximum and minimum solubility rates (R_{max} and R_{min}) obtained by RDA evaluation were substituted into the development parameters. Finally, as the development conditions, the temperature and time inputs of 23 °C and 60 s, respectively, were ensured.

2.3. Direct observation of pattern profile

OFPR-800LB was coated on an 8-inch silicon wafer hydrophobized with HDMS using a spin-coater (Clean Track Act-3, Tokyo Electron) at 700 rpm for 10 s, and subsequently, at 2600 rpm for 30 s. After spin-coating, the wafer was prebaked at 90 °C for 1 min. The exposure was conducted using an i-line stepper (NSR-2005iC9, Nikon), and the exposed amount was 60–140 mJ/cm^2; the depth of focus ranged from -4 mm to +8 mm. Thereafter, the resists were exposed and baked again at 90 °C for 1 min. Subsequently, resists were developed with 500 mL of 2.38% TMAH aqueous solution or 2.38% TMAH and 2.00% glycerol aqueous solution for 2 min. Moreover, the observed shape and lithographic properties were determined via SEM (SU8230, Hitachi High Tech), and the resolution of the pattern was evaluated.

3. Results and discussion

3.1. Evaluation of novolak resist solubility

The sensitivity curve and lithography parameters are shown in Fig. 1. and Table 1. The amounts of resist loss in the unexposed area are 102 nm, 49 nm, and 41 nm corresponding to TMAH 2.38% aq., TMAH 2.38%/Gly 2% aq., and TMAH 2.38%/Gly 4% aq., respectively. The amounts of exposure necessary for complete dissolution of the resist (Eth) are 37.5 mJ/cm^2, 44.0 mJ/cm^2, and 120 mJ/cm^2, corresponding to TMAH 2.38% aq., TMAH 2.38%/Gly 2% aq., and TMAH 2.38%/Gly 4% aq. The solubility of the novolak resist decreases as the amount of glycerol in the alkali developer increases. The γ values of the sensitivity curve calculated at $E_{0.8}$ were 0.40, 0.63, and 0.58, corresponding to TMAH 2.38% aq., TMAH 2.38%/Gly 2% aq., and TMAH 2.38%/Gly 4% aq. The sensitivity curve results indicate that the developer containing glycerol inhibits the resist dissolution of the unexposed area and improves the

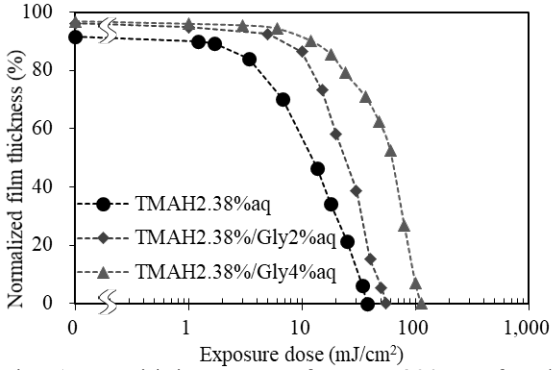

Fig. 1. Sensitivity curve of OFPR-800LB, for the developer, TMAH 2.38% aq. (●), TMAH 2.38%/Gly 2.0% aq. (◆), and TMAH 2.38%/Gly 4.0% aq. (▲).

novolak resist resolution. The optimized amount of glycerol was considered to be 2.0% because of the highest γ value and a small increase in Eth.

Table 1. Lithography parameter of sensitivity curve.

Developer	TMAH 2.38% aq.	TMAH 2.38%/Gly 2% aq.	TMAH 2.38%/Gly 4% aq.
Resist loss (nm)	102	49	41
Eth (mJ/cm^2)	37.5	44.0	120
γ value	0.40	0.63	0.58

3.2. RDA evaluation of resist solubility

To thoroughly examine the resist solubility, we developed a novolak resist in TMAH 2.38% aq. and TMAH 2.38%/Gly 2% aq., through RDA. Figure 2. and Table 2. show the exposure dose vs. solubility curve and the R_{max}, R_{min}, and development contrast (R_{max}/R_{min}). The solubility rate of the novolak resist decreases in both the exposed and unexposed areas by adding glycerol to the developer. However, consequently, the solubility contrast increases because R_{min} decreases to approximately 1/6th the initial value, whereas the value of R_{max} is almost halved.

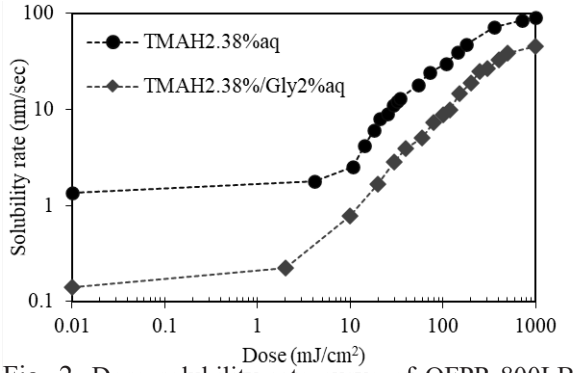

Fig. 2. Dose solubility rate curve of OFPR-800LB developed with TMAH 2.38% aq. (●) and TMAH 2.38%/Gly 2.0% aq. (◆).

Table 2. Evaluation of resist solubility by RDA

Developer	TMAH 2.38% aq.	TMAH 2.38% /Gly 2% aq.
R_{max} (nm/sec)	90.4	55.7
R_{min} (nm/sec)	1.37	0.22
R_{max}/R_{min}	66.0	251.0

3.3. Evaluation of resist resolution

3.3.1. Simulation of pattern profile

We compared the resolution of the novolak resist developed in TMAH 2.38% aq. and 2.38%/Gly 2% aq. L/S =1 μm/1 μm and the thickness of 1.3 μm; the pattern was simulated by the PROLITH input solubility rate obtained from the RDA evaluation. The simulated patterns and their profiles are shown in Fig. 3. and Table 3. The optimized conditions for the exposure dose and depth of focus were 118 mJ/cm^2 and +0.50 μm in TMAH 2.38% aq., and 159 mJ/cm^2 and +0.48 μm in TMAH 2.38%/Gly 2% aq., respectively. The resist loss and sidewall angle of the optimized pattern profile were 164 nm and 83.6° in TMAH 2.38% aq., and 25 nm and 86.8° in TMAH 2.38%/Gly 2% aq., respectively. The simulation indicated that glycerol improved the novolak resist resolution, as shown by the decreased resist loss and the sidewall angle approaching 90°. Furthermore, glycerol lowered the resist sensitivity, as indicated by the larger value of the optimized exposure.

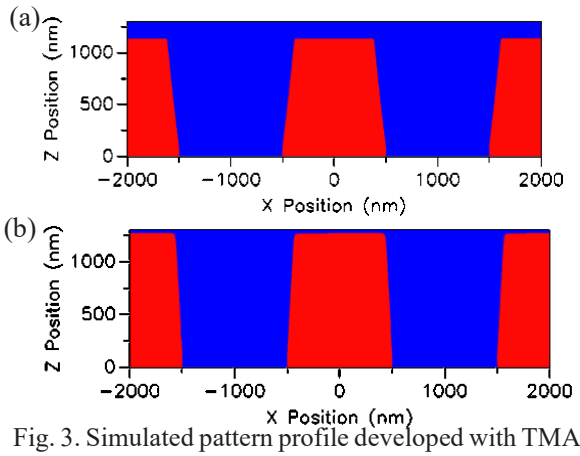

Fig. 3. Simulated pattern profile developed with TMAH 2.38% aq. (a) or TMAH 2.38%/Gly 2.0% aq(b).

Table 3. Pattern profile from PROLITH.

Developer	TMAH 2.38% aq.	TMAH 2.38% /Gly 2% aq.
Optimized focus (μm)	0.50	0.48
Optimized exposure (mJ/cm^2)	118	159
Resist loss (nm)	164	25
Sidewall angle (°)	83.6	86.8

3.3.2. Direct observation of pattern profile

The L/S =1 μm/1 μm and the thickness of 1.3 μm in the pattern was actually developed in TMAH 2.38% aq. and TMAH 2.38%/Gly 2% aq. Moreover, the shape of the pattern profile was observed using SEM micrograms. The pattern image and scaled parameters are shown in Fig. 4. and Table 4. The resist loss and sidewall angle are 181 nm and 73.8°

in TMAH 2.38% aq., and 72 nm and 77.2° in TMAH 2.38%/Gly 2.0% aq., respectively. In the pattern developed in TMAH 2.38%/Gly 2.0% aq., the resist loss was smaller, and an improved shape was observed. The SEM images indicated that glycerol improved the novolak resist resolution because of the decreased resist loss and the sidewall angle approaching 90°. This was because glycerol inhibited the dissolution of the unexposed area more effectively than that of the exposed area.

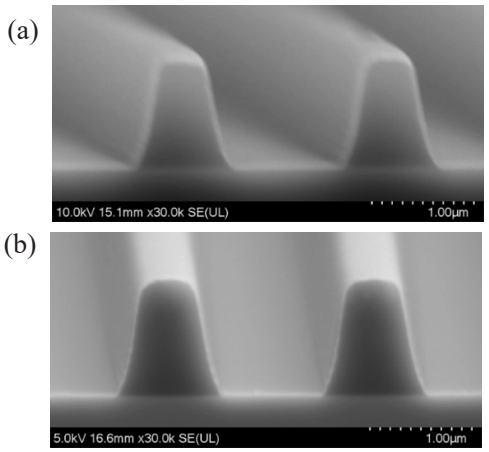

Fig. 4. SEM images of 1 μm line and space pattern developed with TMAH 2.38% aq. (a) and TMAH 2.38% /Gly 2.0% aq. (b).

Table 4. Pattern profile from direct observation.

Developer	TMAH 2.38% aq.	TMAH 2.38% /Gly 2% aq.
Resist loss (nm)	181	72
Sidewall angle (°)	73.8	77.2
Best exposure (mJ/cm^2)	60	80

4. Conclusions

The addition of glycerol in TMAH aq. improved the resolution of the novolak resist pattern profile in both the simulation and direct observations, compared with that of TMAH 2.38% aq. The fact that glycerol improved the resolution of the novolak resist can be due to an increase in the solubility ratio. These results indicate that adding glycerol to the developer can decrease the dissolution of the novolak resist, particularly in the unexposed area, without any process control.

Acknowledgement

This work was partly supported by Toray Industries, Inc. Shiga Plant Electronic and Imaging Materials Research Laboratories for the i-line stepper exposure and was partly supported by Litho Tech Japan to simulate the pattern profile.

References

1. A. Soyano, *J. Soc. Rubber Sci. Technol. Jpn.,* **85** (2012) 33.
2. R. Haruta, *J. Inst. Electri. Electron. Eng.,* **10** (2007) 353.
3. K. Toriyama, K. Okamoto, S. Kohara, and Y. Orii, *Trans. JIEP,* **14** (2011) 372.
4. G. Mago, *J. Surf. Finish. Soc. Jpn.,* **65** (2014) 349.
5. K. Sakai, K. Nakahira, M. Umeda, and K. Kitami, *J. JSPE*, **83** (2017) 125.
6. H. Horibe, "*Novolak resist optimization of materials and process*" S&T Pub. Inc., (2020-1-25) [in Japanese].
7. M. Hanabata, A. Furuta, and Y. Uemura, *Proc. SPIE,* **771** (1987) 85.
8. M. Hanabata, Y. Uetani, and A. Furuta, *Proc. SPIE,* **920** (1988) 349.
9. M. Hanabata, F. Oi, and A. Furuta, *Polym. Eng. Sci.*, **32** (1992) 1494.
10. Sumitomo Kagaku Kogyo, "*Organic alkali developer for positive tone photo resist*", JPA 1998-259560, 1988-10-26.
11. Shipley, "*Photo resist developer without metallic ion*", JPA 1983-9143.
12. Fuji Shashin Film, "*Developer for positive tone photo resist to manufacturing semiconductor*", JPB 2589823, 1996-12-5.
13. H. Horibe, T. Kumada, and S. Kubota, *Kobunshi Ronbunshu*, **53** (1996) 133 [in Japanese].
14. M. Yamamoto, H. Horibe, A. Sekiguchi, E. Kusano, and S. Tagawa, *J. Photopolym. Sci. Technol.*, **21** (2008) 299.
15. M. Yamamoto, R. Kitai, H. Horibe, A. Sekiguchi, and H. Tanaka, *J. Photopolym. Sci. Technol.*, **22** (2009) 357.
16. Y. Sotokawa, T. Nishiyama, E. Sato, and H. Horibe, *J. Photopolym. Sci. Technol.*, **31** (2018) 399.
17. Y. Sensu, M. Isono, A. Sekiguchi, M. Kadoi, T. Matsuzawa, and Y. Minami, *I.E.E.J. Trans, FM*, **124** (2004) 286.
18. A. Sekiguchi, T. Watanabe, and H. Kinoshita, *J. Photopolym. Sci. Technol.*, **27** (2014) 623.
19. A. Sekiguchi, T. Nishino, H. Minami, Y. Matsumoto, and Y. Kai, *J. Photopolym. Sci. Technol.*, **32** (2019) 677.
20. Y. Ohta, A. Sekiguchi, A. Voigt, and N. Taksatorn, *J. Photopolym. Sci. Technol.*, **33** (2020) 221.

Communication

Journal of Photopolymer Science and Technology
Volume 34, Number 5 (2021) 499−504 ©2021SPST

Removal of Novolac Photoresist with Various Concentrations of Photo-active Compound Using H_2/O_2 Mixtures Activated on a Tungsten Hot-wire Catalyst

Koki Akita [1*], Shota Sogo [1], Ryusei Sogame [1], Masashi Yamamoto [1], Shiro Nagaoka [2], Hironobu Umemoto [3], and Hideo Horibe [4]

[1] Department of Electrical and Computer Engineering, National Institute of Technology, Kagawa College, 355 Chokushi-cho, Takamatsu, Kagawa 761-8058, Japan
[2] Department of Electronic Systems Engineering, National Institute of Technology, Kagawa College, 551 Kohda, Takuma-cho, Mitoyo, Kagawa 769-1192, Japan
[3] Shizuoka University, Joho-ku, Naka, Hamamatsu, Shizuoka 432-8561, Japan
[4] Department of Applied Chemistry and Bioengineering, Graduate School of Engineering, Osaka City University, 3-3-138, Sugimoto-cho, Sumiyoshi, Osaka 558-8585, Japan
**m-yamamoto@t.kagawa-nct.ac.jp*

We earlier reported that addition of a small amount of O_2 gas in the atmosphere where H radicals are generated on a high-temperature tungsten filament improves the photoresist removal rate of positive-tone novolac photoresists for i/g lines. This study investigated effects of photo-active compound (PAC) on the photoresist removal. Addition of more than 1.5 sccm of oxygen to 100 sccm of hydrogen gas flow decreased the removal rate. In pure novolac resin, cross-linking of the resin can be one of the causes of this decrease at temperatures higher than 240 °C. The rate of removal with PAC decreased much more than with pure novolac resin over 240 °C. This removal rate decrease might be ascribed to cross-linking not only between the resin and the PAC but also between the resins. OH radicals can be used effectively for photoresist removal by generating sufficient H radicals to prevent such cross-linking.

Keywords: Crosslinking, Hardening, H_2/O_2 mixture, Photo-active compound (PAC), Radical, Removal

1. Introduction

Photoresists are used widely to fabricate fine patterns on substrates in nano-device and micro-device manufacturing processes. Photoresists play extremely important roles in processes such as etching and ion implantation, to protect predetermined areas. However, when its role has been fulfilled, it must be removed for later processes.

Chemicals are commonly used for photoresist removal [1], but they are expensive and have deleterious environmental effects. Such chemicals that are used leave organic residue that must be cleaned and purified. Therefore, some processes use dry processes with oxidizing gases such as ozone [2] and oxygen plasma [3]. During drying, oxidizing gases are used to ash the photoresist. Some concern arises that oxidation can degrade device quality.

Removal using H-radicals, which have excellent reducing ability, can be effective to resolve these difficulties [4–6]. Actually, H radicals can be generated by catalytic decomposition of molecular hydrogen on the surface of a heated metal filament [7]. Because this method uses no chemicals or plasma, it reduces the environmental effects and avoids plasma damage to the device. Nevertheless, the slow removal rate is a persistent difficulty with this method.

Increasing the removal rate somewhat is

Received March 31, 2021
Accepted May 5, 2021

technically feasible by optimizing the process conditions [5]. However, the removal rate is limited by the reaction rate of H radicals on the photoresist surfaces. As long as only hydrogen radicals are used, the removal rate improvement is limited. Therefore, we specifically examined OH radicals, which generally have higher reactivity [8, 9].

According to Umemoto and Moridera, when an H_2/O_2 mixture gas is activated on the tungsten filament surface, a small amount of OH radicals (about 1/100th of the H radicals produced) are generated [10]. We have reported that, by optimizing the amount of oxygen introduced, the removal rate of positive-tone novolac photoresists for i/g lines can be improved by 1.7 times [11]. However, introduction of an excessive oxygen decreases the removal rate.

Presumably, the decrease in the amount of H radicals produced decreases the removal rate because the catalytic poisoning effect of O radicals occurring on the catalyst surface [10]. The removal rate rises in directly proportion to the amount of H radicals generated [12]. Besides this, however, the cross-linking and hardening of the photoresist may also cause the reduction of the removal rate [13].

Positive-tone novolac photoresists for i/g lines mainly consist of novolac resin and a photo-active compound (PAC; diazonaphthoquinone sulfonate acid ester). The novolac thermosetting resin is cross-linkable when cured at 250–300 °C [5, 14]. Generally, PAC is placed to fill gaps in the polymer chains of the novolac resin; diazo couplings can be formed between the resins when unexposed [15–17]. In dry processes such as the method used for this study, the photoresist substrate is often heated to increase the removal rate. Then PAC might be altered and might play an intermediary role in cross-linking between the resins. This study examined photoresist removal rates using various amounts of PAC with a H_2/O_2 gas mixture activated on the tungsten hot filament surface.

2. Experimental

2.1. Preparation of novolac photoresists

For the photoresist, we used positive-tone novolac photoresists prepared using the ratio shown in Table 1. Solids (novolac resin and PAC) were dissolved in liquid (propylene glycol methyl ether acetate (PGMEA)) at a ratio of 78 wt% (liquid) / 22 wt% (solid) [18, 19]. The PAC contents were 0, 9.4, and 18.7 wt% of solids in the photoresist. In general, the amount of PAC in positive-tone novolac photoresists is said to be about 20% of the solid content. The base resin of this photoresist was polymerized from *m*-cresol (*m*), *p*-cresol (*p*) and 2.4, 2.5-xylenol (*Xyl*), in a ratio of 50 (*m*) / 35 (*p*) / 15 (*Xyl*). The weight- averaged molecular weight was 6500-7900. The PAC used was naphthoquinone diazo esterified with 2, 3, 4, 4'-tetrahydroxybenzophenone. The esterification ratio of PAC is 75%.

Table 1. Photoresist preparation ratio with different PAC contents

Content of PAC [%]	Content rate [wt%]		
	Solid		Liquid
	Novolac resin	PAC	PGMEA
18.7	17.88	4.12	78.0
9.4	19.94	2.06	78.0
0	22.00	0.00	78.0

After these photoresists were spin-coated onto Si wafers at 2.6×10^3 rpm for 20 s using a spin coater (K-359 S-1; Kyowa Riken Co., Ltd.), they were pre-baked in an oven (CLO-2AH; Koyo Thermo Systems Co., Ltd.) at 100 °C for 60 s. The initial film thickness of each sample after spin coating was 1.0 ± 0.2 μm, as measured using a surface profiler (Surfcom 480A; Tokyo Seimitsu Co., Ltd.).

2.2. Conditions for photoresist removal

The experiment apparatus and the procedure were similar to those described elsewhere [5–8]. The H_2 gas (≥99.99%; Takamatsu Teisan Co.) flow rate was fixed at 100 sccm using a mass flow controller. (SEC-400MK2; STEC Inc.). The O_2 gas (≥99.5%; Iwatani Sangyo Co. Ltd.) flow rate was varied between 0 and 2.5 sccm using another mass flow controller (SEC-400MK3; STEC Inc.): i.e., the amount of added oxygen (flow rate ratio of O_2 to H_2) was varied between 0 and 2.5%. The typical total pressure under processing was 2.7 kPa. A resistively heated coiled tungsten filament (99.9%, 0.5 mm diameter; The Nilaco Corp.) was used for radical generation. The filament length was 0.36 m. The coils in the coiled section were 12, with 28 mm length and 8 mm diameter. The substrate–filament distance was set to 20 mm. A DC current source (EX-750L2; Takasago Ltd.) was used to heat the filaments. The filament temperature, set to 1600 °C, was measured through a quartz window using a two-wavelength (0.80 and 1.05 μm) infrared radiation thermometer.

The change in film thickness during photoresist removal was evaluated using thin-film interference of the photoresist [8]. By thin film interference, the peaks and valleys of the reflected light intensity are

observed alternately during the film thickness change. The film thickness was calculated from this change in reflected light intensity. A green laser beam (520 nm, 150 mW, CivilLaser; Naku Technology Co. Ltd.) was used as the light source. This light was incident on the center of the stage at an angle of incidence of 76° to the substrate surface. A reverse-biased Si photodiode (S1787-04; Hamamatsu Photonics KK) was used as a photodetector to measure the intensity of light reflected from the substrate. DC +5 V was connected to its cathode through a 60 kΩ photoresistor. The reflected light intensity was found by correcting the voltage across the photoresistor.

The substrate was heated using a substrate stage heater. The dependence of the removal rate on the substrate surface temperature was evaluated. The removal rate includes not only the decrease in film thickness because of the photoresist decomposition, but also the decrease in film thickness because of photoresist shrinkage. A sheathed thermocouple (TK ϕ1.6×L300; AS One Corp.) was used for surface temperature measurements. The thermocouple was placed on the substrate surface at a 20 mm distance from the center of the stage. The temperature and film thickness were measured simultaneously at 0.2 s intervals. Table 2 shows the initial temperature of the substrate surface, the temperature reached, and the rate of temperature increase. The removal rate was calculated from the average film thickness decrease during 2 s.

3. Results and discussion

Figure 1 shows the substrate surface temperature dependence of the photoresist removal rates with various PAC contents. The removal rate curves shown in Fig. 1(a) are explained first. The increase in the removal rate at surface temperatures of 100 °C to 150 °C is ascribed to thermal shrinking caused by volatilization of the residual solvent, which is probably PGMEA (boiling point 146 °C) left in the photoresist film [5]. The removal rate with 1.0 sccm of oxygen at temperatures higher than 150 °C was slightly higher than that in the pure hydrogen system. When H_2/O_2 gas mixture is

Table 2. Initial temperature, attained temperature and the average rate of temperature rise of the substrate surface.

Amount of oxygen added [sccm]	Initial temperature [°C]	Attained temperature [°C]	Average temperature rise rate [°C/min]
0.0	25.3	281	22.3
0.5	25.3	277	21.3
1.0	25.4	283	20.8
1.5	25.4	284	21.5
2.0	25.1	255	21.9
2.2	25.4	266	20.4
2.5	25.2	265	21.7

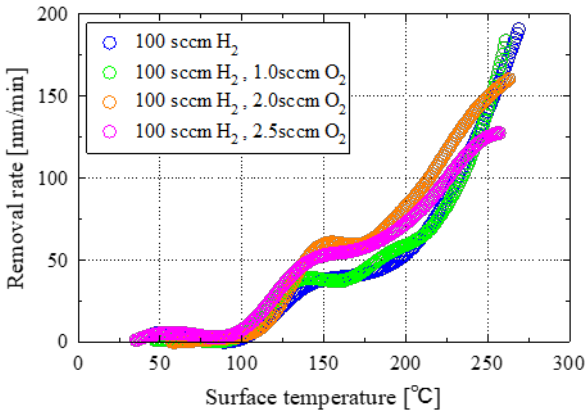

(a) Novolac resin only

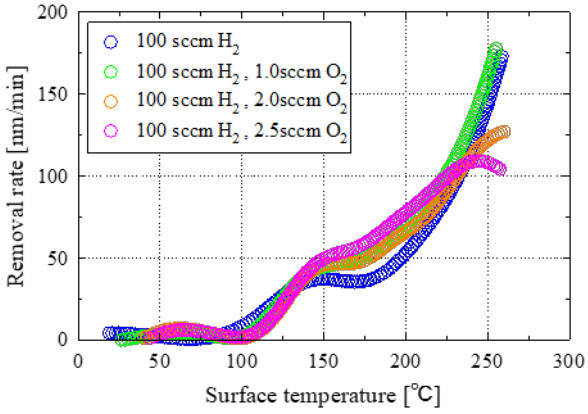

(b) Novolac resin + PAC 9.4 wt%

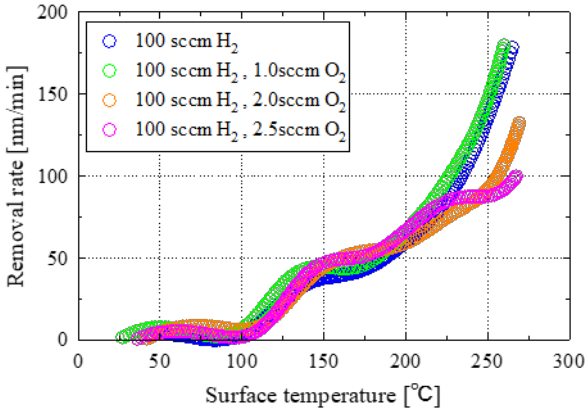

(c) Novolac resin + PAC 18.7 wt%

Fig. 1. Surface temperature dependence of the removal rate of the prepared resists: (a) novolac resin only; (b) novolac resin + PAC 9.4 wt%; (c) novolac resin + PAC 18.7 wt%.

activated using a tungsten hot filament, not only H radicals but also O and OH radicals are generated [10]. Among them, OH radicals are an extremely active species, with strong oxidizability [8]. Therefore, the OH radicals can induce the removal rate increase. However, when the oxygen additive amount is 2.5 sccm, the H radicals population decreases because of catalytic poisoning by oxygen [10]. The decrease in the removal rate associated with low H-radical density can be observed at temperatures higher than 250 °C.

Figure 1(b) also shows that the removal rate at 1.0 sccm of oxygen addition is higher than that of 100% H_2. On the other hand, those over 2.0 sccm were smaller, when the temperature was higher than 225 °C. Although the photoresist removal rate generally changes according to the Arrhenius equation with respect to the surface temperature [12, 20], this removal rate curve exhibited different behavior from that implied by the Arrhenius equation. The slope of the curves in the temperature range of 225–260 °C are smaller than those in Fig. 1(a).

As shown in Fig. 1(c), when the oxygen flow rate was more than 2.0 sccm, the decrease in the removal rate for 18.7 wt% PAC was larger than that for 9.4 wt% PAC. The behavior of 9.4 wt% PAC described above is intermediate between the pure resin (Fig. 1(a)) and the 18.7 wt% PAC.

Explaining the decrease in the removal rate of PAC-containing photoresists is difficult by the decrease in the H radical population solely. Cross-linking and hardening of the photoresist must take place at a temperature over 225 °C, besides the degradation. Differences in the removal rate curves involved in these competition reactions are discussed later.

To clarify the PAC effects on the removal rate when oxygen is added, we plotted the O_2 additive amount dependence of the removal rate. Figures 2(a)–(c) show dependence at three temperatures. In Fig. 2(a) (surface temperature 200 °C), no marked change is evident in the removal rate with the additive amount of oxygen. In Fig. 2(b) (surface temperature 225 °C), the behavior is almost identical. Fig. 2(c) (surface temperature 250 °C) shows that, above 1.0 sccm, the removal rate decreases slowly with increased oxygen. For samples containing more than 9.4 wt% PAC, the decrease is more pronounced than in samples without PAC. The cause of this will be discussed below.

In general, in the photoresist removal by radicals, the decomposition processes compete with cross-linking, and hardening by external stimuli such as heat. Even for a pure resin, the temperature increase causes thermal cross-linking [5, 14]. When the resin is heated, the hydroxyl group itself and H of hydroxyl or methyl group on the side chain of novolac resin desorb and dangling bonds are

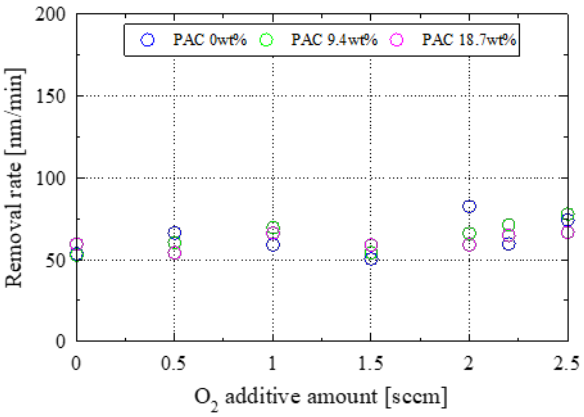

(a) Surface temperature: 200 °C

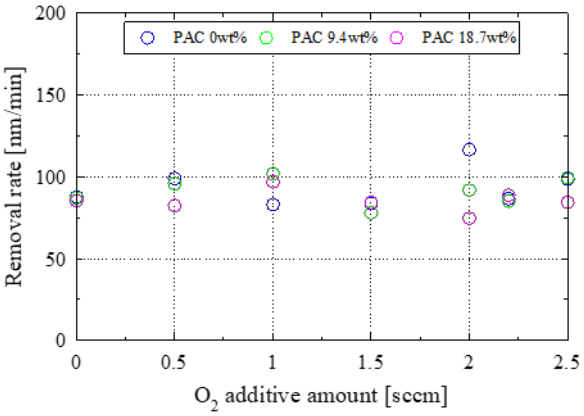

(b) Surface temperature: 225 °C

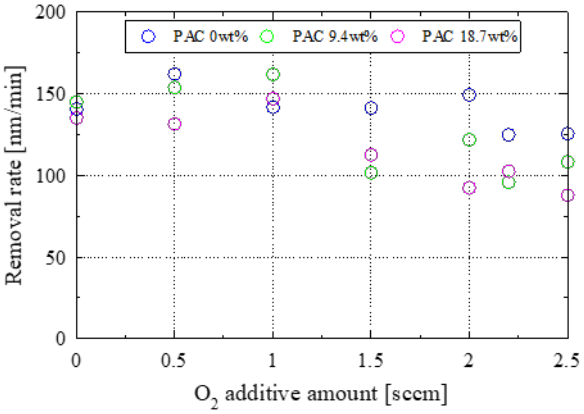

(c) Surface temperature: 250 °C

Fig. 2. Dependence of the removal rate of the prepared resist on the amount of oxygen added: (a) surface temperature 200 °C; (b) surface temperature 225 °C; (c) surface temperature 250 °C.

produced. When the amount of added oxygen is slight, H radicals are generated sufficiently on wire surfaces. Then the dangling bonds, if produced, might be terminated by hydrogen radicals before cross-linking. Consequently, the cross-linking can be prevented. Therefore, the decrease in the removal rate is minor if the temperature is raised. However, the addition of an excessive amount of O_2 decreases the population of H-radicals generated. In this case, the cross-linking via side chains (thermal cross-linking) must proceed because the hydrogen termination of dangling bonds should be suppressed. Accordingly, the removal rate can be inferred to have decreased in the high temperature range, as presented in Fig. 1(c).

Here we consider that not only PAC-mediated crosslinking but also the thermal crosslinking has taken place in the resins containing PAC. Actually, PACs are inherently unstable. Some examples are that they easily induced a chemical change by ultraviolet light. They are perhaps more sensitive than novolac resin. When novolac resin contains PAC, then the H radicals must also terminate the dangling-bonds on PAC. In any case, if the population of generated H radicals is sufficient, the dangling bonds can be terminated. Therefore, in a pure hydrogen system, the effect of the presence or absence of PAC is slight. However, the addition of an excessive amount of O_2 decreases the population of generated H-radicals. Hydrogen termination might become less likely. Fundamentally, PAC is placed to fill in the space between the polymer chains of the novolac resin. When unexposed, PAC builds diazo coupling with the novolac resin [15–17]. Cross-linking via PAC might proceed more rapidly than hydrogen termination. Therefore, at high temperatures, the removal rate with PAC might be lower than that without PAC.

4. Conclusion

This study examined photo-active compound (PAC) effects on photoresist removal. Specifically, the removal rate of photoresists containing various amounts of PAC were investigated using a tungsten filament activated H_2/O_2 gas mixture. The findings of this study are explained below.

(a) Both with and without PAC, the removal rate was raised by adding oxygen less than 1.0 sccm. However, when more than 1.5 sccm of oxygen was added, the removal rate decreased in the high-temperature range. This finding might be attributable not only to a decrease in the population of H-radicals generated, but also to the associated thermal cross-linking.

(b) In the high-temperature range (over 240°C), the decrease in the removal rate that occurred when more than 1.5 sccm of oxygen was added became more pronounced as the amount of added PAC was increased. This finding might be attributable not only to thermal cross-linking of the resin but also to cross-linking through PAC. It is concluded that the presence of PAC affected photoresist removal.

Thermal cross-linking and PAC-mediated cross-linking described above might be attributed to the decreased population of H-radicals generated. Therefore, the highly reactive OH radicals can be used effectively photoresist removal by generating sufficient H radicals to prevent cross-linking. PAC is fundamentally important because they provide photosensitizing effects, which is indispensable for photoresists. However, if it causes cross-linking, then it will have a negative effect on removal. Therefore, if a photoresist with photosensitivity but which does not cause cross-linking could be used, then one could expect further improvement in removal performance in an environmentally friendly method such as that used for this study.

Acknowledgments

This work was supported by JSPS KAKENHI Grant Number 19K04543.

References

1. H. Morinaga, T. Futatsuki, T. Ohmi, E. Fuchita, M. Oda, and C. Hayashi, *J. Electrochem. Soc.,* **142** (1995) 966.
2. T. Miura, M. Kekura, H. Horibe, and M. Yamamoto, *J. Photopolym. Sci. Technol.,* **21** (2008) 311.
3. K. Shinagawa, H. Shindo, K. Kusaba, T. Koromogawa, J. Yamamoto, and M. Furukawa, *Jpn. J. Appl. Phys.,* **40** (2001) 5856.
4. A. Izumi and H. Matsumura, *Jpn. J. Appl. Phys.,* **41** (2002) 4639.
5. M. Yamamoto, H. Horibe, H. Umemoto, K. Takao, E. Kusano, M. Kase, and S. Tagawa, *Jpn. J. Appl. Phys.,* **48** (2009) 026503.
6. M. Yamamoto, H. Umemoto, K. Ohdaira, S. Nagaoka, T. Shikama, T. Nishiyama, and H. Horibe, *J. Photopolym. Sci. Technol.,* **28** (2015) 303.
7. H. Umemoto, *Chem. Vapor Deposition*, **16** (2010) 275.

8. H. Sugimitsu, "*Ozone no Kiso to Oyo (Basis and Application of Ozone)*", Korin, Tokyo, 1996, p. 20 (in Japanese).
9. S. Fujimura, K. Shinagawa, M. T. Suzuki, and M. Nakamura, *J. Vac. Sci. Technol.* **B9** (1991) 357.
10. H. Umemoto and M. Moridera, *J. Appl. Phys.,* **103** (2008) 034905.
11. M. Yamamoto, H. Umemoto, K. Ohdaira, T.Shikama, T. Nishiyama, and H. Horibe, *Jpn. J. Appl. Phys.,* **55** (2016) 076503.
12. M. Yamamoto, T. Maruoka, A. Kono, H. Horibe, and H. Umemoto, *Appl. Phys. Express,* **3** (2010) 026501.
13. T. Maruoka, Y. Goto, M. Yamamoto, H. Horibe, E. Kusano, K. Takao and S. Tagawa, *J. Photopolym. Sci. Technol.,* **22** (2009) 325.
14. Ed. Osaka Municipal Technical Research Institute and Japan Society of Plastics Technology, "*Plastic Dokuhon*", Plastic Age, Tokyo, 1985, 14th ed. (in Japanese).
15. M. Hanabata, Y. Uetani, and A. Furuta, *J. Vac. Sci. Technol.,* **B7** (1989) 640.
16. M. Hanabata, F. Oi, and A. Furuta, *Proc. SPIE,* **1466** (1991) 132.
17. A. Furuta and M. Hanabata, *J. Photopolym. Sci. Technol.,* **2** (1989) 383.
18. M. Yamamoto, R. Kitai, Y. Horibe, A. Sekiguchi, and H. Tanaka, *J. Photopolym. Sci. Technol.,* **22** (2009) 357.
19. S. Saito, K. Ishiguro, S. Takahashi, A. Kawano, J. Sekiguchi, K. Taniguchi, H. Tanaka, and H. Horibe, *Kobunshi Ronbunsu.,* **69** (2012) 639.
20. M. Yamamoto, T. Maruoka, A. Kono, H. Horibe, and H. Umemoto, *Jpn. J. Appl. Phys.,* **49** (2010) 016701.

Communication

Journal of Photopolymer Science and Technology
Volume 34, Number 5 (2021) 505−509 ©2021SPST

Nodule Deformation on Cleaning of PVA Roller Brushes and its Relation to Cross-contamination

Atsuki Hosaka[1], Tsubasa Miyaki[1], Yuki Mizushima[2], Satomi Hamada[3] Ryota Koshino[3], Akira Fukunaga[3], and Toshiyuki Sanada[2*]

[1] Graduate School of Integrated Science and Technology, Shizuoka University, 3-5-1 Johoku, Naka-ku, Hamamatsu, Shizuoka 432-8561, Japan
[2] Department of Mechanical Engineering, Shizuoka University, 3-5-1 Johoku, Naka-ku, Hamamatsu, Shizuoka 432-8561, Japan
[3] Ebara Corporation, 4-2-1 Honfujisawa, Kanagawa, 251-8502, Japan
**sanada.toshiyuki@shizuoka.ac.jp*

This study investigates nodule deformation and contact area during PVA roller-type brush scrubbing to clarify their relationship with cross-contamination. Two high-speed video cameras with collimating LED light sources and an evanescent field on a prism enabled us to observe brush nodule deformation and contact area. Deformation analysis showed that the volume of a roller-type brush changes gradually at the beginning of compression, deforms more when vertically pushed at maximum compression, and then recovers rapidly at the end of compression. The brush contact area changes according to the brush and wafer rotation speed. The contact area can be categorized into three: the front, rear side face in the brush traveling direction, and vertically pushed bottom face on the surface. We analyzed the three types of brush contacts on a 100 mm type wafer and observed that the vertical compression type significantly affected the cross-contamination region.
Keywords: Cleaning, PVA brushes, Deformation, Cross-contamination, Nanoparticles

1. Introduction

Cleaning is a necessary process in semiconductor device manufacturing. In semiconductor cleaning, chemical and physical actions are used [1] owing to the need to remove ultrafine impurities in a limited time. A variety of physical cleaning methods are utilized including ultrasonic waves [2-4], droplet impingements [5-7], brush scrubbing [8-10], and lasers [11-13].

Brush scrubbing, a type of contact cleaning widely used for post-CMP cleaning, causes cross-contamination [14-15]. Contamination involves transferring the characteristic brush nodule shape patterns on a wafer after cleaning [16-17]. However, the effects of rotating both the brush and wafer have not been clarified. Besides, improving liquid mixing near the wall surface plays an important role in brush cleaning [18]. Nevertheless, the relationship between brush nodule deformation during scrubbing and liquid mixing has not been clarified.

In this study, we investigated the deformation and contact behavior of a roller-type PVA brush on a rotating wafer. We observed brush nodule deformation during rotation using two high-speed cameras and a collimated LED light source. We developed a device that reproduces the relative motion of the wafer and brush, and the brush contact was observed using the evanescent field generated on the prism. We analyzed the relationship between nodule deformation and cross-contamination patterns as reported in [16-17].

2. Experimental

Two experimental setups were used in this study. Fig. 1 shows a schematic of the experimental setup for observing the nodule deformation of a roller-type PVA brush during rotation and contact with a surface. The shape of the brush used is shown in the figure. A servo motor rotates the PVA roller brushes. A wide range of brush shapes can be obtained as the L-shaped gearbox changes the servomotor's rotation. The image was captured using two high-speed

Received March 31, 2021
Accepted April 13, 2021

cameras and a collimating light source as a backlight. The brush nodule was compressed by 1 mm when it was located on the bottom surface. The brush rotation speed was set to 10 rpm. The volume change of the nodules was calculated from the reconstructed images by applying a series of image analyses obtained from the two directions. A frame rate of 300 fps and a resolution of 1280 × 800 pixels of recording conditions were used.

Fig. 2 shows a method for observing the contact surface. This setup enabled us to distinguish the contact of the solid part of the PVA brush from the liquid or gas on the prism using the principle of total internal reflection. Details of this method are presented in Sanada et al. [19]. Furthermore, the relative motion of a roller brush rotating on the horizontal axis on a wafer (ω_W) rotating on the vertical axis (ω_B) was reproduced by two servomotors; see Miyaki et al. [18] for details. In this study, the relative behavior of all positions on a 100 mm wafer was visualized by changing the rotation speeds of the two motors and the contact positions of the brushes. A frame rate of 300 or 60 fps and a resolution of 1024 × 1024 or 2592 × 2048 pixels of recording conditions were used.

The obtained results were analyzed using image processing. Fig. 3 shows an example of an image captured in a nodule deformation experiment and the image processing results such as background processing, binarization, and size correction. Next, the volume change of the nodules was calculated. As shown in the figure, the nodule root was first detected. Then, the width of the nodules was calculated for the area below the line segment. Let these segments be L_x and L_y at different observation directions. The nodule widths L_x and L_y were calculated for each pixel up to the contact surface. In this experiment, the nodules do not cause excessive deformation as the rotation speed was as low as 10 rpm. Therefore, we assumed that the nodules maintained the shape of an ellipsoid, even though they were deformed. An ellipse was formed from the nodule widths L_x and L_y at each height, and they were stacked to reconstruct a solid. The volume was calculated by adding the areas of the ellipses and multiplying them by the conversion coefficient.

Fig. 4 shows an example of visualization of the contact surface. Background processing was performed after correcting the aspect ratio because the image was recorded using a tilted camera. An inversion processing was performed to emphasize the brightness.

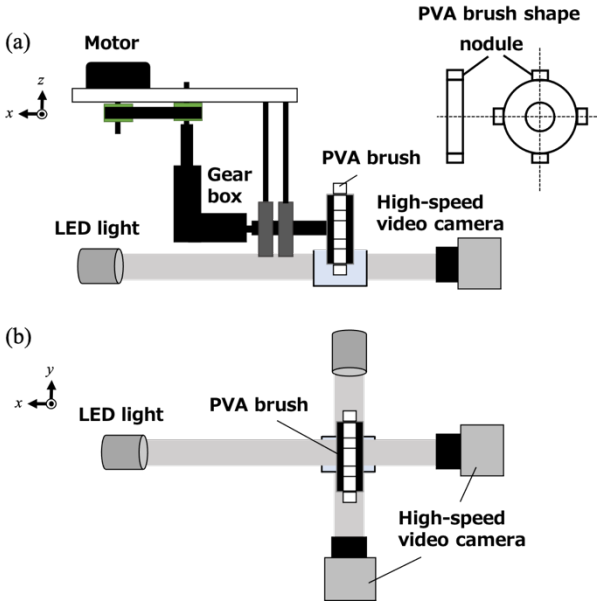

Fig. 1. Experimental setup for nodule deformation observation, (a) side view, (b) top view.

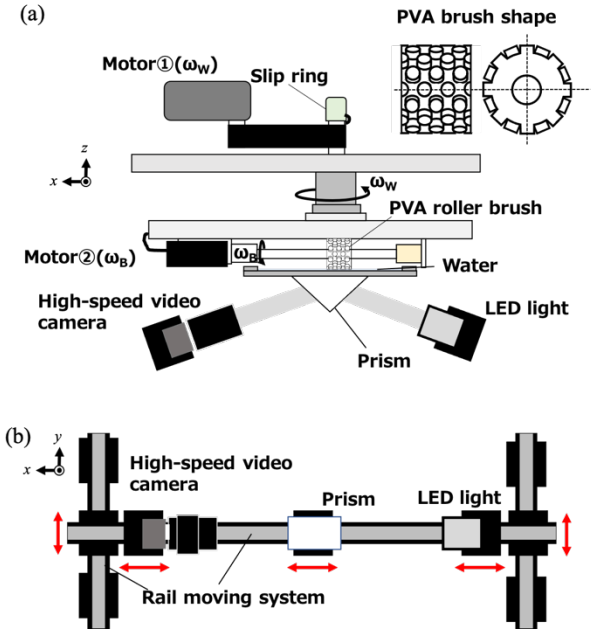

Fig. 2. Experimental setup for contact condition visualization, (a) side view, (b) top view.

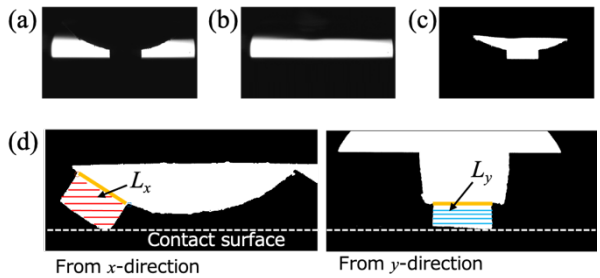

Fig. 3. Image processing for nodule deformation analysis, (a) original image, (b) background, (c) background processing and binarization, (d) volume change evaluation.

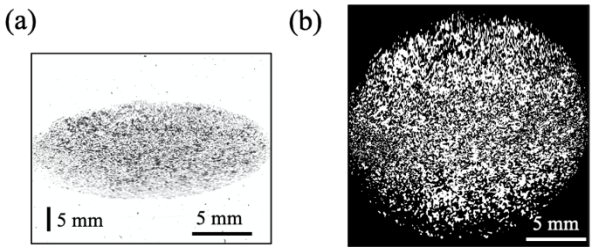

Fig. 4. Image processing for contact condition, (a) original image, (b) aspect ratio correction, binarization and black/white reversal.

3. Results and discussion

3.1. Brush nodule deformation

Fig. 5 shows an example of the nodule deformation of a PVA roller brush. Fig. 5 (a) shows an image taken from the *x*-direction and subjected to image processing. As shown in the figure, the brush makes contact with the edge, and the front side face of the nodule leading direction is pulled into the contact face. The shape of the brush quickly returns to its original form as the entrained surface recovers and separates from the surface. Fig. 5 (b) shows the three-dimensional reconstructed image of the nodules on the rotating brush at a given time. The result indicates that approximating the nodules to an ellipse to obtain the volume is a good approach. Fig. 5 (c) shows the change in the nodule volume per rotation. In the figure, the initial nodule volume of 98.96 mm^3 and the volume of the nodules when vertically pushed to 1 mm at the location of the nodule on the bottom surface are indicated. We compared the interference volume, which defines interference with the contact surface when a rigid nodule is rotating.

Figure 5 (c) shows that the volume of the roller brush during sliding changes more than when vertically pushed in by 1 mm. We considered that this is because the side face in the nodule leading direction is pulled into the contact surface, as shown in Fig 5 (a), resulting in a large volume change. Second, the volume change differs from the interference volume of the rigid nodule. The nodule volume gradually decreases at the beginning of compression, and recovers speedily at the end of compression. This is also related to the side face of the nodule. When the side face of the nodule is released from the contact surface, the nodule rapidly returns to its original shape, as shown in Fig. 5 (a). The volume change is different from the rigid nodule interference volume because of this motion. This result suggests that the volume of a normal brush nodule changes significantly each time it collides with a cleaning surface, and water retained in the brush desorb and adsorb each time. We considered that this water motion plays an important role in cleaning.

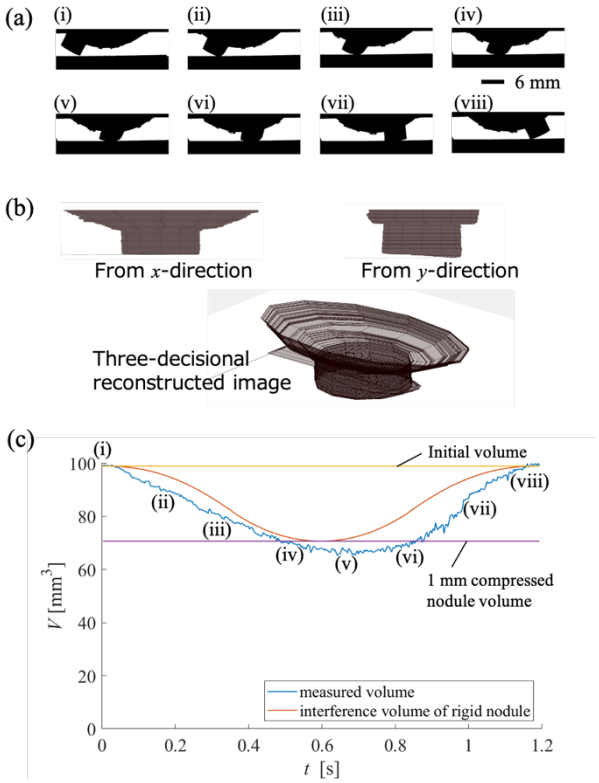

Fig. 5. Nodule deformation of a roller brush, (a) image sequence, (b) example of reconstructed image, (c) volume change.

3.2. Contact shape

The superimposed technique of 20 images was used to observe the path lines of the brush nodule contact. Figure 6 shows the path line of the three deformation patterns (Fg, Rg, and Pr type) defined by Miyaki et al. [18].

In the Fg type, which was observed in both large rotations of the brush and wafer, that is, a relatively large velocity condition, the sliding distance per nodule is small, limiting the line distance. In addition, the Fg type path line shows that the start and end of the nodule contacts are linear owing to deformation of the nodule side face, as discussed in the previous section.

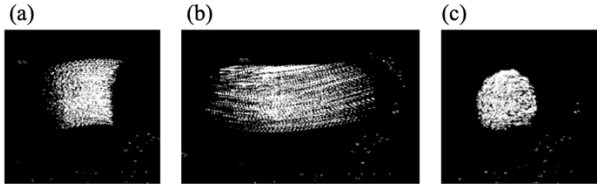

Fig. 6. Superimposed image of brush contact, (a) Front gap type (Fg), (b) Rear gap type (Rg), (c) Press type (Pr).

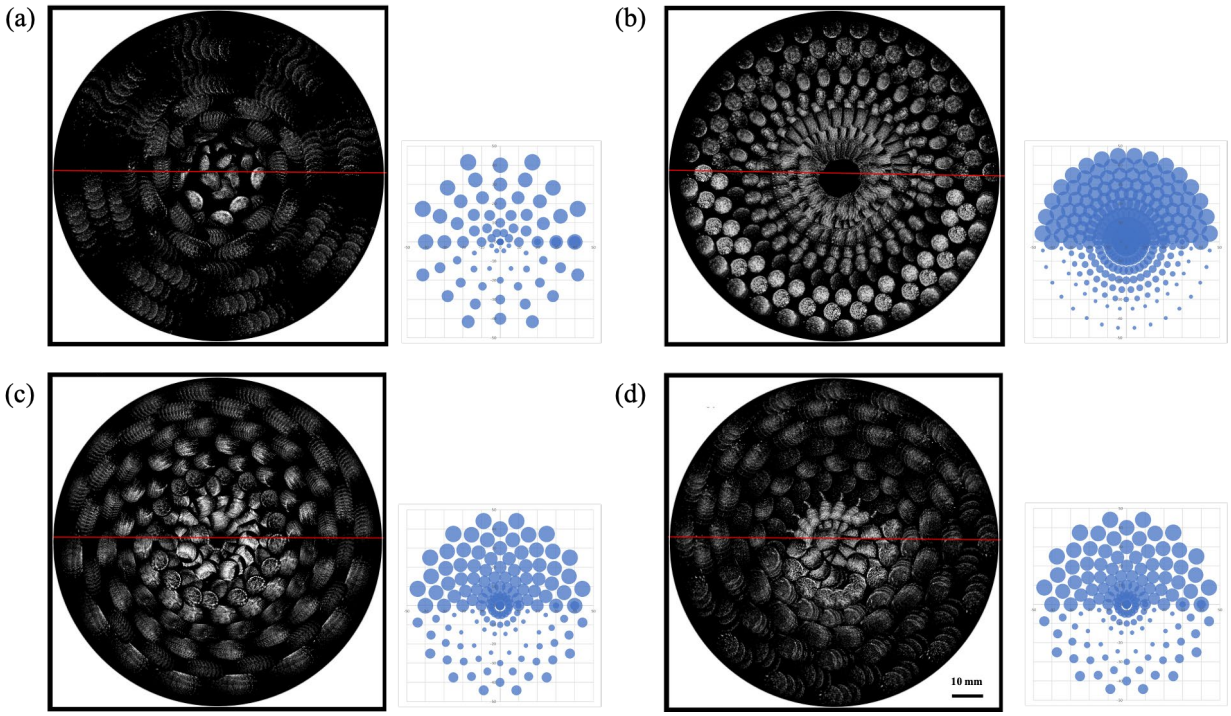

Fig. 7. Superimposed image of brush contact of 10 images on a 100 mm wafer until turning the half rotation and bubble chart for the relative velocity, (a) $\omega_B = 25$ rpm, $\omega_W = 50$ rpm, (b) $\omega_B = 50$ rpm, $\omega_W = 25$ rpm, (c) $\omega_B = 25$ rpm, $\omega_W = 25$ rpm, (d) $\omega_B = 50$ rpm, $\omega_W = 50$ rpm.

On the other hand, the sliding distance per nodule is large in the Rg type observed in the large wafer rotation and the same relative velocity direction, increasing the trajectory range. Furthermore, in the Rg type and deformation in which the nodules make smooth contact, the deformation is gradually pulled up while being relaxed. Therefore, both the start and end points of the nodule contacts have a semicircular shape. Finally, in the Pr type, one nodule is pushed in without sliding like a stamp so that its trajectory becomes circular. The nodule rotates during pushing and a clear path can be observed in the vertical compression type.

From our experience, a high cleaning performance can be generally achieved in the Fg type. Therefore, the Fg type, which compresses and slides simultaneously, plays an important role in cleaning compared with the Pr type, which only pushes vertically, and the Rg type, which has a long sliding distance. We considered that both deformation and sliding of the nodule are effective for mixing cleaning liquids.

3.3. Contact map

Fig. 7 shows the nodule contact path line shown in Fig. 6 at the contact position on a 100 mm wafer simulated by applying different wafer and brush rotations. It shows the nodule path lines of 10 images until turning the half wafer rotation, and the red line shows the starting point of the wafer rotation. The figure also shows the absolute value of the relative velocity between the nodule and the wafer in a bubble chart. The relative velocity is large in the upper half, and a negative relative velocity can be observed in the lower half. There is no relative velocity region in-between these two areas.

Figures 7 (a) and (c) show a comparison of the nodule contact conditions of the same brush rotation and different wafer rotation speeds. Because the rotation speed of the wafer in Fig. 7 (a) is larger than that in Fig. 7 (c), the angle of wafer rotation increases while a nodule collides with the next nodule so that the number of contacts made by the brush nodules decreases. Therefore, the sliding distance of one brush nodule becomes large, although there are many places where the PVA brush does not make contact with the wafer at half rotation. On the other hand, the positions where the relative velocity becomes zero in Fig. 7 (c) are far from the center of the wafer in Fig. 7 (a). The same trend is observed by comparing Figs. 7 (b) and (d). The zero relative velocity positions in Fig. 7 (b), which lower the wafer rotation, are separated from the center.

Next, we compared Figs. 7 (c) and (d), where the brush and wafer rotations are the same. There is no

significant change in the relative speed, and the brush path pattern is similar. However, even if the speed ratio between the wafer rotation and the brush rotation is constant, the relative speed becomes zero positions in the radial direction changes depending on the absolute value of the speed. The position where the Pr type appears at zero relative velocity in Fig. 7 (c) is located on the outer side compared with that in Fig. 7 (d). In Fig. 7 (d), the maximum positive and negative relative velocities are located on the upper and lower semicircles so that the characteristic shapes in Fig. 6 clearly show these positions. Unfortunately, the contact path shape near the wafer center has a short sliding distance, which is similar to the Pr type path shape. Therefore, it is difficult to distinguish the Fg type or Rg type deformation model near the wafer center from the contact path. The original movie should be confirmed.

3.4. Relation to cross-contamination

Kim et al. [17] reported the distribution of residual particles due to cross-contamination on a wafer when the wafer rotation speed and brush gap are changed, that is, the amount of compression of a PVA roller brush. The authors reported the generation of a characteristic recontamination pattern that transfers brush nodule shapes. We compared this result with Fig. 7 and found that the contamination map and the Pr type position show good agreement. As shown in Fig. 5, the Pr type contact is pushed in like a stamp, resulting in twisting at that point [18]. Therefore, this result suggests that the Pr type nodule contact has a strong influence on cross-contamination. We considered that preventing Pr type contact by improving the nodule or brush shape or changing the rotation speed is important.

4. Conclusion

We observed the nodule deformation of rotating PVA brushes and the path of the contact point using high-speed photography. The nodule compresses gradually and immediately expands due to entrainment of the nodule side face during contact. We also showed that the vertically pushed type compression correlates with the location of cross-contamination. In the future, we plan to examine the relationship between nodule deformation and cleaning performance in detail.

References

1. T. Hattori, *ECS Trans.*, **25** (2009) 3.
2. A. A. Busnaina, I. I. Kashkoush, and G. W. Gale, *J. Electrochem. Soc.*, **142** (1995) 2812.
3. W. Kim, T. H. Kim, J. Choi, and H. Y. Kim, *Appl. Phys. Lett.* **94** (2009) 081908.
4. S. Brems, M. Hauptmann, E. Camerotto, A. Pacco, A., T. G. Kim, X. Xu, K. Wostyn, P. Martens and S. De Gendt, *ECS J. Solid State Sci. Technol.*, **3** (2013) N3010.
5. I. Kanno, N. Yokoi, and K. Sato, *ECS Proc.*, **35** (1998) 54.
6. H. F. Okorn-Schmidt, F. Holsteyns, A. Lippert, D. Mui, M. Kawaguchi, C. Lechner, P. E. Frommhold, T. Nowak, F. Reuter, M. B. Piqué, C. Cairós, and R. Mettin, *ECS J. Solid State Sci. Technol.* **3** (2014) N3069.
7. T. Sanada, and M. Watanabe, *J. Photopolym. Sci. Technol*., **28** (2015) 289.
8. A. A. Busnaina, H. Lin, N. Moumen, J. W. Feng, and J. Taylor, *IEEE Trans. Semicond. Manuf.*, **15** (2002) 374.
9. A. Philipossian and L. Mustapha, *J. Electrochem. Soc.*, **151** (2004) G456.
10. K. Xu, R. Vos, G. Vereecke, G. Doumen, W. Fyen, P. W. Mertens, M. M. Heyns, C. Vinckier, and J. Fransaer, *J. Vac. Sci. Technol.*, **22** (2004) 2844.
11. H. Horibe, T. Kamiura, K. Yoshida, *J. Photopolym. Sci. Technol*., **18** (2005) 181.
12. Hattori, T., *ECS J. Solid State Sci. Technol.*, **3** (2013) N3054.
13. T. Kamimura, Y. Umeda, H. Kuramae, K Nuno, R. Nakamura, and H. Horibe, *J. Photopolym. Sci. Technol*., **31** (2018) 413.
14. J. H. Lee, M. Purushothaman, K. M. Han, H. Y. Ryu, N. P. Yerriboina, T. G. Kim, Y. Wada, S. Hamada, H, Hiyama, and J. G. Park, *Polymer Testing*, **77** (2019) 105921.
15. J. H. Lee, M. K. Poddar, K. M. Han, H. Y. Ryu, N. P. Yerriboina, T. G. Kim, Y. Wada, S. Hamada, H, Hiyama, and J. G. Park, *Polymer Testing*, **90** (2020) 106669.
16. K. Xu, R. Vos, G. Vereecke, G. Doumen, W. Fyen, P. W. Mertens, M. M. Heyns, C. Vinckier, J. Fransaer, and F. Kovacs, *J. Vac. Sci. Technol.*, **23** (2005) 2160.
17. H. J. Kim, G. Bohra, H. Yang, S. G. Ahn, L. Qin, and D. Koli, *Microelectron. Eng.*, **136** (2015) 36.
18. T. Miyaki, Y. Mizushima, S. Hamada, R. Koshino, A. Fukunaga, and T. Sanada, *Solid State. Phenom.*, **314** (2021) 253.
19. T. Sanada, M. Hanai, A. Fukunaga, and H. Hiyama, *Solid State. Phenom.*, **282** (2018) 73.

Journal of Photopolymer Science and Technology
Volume 34, Number 5 (2021) 511−515 ©2021SPST

Birefringent Control of Photo-Oriented Polymeric Films by *in situ* Exchange of Functional Moieties

Yunosuke Norisada[1], Mizuho Kondo[1], Tomoyuki Sasaki[2], Moritsugu Sakamoto[2], Hiroshi Ono[2], and Nobuhiro Kawatsuki[1*]

[1] *Department of Applied Chemistry, Graduate School of Engineering, University of Hyogo, 2188 Shosha, Himeji 671-2280 Japan*
[2] *Department of Electrical Engineering, Nagaoka University of Technology, 1603-1 Kamitomioka, Nagaoka 940-2188 Japan*
**kawatuki@eng.u-hyogo.ac.jp*

Thermally stimulated photoinduced molecular reorientation with high dichroism (D>0.6) is explored in liquid crystalline (LC) copolymerthacrylate films comprising of 4-methoxy-*N*-benzylideneaniline (MNBA) and benzoic acid (BA) side groups. Thermal hydrolysis of MNBA side groups induces free phenyl aldehyde (PA) side groups in the oriented film. Birefringence of the oriented films is adjusted by introducing 2,7-diaminofluorene (FL) to form new imine bonds with free PA side groups. Meanwhile, *in situ* exchange from MNBA to FL-based imine also controls the birefringence of the oriented film. The initial birefringence of the oriented copolymer film increases up to 0.22 after introducing oriented FL moieties.

Keywords: Photoalignment, Molecular orientation, Birefringence, Liquid crystalline polymer

1. Introduction

Photoalignment of photosensitive polymeric films is applicable to fabricating optical and display devices [1–8]. Basically, axis-selective photoreaction of the photosensitive moieties generates optical anisotropy and/or molecular reorientation, which attains the birefringence of the film [4–8]. Direct fabrication of a molecularly oriented structure of the polymeric films is achieved using photoalignable liquid crystalline (LC) polymers by means of linearly polarized (LP) light exposure, and in some cases, thermally stimulated self-organization [6– 9].

Photoalignable LC polymers containing cinnamate or azobenzene-containing materials have been explored to realize thermally stimulated photoinduced molecular reorientation based on axis-selective photo-cross-linking or *trans-cis-trans* photoisomerization [6–13]. We have been carried out a systematic study on thermally stimulated photo-induced molecular reorientation of LC (co)polymers with 4-methoxy-*N*-benzylideneaniline (MNBA) side groups [14–16], which undergo axis-selective *trans-cis-trans* photoisomerization likewise the photoinduced reorientation of azobenzene-containing polymeric films.

Because an aromatic imine (C=N) bond is easily formed from aromatic aldehyde and amine derivatives [17,18], position-selective formation of MNBA side groups in a polymethacrylate film with phenyl aldehyde (PA) side groups by coating of 4-methoxyphneyl amine (AN) molecules leads to a photoinduced birefringent pattern [15]. Additionally, thermal hydrolysis of the reoriented MNBA side groups in an LC copolymethacrylate with benzoic acid (BA) and MNBA side groups after the cooperative molecular reorientation converts a photoinactive oriented film with free PA side groups [16,19]. In this case, re-coating the aromatic amine derivatives other than AN molecules by means of sublimation and/or inkjet printing controls the optical and thermal property of the oriented film [16]. To improve the birefringence of the reoriented film *via* this technique, it is acceptable to increase the composition of free PA side groups in the reoriented copolymer film and introduction of

Received March 21, 2021
Accepted April 27, 2021

aromatic amine derivatives with high inherent birefringence.

This paper describes the thermally stimulated photoinduced molecular reorientation of LC copolymethacrylate films comprising of MNBA and BA side groups (Fig. 1). The influence of the copolymer composition on the photoinduced reorientation and thermal hydrolysis of the oriented film is investigated. Birefringence control using 2,7-diaminofluorene (FL) on the hydrolyzed oriented copolymer film and simultaneous amine-exchange technique is explored to reveal an increased birefringence from 0.14 to 0.22.

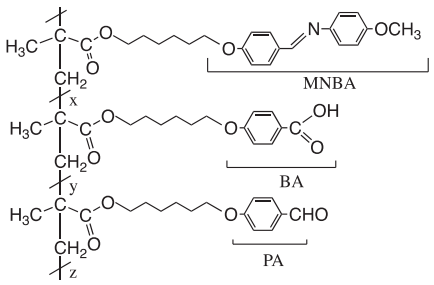

Fig. 1. Chemical structure of LC copolymethacrylates **P1**–**P5** used in this study.

2. Experimental

2.1. Materials

All starting materials were used as received from TCI. FL was recrystallized from ethanol prior to use. Copolymers with BA and BA side groups (Fig. 1, **P1** – **P5**) were synthesized by a free radical polymerization from the corresponding methacrylate monomers using AIBN as an initiator in tetrahydrofuran (THF) [20]. Table 1 summarizes composition, molecular weight, thermal property and spectroscopic data of copolymers.

Table 1. Composition, molecular weight, and thermal property of copolymers.

Copolymer	x[a]	y[a]	z[a]	Molecular weight[b] M_n	M_w/M_n	Thermal property[c]	λ_{max}[d]
P1	21	75	4	26000	2.5	G 70 N 139 I	262
P2	38	59	3	81000	1.6	G 45 N 139 I	266
P3	44	51	5	110000	1.6	G 31 N 126 I	268
P4	56	40	4	19000	2.3	G 47 N 121 I	269
P5	60	37	3	27000	2.5	G 69 N 120 I	276

a) Determined by ^{1}H-nmr. b) Measured by GPC, polystyrene standards. c) Measured by DSC. G: amorphous glass, N: nematic, I: isotropic. d) Absorption maxima of a film on quartz substrate.

2.2. Film preparation and photoirradiation

Copolymer films (thickness; approximately 200 nm) were prepared by spin-coating a THF solution onto quartz substrates.

Photoreactions were carried out using a high-pressure Hg lamp equipped with a glass plate placed at Brewster's angle and a 365-nm bandpass filter (Asahi Spectra REX-250), yielding a light intensity of 30 mW/cm^2 at 365 nm. After photoirradiation, the films were annealed at elevated temperatures to thermally stimulate molecular reorientation under a dry N_2 atmosphere.

2.3. Characterization

^{1}H-NMR spectra using a Bruker DRX-500 FT-NMR and FT-IR spectra (JASCO FTIR-6600) confirmed the copolymers. The molecular weight of the copolymer was measured by GPC (JASCO PU-2080 and RI-2031 GPC system with a Shodex column using THF as the eluent) calibrated using polystyrene standards. The thermal properties were examined using a POM (Olympus BX51) equipped with a Linkam TH600PM heating and cooling stage as well as differential scanning calorimetry (DSC; Seiko-I SSC5200H). As a measure of the photoinduced optical anisotropy, the photoinduced in-plane dichroism (D) was evaluated from the polarization absorption spectra with a Hitachi U-3010 spectrometer equipped with Glan-Taylor polarization prisms. D is estimated as

$$D=(A_\perp-A_\parallel)/(A_\perp+A_\parallel) \qquad (1),$$

where $A_\parallel$ and $A_\perp$ are the absorbances parallel and perpendicular to the polarization (**E**) of LP 365 nm light, respectively. Birefringence of the oriented films was measured by the Senarmont method at 633 nm.

3. Results and discussion

3.1. Synthesis and thermally stimulated photoinduced reorientation of copolymer films

All copolymers were synthesized by a free radical copolymerization from corresponding methacrylate monomers [20]. Upon the reprecipitation process under the humid condition (RH=30–50%), partial hydrolysis of MNBA side groups occurs, resulting in that the copolymers partially include PA side groups (<5 mol%, Table 1). The synthesized copolymers show a nematic LC characteristics, where the isotropic transition temperature (T_i) increases as the content of BA side groups increases. Figure 2a shows absorption spectra of copolymer films, showing that the absorption maximum (λ_{max}) slightly shifts to longer wavelength as decreasing the BA content due to the absorption of MNBA moiety at longer wavelength.

When the copolymer films are exposed to LP 365 nm light, negative photoinduced reorientation

occurs due to the axis-selective photoisomerization of MNBA side groups ($\Delta A = A_{\parallel} - A_{\perp} < 0$), and the subsequent annealing at the LC temperature range of the film under dry N_2 atmosphere amplifies the cooperative molecular reorientation of both mesogenic side groups [16,20]. Figures 2b – f show the change in the polarized absorption spectra of **P1** – **P5** films before and after exposure to LP 365 nm light for 2 – 15 J/cm^2, and subsequent annealing at LC temperature range of the material for 10 min. For all films, the photoinduced negative optical anisotropy is significantly amplified after the annealing, where $D_{\lambda max}$ (D_{335}) is 0.74 – 0.77 (0.68 – 0.75) (Table 2). At present, the amplified D values are larger than those previously reported because the hydrolysis of MNBA groups is restricted since the annealing process is carried out under dry N_2 condition [16,20]. Additionally, Δn of the reoriented film slightly increases when the BA composition decreases while the generated D values are similar to each other. This is due to larger inherent birefringence of MNBA side groups than that of BA.

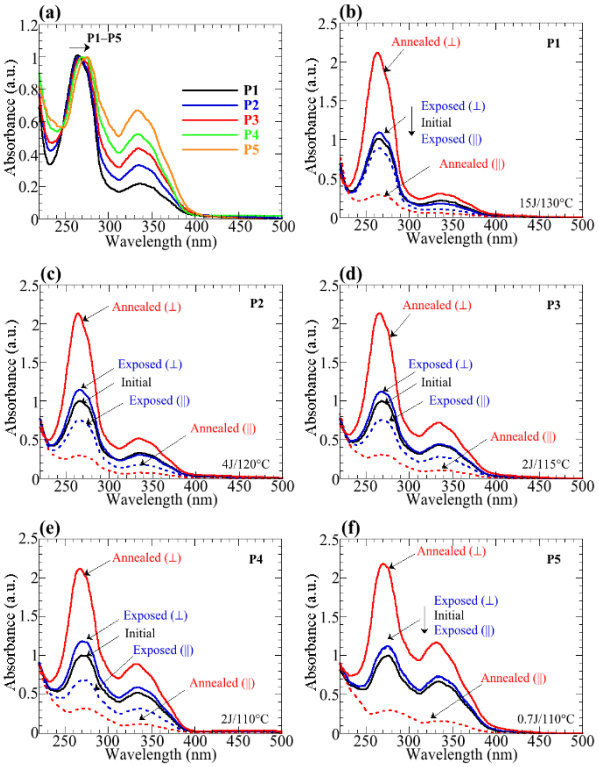

Fig. 2. (a) Absorption spectra of copolymer films on quartz substrate. (b – f) Changes in the polarized absorption spectra of copolymer films before and after exposure to LP 365 nm light and subsequent annealing for 10 min. Copolymer, exposure energy and annealing temperature are shown in each figure.

3.2. Thermal hydrolysis of MNBA side groups of the reoriented films

Table 2. Dichroism (D), birefringence (Δn), and degree of hydrolysis (DH) of the reoriented copolymer films and FL-introduced film.

Co-polymer	Photoinduced D[a]			Hydrolysis[c]		Introduction of FL			
	$D_{\lambda max}$	D_{335}	Δn[b]	DH[d]	$D_{\lambda max}$	FL%[e]	$D_{\lambda max}$	D_{375}	Δn[b]
P1	0.77	0.68	0.14	85	0.69	69	0.72	0.74	0.18
P2	0.75	0.74	0.15	63	0.69	70	0.68	0.73	0.19
P3	0.74	0.74	0.15	58	0.63	60	0.67	0.70	0.20
P4	0.74	0.75	0.15	-	-	85	0.60	0.69	0.22
P5	0.75	0.75	0.16	-	-	90	0.60	0.64	0.22

a) D values of oriented films in Fig. 2. b) At 633 nm. c) Thermal hydrolysis. d) Degree of hydrolysis (%). e) FL introduction to calculated free PA side groups.

We have previously reported that the oriented MNBA moieties are hydrolyzed to form free PA side groups with maintaining the oriented structure of the film, when the reoriented film is annealed under humid condition [16]. Figures 3a – c show change in the polarized absorption spectra of oriented **P1** – **P3** films before and after annealing under air (RH = 35%) at 125 °C for 80 min for **P1**, at 100 °C for 180 min for **P2**, and at 90 °C for 540 min for **P3**, respectively. After the annealing, absorption band of MNBA decreases [degree of hydrolysis (DH) = 85% (**P1**), 63% (**P2**), and 58% (**P3**)], while the orientational order almost unchanges ($D_{\lambda max}$ = 0.69, 0.69, and 0.63) (Tab. 2). In contrast, orientational structure of the **P4** film is collapsed when the film is annealed for 30 min at 100 °C (DH = 65%), but 10 min-annealing (DH = 26%) keeps the orientational structure (D_{269} = 0.70, Fig. 3d). For **P4**, LC characteristics of the oriented film diminishes when the DH increases due to higher content of MNBA side groups, resulting in the random orientation of

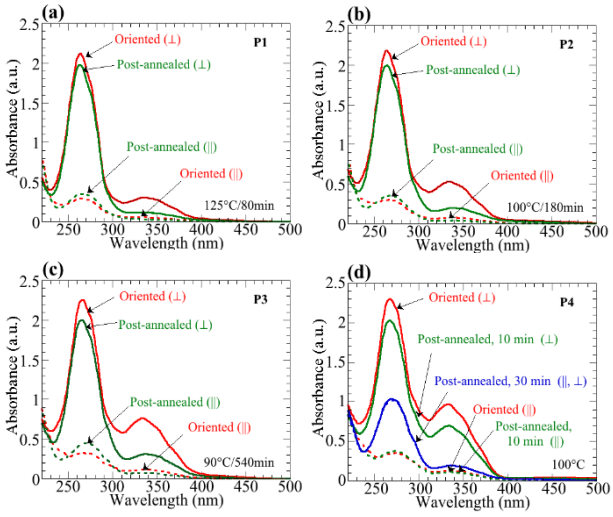

Fig. 3. (a) Changes in the polarized absorption spectra of oriented copolymer films before and after post-annealing at elevated temperature under humid air (RH =35%). (a) **P1**, (b) **P2**, (c) **P3** and (d) **P4**. Post-annealing condition is shown in each figure.

the film at elevated temperature.

When the hydrolysis of MNBA side groups proceeds, transition temperature to the isotropic state (T_i) of the film decreases. Additionally, LC characteristics of the hydrolyzed film will disappear when the composition of PA side groups is larger than 50%, which is expected by evaluating the thermal property of copolymethacrylate with BA and PA side groups (Fig. 4). Therefore, the hydrolyzed oriented **P4** film could hold the LC state at 100 °C when DH is 26%, but further hydrolysis no longer shows LC characteristics of the film at 100 °C, resulting in the random orientation. Namely, thermal hydrolysis to form free PA moieties should be carried out with maintaining the LC characteristics to hold the orientational structure of the film.

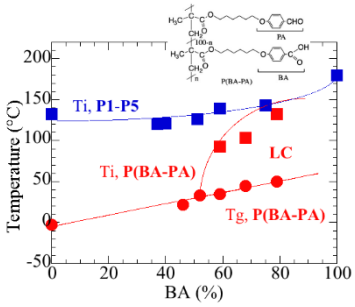

Fig. 4. Glass transition temperature (Tg), and isotropic transition temperature (Ti) of copolymethacrylate with BA and PA side groups and Ti of LC copolymers (**P1** – **P5**) as a function of BA composition.

3.3. Introduction of FL molecules into the oriented films

When the oriented film includes free PA side groups, introducing the different phenyl amine derivatives to form a new imine (C=N) bonds changes the optical and thermal properties of the film [16]. For **P1**, **P2** and **P3**, *in situ* condensation of FL molecules with free PA side groups in the hydrolyzed oriented film is achieved. Figure 5a (b) shows change in the polarized absorption spectra of a hydrolyzed oriented **P1** (**P2**) film [DH = 85% (63%)] before and after introducing FL molecules, where the film is coated using a methanol solution of FL molecules and annealed at 120 °C (100 °C) followed by rinsing with methanol and diethyl ether. New absorption at 375 nm (D_{375}=0.74, D_{266}=0.72 for **P1**, D_{375}=0.73, D_{266}=0.68 for **P2**) appears, which is assigned FL molecules with C=N formation. Similar introducing of oriented FL molecules to form C=N bonds is observed for a **P3** film (Fig. 5c).

In contrast, simultaneous exchange of AN to FL is attained for the oriented **P4** and **P5** films since the

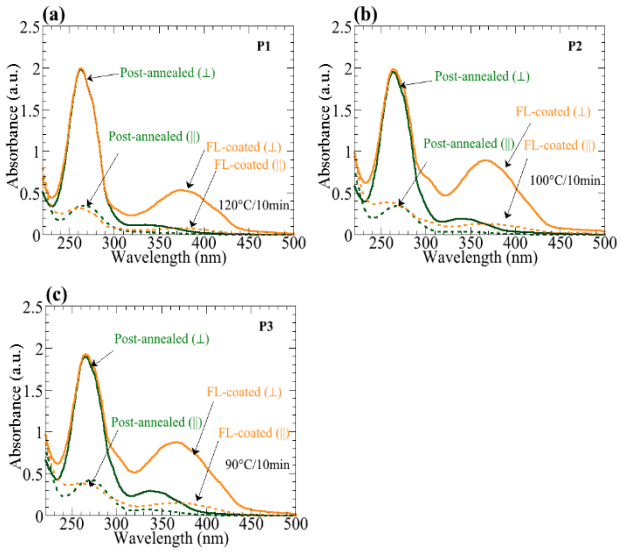

Fig. 5. Changes in the polarized absorption spectra of hydrolyzed oriented copolymer films before and after coating FL molecules followed by annealing at elevated temperature under N_2 atmosphere. (a) **P1**, (b) **P2**, and (c) **P3**. Annealing condition is shown in each figure.

hydrolyzed oriented **P4** and **P5** films cannot be obtained. Because AN is sublimed at 100 –110 °C upon the thermal hydrolysis and FL molecules do not sublime at this temperature, condensation between free PA side groups and FL molecules will simultaneously occur. Figure 6a shows change in the polarized absorption spectra of an oriented **P4** film before FL-coating and after annealing the FL-coated film at 110 °C for 60 min under N_2 atmosphere. In this case, FL molecules are coated from ethylene glycol solution and the excess FL molecules are eliminated by rinsing using diethyl ether and methanol after the annealing. Similar to the introduction of FL molecules into hydrolyzed **P1** – **P3** films, absorption band at 375 nm (D_{375}=0.69, D_{269}=0.60) appears, indicating the simultaneous hydrolysis of MNBA and formation of a new C=N bond of FL molecules. Similar spectral change is observed for a **P5** film (Fig. 6b).

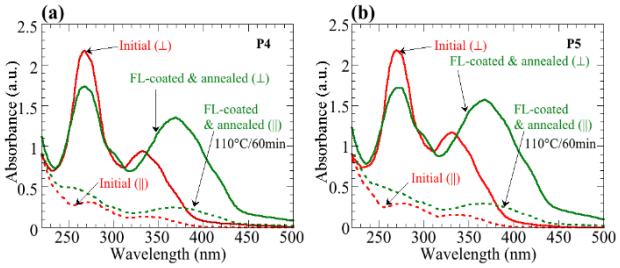

Fig. 6. Changes in the polarized absorption spectra of oriented copolymer films before and after *in situ* exchanging from MNBA to FL-based Schiff-base. (a) **P4**, and (b) **P5**. Annealing condition is shown in each figure.

The introduction of FL molecules into the oriented film leads improvement of birefringence and thermal stability of the film due to the cross-linked structure. Table 2 summarizes changes in D values and birefringence of **P1** – **P5** films before and after introducing FL molecules. The introduction of FL moieties is 70 – 95% as compared to the hydrolyzed PA groups, and D_{375} is 0.60 – 0.72, while the birefringence increases up to 0.22 as increasing the FL moieties in the oriented film. Additionally, thermal stability increases approximately up to 170 °C for all the films, at which the collapse of the hydrogen bonds of dimerized BA side groups occur (Fig. 7). However, the orientation structure is partially stable above this temperature when the composition of BA side groups decreases due to the higher density of crosslinking.

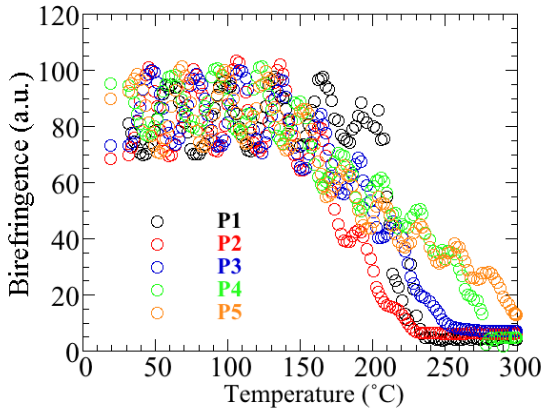

Fig. 7. Thermal stability test (birefringence) of FL-introduced oriented copolymer films in Figs. 5 and 6 when the film is annealed at elevated temperature.

4. Conclusion

Thermally stimulated photoinduced molecular reorientation of LC copolymethacrylate with MNBA and BA side groups is investigated. Cooperative molecular orientation with high dichroism (D>0.6) is achieved for all copolymer films. Thermal hydrolysis of MNBA side groups attains the oriented copolymer film with free PA side groups when the MNBA composition is below 44 %, while the orientational structure is collapsed for the copolymer with higher MNBA composition. Introduction of FL molecules to form a new imine bonds in the oriented hydrolyzed film improves the birefringence and thermal stability of the film. The *in situ* exchange of the imine side groups from MNBA to FL-introduced side groups for the copolymer with higher MNBA composition attains the birefringence of the oriented film up to 0.22.

Acknowledgement

This work was partially supported by Grants-in-Aid for Scientific Research from JSPS (B18H02039 and S16H06355).

References

1. V. G. Chigrinov, V. M. Kozenkov, and H.-S. Kwok, "*Photoalignment of Liquid Crystalline Materials*", John Wiley & Sons, West Sussex, England, 2008.
2. O. Yaroshchuk and Y. Reznikov, *J. Mater. Chem.* **22**, (2012) 286.
3. T. Seki, *Polym J.* **46**, 2014 751.
4. K. Ichimura, *Chem. Rev.* **100** (2000) 1847.
5. A. Natansohn and P. Rochon, *Chem. Rev.* **102** (2002) 4139.
6. N. Kawatsuki and H. Ono, "*Organic Electronics and Photonics*", Vol. 2, H. S. Nalwa Ed. American Sci. Publishers, Stevenson Ranch, CA, 2008, p. 301.
7. N. Kawatsuki, *Chem. Lett.* **40** (2011) 548.
8. N. Kawatsuki, K. Goto, T. Kawakami, and T. Yamamoto, *Macromolecules* **35** (2002) 706.
9. Y. Wu, Y. Demachi, O. Tsutsumi, A. Kanazawa, T. Shiono, and T. Ikeda, *Macromolecules* **31** (1998) 1104.
10. A. Shishido, *Polym. J.* **42** (2010) 525.
11. X. Wang, "*Photoinduced Orientation and Anisotropy. Azo Polymers*", Springer-Verlag, Berlin, Heidelberg, 2017 p. 117.
12. T. Ikeda, *J. Mater. Chem*. **13** (2003) 2037.
13. M. Han and K. Ichimura, *Macromolecules* **345** (2001) 90.
14. N. Kawatsuki, H. Matsushita, M. Kondo, T. Sasaki, and H. Ono, *APL Materials* **1** (2013) 022103.
15. N. Kawatsuki, K. Miyake, and M. Kondo, *ACS Macro Lett.* **4** (2015) 764.
16. A. Ito, Y. Norisada, S. Inada, M. Kondo, T. Sasaki, M. Sakamoto, H. Ono, and N. Kawatsuki, *Langmuir* **37** (2021) 1164.
17. J. J. Charette and E. Hoffmann, *J. Org. Chem.* **44** (1979) 2256.
18. R. L. Reeves, *J. Org. Chem.* **30** (1965) 3129.
19. N. Kawatsuki, K. Miyake, and M. Kondo, *Mol. Cryst. Liq. Cryst.* **617** (2015) 14.
20. N. Kawatsuki, S. Inada, R. Fujii, and M. Kondo, *Langmuir* **34** (2018) 2089.

Journal of Photopolymer Science and Technology
Volume 34, Number 5 (2021) 517−524 ©2021SPST

Siloxane Oligomer with Random Structure for Use in Photosensitive White Decorative Coatings

Mitsuhito Suwa*, Toru Okazawa, and Hideyuki Kobayashi

Electronic and Imaging Materials Research Laboratories, Toray Industries, Inc., Sonoyama 3-chome, Otsu, Shiga 520-0842, Japan
**mitsuhito.suwa.e3@mail.toray*

A siloxane oligomer (Si-OLIGO-1) was produced by introduction of a bifunctional alkoxysilane into a silsesquioxane composed of a trifunctional alkoxysilane. The oligomer, which can form a thick film, was synthesized by a sol–gel method. This organic/inorganic hybrid material had good transparency and heat resistance. Infrared absorption spectroscopic analysis indicated that Si-OLIGO-1 had a random structure with many acidic silanol groups capable of alkaline development. A novel negative photosensitive white decorative coating that consisted of Si-OLIGO-1 as the base resin and 40 wt% TiO_2 (particle size 250 nm) as a white pigment was produced. The coating enabled facile complex decoration. A white cured film of thickness 10 μm had the brightness (L^*) and color (a^*, b^*) required for the white frame of a display product. Although the coating did not transmit straight light of wavelength 300–700 nm, it gave a good patterning performance (resolution and pattern shape) on irradiation with ultraviolet light at a dose of 200–250 mJ/cm^2. This is because it transmitted both g-line and h-line scattered light.
Keywords: Photosensitive, white decorative, TiO_2, siloxane oligomer, random

1. Introduction

In recent years, many optical materials have been developed for use in devices such as smartphones, tablets, and touch screens. Black or white decorative materials, which contain carbon black or TiO_2, respectively, are applied to glass covers to conceal the wiring pattern on the substrate and for decoration [1–6]. Figure 1 shows an example of white decoration on a smartphone.

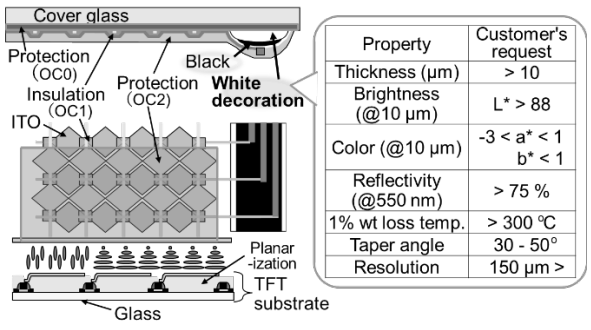

Fig. 1. Example of touch panel with integrated cover glass.

Received March 3, 2021
Accepted April 30, 2021

It is generally difficult to endow such decorative materials with photosensitivity because the pigment absorbs not only visible light but also the ultraviolet (UV) light required for photosensitivity. Non-photosensitive materials are usually used for decoration and these cannot form fine patterns for screen-printed complex decoration [1–4]. Photosensitive coatings (PS-coatings) with sufficient heat resistance for post-process curing at 230 °C are therefore needed. This led to the development of black decorative coatings with larger amounts of black pigment [7–9] in a negative photosensitive black matrix for color filters [5, 6]. However, organic resins with photopolymerizable groups such as methacrylic/acrylic groups, which are used as negative photosensitive base resins for decoration, cannot be used in white decorative coatings because they turn yellow as a result of oxidative deterioration during heat treatment. Furthermore, black decorative materials develop color by absorption, but white decorative materials develop color by using light reflection, therefore films of

thickness greater than 10 μm are required. This increases the need for base resins with heat resistance.

We focused on the heat-resistant materials silsesquioxanes (SQs), which have organic groups that can be used to modify the properties of siloxane materials. These are organic/inorganic hybrid materials with siloxane bonds (–Si–O–Si–) [10–16]. If this siloxane material is used as a base resin, it is unlikely to suffer oxidative deterioration, therefore it can suppress coloring of white decorative materials during heat treatment. As shown in Fig. 2, SQs consist of trifunctional alkoxysilanes and can have highly regular cage and ladder structures, and random structures [11, 16–20].

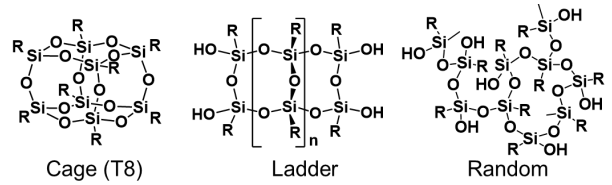

Fig. 2. Higher-order structures of three types of SQ.

The highly regular cage and ladder structures contain few silanol groups, whereas the random structure contains many silanol groups [21–27]. SQ oligomers with phenyl and acrylic organic groups have been synthesized by sol–gel methods [28, 29]. Negative photosensitive siloxane coatings have been developed by forming a thin cured film of thickness 2 μm with oligomers like Si-OLIGO-0, which will be described later, as the base resin. Such coatings are used as insulating materials because the cured product obtained by heat treatment at 230 °C shows colorless transparency and heat/chemical resistance. We attempted to use the SQ oligomer of Si-OLIGO-0 as a base resin for white decorative coatings. However, because the oligomer consists of trifunctional alkoxysilanes, cracks occur when a cured film of thickness greater than 2-5 μm depending on the added amount of TiO_2 is formed as a result of the increased stress associated with a high crosslinking density. Use of this oligomer in practical applications is therefore difficult. The crosslinking density could be decreased by using a siloxane oligomer with a random structure, which could be obtained by introduction of a bifunctional alkoxysilane. This oligomer has decreased stress, which prevents crack formation. It also contains a large amount of silanol groups (pK_a = 9.5) [30], which are as acidic as phenolic hydroxyl groups (pK_a = 10) [31]. This oligomer can therefore be easily dissolved in a 2.38 wt% tetramethylammonium hydroxide (TMAH) aqueous solution as a resist developer, regardless of the film thickness.

We therefore decided to work on imparting negative photosensitivity by using a novel siloxane oligomer with a random structure as the resin material, to give a cured product with colorless transparency, heat resistance, and chemical resistance, and TiO_2 of average particle size 250 nm, which is generally used as a white pigment.

The purpose of this study was to create a new negative photosensitive white decorative siloxane coating that gives white cured films with appropriate brightness (L^*), color (a^*, b^*), reflectance, heat resistance, and chemical resistance. Despite UV absorption by the TiO_2 pigment, the coatings give excellent patterning performances, i.e., good resolution and shape on a film of thickness about 10 μm.

2. Experimental

2.1. Materials

Commercially available raw materials were used without purification. The raw materials for the siloxane oligomer preparation solutions were phenyltrimethoxysilane (KBM-103), 3-(methacryloyloxy)propyltrimethoxysilane (KBM-503), dimethoxydimethylsilane (KBM-22), [3-(trimethoxysilyl)propyl]succinic anhydride (X-12-967C) (Shin-Etsu Chemical Co., Ltd.), phosphoric acid (Tokyo Chemical Industry Co., Ltd.), and propylene glycol monomethyl ether acetate (PGMEA, Kuraray Co., Ltd.) The acrylic polymer, which was a partial adduct of glycidyl methacrylate and a copolymer of methacrylic acid, styrene, and dicyclopentanyl methacrylate, was prepared from a PGMEA solution of SPCR-24X [weight-average molecular weight (M_w): 14000, solid content = 40 wt%, Showa Denko K.K.]. Epoxide-modified isocyanurate diacrylate (ARONIX M-315, Toagosei Co., Ltd.) was used as the acrylic monomer. Bis(2,4,6-trimethylbenzoyl)phenylphosphine oxide (Omnirad 819, IGM Resins B.V.) was used as a photoinitiator. The white pigment was a TiO_2 dispersion (S-5052, solid content = 65.3 wt%, Dainichiseika Kogyo Co., Ltd.) It consisted of CR-97 (TiO_2 of average particle size 250 nm, Ishihara Sangyo Kaisha, Ltd.) dispersed in the manufacturer's undisclosed dispersant in PGMEA at 5.1 wt% (relative to TiO_2). A resist stripper, i.e., N-300 [a mixture of monoethanolamine (MEA)

and diethylene glycol monobutyl ether (DGBE), MEA/DGBE = 30/70 weight ratio, Nagase ChemteX Co.] and an indium tin oxide (ITO) etchant, i.e., oxalic acid solution (0.05 mol/L, FUJIFILM Wako Pure Chemical, Co.) were used for chemical resistance.

Two types of siloxane oligomer solution were prepared by the following general procedure. KBM-103 (0.45 mol), KBM-503 (0.3 mol), X-12-967C (0.05 mol), KBM-22 (0.20 mol) as a bifunctional alkoxysilane, and PGMEA (149 g, 75 wt% with respect to charged alkoxysilanes) were placed in a 500 mL three-necked flask. An aqueous solution, which was prepared by dissolving a phosphoric acid catalyst (0.3 wt% with respect to the charged alkoxysilanes in the flask) in water (2.85 mol), was added over 30 min under stirring at room temperature. The flask was immersed in an oil bath at 40 °C and the solution was stirred for 60 min. The temperature of the oil bath was raised to 70 °C and the solution was stirred for 60 min. The temperature of the oil bath was then set at 110 °C. The internal temperature of the flask reached 100 °C after 45 min, and the solution was then stirred for approximately 1.5 h (the internal temperature was 100–110 °C). This step was performed to adjust the dissolution rate of the siloxane oligomer in a 2.38 wt% TMAH aqueous solution (ELM-D, Mitsubishi Gas Chemical Company, Inc.) of the alkaline resist developer. During this period, the methanol and water by-products were removed by distillation. The catalyst was removed by adding 3 wt% Amberlyst A21 (Organo Co.), which is an anion-exchange resin, to the obtained solution and stirring the mixture for 12 h at room temperature. The ion-exchange resin was removed by wire-mesh filtration (100 mesh). The obtained siloxane oligomer solution (approximately 1 g) was transferred to an aluminum cup. The cup was placed on a hot plate at 120 °C, and heated to 250 °C in air for 30 min. The aluminum cup was then allowed to cool and the concentration of the solution was calculated by assuming that the dehydration condensation reaction was complete and gave a fully cured siloxane (FS). PGMEA was added to give a solution of concentration 50 wt%; this solution was labeled Si-OLIGO-1. For comparison with Si-OLIGO-1, a solution of the SQ oligomer, labeled Si-OLIGO-0, which was developed for negative photosensitive transparent insulation, was prepared by the same method as was used for Si-OLIGO-1 preparation, but KBM-103, KBM-503, and X-12-967C (1 mol total) at molar ratios of 65:30:5 were used. A 50 wt% Si-OLIGO-0 solution was obtained under the same conditions as those described above, but with PGMEA (161 g; 75 wt% with respect to charged alkoxysilanes) and water (3.05 mol).

Transparent PS-coatings were prepared by adding ARONIX M-315, Omnirad 819, and PGMEA to resin solutions of the prepared Si-OLIGO-1, or SPCR-24X. Furthermore, white PS-coatings were prepared by adding S-5052 to the transparent PS-coatings; details are shown in Table 1. The coatings were stirred by shaking under yellow light with a rotary shaker to obtain a uniform solution. The solution was filtered through a 0.45 μm polypropylene syringe filter to give the PS-coatings. Solutions of Si-OLIGO-1 and Si-OLIGO-0 were also filtered under the same conditions for characterization of the siloxane oligomers.

2.2. Preparation of prebaked film, cured film, heat-treated film, and sample for evaluating patterning properties

The PS-coatings were spin-coated on a non-alkaline glass substrate (OA-10G, Nippon Electric Glass Co., Ltd.), ITO, and Cr substrates

Table 1. Compositions of transparent PS-coatings (a) and (b), and white PS-coatings (c)–(f).

PS-coatings	Composition (weight ratio)						
	Siloxane oligomer	Acrylic polymer	White pigment	Additives	Monomer	Photo-initiator	Solvent
	Si-OLIGO-1	SPCR-24X	S-5052 (TiO_2: 250 nm)	Dispersant	M-315	Omnirad 819	PGMEA
(a)	40[a]	-	-	-	18	2	60
(b)	-	40[a]	-	-	18	2	60
(c)	40[a]	-	20[a]	1	18	2	80
(d)	-	40[a]	20[a]	1	18	2	80
(e)	40[a]	-	40[a]	2	18	2	100
(f)	-	40[a]	40[a]	2	18	2	100

[a] Converted solid content to 100 wt%

(GEOMATEC Co., Ltd.) with a spin coater (1H-360S, Mikasa Co., Ltd.) to obtain a post-curing thickness of 10 μm. The spin-coated substrates were dried at 100 Pa for 60 s in a vacuum dryer (Micro Engineering Inc.), and then baked at 100 °C for 180 s on a hot plate (HPD-3000BZN, AZ One Co.) to prepare prebaked films of thickness 11.7 μm. After baking, the film thickness was determined by scanning electron microscopy (SEM; S-4800, Hitachi High-Tech Co.) These prebaked substrates were exposed at 300 mJ/cm^2 (calculated from the i-line value) without a mask on three substrates, or at 100–300 mJ/cm^2 through a mask with a gap of 50 mm on glass substrates by using an exposure tool (g-, h-, and i-lines, PLA-501F, Canon Inc.) with a high-pressure mercury lamp as a light source. The mask had a one-line and one-space pattern in the range 10–200 μm. The exposed substrates were showered with 2.38 wt% TMAH aqueous solution for 30 s (shower development) by using automatic developing equipment (AD-2000, Takizawa Sangyo Co., Ltd.) The substrates were then rinsed with water for 30 s and air dried. The air-dried substrates were post-baked (cured) in an oven (DN43HI, Yamato scientific Co., Ltd.) at 230 °C for 30 min in air. Some of the cured glass substrates were heat treated by post-baking in an oven under the above conditions but at 250 °C for 30 min. The film thicknesses were determined from SEM images. The cured films and samples for patterning property evaluation were prepared from cured substrates, which were obtained from the exposed substrates without or with masks. The filtered solutions of Si-OLOGO-1 and Si-OLIGO-0 were spin-coated on 6-inch silicon wafers under the above conditions to prepare prebaked films of thickness 11.7 μm.

2.3. Evaluation

2.3.1. Gel-permeation chromatography (GPC) and infrared (IR) spectroscopy

The siloxane oligomer solution was diluted with tetrahydrofuran (THF) to give an FS concentration of 0.1 wt%, on the assumption that the hydrolysis/dehydration condensation reaction was complete. The M_w and molecular-weight distribution were determined by GPC with polystyrene as the standard. GPC was performed at 30 °C and a flow rate of 1.0 mL/min, with THF as the developing solvent; a chromatographic system (e2695, Waters Co.) equipped with a refractometer detector and two columns (TSKgel G4000HXL, TSKgel G1000HXL, Tosoh Co., Ltd.) was used. The IR spectra of the prebaked films of Si-OLIGO-1 or Si-OLIGO-0 on silicon wafers were recorded in transmission mode (FT-720, HORIBA, Ltd.) A silicon wafer was used as a blank. The spectra were used to characterize the siloxane oligomers.

2.3.2. Transparencies of prebaked and cured films

The straight (8°) and scattered transmittances of the prebaked film (11.7 μm) and straight (8°) transmittance of a cured film (thickness 10 μm) on a glass substrate were determined by UV spectroscopy (UV-4100, Hitachi High-Tech Co.).

2.3.3. *L**, *a**, *b**, and reflectivity

The brightness (*L**), color (*a**, *b**), and reflectivity of the cured film (thickness 10 μm) on a glass substrate were determined in specular component inclusion mode by using a split color meter (CM-2600d, Konica Minolta, Inc.); *a** is the redness and *b** denotes the yellow tint.

2.3.4. Heat resistance

The 1%, 3%, and 5% weight-loss temperatures of the cured film (thickness 10 μm) on a glass substrate were determined by using a thermogravimetric analyzer (TGA-50, SHIMADZU Co.)

2.3.5. Chemical resistance

The chemical resistances of the cured film (thickness 10 μm) of PS-coating (e) on glass, ITO, and Cr substrates were determined by immersion in chemicals under various conditions (2.38 wt% TMAH aqueous solution at 23 °C for 3 min; N-300 at 45 °C for 3 min; oxalic acid solution 35 °C for 3 min). Changes in the film state were evaluated visually.

2.3.6. Thickness, pattern profile, taper angle, and resolution

The prebaked and cured film thicknesses on their respective substrates were determined from SEM images. The cured pattern profiles and resolutions on glass substrates were observed by SEM. The taper angles and resolutions were determined from SEM images. The pattern resolution was defined as the smallest cured pattern size at which the pattern could be developed without a leaving a residue at each exposure.

3. Results and discussion

3.1. Structure of synthesized Si-OLIGO-1

Si-OLIGO-0 was synthesized by using a trifunctional alkoxysilane [organic groups: phenyl (Ph), methacryloylpropyl (Mac), and succinic acid propyl (Suc)]; it provides film insulation. Si-OLIGO-1, which can form 10 μm thick films suitable for white decorative coatings, was designed and synthesized by introducing a bifunctional alkoxysilane (organic group: dimethyl, Dime) into Si-OLIGO-0. The effects of bifunctional alkoxysilane introduction were examined by comparing them. The structural formulas are shown in Fig. 3.

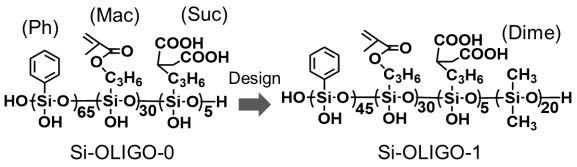

Fig. 3. Structural formulas of synthesized siloxane materials.

GPC was used to determine the M_ws and polydispersity indexes (M_w/M_n; M_n = number-average molecular weight) of Si-OLIGO-0 and Si-OLIGO-1. The organic group ratios (mol%) of the charged alkoxysilanes and GPC results are shown in Table 2.

Table 2. Organic group ratios, M_w, and M_w/M_n of siloxane materials.

Siloxane oligomer	Organic group ratio (mol%)				M_w	M_w/M_n
	(Ph)	(Mac)	(Suc)	(Dime)		
Si-OLIGO-0	65	30	5	-	3000	1.7
Si-OLIGO-1	45	30	5	20	2820	1.7

The results show that Si-OLIGO-0 and Si-OLIGO-1 had M_ws of 3000 and 2820, respectively. This confirms that they are siloxane oligomers.

IR spectroscopy was used to confirm the structures having synthesized siloxane oligomers. IR spectra of prebaked films prepared from these solutions were recorded. First, we investigated the presence of absorption peaks near 900 cm^{-1} [22, 32], which are attributed to Si–OH stretching. As shown in Fig. 4, signals near 900 cm^{-1} were observed in the spectra of Si-OLIGO-0 (906 cm^{-1}) and Si-OLIGO-1 (902 cm^{-1}).

However, it has been reported that almost no Si–OH groups are present in SQs with highly regular cages and ladders [22, 23, 25–27]. The IR spectra therefore indicate that both of these siloxane oligomers have a random structure. Also, the Si–OH signal in the Si-OLIGO-1 spectrum is similar to that in the Si-OLIGO-0 spectrum despite reducing trifunctional groups due to the introduction of bifunctional Dime groups.

Next, we investigated the absorption peaks near 1100 cm^{-1}, which correspond to Si–O–Si stretching [10, 22–27, 32–37]. The Si-OLIGO-0 spectrum has a strong, broad absorption peak at 1134 cm^{-1}, which corresponds to asymmetric ring stretching of Si–O. The Si-OLIGO-1 spectrum shows two strong signals, at 1134 and 1094 cm^{-1}. It has been reported that for trifunctional SQs with highly regular structures, the cage structure gives one sharp peak near 1100 cm^{-1} [25, 26], and the ladder structure gives two strong absorptions, at 1150 and 1050 cm^{-1}, which correspond to asymmetric ring stretching and symmetric ring stretching, respectively [10, 22, 24, 27, 34–36]. The absorption peaks in the spectrum of the synthesized Si-OLIGO-0 differ significantly from those in the spectra of compounds with cage and ladder structures. This strongly suggests a random structure [23, 32, 33, 35, 37]. Si-OLIGO-1 has two strong absorption peaks separated by only 40 cm^{-1}, which is significantly different from the separation in the case of the ladder structure (100 cm^{-1}). This strongly suggests that this is also a random structure. It is assumed that the absorption peaks of the synthesized siloxane oligomers differ because the randomness of the Si-OLIGO-1 structure is greater. This is because the degree of crosslinking in Si-OLIGO-1 is lower than that in Si-OLIGO-0 because of the introduction of bifunctional Dime groups. This spectroscopic analysis of Si–OH and Si–O–Si groups shows that the synthesized Si-OLIGO-1 and Si-OLIGO-0 both have random structures.

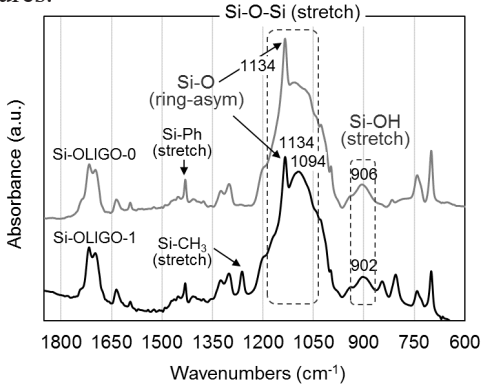

Fig. 4. IR spectra of prebaked films with Si-OLIGO-0 (gray line) and Si-OLIGO-1 (dark line).

3.2. White decorative coating applications

3.2.1. Properties of base resin

The suitability of the synthesized Si-OLIGO-1 as a base resin for white decoration was investigated by comparing its performance with that of an acrylic polymer (SPCR-24X), which is expected to turn yellow because of oxidative degradation.

First, the transparency and heat resistance (determined from the 1% weight-loss temperature) were determined for 10 μm thick cured films of PS-coatings (a) and (b), which contain no white pigment (Table 1).

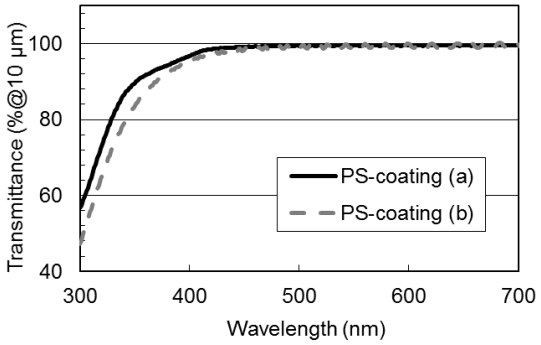

Fig. 5. Comparison of base resins from transmittances of cured films.

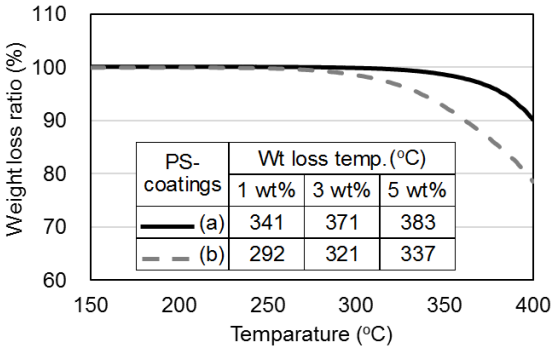

Fig. 6. Comparison of base resin heat resistances from weight-loss temperatures of cured films.

The results show that both PS-coatings have the same good transparency (Fig. 5). The 1% weight-loss temperature of the PS-coating (a) is higher than that of the PS-coating (b) (Si-OLIGO-1, 341 °C; SPCR-24X, 292 °C). This shows that Si-OLIGO-1 has good heat resistance, as expected (Fig. 6). These results show that Si-OLIGO-1 is a suitable base resin for white decoration because the siloxane main chain is less susceptible to oxidative degradation.

3.2.2. White cured film characteristics

The abilities of the coatings to impart good white properties were investigated by determining the brightness (L^*), color (a^*, b^*), and reflectivity–wavelength dependences of films cured at 230 °C for 30 min with 10 μm-thick PS-coatings (c)–(f), which contain a white pigment. The results (Table 3) show that to satisfy the customer's requirements ($L^* > 88$; $-3 < a^* < 1$, $b^* < 1$; reflectivity > 75%; Fig. 1), over 40 wt% of 250 nm TiO_2 pigment is needed, e.g., PS-coatings (e) and (f).

Table 3. Effects of TiO_2 content and base resin on white cured film characteristics.

Thickness (10 μm)	PS-coatings			
	(c)	(d)	(e)	(f)
L*	83.9	84.4	89.3	89.9
a*	-2.07	-2.26	-2.23	-2.46
b*	-2.38	-1.32	-0.96	1.57
Reflectivity (%) @550 nm	63.9	62.8	75.8	75.3

The b^* values of PS-coatings (c) and (e) were smaller than those of PS-coatings (d) and (f) (−2.38, −0.96 and −1.32, 1.57, respectively). The results show that the susceptibility of base resin Si-OLIGO-1 to oxidative degradation during curing at 230 °C is lower than that of the acrylic polymer SPCR-24X. The reflectivity–wavelength dependence (Fig. 7) shows that when 40 wt% of the TiO_2 pigment was introduced, the reflectivity was over 75% in the visible-light region.

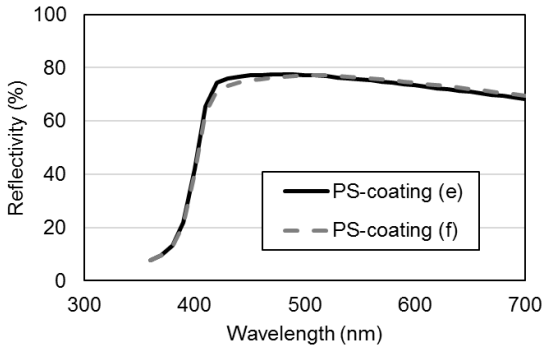

Fig. 7. Dependence of PS-coating (e) and (f) reflectivity on wavelength.

Next, the effect of heat treatment of PS-coatings (e) and (f) on the white film characteristics were investigated. A cured film was prepared by heating at 230 °C for 30 min and then heating at 250 °C for 30 min. The L^*, a^*, and b^* values of the cured film and the film that was further heated were determined. The results (Table 4) show that the PS-coating (e) has good white film characteristics

because of the smaller change in *b**, which denotes yellowness, compared with that for the PS-coating (f) (1.7 and 3.62, respectively). It is presumed that this is also because the siloxane main chain is less susceptible to oxidative degradation.

Table 4. Comparison of white film characteristics after heat treatment.

Thickness (10 μm)	PS-coating (e)		PS- coating (f)	
	no treat.	250℃ /30 min (Δ)	no treat.	250℃ /30 min (Δ)
L*	89.3	89 (-0.3)	89.9	89.1 (-0.8)
a*	-2.23	-2.52 (-0.29)	-2.46	-2.48 (-0.02)
b*	-0.96	0.74 (1.7)	1.57	5.19 (3.62)

Δ = treatment change value

The chemical resistance of a cured film of PS-coating (e) to various chemicals was investigated on various substrates. The results (Table 5) show that there were no visible changes to the film, e.g., peeling or color changes, and that the film had good white film characteristics.

Table 5. Chemical resistance of cured film derived from PS-coating (e).

Chemicals	Condition	Substrate	Result
TMAH (2.38 wt%)	23 °C/3 min	Glass	no change
		ITO	no change
		Cr	no change
Resist stripper N-300*	45 °C/3 min	Glass	no change
		ITO	no change
		Cr	no change
Oxalic acid (0.05 mol/l)	35 °C/3 min	Glass	no change
		ITO	no change
		Cr	no change

*N-300; MEA/DGBE = 30/70 wt ratio.

These results show that PS-coating (e), with 40 wt% of TiO_2 pigment introduced into Si-OLIGO-1 with a siloxane oligomer as the base resin, was suitable for use as a white decorative film.

3.2.3. Patterning performance

Before patterning the PS-coating (e), the straight transmittance of a prebaked film formed on a glass substrate (11.7 μm) was determined in the wavelength range 300–700 nm; this includes exposure to g-line (436 nm), h-line (405 nm), and i-line (365 nm) light. As shown in Fig. 8, no light was transmitted because of the effects of reflection and absorption by TiO_2. Next, the scattering transmittance was determined in the same range. The results show that some of the g-line and h-line light was transmitted by scattered light. It is therefore assumed that the light reaches the bottom of the film and a pattern can be formed.

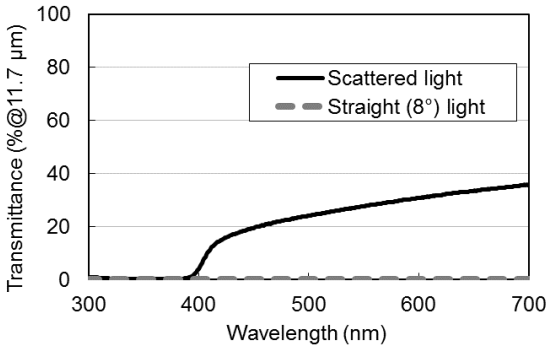

Fig. 8. Straight and scattered transmittances of cured film.

Patterning was performed using a mask and PS-coating (e). The results (Table 6) show a good resolution and pattern shape (taper angle), which satisfy customer requirements (resolution < 150 μm; taper angle 30°–50°), at an exposure of 200–250 mJ/cm^2.

Table 6. Patterning performance of PS-coating (e).

	PS-coating (e)				
Expo. dose (mJ/cm^2)	175	200	225	250	275
Resolution (μm)	80	80	100	100	150
Taper angle (°)	65	40	35	35	30
SEM image					

We successfully created a novel negative photosensitive white decorative siloxane coating, which contained a siloxane oligomer Si-OLIGO-1 as a base resin and 40 wt% of TiO_2 (particle size 250 nm) as the pigment. This coating can endow white film characteristics and ensure a good patterning performance.

4. Conclusion

A siloxane oligomer (Si-OLIGO-1) that can form a thick film was synthesized by introducing a bifunctional alkoxysilane into a SQ composed of a trifunctional alkoxysilane via a sol–gel method. IR spectroscopic analysis showed that Si-OLIGO-1 has a random structure with many acidic silanol groups capable of alkaline development. The transparency of a cured film formed from Si-OLIGO-1 was approximately the same, and the heat resistance was better, than those of an acrylic polymer. A white pigment was introduced into

Si-OLIGO-1 to create a negative photosensitive white decorative coating. When 40 wt% of TiO_2 (particle size 250 nm) was introduced as the white pigment, a white cured film of thickness 10 μm had the brightness (L^*) and color (a^*, b^*) required for white frames of display products. This coating also has potentially good chemical resistance when used in practical applications. This white decorative coating did not transmit straight light in the exposure light range required for negative pattern processing, but partly transmits scattered g-line and h-line light. This coating therefore gave the good resolution and pattern shape that were required by a customer at an exposure dose of 200–250 mJ/cm^2.

The novel negative photosensitive white decorative siloxane coatings created by this method have good film properties and give good patterning performances. They are suitable for complex white decorations, and modified formulations can be applied to devices such as smartphones and tablets.

Acknowledgement

We would like to thank the staff of the Electronic and Imaging Materials Research Laboratories, Toray Industries, Inc., for their cooperation in carrying out this research.

References

1. *Japanese patent* No. 6008436.
2. *Japanese patent* No. 6405004.
3. *Japanese patent* No. 5860419.
4. *Japanese patent* No. 6192556.
5. *Japanese patent* No. 6139894.
6. *Japanese patent* No. 6167805.
7. *Japanese patent* No. 5751929.
8. *Japanese patent* No. 6365118.
9. *Japanese patent* No. 6375236.
10. J. F. Brown Jr., L. H. Vogt Jr., A. Katchman, J. W. Eustance, K. M. Kiser, and K. W. Krantz, *J. Am. Chem. Soc.*, **82** (1960) 6194.
11. J. F. Brown, L. H. Vogt, and P. I. Prescott, *J. Am. Chem. Soc*., **86** (1964) 1120.
12. M. Smaihi and T. Jermoumi, *Chem. Mater.*, **7** (1995) 2293.
13. E. Lee and Y. Kimura, *Polym. J.*, **30** (1998) 730.
14. J. J. Schwab and J. D. Lichtenhan, *Appl. Organometal. Chem.*, **12** (1998) 707.
15. N. Takamura, T. Gunji, H. Hatano, and Y. Abe, *J. Polym. Sci.*, *Part A, Polym. Chem.*, **37** (1999) 1017.
16. F. J. Feher, R. Terroba, and J. W. Ziller, *Chem. Commun*. (1999) 2309.
17. N. Yasuda, S. Yamamoto, S. Minami, H. Nobutoki, Y. Wada, and S. Yanagida, *Jpn. J. Appl. Phys.*, **41** (2002) 624.
18. R. Duchateau, *Chem. Rev*., **2** (2002) 3525.
19. M. Unno and H. Matsumoto, *J. Organometal. Chem.*, **692** (2007) 307.
20. H. Seki, T. Kajiwara, Y. Abe, and T. Gunji., *J. Org. Chem.*, **695** (2010) 1363.
21. J. J. Schwab and J. D. Lichtenhan, *Appl. Organometal. Chem.*, **12** (1998) 707.
22. E. S. Park, H. W. Ro, C. V. Ngnyen, R. L. Jaff, and D. Y. Yoon, *Chem. Matter.*, **20** (2008) 1548.
23. Z. X. Chang, J. Hao, P. Xie, X. Zhang, C. C. Han, and R. Zhang, *Chem. Mater.*, **20** (2008) 1322.
24. M. Handke, B. Handke, A. Kowalewska, and W. Jastrzebski, *J. Mol. Struct.*, **924** (2009) 254.
25. M. Dutkiewicz, M. Szołyga, H. Maciejewski, and B. Marciniec, *J. Therm. Anal. Calorim.*, **117** (2014) 259.
26. M. M. Rahman, V. Filiz, M. M. Khan, B. N. Gacal, and V. Abetz, *Reac. Funct. Polym.*, **86** (2015) 125.
27. Y. Tashiro, A. Miyazato, and K. Ebitani, *J. Inorg. Organomet. Polym.*, **25** (2015) 1353.
28. T. Okazawa, K. Ono, and M. Suwa, *J. Photopolym. Sci. Technol.*, **25** (2012) 349.
29. Y. Nakahara, H. Kawa, J. Yoshiki, M. Kumei, H. Yamamoto, F. Oi, H. Yamakado, H. Fukuda, and K. Kimur, *Thin Solid Films* **520** (2012) 7195.
30. J. A. Tossell and N. Sahai, *Geochim. Cosmochim. Acta*, **64** (2000) 4097.
31. M. M. Fickling, A. Fischer, B. R. Mann, J. Packer, and J. Vaughan, *J. Am. Chem. Soc.*, **81** (1959) 4226.
32. N. Takano, T. Fukuda, and K. Ono, *Kobunshi Ronbunshu*, **57** (2000) 743 (in Japanese).
33. Y. Tashiro, T. Sekito, T. Iwata, D. Yokoyama, and T. Nonaka, *Proc. SPIE,* **7140** (2008) 71402O.
34. Y. Kaneko and N. Iyi, *Kobunshi Ronbunshu*, **67** (2010) 280 (in Japanese).
35. A. Kolezynski, W. Tastrzebski, and W. Sitarz, *J. Mol. Struct.*, **1044** (2013) 314.
36. W. Szczypka, K. Jelen, and K. Andrzej, *J. Mol. Struct.*, **75** (2014) 599.
37. Y. Tashiro, A. Miyazato, and K. Ebitani, *J. Photopolym. Sci. Technol.*, **28** (2015) 239.

Communication

Journal of Photopolymer Science and Technology
Volume 34, Number 5 (2021) 525−528 ©2021SPST

Emission Properties of Hybrid Films of Benzylideneaniline-based Amorphous Molecular Materials with Organic Acids

Takuma Tsukada and Hideyuki Nakano*

Department of Applied Chemistry, Muroran Institute of Technology
27-1 Mizumoto-cho, Muroran, Hokkaido 050-8585, Japan
**nakano@mmm.muroran-it.ac.jp*

A novel emitting amorphous molecular material, 4-[bis(9,9-dimethylfluoren-2-yl)-amino]benzylideneaniline (BFBZA), was designed and synthesized. BFBZA provided moisture-sensitive hybrid film combined with benzoic acid (BA) that exhibited reversible change in emission color in response to moisture like as hybrid films of 4-[bis(4-methylpheyl)amino]benzylideneaniline with pentafluorobenzoic acid (PFBA) and BA. On the other hand, another hybrid film of BFBZA combined with PFBA did not exhibit such reversible change in emission color. The balance of acidity level of organic acid and basicity level of the emitting amorphous molecular materials was suggested to play a role for exhibiting reversible change in emission color.

Keywords: Emitting amorphous molecular material, Organic acid, Fluorescence, Basicity, Excited-state intermolecular proton transfer

1. Introduction

Stimuli-responsive organic solid materials that exhibit reversible changes in object colors and/or emission colors triggered by external stimuli are the subjects of interest from both viewpoints of fundamental sciences including elucidation of the mechanism of the switching functions and practical applications such as displays, memories, and visible sensors. The phenomena of reversible changes in object color and emission color triggered by chemical vapors such as moisture, volatile organic molecules, and gaseous acids and bases in the surroundings of the materials are referred to as "vapochromism" and "vapochromic emission", respectively. A variety of materials exhibiting such phenomena have been created in recent years, including organic crystals, polymer films, organometallic and coordination complexes that exhibit change in their object colors and/or emitting colors due to change in, e.g., interactions to volatile molecules, conformation of the molecules, and/or crystal structures upon exposure to vapors [1-7].

We have been studying the creation of stimuli-responsive emitting amorphous molecular materials [8–12]. For example, we have reported that spin-coated films of diarylaminobenzaldehyde-based emitting amorphous molecular materials exhibited vapochromic emission [11]. In addition to such materials with single component systems, we have recently been studying the creation of hybrid systems of amorphous molecular materials with other materials exhibiting smart functions [13–23]. We have reported that the hybrid films of aminoazobenzene-based amorphous molecular materials with organic acids exhibited drastic and reversible color changes in response to moisture [20]. Novel moisture-sensitive hybrid films composed of diarylaminobenzaldehyde-based emitting amorphous molecular materials with p-toluenesulfonic acid were found to exhibit OFF–ON switching of fluorescent in response to moisture [22]. Very recently, we have investigated the response of emission properties to moisture for hybrid films composed of 4-[bis(4-methylphenyl)-amino]benzylideneaniline (BMBZA) with a variety of organic acids, and finally found that hybrid films of BMBZA with organic acids with appropriate acidities, benzoic acid (BA) and pentafluorobenzoic

Received March 28, 2021
Accepted April 30, 2021

acid (PFBA), exhibited the emission color changes in response to moisture [23].

In the present study, a novel amorphous molecular material, 4-[bis(9,9-dimethylfluoren-2-yl)amino]benzylideneaniline (BFBZA), has been designed and synthesized. It was found that a hybrid film of BFBZA with BA exhibited reversible change in emission color in response to moisture. Chemical structures of BMBZA and BFBZA are shown in Scheme 1.

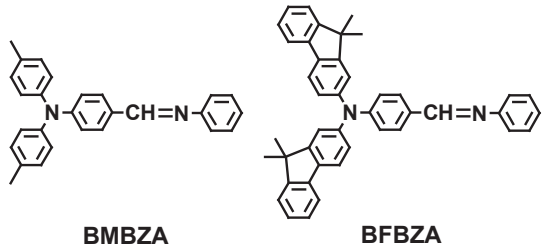

Scheme 1. Chemical structures of BMBZA and BFBZA.

2. Experimental

BA and PFBA were purchased commercially and used without further purification. BFBZA was prepared as follows. A mixture of 4-[bis(9,9-dimethylfluoren-2-yl)amino]benzaldehyde (200 mg, 0.40 mmol) and aniline (5 cc) was stirred for more than 6 hours at 120 °C. Resulting mixture was poured into the mixed solution of water and ethanol (1:1 v/v) and the precipitate was collected. The crude product was recrystallized from ethanol to give yellow needles. Yield: 160 mg (70 %); m.p. 198 °C; ^{1}H NMR (500 MHz, $CDCl_3$): δ (ppm) = 8.38 (s, 1H), 7.77 (d, 2H, J = 8.6 Hz), 7.66 (d, 2H, J = 7.2 Hz), 7.63 (d, 2H, J = 8.0 Hz), 7.39 (d, 2H, J = 7.1 Hz), 7.36 (d, 2H, J = 8.0 Hz), 7.32 (t, 2H, J = 8.1 Hz), 7.28 (d, 2H, J = 8.6 Hz), 7.26 (s, 2H), 7.23-7.18 (m, 5H), 7.14 (d, 2H, J = 6.0 Hz), 1.42 (s, 12H); ^{13}C NMR (100 MHz, $CDCl_3$): δ (ppm) = 159.75, 155.34, 153.70, 152.59, 151.05, 146.60, 138.90, 135.29, 130.07, 129.73, 129.23, 127.17, 126.88, 125.63, 124.18, 122.65, 122.11, 121.01, 120.87, 119.70, 119.66, 47.00, 27.14.

Hybrid films were prepared by spin coating onto transparent glass substrates (1500 rpm at room temperature) from THF solutions (0.5 ml) including BFBZA with BA or PFBA with a molar ratio of 1:1. Electronic absorption and fluorescence spectra upon excitation with 400 nm under the dry atmosphere were measured at ambient conditions (less than 50%RH at ca. 25 °C). In order to measure the spectra under wet atmosphere, the hybrid film was put into the sealed transparent quartz cell with ca. 0.3 ml of water and kept for more than one hour before measurements. Electronic absorption and fluorescence spectroscopies were made by means of U-3500 spectrophotometer (HITACHI Ltd.) and FP-8300 spectrofluorometer (JASCO Co), respectively.

3. Results and discussion

BFBZA was synthesized by condensation reaction of 4-[bis(9,9-dimethylfluoren-2-yl)amino]-benzaldehyde and aniline. BFBZA was found to readily form amorphous glass by cooling the melt sample. A glass-transition temperature of BFBZA was 107 °C determined by differential scanning calorimetry.

Fig. 1 shows electronic absorption and fluorescence spectra of single BFBZA film. Electronic absorption band with a λ_{max} of 370 nm with a shoulder around 400 nm was observed, being in the similar wavelength region to the single BMBZA film [23]. With regard to fluorescence spectrum, the emission band of BFBZA film with a λ_{max} of ca. 500 nm was somewhat red-shifted relative to that of BMBZA film [23]. The result might be due to the fact that the π-conjugation system was more extended by introduction of fluorenyl groups.

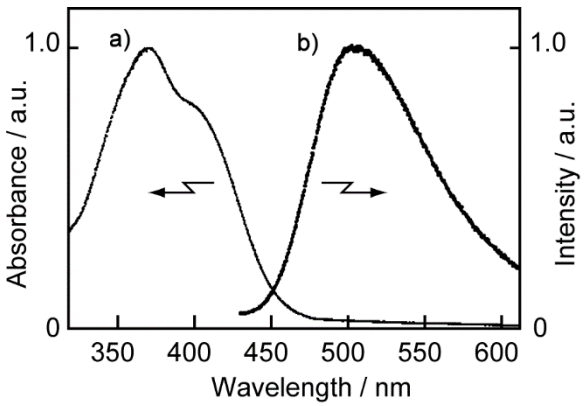

Fig. 1. (a) Electronic absorption and (b) fluorescence spectra of BFBZA film (λ_{ex}: 400 nm).

As well as BMBZA–BA and BMBZA–PFBA films [23], a novel hybrid film of BFBZA–BA was found to exhibit reversible change in emission color in response to exhaled breath. The film emitted orange in color upon irradiation with UV lamp (365 nm) under ambient dry atmosphere. When we breathed onto the film, emission color changed immediately to yellowish green. When pausing the breath, the emission color of the film returned to

the original. The phenomenon was due to moisture in the breath. Fig. 2 shows fluorescence spectra of the BFBZA–BA film. Under dry atmosphere, the emission band was observed around 630 nm (Fig. 2a), being considerably red-shifted from that observed for BFBZA (Fig. 1b). When the sample placed under wet atmosphere, the spectrum was drastically changed to be similar to that for the BFBZA film (Fig. 2b). These results were quite similar to those observed for BMBZA–BA film [23], and therefore, the emission bands in the shorter wavelength region around 500 nm and in the longer wavelength region around 600 nm were attributable to the emissions from excited states of BFBZA (BFBZA*) and its protonated iminium ion (BFBZA-H^+*), respectively.

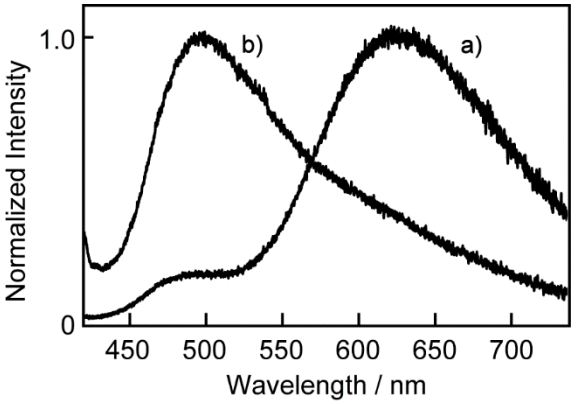

Fig. 2. Fluorescence spectra of BFBZA–BA film under (a) dry and (b) wet atmospheres (λ_{ex}: 400 nm).

On the other hand, BFBZA–PFBA film did not show such change in fluorescent color. Orange emission was observed both under dry and wet atmospheres. As shown in Fig. 3, emission spectra of BFBZA–PFBA film under dry and wet atmospheres were almost similar to each other, the emission bands being in the longer wavelength region attributable to the fluorescence from BFBZA-H^+*.

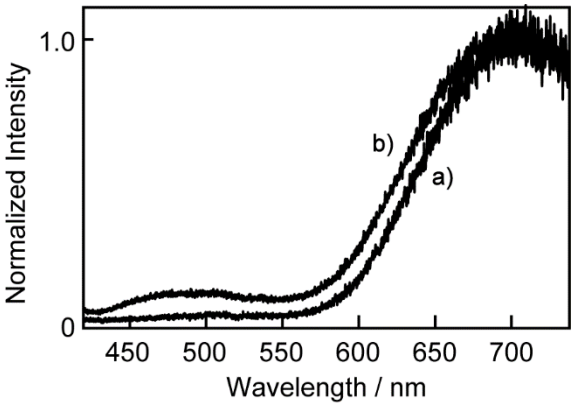

Fig. 3. Fluorescence spectra of BFBZA–PFBA film under (a) dry and (b) wet atmospheres (λ_{ex}: 400 nm).

In order to gain further information, electronic absorption spectral changes of these films were investigated. With regard to BFBZA–BA film, the electronic absorption spectral change was quite similar to that observed for BMBZA–BA film [23]. As shown in Fig. 4, the spectrum under dry atmosphere was almost similar to that of the BFBZA (Fig. 1a) and did not change when the film placed under wet condition. The result suggested that BFBZA-H^+ was scarcely produced in the hybrid film both under dry and wet atmospheres and the orange emission from BFBZA-H^+* (Fig. 2a) took place through excited-state intermolecular proton transfer from BA to BFBZA* like as BMBZA–BA film [23].

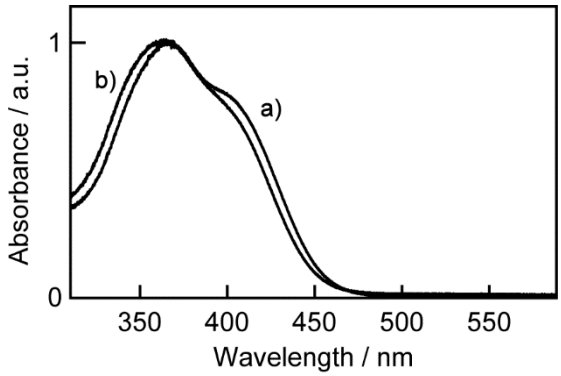

Fig. 4. Electronic absorption spectra of BFBZA–BA film under (a) dry and (b) wet atmospheres.

With regard to BFBZA–PFBA film under dry atmosphere, two absorption bands were observed (Fig. 5a). The band in shorter wavelength region around 350 nm was attributable to the absorption of BFBZA since the band was almost similar to that of BFBZA (Fig. 1a). On the other hand, the broad band in longer wavelength region around 485 nm was suggested to be the protonated iminium ion, BFBZA-H^+. The result was similar to that observed for BMBZA–PFBA film and suggested that protonation to BFBZA by PFBA took place in the film to produce BFBZA-H^+. When the film was placed under wet atmosphere, the absorption band in the longer wavelength region relatively reduced due to moisture as shown in Fig. 5b. However, the band in the longer wavelength region remained whereas the corresponding band for BMBZA–PFBA film was completely disappeared under wet condition [23]. The facts suggested the incomplete deprotonation of BFBZA-H^+ took place

under wet atmosphere, resulting in no change in emission color of BFBZA–PFBA film. Since the emission band attributable to BFBZA* was well overlapped with the absorption band of BFBZA-H^+, effective FRET from BFBZA* to BFBZA-H^+ might take place to exhibit orange emission for BFBZA–PFBA film both under dry and wet atmospheres. Incomplete deprotonation in the present film might be due to larger basicity of BFBZA than BMBZA.

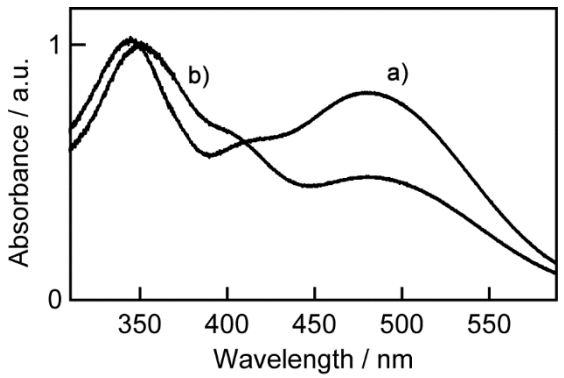

Fig. 5. Electronic absorption spectra of BFBZA–PFBA film under (a) dry and (b) wet atmospheres.

4. Conclusion

We have designed and synthesized of a novel molecule, BFBZA, and found that the hybrid amorphous film of BFBZA with BA exhibited reversible change in emission color in response to exhaled breath whereas BFBZA–PFBA film did not change the emission color. In our previous paper [21,23], acidity levels of organic acids were the important factor for providing hybrid films that exhibit reversible changes in object colors and emission colors in response to moisture. The present study suggested that the basicity level of emitting material was also the important factors, that is, the balance of acidity level of organic acid and basicity level of emitting amorphous molecular materials plays a role for exhibiting reversible change in emission color. Further studies are in progress.

Acknowledgement

This work was partly supported by JSPS KAKENHI Grant Number JP26107006 in Scientific Research on Innovative Areas “Photosynergetics”.

References

1. X. Zhang, B. Li, Z.-H. Chen, and Z.-N. *Chen, J. Mater. Chem.*, **22** (2012) 11427.
2. H. Iida, S. Iwahana, T. Mizoguchi, and E. Yashima, *J. Am. Chem. Soc.*, **134** (2012) 15103.
3. O. S. Wenger, *Chem. Rev.*, **113** (2013) 3686.
4. T. Hayashi, A. Kobayashi, H. Ohara, M. Yoshida, T. Matsumto, H.-C. Chang, and M. Kato, *Inorg. Chem.*, **54** (2015) 8905.
5. R. Ishizaki and R. Katoh, *Chem. Phys. Lett.*, **652** (2016) 36.
6. Y. Shigeta, A. Kobayashi, M. Yoshida, and M. Kato, *Inorg. Chem.*, **58** (2019) 7385.
7. E. Li, K. Jie, M. Liu, X. Sheng, W. Zhua, F. Huang, *Chem. Soc. Rev.*, **4** (2020) 1517.
8. K. Mizuguchi, H. Kageyama, H. and Nakano, *Mater. Lett.*, **65** (2011) 2658.
9. K. Mizuguchi and H. Nakano, *Dyes Pigm.*, **96** (2013) 76.
10. K. Okoshi and H. Nakano, *J. Photopolym. Sci. Technol.*, **27** (2014) 535.
11. K. Ogura and H. Nakano, *Kobunshi Ronbunshu*, **72** (2017) 199.
12. S. Manabe, E. Nagata, and H. Nakano, *Rapid Commun. Photosci.*, **3** (2014) 38.
13. H. Nakano, *Chem. Lett.*, **40** (2011) 473.
14. H. Nakano and M. Suzuki, *J. Mater. Chem.*, **22** (2012) 3702.
15. R. Ichikawa and H. Nakano, *Appl. Phys. Express*, **6** (2013) 035602.
16. H. Nakano, R. Ichikawa, and R. Matsui, *Micromachines*, **4** (2013) 128.
17. R. Ichikawa and H. Nakano, *J. Photopolym. Sci. Technol.*, **30** (2017) 661.
18. H. Nakano, R. Ichikawa, and Y. Doi, *J. Photopolym. Sci. Technol.*, **31** (2018) 81.
19. H. Nakano, R. Ichikawa, H. Ukai, and A. Kitano, *J. Phys. Chem. B*, **122** (2018) 7775.
20. R. Ichikawa, E. Nagata, and H. Nakano, *RSC Adv.*, **5** (2015) 2934.
21. Y. Kitamura, R. Ichikawa, and H. Nakano, *Mater. Chem. Front.*, **2** (2018) 90.
22. H. Nakano, T. Nishimura, E. Nagata, R. Ichikawa, *ChemistrySelect*, **1** (2016) 1737.
23. T. Tsukada, Y. Kitamura, and H. Nakano, *Asian J. Org. Chem.*, **10** (2021) 588.

Communication

Journal of Photopolymer Science and Technology
Volume 34, Number 5 (2021) 529−532 ©2021SPST

Synthesis of Amino Acid-derived Curing Reagents Containing a Disulfide Bond and Their Application to Anionic UV Curing Materials

Masahiro Furutani*, Kako Maeno, and Arata Tanaka

Department of Chemistry and Biology, National Institute of Technology, Fukui College, Geshi-cho, Sabae, Fukui 916-8507, Japan
**furutani@fukui-nct.ac.jp*

Anionic UV curing has been applied for many kinds of industrial resins, because it overcomes technical problems in conventional radical and cationic UV curing. In this study, a cystine-based latent curing reagent was designed, and synthesized from L- and D-cysteine. The reagents showed not only good solubility toward organic media, but also good thermal decomposition behavior in the presence of basic species. Using them with a photo-base generator and an epoxy resin having a disulfide bond, UV-cured films of B-to-3B grade of pencil-hardness were fabricated successfully, after 10 J/cm^2 of 365 nm-light irradiation and subsequent heating at 120-160°C for 30 min. Furthermore, two glass substrates were adhered by using this anionic UV curing system, and 1.6-3.7 MPa of shear stress was recorded in the photo-adhesion and re-adhesion experiments.

Keywords: Curing reagent, Disulfide bond, Anionic UV curing, Cystine, Photo-adhesion, Re-adhesion

1. Introduction

UV curing is one of powerful tools in various kinds of industries, and it has been applied to manufacturing, printing, maintenance and so on [1-7]. Generally, UV curing materials are consisted of a photo-initiator and reactive resins. Radical, cationic (acidic), or anionic (basic) species are generated from respective photo-initiators. Among the three curing systems, anionic UV curing has been paid much attention, because the curing system circumvents some problems in radical or cationic UV curing systems, such as polymerization inhibition by oxygen and metallic corrosion [5]. Furthermore, base amplifiers (BAs) have been proposed by Arimitsu [8-10]. BAs increase concentration of base through their auto-catalytic decomposition reactions (base proliferation reactions) triggered by photo-generated bases from photo-base generators (PBGs), resulting in improvement of photo-sensitivity of the photo-reactive materials [8-15].

As one of applications of BAs, a thermal dismantlable photo-adhesive material has been fabricated with a PBG, an epoxy resin, and a BA having a disulfide bond [16]. This anionic UV curing system had a problem that the BA was not miscible toward organic media, probably due to its molecular symmetry [17]. In this study, cystine-based curing reagents have been designed and synthesized by using L- and D-cysteine compounds at once (Fig. 1). It is known that derivatives of several kinds of amino acid including cystine (LL isomer) work as BA where the amino group is protected with 9-fluorenyl-methoxycarbonyl (Fmoc) group [18]. A disulfide bond is formed by oxidation reactions of two thiol groups of cysteine, obtaining three kinds of cystine derivatives (LL, DD, and LD isomers). It is

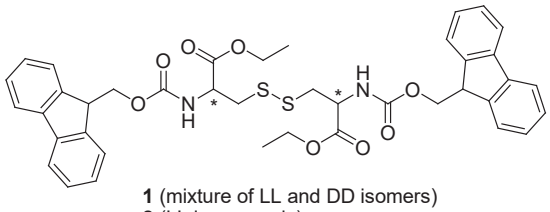

1 (mixture of LL and DD isomers)
2 (LL isomer only)

Fig. 1. Cystine-derived reagents **1** and **2**, designed and synthesized in this study.

Received March 30, 2021
Accepted April 30, 2021

expected that both a steric effect of ester moieties and blending three isomers would contribute to improve the solubility and miscibility. Resulting curing reagent was used with **PBG** and **EP** (Fig. 2), which was applied to photo-adhesion as well as anionic UV curing.

2. Experimental

Fmoc-L-Cys(Tr)-OH (*N*-α-(9-fluorenylmethoxy-carbonyl)-*S*-trityl-L-cysteine, Fmoc-D-Cys(Tr)-OH (D-isomer of Fmoc-L-Cys(Tr)-OH), and WSCI HCl (water soluble carbodiimide hydrochloride, 1-ethyl-3-(3-dimethylaminopropyl) carbodiimide hydrochloride) were purchased from WATANABE CHEMICAL INDUSTRIES, Ltd. (Hiroshima, Japan). Ethanol, iodine, tetrahydrofuran (THF), toluene, dichloromethane, and sodium sulfite were purchased from FUJIFILM Wako Pure Chemical Corporation (Osaka, Japan). DMAP (dimethyl-aminopyridine), methanol, chloroform, acetone, and ethyl acetate were purchased from NACALAI TESQUE, INC. (Kyoto, Japan). 1,3-Di-4-piperidylpropane was purchased from Tokyo Chemical Industry Co., Ltd. (Tokyo, Japan). Polystyrene (PSt, M_w: 35000) and thin layer chromatography plate (TLC Silica gel 60 F_{254}) were purchased from Sigma-Aldrich Co. LLC (St. Louis, United States). All reagents were used without further purification.

^{1}H- and ^{13}C-NMR spectra were recorded using a Bruker AVANCEIII. APCI-MS measurements were performed using an AB Sciex API2000. FT-IR spectral measurements were performed using a Perkin Elmer Spectrum100. Anionic UV curing and photo-adhesion experiments were performed with 3UV™-36UVLamp (Analytik Jena AG), UIT-250/UVD-C365 ultraviolet radiometer (Ushio Inc.), and SA-201 applicator (TESTER SANGYO Co., Ltd.). Glass substrates were washed by ultrasonic treatment in acetone and then chloroform. Pencil-hardness test was carried out with MJ-PHT tester (Sato Shouji Inc.). Shear stress was recorded using MCT-1150 (A&D, Co., Ltd., tensile rate: 10 mm/min).

2.1. Synthesis

PBG [19] and **EP** [16] were synthesized and purified according to the related literatures reported previously.

Synthesis of **1**. To a dried flask were added Fmoc-L-Cys(Tr)-OH (0.25 g, 0.43 mmol), Fmoc-D-Cys(Tr)-OH (0.25 g, 0.43 mmol), and WSCI HCl (0.18 g, 0.95 mmol) in dichloromethane (20 mL) under nitrogen atmosphere. The mixture was stirred at 0°C, followed by adding DMAP (8.1 mg, 6.6 μmol) and ethanol (0.60 g, 13 mmol). After stirring at room temperature for 3 days, solvents were evaporated, and the residue was triturated in water. The mixed equal amount of ethyl ester compounds (Fmoc-L-Cys(Tr)-OEt and Fmoc-D-Cys(Tr)-OEt) were obtained quantitatively as a white solid, confirmed by ^{1}H-NMR spectral measurement. ^{1}H-NMR (400 MHz, $CDCl_3$): δ 1.28 (t, 3H, J = 7.0 Hz, -CH_3), 2.67 (m, 2H, -CH_2S-), 4.2-4.4 (m, 6H, -CH_2O-, C*H, >CH-CH_2-), 5.30 (d, 0.8H, J = 8.0 Hz, -NH-), 7.2-7.4 (m, 19H, Ar-H), 7.64 (d, 2H, J = 4.8 Hz, Ar-H), 7.79 (t, 2H, J = 4.8 Hz, Ar-H). Product was used for the next reaction without further purification.

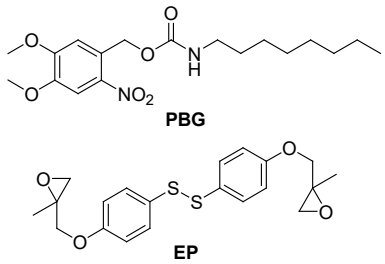

Fig. 2. Chemical structures of a photo-base generator, **PBG**, and an epoxy resin, **EP**.

The mixture of ethyl ester compounds (0.48 g) in dichloromethane (20 mL) was added to a dried flask, followed by adding iodine (0.20 g, 0.79 mmol). The solution was stirred at room temperature for 66 h, and then quenched by 1% of sodium sulfite aqueous solution. The organic layer was washed twice with brine, and evaporated to be subjected to column chromatography on silica gel (eluent: chloroform to chloroform/methanol = 10/1, v/v). A mixture of LL and DD isomers of cystine derivatives was obtained as a white solid in 73% total yield. ^{1}H-NMR (400 MHz, $CDCl_3$): δ 1.31 (m, 6H, -CH_3), 3.23 (m, 4H, -CH_2S-), 4.2-4.7 (m, 12H, -CH_2O-, C*H, >CH-CH_2-), 5.78 (d, 2H, J = 5.2 Hz, -NH-), 7.3-7.4 (m, 8H, Ar-H), 7.63 (br, 4H, Ar-H), 7.78 (t, 4H, J = 7.6 Hz, Ar-H). ^{13}C-NMR (100 MHz, $CDCl_3$): δ 14, 41, 47, 53, 62, 67, 120, 125, 127, 128, 141, 144, 156, 170. APCI-MS: *m*/*z* calcd for $C_{40}H_{40}O_8N_2S_2$: 740.96; found: 741.5.

Compound **2** was also synthesized and purified through the same procedure, obtaining as a white solid in 44% total yield. ^{1}H-NMR (400 MHz, $CDCl_3$): δ 1.31 (m, 6H, -CH_3), 3.23 (m, 4H, -CH_2S-), 4.2-4.7 (m, 12H, -CH_2O-, C*H, >CH-CH_2-), 5.77 (d, 2H, J = 7.6 Hz, -NH-), 7.3-7.4 (m, 8H, Ar-H), 7.63 (br, 4H, Ar-H), 7.78 (d,

4H, J = 7.6 Hz, Ar-H). APCI-MS: m/z calcd for $C_{40}H_{40}O_8N_2S_2$: 740.96; found: 741.5.

2.2. Thermal decomposition behavior of **1**

PSt, **1** (167 wt% toward PSt), and 1,3-di-4-piperidyl- propane (0 or 5 mol% toward **1**) were dissolved into THF. Each solution was dropped on a silicon wafer, and dried in air. The samples were heated at 160 or 120°C with FT-IR spectral measurements at 2-10 min intervals.

2.3. Anionic UV curing

EP, **1** (100 mol% toward **EP**), and **PBG** (10 mol% toward **EP**) were dissolved into THF. The solution was bar-coated on a glass substrate with an applicator (4 mil), followed by pre-baking at 80°C for 1 min. The samples were then subjected to 0-10 J/cm^2 of 365-nm light irradiation (3.9 mW/cm^2), followed by post-baking at 120-160°C for 30 min.

2.4. Photo-adhesion and re-adhesion

Glass substrates coated partially with the mixture of **EP**, **1**, and **PBG** were prepared according to the same method mentioned above. Each coating area was subjected to 10 J/cm^2 of 365-nm light irradiation (3.9 mW/cm^2). Two glass substrates were then stuck with each other through the UV- irradiated area (*ca.* 50-70 mm^2), followed by post-baking at 160°C for 30 min with at least 0.03 kgf of weight-bearing. Shear stress of each sample was recorded at room temperature (22°C). After that, the two fracture surfaces were stuck again with weight-bearing, which was heated at 90°C for few minutes and then cooled to room temperature, to be subjected to shear stress test under the same experimental conditions.

3. Results and discussion

3.1. Synthesis of **1**

In the oxidation reaction with a mixture of L- and D-isomers of cysteine derivatives, LL, DD, and LD isomers of cystine derivative would be synthesized stochastically. It was confirmed that **1** consists of LL and DD isomers, from the results on ^{1}H-NMR and thin layer chromatography (TLC, R_f = 0.85, eluent: chloroform/methanol = 30/1, v/v) of **1** and **2**. On the other hand, another fraction (single spot on TLC plate, R_f = 0.60, eluent: chloroform/methanol = 6/1, v/v) was obtained in the purification process. ^{1}H-NMR spectrum of the fraction ($CDCl_3$) was complicated, and multiple spots were observed in a TLC after the NMR measurement. These results imply the presence of the LD isomer in $CDCl_3$ that would be unstable.

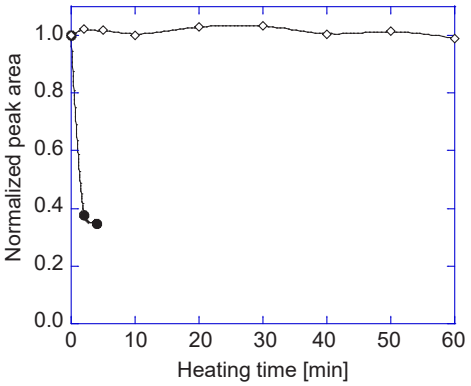

Fig. 3. Thermal decomposition behavior of **1** in a PSt matrix in the presence of 5 mol% of base at 120°C (closed, circle), and in the absence of base at 160°C (open, diamond).

Cystine derivatives **1** and **2** showed good solubility toward general organic solvents, such as acetone, THF, chloroform, and ethyl acetate. A cystamine analogue reported previously showed poor solubility [7], which indicates that ester moieties in the chemical structure of **1** or **2** would contribute to improvement of the solubility.

3.2. Thermal decomposition behavior of **1**.

In FT-IR spectral measurements, a peak around 1700 cm^{-1} was assigned to stretching vibration of C=O bonds of **1**, and decrease of the peak area was monitored. The peak area decreased dramatically within 2 min by heating at 120°C in the presence of catalytic amount of base (Fig. 3). In contrast, the area did not decrease even after heating at 160°C for 60 min without bases. These results indicated not only auto-catalytic decomposition behavior of **1**, but also good thermal stability of **1**. There are three requirments for BAs [10]: 1) thermal stability in the absence of base, 2) auto-catalytic decomposition in the presence of base, and 3) generation of bases to have enough basicity for the following reactions. Cystine derivative **1** satisfied the first and second requirements.

3.3. Anionic UV curing

To examine whether **1** also satisfies the third requirement, UV-cured films were fabricated with a homogeneous composition of **PBG**, **1**, and **EP**. In the pencil-hardness tests (JIS K5400), the hardness is arranged as follows: 6B (softest), 5B, ... , B, HB, F, H, 2H, ... , 9H (hardest). In this test, the pencil is moved scratching over the surface of the coating at a 45° angle with a constant pressure (1 kgf). In the case at 120°C, film was

not cured with 0 or 1 J/cm^2 of UV irradiation, because trigger bases for the following reactions were not generated enough. Increasing irradiation energy, films were cured successfully, which indicates that **1** was converted into its diamine to form cross-linked networks through reactions with epoxy resins. Similar tendency was observed in the cases at 140ºC or 160ºC, although dark reactions were caused. Nevertheless, B-to-3B grades of UV-cured films were obtained, probably resulting from photo-triggered base proliferation reactions.

3.4. Photo-adhesion and re-adhesion.

Using the anionic UV curing system, two glass substrates were stuck successfully where 1.6 MPa of the maximum shear stress was recorded (Fig. 4). Rough surface of the adhesive layer was remained on each substrate, which became soften over 50ºC. Re-adhesive samples were subjected to shear stress test again, which shear stress became higher up to 3.7 MPa that was comparable with the value required for products in our daily life (*ca.* 4 MPa). It was probably due to annealing of the adhesive layers in which exchange reactions between disulfide bonds would be caused [16, 20].

4. Conclusion

Oxidation reactions of L- and D-cysteine derivatives gave a mixture of LL and DD isomers of cystine derivatives that dissolved into organic media. The blending reagents worked as a BA, and anionic UV curing of an epoxy resin was performed, which was applied to photo-adhesion and re-adhesion. The UV-cured material containing disulfide bonds would also be dismantled by gentle heating.

Acknowledgement

MF acknowledges Prof. Eiki Matsui at National Institute of Technology, Fukui College for the use of APCI-MS instrument.

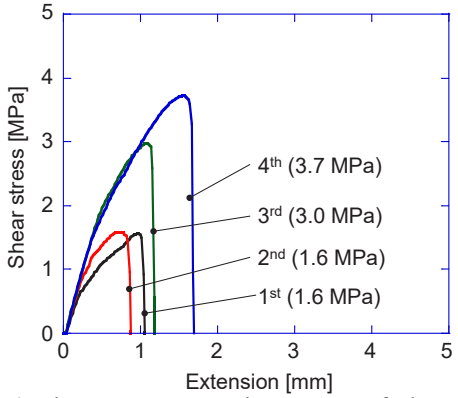

Fig. 4. Shear stress-extension curves of glass-glass adhesive samples fabricated with **PBG**, **1**, and **EP** (1st: photo-adhesion, 2nd-4th: re-adhesion). The maximum shear stress of each sample is also shown.

References

1. M. Pagac, J. Hajnys, Q. Ma, L. Jancar, J. Jansa, P. Stefek, and J. Mesicek, *Polymers*, **13** (2021) 598.
2. H. Wang, C. Chen, F. Yang, Y. Shao, and Z. Guo, *Mater. Today Commun.*, **26** (2021) 102037.
3. M. Yuan, S. Wang, G. Li, S. He, W. Liu, H. Liu, M. Huang, and C. Zhu, *Mater. Res. Express*, **8** (2021) 035134.
4. T. Distler and A. R. Boccaccini, *Acta Biomaterialia*, **101** (2020) 1.
5. N. Zivic, P. K. Kuroishi, F. Dumur, D. Gigmes, A. P. Dove, and H. Sardon, *Angew. Chem. Int. Ed.*, **58** (2019) 2.
6. H. Nakano, R. Kato, C. Kakami, H. Okamoto, K. Mamada, and K. Maki, *J. Photopolym. Sci. Technol.*, **32** (2019) 209.
7. V. Shukla and M. Bajpai, *Pigment and Resin Technol.*, **33** (2004) 272.
8. K. Arimitsu, M. Miyamoto, and K. Ichimura, *J. Photopolym. Sci. Technol.*, **12** (1999) 317.
9. M. Miyamoto, K. Arimitsu, and K. Ichimura, *J. Photopolym. Sci. Technol.*, **12** (1999) 315.
10. K. Arimitsu, M. Miyamoto, and K. Ichimura, *Angew. Chem. Int. Ed.*, **39** (2000) 3425.
11. Y. Morikawa, K. Arimitsu, T. Gunji, Y. Abe, and K. Ichimura, *J. Photopolym. Sci. Technol.*, **16** (2003) 81.
12. K. Arimitsu and K. Ichimura, *J Mater. Chem.*, **14** (2004) 336.
13. A. Igarashi, K. Arimitsu, T. Seki and K. Ichimura, *J Mater. Chem.*, **18** (2008) 560.
14. K. Arimitsu, D. Iijima, M. Furutani, Y. Yamada, and T. Wakiya,, *Chem. Lett.*, **43** (2014) 1921.
15. M. Furutani, H. Kobayashi, T. Gunji, Y. Abe, and K. Arimitsu, *J. Polym. Sci. A:Polym. Chem.*, **53** (2015) 1205.
16. M. Furutani, A. Kakinuma, and K. Arimitsu, *J. Polym. Sci. A:Polym. Chem.*, **56** (2018) 237.
17. M. Furutani, A. Kakinuma, and K. Arimitsu, *J. Photopolym. Sci. Technol.*, **29** (2016) 607.
18. M. Furutani, D. Yamakawa, and K. Arimitsu, *Mater. Technol.*, **34** (2016) 113.
19. M. Furutani and K. Kudo, *J. Mater. Chem.*, **22** (2012) 3139.
20. M. Furutani, K. Okuma, and K. Arimitsu, *J. Photopolym. Sci. Technol.*, **32** (2019) 623.

Communication

Journal of Photopolymer Science and Technology
Volume 34, Number 5 (2021) 533−536 ©2021SPST

Characterization of Shape of Polymer Nano-Films Possessing Various Crosslinking Chain Length

Shin-ichi Kondo[1*], Naoki Doi[1], Yasushi Sasai[2], Yukinori Yamauchi[3], and Masayuki Kuzuya[4]

[1] Laboratory of Pharmaceutical Physical Chemistry, Gifu Pharmaceutical University, 1-25-4 Daigaku-Nishi, Gifu 501-1196, Japan
[2] Faculty of Pharmacy, Gifu University of Medical Science, 4-3-3 Nijigaoka, Kani-shi, Gifu 509-0293, Japan
[3] Department of Pharmaceutical Physical Chemistry, College of Pharmaceutical Sciences, Matsuyama University, 4-2 Bunkyo-cho, Matsuyama, Ehime 790-8578, Japan
[4] Department of Health and Welfare, Faculty of Human Welfare, Chubu Gakuin University, 2-1 Kirigaoka, Seki-shi, Gifu 501-3993, Japan
**skondo@gifu-pu.ac.jp*

In this paper we studied on the size and morphology of polymer nano-film synthesized with the linker possessing the various length. Although the size measured by Zetasizer was larger than that by AFM, it was considered that polymer nano-film might be expanded due to solvation in PBS. The morphology of the polymer nano-film synthesized from succinic acid and glutaric acid showed square morphology rather than sphere. On the other hand, the polymer nano-film from azelaic acid showed spherical morphology. It was suggested that the difference among them might be ascribe to the flexibility of a polymer nano-film. Thus, the longer crosslinking chain length could be a more flexible polymer nano-film.
Keywords: Polymer nano-film, Crosslinking chain length, Plasma irradiation, Self-assembled phospholipid layer, Cyclodextrin

1. Introduction

The nano-film (or nano-sheet) is a new type of material that possesses a two-dimensional polymeric structure with nano-meter thickness. Many of nano-film needs the supporting material [1-5]. Recently, free standing nano-films fabricated from molecular, atomic, and ionic components have been extensively investigated for systems with analytical and biomedical applications, such as separation matrices and drug delivery carriers [6-11].

We have developed the method to introduce a durable surface wettability on several hydrophobic polymers by plasma-assisted method [12-16], and to fabricate a self-assembled phospholipid (phosphatidyl choline (PC)) layer (LDPE-PC-SA) on it [17]. It was also confirmed that LDPE-PC-SA possessed fluidity resembling to cellular membrane.

In recent years we have developed the polymer nano-film possessing hydrophilic and hydrophobic surface by using LDPE-PC-SA containing stearic acid (StA) (Fig. 1). The morphology of polymer nano-film in organic solvents (methanol and chloroform) and water was estimated by ^{1}H-NMR spectra measurement and atomic force microscope (AFM) measurement [18-20].

It was assumed that the length of linker moiety might affect on the size and morphology of the polymer nano-film. In this paper we studied on the size and morphology of polymer nano-film synthesized with the linker possessing the various length according to the previous method [18, 19]. We selected three kinds of linker shown in Fig. 2, succinic acid, glutaric acid and azelaic acid. The particle size and distribution of polymer nano-film in phosphate buffer solution was estimated by using Zeta sizer by dynamic light scattering. The morphology of polymer nano-film in dry state was also estimated by atomic force microscope (AFM).

Received April 1, 2021
Accepted May 3, 2021

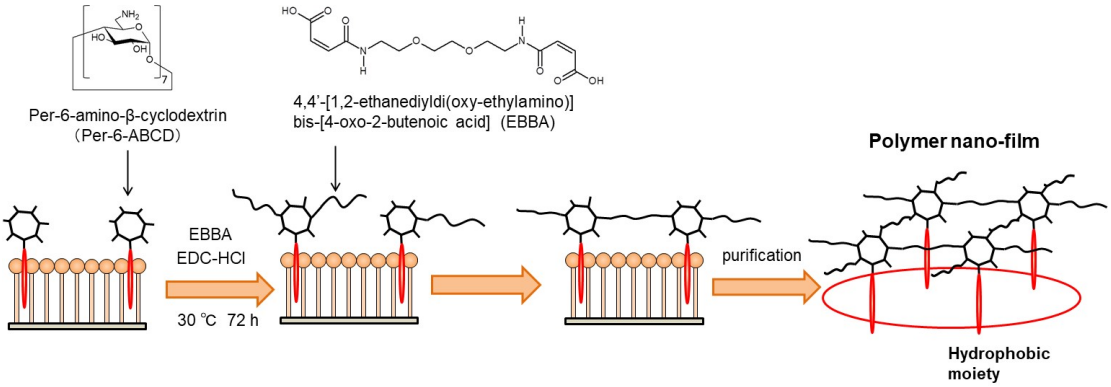

Fig. 1. Schematic illustration of the fabrication of polymer nano-film possessing hydrophilic and hydrophobic side with the self-assembled phospholipid layer containing stearic acid.

$$HOOC-(CH_2)_n-COOH$$

n=2 ; succinic acid
n=3 ; glutaric acid
n=7 ; azelaic acid

Fig. 2. Structures of linker moiety (dicarboxylic acid) which replaced EBBA shown in Fig. 1.

2. Experimental

2.1. Materials

Succinic acid was purchased from Kishida Chemical Co., Ltd. Glutaric acid and azelaic acid were obtained from Nakalai Tesque Inc. Per-6-amino-β-cyclodextrin (Per-6-ABCD) was synthesized according to the literatures [21].

2.2. Preparation of polymer nano-film

According to the literatures, the self-assembled phospholipid layer incorporating stearic acid (StA) (LDPE-StA-PC-SA) was fabricated, and then Per-6-ABCD was immobilized on the LDPE-StA-PC-SA film [17, 18]. To 100 mL of water was added 1 mL of 0.047 μmol/ml 1-ethyl-3-(3-dimethylaminopropyl) carbodiimide hydrochloride (EDC-HCl) water solution and 50 μL of 29 μmol/ml succinic acid in water. This solution was kept at 30 ºC for 30 min. The LDPE-StA-PC-SA film immobilizing Per-6-ABCD (1 x 3 cm, 40 films) was soaked into this solution at 30 ºC for 18 h. These films were washed with water. The films were immersed into 60 mL of ethanol and kept at 30 ºC for 3 h. This ethanol solution was concentrated to about 7 mL in vacuo. The concentrated solution was transferred into a pre-swollen semi-permeable membrane (Spectra/Por® 1 Dialysis Membrane Standard RC Tubing MWCO: 6 - 8 kD, Spectrum Laboratories, Inc.). The both sides of the tube were sealed with dialysis tubing closures (Dialysis Tubing Closures Standard Closure Type, 80 mm). The solution was dialyzed against 300 mL of methanol for 15 h. And then the dialysis membrane was immersed into 300 mL of pH 7.4 phosphate buffer saline (PBS) to obtain the polymer nano-film solution. The polymer nano-films crosslinked with glutaric acid or azelaic acid were also prepared in the similar manner.

2.3. Size analysis and particle distribution

The particle size (hydrodynamic radius and mean-square radius of gyration) and distribution of polymer nano-film were determined by using Zeta sizer by dynamic light scattering (Malvern Zetasizer nano ZS, Malvern instruments, UK). Three replicates were measured.

2.4 Atomic force microscope measurement in dynamic force mode

The PBS solution of polymer nano-film was exchanged into distilled water. The water solution of polymer nano-film was casted on mica, and then dried to obtain AFM sample. The morphology of polymer nano-film was investigated by AFM with dynamic force mode employing Scanning Probe Microscopy AFM-5400L (Hitachi High-Technologies Co.) and cantilever (MPP-11100-10, Veeco). AFM measurement was performed under atmospheric conditions.

3. Results and Discussion

3.1. Particle size of polymer nano-film in PBS

The particle size and distribution of polymer nano-film was measured by Zetasizer in PBS. Figure 3 shows the number average particle diameter and size distribution of polymer nano-film synthesized with various linker (dicarboxylic acid).

The character in the parentheses denotes the number of methylene carbon in the linker. The particle diameter of polymer nano-film synthesized from succinic acid was smallest among them, and that from glutaric acid was largest. The size distribution of the polymer nano-film from succinic acid was narrower than the others. The ρ value was represented by the ration of the mean-square radius of gyration ($<S^2>$) and the hydrodynamic radius (R_h), $\rho = <S^2>/ R_h$, and used to estimate the morphology of polymer in a solution. The ρ values of polymer nano-film from succinic acid and azelaic acid were about 1.3 and 0.5, respectively. When the ρ value was less than 1, the morphology of polymer was estimated as a shrink form such as spherical structure. On the other hand, in the case of more than 1 the morphology was assumed as an expanded form and the gaussian chain was expected in the case of 1.5. Therefore, it was suggested that the polymer nano-film from succinic acid might be an expanded morphology like a film and that the structure in the case of azelaic acid might be spherical.

3.2. Morphology estimation of polymer nano-film in dry condition by AFM measurement

The water solution of polymer nano-film was casted on mica, and then dried to obtain the AFM sample. Figure 4 shows the AFM images of polymer nano-film synthesized form three kinds of linkers.

Although the number average particle diameter estimated on AFM measurement was clearly smaller than those on Zetasizer, the order of average diameter from AFM measurement was coincident with those from Zetasizer. It was considered that polymer nano-film might be expanded due to solvation in PBS. The morphology of polymer nano-film from succinic acid showed nearly rectangle shape, and the average height was lowest among them. It was presumed that the shorter linker length might cause the steric hindrance between Per-6-ABCDs under crosslinking process, so that the smaller polymer nano-film could be formed. As described above it was assumed that the morphology of this polymer nano-film could be an expanded form from the ρ value. As shown in Fig. 4(B) the polymer nano-film synthesized from glutaric acid demonstrated square morphology rather than sphere and the largest size among them. On the other hand the polymer nano-film synthesized from azelaic acid showed spherical morphology and its size was smaller than that from glutaric acid. It was considered from these results that glutaric acid might produce a larger polymer nano-film than that from succinic acid due to longer linker. As the polymer nano-film of azelaic acid had a long alkyl group, it was expected that this nano-film would possess high flexibility. Therefore, it was considered that this polymer nano-film could show the spherical morphology having hydrophobic surface inside. The similar result was obtained from the ρ value. We had reported that the polymer nano-film possessing longer linker chain than azelaic acid showed spherical morphology by observing AFM measurement [19].

4. Conclusion

The conclusions drawn from the present study can be summarized as follows.

Although the size measured by Zetasizer was larger than that by AFM, it was considered that polymer nano-film might be expanded due to solvation in PBS. The morphology of the polymer nano-film synthesized from succinic acid and glutaric acid showed square morphology rather than sphere. On the other hand, the polymer nano-film from azelaic acid showed spherical morphology. It was suggested that the difference among them might be

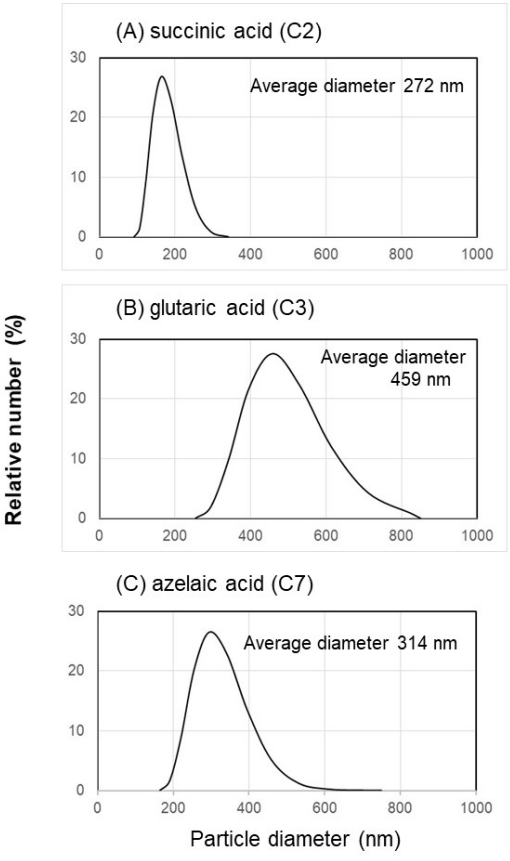

Fig. 3. Number average particle diameter and size distribution of polymer nano-film synthesized form (A) succinic acid, (B) glutaric acid, and (C) azelaic acid.

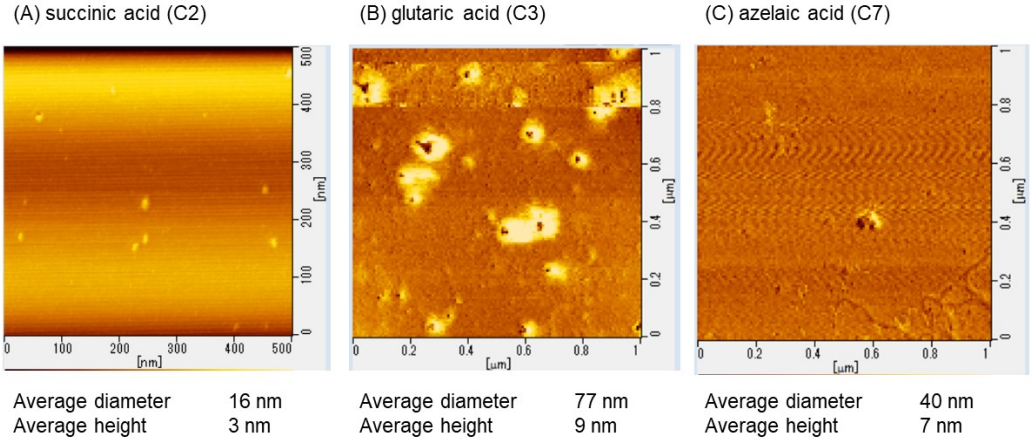

Fig. 4. AFM images of polymer nano-film synthesized form (A) succinic acid, (B) glutaric acid, and (C) azelaic acid.

ascribe to the flexibility of a polymer nano-film. Thus, the longer crosslinking chain length could be a more flexible polymer nano-film.

We are now actively elaborating the application to a drug carrier possessing more effective drug release property using polymer nano-film.

Acknowledgment

This work was financially supported in part by the OGAWA Science and Technology Fundation, which is gratefully acknowledged.

References

1. H. Tanak, M Mitsuishi, and T. Miyashita, *Chem. Lett.*, **34** (2005) 1246.
2. H. Endo, Y. Kado, M. Mitsuishi, and T. Miyashita, *Macromolecules*, **39** (2006) 5559.
3. H. Zhu, M. Mitsuishi, and T. Miyashita, *Macromolecules*, **45** (2012) 9076.
4. K. Takada, R. Sakamoto, S.-T. Yi, S. Katagiri, T. Kambe and H. Nishihara, *J. Am. Chem. Soc.*, **137** (2015) 4681.
5. C. Kuru, C. Choi, A. Kargar, D. Choi, Y. J. Kim, C. H. Liu, S. Yzvuz, and S. Jin, *Adv. Sci.*, **2** (2015) 1500004.
6. T. Bauer, Z. Zheng, A. Renn, R. Enning, A. Stemmer, J. Sakamoto, and A. D. Schlüter, *Angew. Chem.*, **50** (2011) 7879.
7. S. Motoyama, R. Makiura, O. Sakata, and H. Kitagawa, *J. Am. Chem. Soc.*, **133** (2011) 5640.
8. Z. Zheng, L. Opilik, F. Schiffmann, W. Liu, G. Bergamini, P. Ceroni, L.-T. Lee, A. Schlütz, J. Sakamoto, R. Zenobi, J. VandeBondele, and A. D. Schlüter, *J. Am. Chem. Soc.*, **136** (2014) 6103.
9. B. Ni, M. Huang, Z. Chen, Y. Chen, C.-H. Hsu, Y. Li, D. Pochan, W.-B. Zhang, S. Z. D. Cheng, and X.-H. Dong, *J. Am. Chem. Soc.*, **137** (2015) 1392.
10. N. Idota, S. Fukuda, T. Tsukahara, and Y. Sugahara, *Chem. Lett.*, **44** (2015) 203.
11. B. P. Nsdyskoyi, Y. Li, M. Imura, N. Miyamoto, T. Nakato, T. Sasaki, and Y. Yamauchi, *Angew. Chem.*, **54** (2015) 4222.
12. M. Kuzuya and T. Yamashiro, *J. Photopolym. Sci. Technol.,* **8** (1995) 381.
13. M. Kuzuya, Y. Matsuno, T. Yamashiro, and M. Tuiki, *Plasmas Polym.,* **2** (1997) 79.
14. M. Kuzuya, T. Yamashiro, S. Kondo, and M. Tuiki, *Plasmas Polym.,* **2** (1997) 133.
15. M. Kuzuya, T. Sawa, T. Yamashiro, S. Kondo, and O. Takai, *J. Photopolym. Sci. Technol.,* **14** (2001) 87.
16. S. Kondo, Y. Sasai, and M. Kuzuya, *Thin Solid Films,* **515** (2007) 4136.
17. S. Kondo, Y. Sasai, Y. Yamauchi, and M. Kuzuya, *J. Photopolym. Sci. Technol.,* **22** (2009) 477.
18. S. Kondo, T. Kusumoto, Y. Sasai, N. Doi, Y. Yamauchi, and M. Kuzuya, *J. Photopolym. Sci. Technol.,* **29** (2016) 439.
19. S. Kondo, Y. Sasai, Y. Yamauchi, and M. Kuzuya, *J. Photopolym. Sci. Technol.,* **31** (2018) 385.
20. S. Kondo, Y. Sasai, Y. Yamauchi, and M. Kuzuya, *J. Photopolym. Sci. Technol.,* **32** (2019) 541.
21. S. Kondo, M. Suzuki, Y. Sasai, Y. Yamauchi, and M. Kuzuya, *J. Photopolym. Sci. Technol.,* **26** (2013) 545.

Communication

Journal of Photopolymer Science and Technology
Volume 34, Number 5 (2021) 537−542 ©2021SPST

Viscoelastic Properties of Cholesteric Liquid Crystals from Hydroxypropyl Cellulose Derivatives

Yuki Ogiwara[1], Naoto Iwata[1], and Seiichi Furumi[1*]

[1] Department of Applied Chemistry, Faculty of Science, Tokyo University of Science, 1-3 Kagurazaka, Shinjuku, Tokyo 162-8601, Japan
**furumi@rs.tus.ac.jp*

In this study, we investigated the rheological behavior of a cholesteric liquid crystalline polymer prepared by esterification of hydroxyl propyl cellulose (HPC) with propionyl chloride. The HPC ester tethering propionyl side chains (HPC-Pr) showed thermotropic cholesteric liquid crystal (CLC) phase with visible Bragg reflection in the temperature range between 100 ºC and 135 ºC. Although visible Bragg reflection of HPC-Pr disappeared even after cooling from the temperature above isotropic phase transition temperature, we observed birefringence under crossed Nicols. Therefore, at this state, the molecular structure of HPC-Pr might be partially isotropic. The partially isotropic HPC-Pr had a relatively high viscosity as confirmed by rheological measurements. On the other hand, the viscosity decreased by shearing.

Keywords: Cellulose derivative, Cholesteric liquid crystals, Bragg reflection, Rheology, Viscoelasticity

1. Introduction

Cellulose is the most abundant polymer on the earth, and its derivatives often show liquid crystalline phase [1]. Especially, hydroxypropyl cellulose (HPC) is one of the most frequently investigated cellulose derivatives. For instance, HPC derivatives possessing acyl groups are known to show cholesteric liquid crystal (CLC) phase [2-4]. At the CLC phase, the chiral molecules are self-organized to form the helicoidal molecular structure with a periodic helical pitch. When unpolarized light propagates into the CLC, right-handed or left-handed circularly polarized light of a specific wavelength is reflected depending on the handedness of helical molecular structure. The specific reflection peak wavelength (λ_{ref}) by CLC is quantitatively determined by the following formula:

$$\lambda_{\mathrm{ref}} = np \qquad (1)$$

where n is the average refractive index of CLC and p is the helical pitch length [5]. Such a light reflection phenomenon can be regarded as a sort of Bragg reflection.

Previous report on the HPC derivatives with various acyl groups have shown that their average refractive indices are approximately 1.46 regardless of the alkyl chain length of their substitution groups [6]. By considering the experimental result, the reflection peak wavelength can be tuned by controlling the CLC helical pitch length by external stimuli. In the case of thermotropic CLCs, the helical pitch length is changed by temperature due to the thermodynamic motion of CLC molecules. Consequently, the reflection wavelength of CLC can be tuned by controlling the temperature [7].

The rheological behavior of HPC derivatives possessing acyl groups is interesting. Previous studies reported that sticky products are obtained by acylation of HPC [3,4,8-10]. This phenomenon is quite strange in that sticky polymer melts are produced from a powdery raw material of pristine HPC after the simple acylation. In addition, the fundamentals and applications of HPC derivatives with acyl groups are numerously discussed, focusing on their environmental-friendliness and CLC properties [10-15]. As well as the other CLC materials, it is expected to be applied for versatile

Received March 30, 2021
Accepted April 28, 2021

photonic devices such as temperature sensors and reflective color displays. In the perspective of practical realization of them, the knowledge of their basic physical and mechanical properties is of prime importance. However, a limited number of studies on rheological behavior of acylated HPC derivatives have been reported, while there are many papers on that of HPC solutions. It is important to comprehend the rheological behavior of polymer melts.

In this report, we describe the optical and rheological properties of a HPC derivative possessing propionyl side chains (HPC-Pr), as shown in Fig. 1. The transmission spectral measurements of HPC-Pr revealed that the reflection peak wavelength is controlled by temperature, arising from the thermotropic CLC feature. Then, the viscoelasticity of HPC-Pr is measured to investigate the rheological behaviors caused by the helical molecular structure of CLC. The present report would pave the way to understand the intrinsic physical properties of HPC derivatives from both scientific and practical viewpoints.

2. Experimental

2.1. Materials

We used a commercially available substance of HPC (Fujifilm Wako Pure Chemical Co.; Viscosity of 2.0 wt% aqueous solution, 2.0~2.9 mPa·s). The number of hydroxypropyl groups per HPC monomer unit, i.e., molar substitution value (*MS*), was determined to be 4.0 by using the ^{1}H-NMR spectrum [16]. HPC was dried under vacuum before use. Anhydrous pyridine (Kanto Chemical Co., Inc.; 99.5%), anhydrous acetone (Kanto Chemical Co., Inc.; 99.5%), and propionyl chloride (Tokyo Chemical Industry Co. Ltd.; 98.0%) were used as received.

Figure 1 shows the chemical structure of a HPC derivative possessing propionyl side chains (HPC-Pr). According to our previous report [14], HPC-Pr was synthesized by the esterification of HPC with propionyl chloride.

2.2. Measurement of optical properties

To fabricate a CLC cell, HPC-Pr was sandwiched between a pair of two glass plates with a gap of approximately 200 μm. Transmission spectra of the CLC cell were measured using a compact CCD spectrometer (Ocean Optics, USB2000+) equipped with a tungsten halogen light source for the probing white light. The temperature of CLC cell was precisely controlled using a hot stage system (Mettler Toledo, HS82 and HS1).

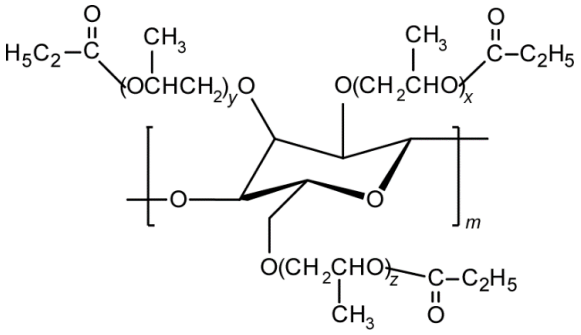

Fig. 1. Chemical structure of a hydroxypropyl cellulose derivative possessing propionyl side chains (HPC-Pr).

2.3. Measurement of rheological properties

The viscosity measurements were performed using a stress-controlled rheometer (Anton Paar, MCR102) equipped with a stainless-steel parallel plate with a diameter of 25 mm. HPC-Pr was sandwiched at the gap of approximately 500 μm. In this experiment, the shear rate ($\dot{\gamma}$) was increased from 0.01 s^{-1} to 100 s^{-1} and then decreased from 100 s^{-1} to 0.01 s^{-1} taking 41 sec in each way. By using a forced convection oven, the temperature of HPC-Pr was maintained at 100 ºC during the measurements. As heated at this temperature of 100 ºC, a reflection peak of HPC-Pr emerged around 400 nm, as mentioned below.

Oscillatory shear rheology measurements were also conducted by using the above-mentioned rheometer. The storage modulus (G') and loss modulus (G'') were measured at angular frequencies (ω) ranging from 100 rad/s to 0.1 rad/s at the temperature between 40 ºC to 100 ºC at the intervals of 20 ºC. The strain amplitude was adjusted in the range of 0.2% to 2.0%, which was sufficiently small to measure the linear viscoelasticity. The master curves were created by shifting the G' and G'' results in logarithmic scales according to the time-temperature superposition principle with reference temperature (T_{ref}) of 100 ºC. When shifting the results, the amounts of horizontal and vertical shifts of the curves at each temperature are called the horizontal shift factor (a_T) and vertical shift factor (b_T), respectively. The values a_T and b_T are dependent on the temperature.

Before each measurement, HPC-Pr was either preheated or presheared to erase any remaining the historical molecular orientation. Hereafter, the samples are noted as Pr-H or Pr-S, respectively. Pr-H was prepared by heating at 155 ºC for 5 min in

the rheometer, which was higher than the isotropic phase transition temperature of HPC-Pr (T_i = 150 ºC) to ensure the random orientation of cholesteric texture confirmed by polarized optical microscopic observation. Pr-S was prepared by shearing at the rate of 10 s^{-1} for 200 sec heated at 100 ºC, which was sufficiently long enough to reach its steady state of molecular alignment.

3. Results and discussion

3.1. Synthesis of HPC-Pr

We confirmed that all hydroxyl groups in the side chains of HPC are completely substituted with propionyl groups to form HPC-Pr. According to the identification method described in our previous report [14], the ^{1}H-NMR spectrum of HPC-Pr in $CDCl_3$ indicated that all hydroxyl groups of HPC are esterified by propionyl chloride. Also, the FT-IR spectrum showed the disappearance of a broad peak around 3500 cm^{-1}, assigned to the O-H stretching vibration of pristine HPC, after the esterification of HPC with propionyl chloride.

3.2. Reflection properties of HPC-Pr

The Bragg reflection peak wavelength of HPC-Pr was dependent on the temperature. Figure 2 shows the changes in the transmission spectrum of a cell of HPC-Pr upon stepwise heating from 100 ºC to 135 ºC at the intervals of 5 ºC. The Bragg reflection peak was continuously red-shifted from 400 nm to 635 nm upon heating from 100 ºC to 135 ºC. Such a shift of Bragg reflection peak can be attributed to the increase of the helical pitch length of the thermotropic CLC induced by temperature [7,17]. Furthermore, we confirmed that the reflection peak is blue-shifted from 635 nm to 400 nm upon cooling process from 135 ºC to 100 ºC. Therefore, the reflection wavelength shift by temperature was found to be fully reversible in the range between 100 ºC and 135 ºC.

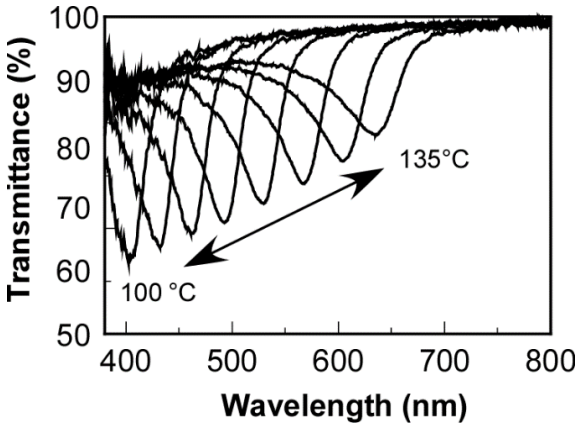

Fig. 2. Transmission spectral changes in the CLC cell of HPC-Pr upon stepwise heating from 100 ºC to 135 ºC at the intervals of 5 ºC. The reflection peak was red-shifted, accompanied by the spectral broadening, upon the heating process.

3.3. Pretreatment of HPC-Pr before rheological measurements [18]

Figure 2 also shows the broadening of reflection band as well as the decrease of reflection intensity by elevating the temperature from 100 ºC to 135 ºC, suggesting that the helical axis of CLC gradually becomes the disordered by heating close to the isotropic phase temperature. This is also supported by the fact that the Bragg reflection is not observed at 100 ºC for at least 3 h after heating at 155 ºC for 5 min once. This result emphasizes that the preheating process deteriorates the orientational order of helical axis of CLC. On the other hand, as HPC-Pr was heated at 155 ºC, followed by 100 ºC, the polarized optical microscopic observation between crossed Nicols confirmed that HPC-Pr shows slight birefringence. However, at this stage, no Bragg reflection color was observed. Taking the overall facts in account, the molecular structure of HPC-Pr after preheating process can be interpreted as follows. Although the CLC molecules form the helicoidal structure at the microscopic scale such as one helical pitch or less, the helical axis is aligned in random directions. As a result, Bragg reflection was not observed due to the randomly-aligned helical axis of CLC structure while the birefringence was observed due to the formation of CLC structure at microscopic scale. This motivated us to investigate the shearing effect of HPC-Pr.

The preshearing time was determined to be 200

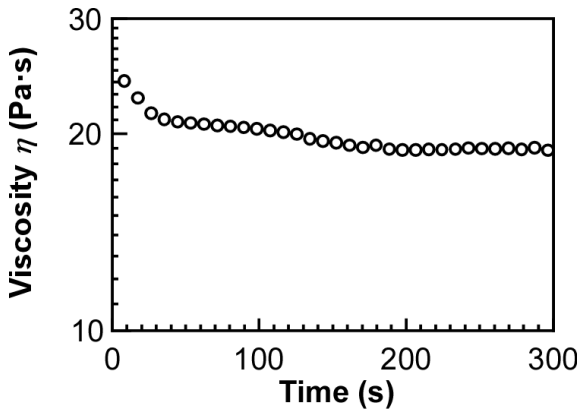

Fig. 3. Time dependence of the viscosity (η) ($\dot{\gamma}$ = 10 s^{-1}, 100 ºC) of a preheated CLC of HPC-Pr, which reached the steady state by shearing at 200 sec.

sec, which is sufficient to align CLC layers. Figure 3 shows the time dependence of viscosity of HPC-Pr measured at 100 ºC by shearing at a constant rate of 10 s^{-1}. The viscosity gradually decreased with taking the measurement time up to 150 sec. However, the viscosity became constant at 19 Pa·s despite the prolonged measurement time of 150 sec or more, suggesting that the sample reached its steady state. This experimental result also implies that the alignment of CLC layers is completed by shearing at 10 s^{-1} for 150 sec.

3.4. Rheological properties of HPC-Pr

Although both Pr-H and Pr-S exhibited shear thinning behavior, their flow curves were different when $\dot{\gamma}$ is increased, as shown in Fig. 4. Shear thinning is a decrease of viscosity with increasing the shear rate, and often occurred by structure deformation of the sample [19]. This indicates that the CLC structure of HPC-Pr is changed by shearing. Thereby, we focus on the difference of viscosity between Pr-H and Pr-S. It is well-known that the viscosity is crucially influenced by the molecular arrangements.

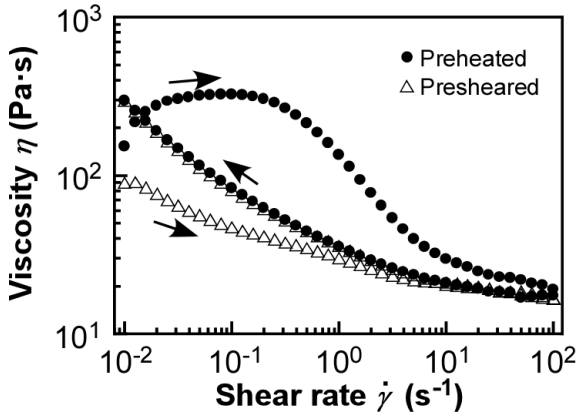

Fig. 4. Shear-rate dependences at 100 ºC of the apparent viscosity of Pr-H and Pr-S samples. The value η of Pr-H was higher than that of Pr-S in the increasing $\dot{\gamma}$ process, whereas they showed the same profiles in the decreasing $\dot{\gamma}$ process.

For instance, the viscosity of polymers whose chains entangle themselves tends to be higher than that of unentangled one [20]. The viscosity of Pr-H at 0.2 s^{-1} was 3.0×10^2 Pa·s, which was up to 7.5 times higher than that of the Pr-S (40 Pa·s). Such high viscosity of Pr-H can be attributed to the randomly oriented CLC layers. When the Pr-H is sheared, the additional force is requisite to generate well alignment of CLC layers from random state [18].

On the other hand, when $\dot{\gamma}$ was decreased, the viscosity of Pr-H and Pr-S were almost identical regardless of $\dot{\gamma}$. This is because the CLC alignment is completed in the process of increasing $\dot{\gamma}$ for both Pr-H and Pr-S.

The flow curve of Pr-H also exhibited shear thickening behavior in the $\dot{\gamma}$ range from 0.01 s^{-1} to 0.1 s^{-1}. In general, the shear thickening behavior appears with structure formation by shear. This fact implies the alignment of CLC layers is induced when $\dot{\gamma}$ is below 0.01 s^{-1}, which is reasonable for considering the randomly-arranged CLC layers. Pr-H seems to be more viscous than Pr-S.

Figures 5 (a) and 5 (b) shows the master curves of G' and G" of Pr-H and Pr-S heated at T_{ref} of 100 ºC. The master curve of Pr-H given in Fig. 5 (a) can be divided into two regions by the difference of relationship between G' and G". In the region of ω below 4.0×10^{-1} rad/s, G' exceeds G" and reaches a plateau, which implies that Pr-H is more solid-like in this region. This rigidity of Pr-H can be caused by the randomly oriented CLC layers as described above. At higher region of ω over 4.0×10^{-1} rad/s, G" became larger than G' and the slopes of G' and G" in the range above $\omega = 1.0 \times 10^2$ rad/s were

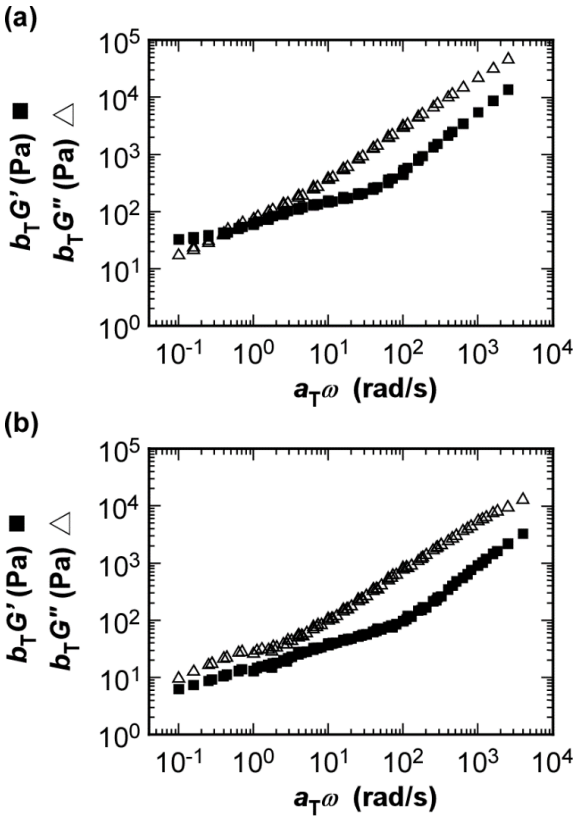

Fig. 5. Master curves of the storage modulus (G') and loss modulus (G") of HPC-Pr heated at T_{ref} of 100 ºC (a) The preheated sample (Pr-H). (b) The presheared sample (Pr-S).

estimated to be approximately 1.0 and 0.8, respectively. These values are different from those of the ideal Newtonian fluid, which would be 2.0 and 1.0, respectively. Such smaller ω dependences of G' and G" can be attributed to the disturbed flow behavior caused by the molecular orientation of CLCs.

The master curve of Pr-S presented in Fig. 5 (b) is reasonably characterized by two differences when compared with that of Pr-H as follows. First, G" exceeded G' in the entire ω range, and no plateau of G' was observed. This indicates that Pr-S is more liquid-like in lower ω regions. This liquid-like behavior might be happened by the aligned CLC structure. Second, both G' and G" of Pr-H were higher than those of Pr-S in the entire ω range. On the other hand, the slopes of both G' and G" in the range above $\omega = 1.0 \times 10^2$ rad/s were approximately 1.0 and 0.8, respectively, which was the same as those of Pr-H.

Considering the overall results, it turned out that Pr-H is more viscous and rigid rather than Pr-S. This rigidity of Pr-H might stem from the randomly oriented CLC layers, as mentioned above.

4. Conclusion

In this study, the rheological behavior of a CLC polymer derived from HPC was investigated. As the CLC polymer was preheated above the isotropic phase transition temperature, the partially isotropic structure remained even after cooling. This was confirmed by the fact that the color derived from Bragg reflection did not appear but birefringence appears in this state. In this way, the preheated CLC polymers behave more viscously and rigidly than the presheared ones, which might be attributed to their randomly oriented CLC layers. The experimental evidence is expected to be available to apply the general CLC polymers for not only the comprehension of physical properties from a scientific standpoint, but also the fabrication of novel photonic devices with CLC materials from a practical standpoint [21-25].

Acknowledgements

All of the authors express sincere thanks to Mr. R. Kawanishi of Anton Paar Japan K. K. for his technical supports and advices on the rheological measurements. Moreover, the authors would like to acknowledge Messrs. K. Hayata, Shimokawa, and Baba and Mses. R. Aoki, A. Kawaguchi, Furukawa, and S. Saito for their helpful discussions. One of the authors (S.F.) is deeply indebted to the financial supports from the Grant-in-Aid for Scientific Research (B) (No. 17H03848 and No. 21H02261) of the Ministry of Education, Science, Sports and Culture (MEXT) of Japan and NEXCO Group Companies' Support Fund to Disaster Prevention Measures on Expressways.

References

1. D. G. Gray, *J. Appl. Polym. Sci.: Appl. Polym. Symp.*, **37** (1983) 179.
2. S.-L. Tseng, A. Valente, and D. G. Gray, *Macromolecules*, **14** (1981) 715.
3. S. L. Tseng, G. V Laivins, and D. G. Gray, *Macromolecules*, **15** (1982) 1262.
4. S. N. Bhadani and D. G. Gray, *Mol. Cryst. Liq. Cryst*., **99** (1983) 29.
5. H. de Vries, *Acta Crystallogr.*, **4** (1951) 219.
6. B. Huang, J. J. Ge, Y. Li, and H. Hou, *Polymer*, **48** (2007) 264.
7. H. Kosho, S. Hiramatsu, T. Nishi, Y. Tanaka, S. Kawauchi, and J. Watanabe, *High Perform. Polym.*, **11** (1999) 41.
8. I. Rusig, J. Dedier, C. Filliatre, M. H. Godhino, L. Varichon, and P. Sixou, *J. Polym. Sci. Part A Polym. Chem.*, **30** (1992) 895.
9. K. Hayata, T. Suzuki, M. Fukawa, and S. Furumi, *J. Photopolym. Sci. Technol.*, **32** (2019) 645.
10. M. Fukawa, A. Kawaguchi, K. Hayata, R. Aoki, M. Furukawa, and S. Furumi, *J. Photopolym. Sci. Technol.*, **32** (2019) 633.
11. R. Aoki, M. Fukawa, and S. Furumi, *J. Photopolym. Sci. Technol.*, **32** (2019) 651.
12. M. Fukawa, K. Suzuki, and S. Furumi, *J. Photopolym. Sci. Technol.*, **31** (2018) 563.
13. N. Tamaoki, *Adv. Mater.*, **13** (2001) 1135.
14. T. Ishizaki, S. Uenuma, and S. Furumi, *Kobunshi Ronbunshu*, **72** (2015) 737 (in Japanese).
15. H. Shimokawa, K. Hayata, M. Fukawa, and S. Furumi, *J. Photopolym. Sci. Technol.*, **33** (2020) 467.
16. F. F. L. Ho, R. R. Kohler, and G. A. Ward, *Anal. Chem.*, **44** (1972) 178.
17. G. V. Laivins and D. G. Gray, *Polymer.*, **26** (1985) 1435.
18. L. Ramos, M. Zapotocky, T. C. Lubensky, and D. A. Weitz, *Phys. Rev. E*, **66** (2002) 031711.
19. W. W. Graessley, *J. Chem. Phys.*, **47** (1967) 5057.
20. M. Doi and S. F. Edwards, "*The Theory of Polymer Dynamics*", Clareodon Press, Oxford, 1986, p. 230-236.

21. S. Furumi, S. Yokoyama, A. Otomo, and S. Mashiko, *Appl. Phys. Lett.*, **82** (2003) 16.
22. S. Furumi, S. Yokoyama, A. Otomo, and S. Mashiko, *Appl. Phys. Lett.*, **84** (2004) 2491.
23. S. Furumi and N. Tamaoki, *Adv. Mater.*, **22** (2010) 886.
24. S. Furumi, *Chem. Rec.*, **10** (2010) 394.
25. S. Furumi, *Polym. J.*, **45** (2013) 579.

Communication

Journal of Photopolymer Science and Technology
Volume 34, Number 5 (2021) 543−548 ©2021SPST

Fabrication of Colloidal Crystal Gel Film Using Poly(*N*-vinylcaprolactam)

Takaki Kaneda[1], Yutaro Seki[2], Naoto Iwata[1], and Seiichi Furumi[1,2]*

[1] Department of Applied Chemistry, Faculty of Science,
[2] Department of Chemistry, Graduate School of Science,
Tokyo University of Science, 1-3 Kagurazaka, Shinjuku, Tokyo 162-8601, Japan
**furumi@rs.tus.ac.jp*

In this report, we successfully fabricated the colloidal crystal (CC) gel films of silica microparticles combined with a temperature-responsive biocompatible hydrogel of poly(*N*-vinylcaprolactam) (VCL). When the CC VCL film was prepared by filling VCL precursor into the void space between silica particles of CC film, followed by the thermal polymerization, the Bragg reflection peak was red-shifted from 475 nm to 535 nm due to the change of refractive index contrast. Subsequently, immersion of the CC VCL film into an excess of water led to the formation of CC VCL gel film, wherein the VCL matrix swelled in water to form the hydrogel state. As elevating the temperature from 25 °C, this CC VCL gel film showed the reflection color changes from red to green, arising from the decrease of lattice constant induced by the shrinkage of VCL hydrogel. Moreover, the reflection color changes of CC VCL gel film were found to be fully reversible. In this way, we believe that such CC VCL gel films can be potentially applied to novel temperature sensors with biocompatibility.

Keywords: Colloidal crystal, Temperature response, Poly(*N*-vinylcaprolactam), Hydrogel, Silica particle, Bragg reflection

1. Introduction

Colloidal crystals (CCs) are three dimensionally ordered arrays composed of monodisperse colloidal particles with the submicrometer size [1-5]. The CCs are also regarded as one of the 3D photonic crystals, which show the photonic band gaps in the visible wavelength range due to the spatial periodicity of the refractive indices [6-9]. Therefore, the CCs can reflect visible light in accordance with the Bragg's law [9,10]. The suspensions of uniform colloidal particles often show Bragg reflection after the deionization. However, the fluid suspensions with CCs would be impractical due to the difficulty in handling. To overcome this issue, the CC gel films, in which the CC structures are stabilized with polymer gels, have been developed for the application to intriguing photonic devices [11-15]. Many polymer gels can alter their volume in response to the changes in environmental conditions such as temperature, solvent, and pH [12-14,16]. Thus, CC gel films are attracting interests due to their ability to manipulate their Bragg reflection colors caused by the changes of lattice constant of CCs accompanied with the swelling or shrinking of gels [12-14]. Such CC gel films have been expected as sensors for detecting and monitoring the environmental fluctuations through its Bragg reflection color changes [12,15].

So far, there have been numerous reports on the temperature responsive CC gel films fabricated using poly(*N*-isopropylacrylamide) (NIPA) derivatives [12-15]. However, it is well known that acrylamide as the basic skeleton of NIPA has strong toxicity and harm for human health. This toxicity is an important concern from both practical and environmental perspectives.

Therefore, we focused on poly(*N*-vinylcaprolactam) (VCL) as a new temperature responsive hydrogel instead of NIPA. Although

Received April 1, 2021
Accepted April 30, 2021

VCL has attracted a great deal of attention for its biocompatibility in the field of biology [17-19], the report on CC gel films combined with VCL has not been made yet. Figure 1 shows the chemical structure of VCL. Because VCL has both hydrophilic and hydrophobic groups in a similar structure to NIPA, VCL hydrogel exhibits the temperature response of volume change [20-25].

In this study, we investigated the volume phase transition behavior of a pristine VCL hydrogel film by temperature. By combining the CC film of silica microparticles with VCL hydrogel, we successfully demonstrated the reflection color changes by temperature. The present report indicates that VCL is an alternative material of NIPA to produce the biocompatible CC gel films.

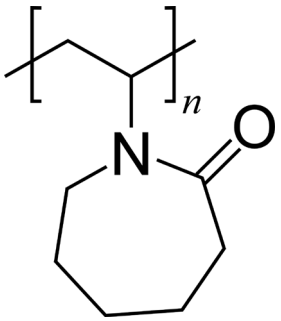

Fig. 1. Chemical structure of a temperature-responsive biocompatible hydrogel of poly(*N*-vinylcaprolactam) (VCL).

2. Experimental

2.1. Materials

As a monomer, *N*-vinylcaprolactam was purchased from Sigma-Aldrich Japan. After recrystallization from hexane and heating above the melting temperature of 38 °C, *N*-vinylcaprolactam was used to prepare the VCL precursor. We adopted 1,4-bis(acryloyloxy)butane (BAOB) as a crosslinking agent and 2,2'-azobis(isobutyronitrile) (AIBN) as a thermal radical initiator, which were obtained from Tokyo Chemical Industry Co., Ltd. The materials were used as received without any further purification. A 20 wt% aqueous suspension of silica microparticles with the diameter of ca. 220 nm was obtained from Nippon Shokubai Co., Ltd.

2.2. Fabrication of pristine VCL gel film

A mixture of *N*-vinylcaprolactam (2.0 g) and BAOB (50~200 μL) was degassed under nitrogen flow at 50 °C. In this time, *N*-vinylcaprolactam showed the supercooled liquid state which maintained the liquid state below its melting temperature. After 20 min, AIBN (6.0 mg) was added into the mixture at room temperature to prepare the VCL precursor. Successively, the VCL precursor was injected into a pair of two glass plates with a gap of 800 μm, and heated at 60 °C for 4 h. The VCL gel film was obtained after exfoliating from the glass plates, and subsequently immersing into an excess of water for swelling of VCL matrix.

2.3. Fabrication of CC films of silica microparticles stabilized with VCL and VCL hydrogel gel

A CC film was formed on a glass substrate by dropping an aqueous suspension of silica microparticles with the diameter of ca. 220 nm on a hydrophilic glass substrate and heating at 90 °C for 40 h. Then, another glass plate was covered on the CC film with a gap of 500 μm, and the VCL precursor was injected into the pair of two glass plates. The CC film stabilized with VCL (CC VCL film) was obtained after heating at 60 °C for 4 h for the thermal polymerization of VCL precursor. Finally, after immersing the CC VCL film in water, we obtained the CC film stabilized with VCL hydrogel (CC VCL gel film).

2.4. Measurement of the volume phase transition temperature of pristine VCL gel film

After the pristine VCL gel film was cut into a disk shape with a diameter of 10 mm, its diameter was measured in the temperature range of 25 °C to 50 °C.

2.5. Measurement of the reflection spectra

The reflection spectra of CC films were measured using a compact CCD spectrometer of Ocean Optics, Inc. equipped with both halogen light source and optical fiber with reflection probe. The reference was taken as the distance between reflection probe and total reflection mirror was set at 2 mm. Then, the reflection spectra of CC film, CC VCL film, and CC VCL gel film were measured at the same distance for the quantitative comparison of spectral shapes and their light intensities. As the white light was irradiated from the surface normal of film, the reflection spectra were measured in the direction of regular reflection.

3. Results and discussion

3.1. Diameter changes of VCL hydrogel film

Figure 2 (A) shows the changes in diameter of a VCL hydrogel film in the temperature range from 25 °C to 50 °C. The diameter of VCL hydrogel film decreased in a sigmoidal way with elevating the

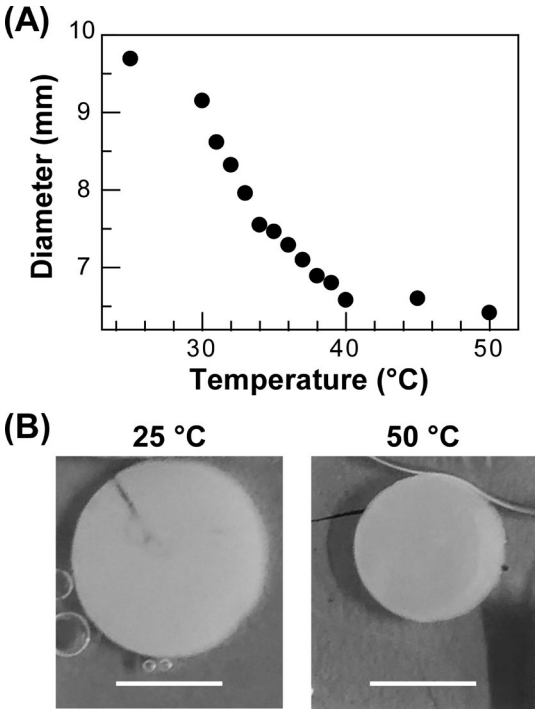

Fig. 2. (A) Changes in diameter of the pristine VCL gel film as a function of temperature from 25 °C to 50 °C. The film thickness was maintained at 800 μm using PTFE spacers during the measurement. (B) Snapshot images of the pristine VCL gel film at 25 °C (left) and 50 °C (right). The scale bars represent 5 mm.

temperature, suggesting the thermally induced shrinkage of VCL gel film. Especially, the VCL hydrogel film shrank drastically in the range from 30 °C to 34 °C. Therefore, it found that the volumetric phase transition of VCL hydrogel film occurs at around 32 °C. Moreover, the VCL hydrogel film shrank by 33% at 50 °C from initial state at 25 °C, as shown in Fig. 2 (B). The shrinkage of VCL hydrogel film upon increasing the temperature can be explained by the interaction between the hydrophilic groups and hydrophobic groups in the chemical structure of VCL [24]. The VCL hydrogel was hydrophilic and swollen state below approximately 32 °C. However, as heating, the VCL hydrogel changed gradually from hydrophilic to hydrophobic because hydrophobic interactions became dominant [24]. As a result, hydrophobic interactions led to the aggregation of polymer chains and shrinkage of VCL hydrogel. Furthermore, it turned out that the volumetric phase transition temperature of VCL hydrogel is nearly equal to that of NIPA gel with the temperature of 32~34 °C [14,15,22]. Thus, we considered that the VCL gel would be applied in the biological realm such as drug delivery system from its volumetric phase transition temperature which is close to human body temperature.

3.2. Fabrication and reflection properties of CC films of silica microparticles stabilized with VCL and VCL hydrogel

As mentioned in the Experimental Section, we fabricated three kinds of films: CC film, CC VCL film, and CC VCL gel film.

Figure 3 shows the reflection spectra of their films. As the CC film of silica microparticles with the diameter of ca. 220 nm, the reflection peak of CC films appeared at 475 nm and the reflectance reached around 60%, which suggests the relatively high uniformity of CC structure. After that, the void space between the silica microparticles in the CC film was filled with VCL precursor, followed by heated at 60 °C for 4 h for the thermal polymerization. In other words, the background medium of CC film was exchanged from air to VCL matrix. At this stage, the reflection peak of CC VCL film appeared at 535 nm and the reflectance was around 20%. The decrease in reflectance can be ascribed to the slight disorder of silica microparticles in the CC structure by immersing the VCL precursor. Finally, after the CC VCL film was immersed into an excess of water to form the CC VCL gel film, the reflection peak was shifted from 535 nm to 640 nm. From the experimental results, we presumed that the reflection wavelength is red-shifted due to the changes of refractive index contrast caused by filling the background of silica microparticles in CC film with air, VCL, and VCL hydrogel.

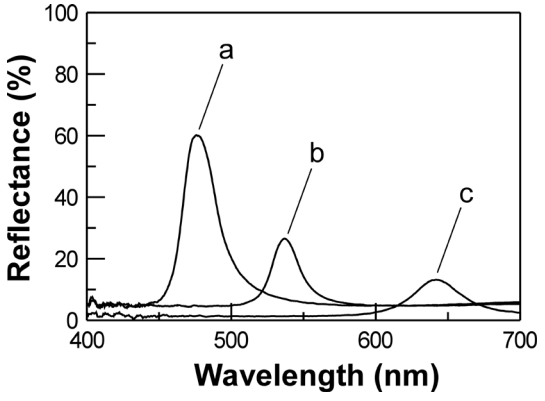

Fig. 3. Reflection spectra of three kinds of CC films of silica microparticles such as CC film (a), CC VCL film (b), and CC VCL gel film (c).

The reflection peak wavelengths of CC film and CC VCL film were reasonable from the theoretical

viewpoint. In general, the reflection peak of CC film stems from the light reflection from the (111) plane of face-centered cubic lattice of microparticles. Taking the geometric structure of CC in account, the lattice spacing along the (111) plane (d_{111}) is theoretically expressed as the following equation.

$$d_{111} = \frac{a}{\sqrt{3}} \quad (1)$$

where a corresponds to the lattice constant of microparticles. Therefore, the reflection peak wavelength (λ) of CCs can be calculated by the following equation.

$$\lambda = \frac{2a(0.74n_P + 0.26n_B)}{\sqrt{3}} \quad (2)$$

where n_P is the refractive index of silica microparticles, n_B is the refractive index of background medium.

In this study, we used silica microparticles. So, n_P is assumed to be 1.43 according to the experimental data given from Nippon Shokubai Co., Ltd. In the case of CC film, n_B is 1.00 because the background medium of CC film is air. According to the equation (2) combined with n_P = 1.43 and n_M = 1.00, the Bragg reflection peak wavelength of CC film was calculated to be 474 nm, which is almost identical to that of measured spectrum (λ = 475 nm). In the case of CC VCL film, n_B is 1.55 because the background medium is VCL. Therefore, theoretical reflection wavelength is theoretically calculated to be 526 nm, which is also well-agreed with that of measured spectrum (λ = 535 nm). However, the theoretical reflection wavelength of CC VCL gel film was not consistent with the measured value. The Bragg reflection peak of VCL gel film appeared at 640 nm, which is much longer than the one calculated by the equation (2) (λ = 505 nm). From this result, we considered that the reflection wavelength shift of CC VCL gel film before and after immersion in water happens probably from not only the change of refractive index contrast, but also the increase of lattice constant of CCs. In fact, the ratio of the Bragg reflection peak between measured value (λ = 640 nm) and theoretically value (λ = 505 nm) regarding CC VCL gel film was 127%. This value is comparable to the swelling degree of CC VCL film before and after immersing into water. In the preliminary experiment, after the CC VCL film was immersed into an excess of water to form the CC VCL gel film, we observed that the CC VCL gel film swells by 135% rather than the state of CC VCL film without water. Therefore, we considered that the ratio of the Bragg reflection peak in CC VCL gel film is caused by changing the volume of CC VCL film before and after immersing into water. This is because the volume change rate was nearly equal to the difference rate of Bragg reflection peak in CC VCL gel film.

3.3. Temperature response of reflection properties of CC films of silica microparticles stabilized with VCL hydrogel

Furthermore, we pursued the changes of reflection spectra of the CC VCL gel film upon stepwise heating from 25 °C. Figure 4 (A) shows the changes in reflection spectrum of CC VCL gel film in the temperature range between 25 °C and 40 °C at the intervals of 5 °C. From this result, it was found that reflection wavelength is blue-shifted by heating from 25 °C to 35 °C. Such a shift of the

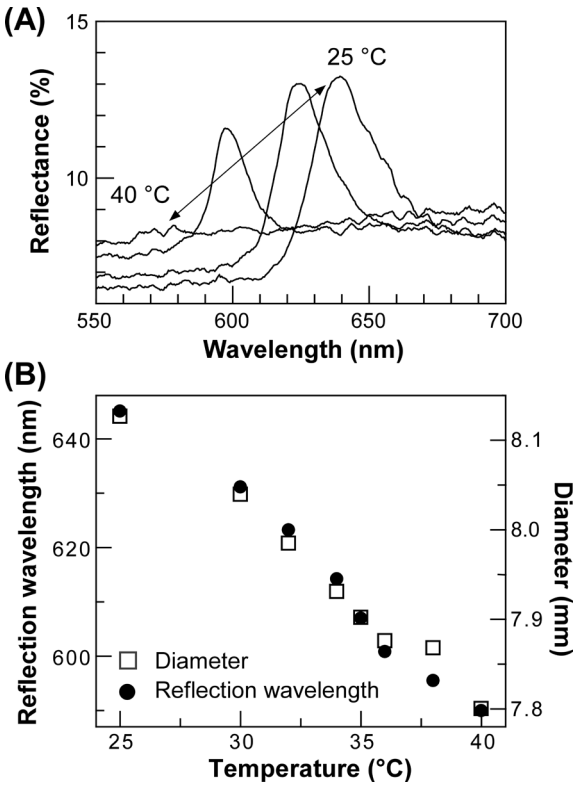

Fig. 4. (A) Reflection spectra of the CC VCL gel film in the range between 25 °C and 40 °C measured at the intervals of 5 °C. (B) Changes in reflection wavelength and diameter of the CC VCL gel film in the range between 25 °C and 40 °C. The film thickness was maintained at 300 μm using PTFE spacer during the measurement.

Bragg reflection peak can be ascribed to the decrease of lattice constant of CCs arisen from the shrinkage of VCL hydrogel triggered by heating.

This is supported by the fact that the Bragg reflection wavelength is continuously blue-shifted exactly in the same manner to the monotonous reductions in diameter of CC VCL gel film, as shown in Fig. 4 (B).

However, the reflection peak thoroughly disappeared as heating above 40 °C because the CC VCL gel film became whitely-turbid. This behavior might be caused by the aggregation of polymer chains due to the shrinkage of VCL hydrogel. On the other hand, this CC VCL gel film showed the revival and red-shift of reflection peak upon cooling process from 40 °C. Moreover, we observed that the reflection peak wavelength observed on cooling process is consistent with the that of observed on heating process at the same temperature. In this way, this CC VCL gel film can be utilized as a temperature sensor with biocompatibility to quantitatively visualize the temperature through the reflection colors because the reflection peak wavelength is reversibly shifted on heating or cooling process.

4. Conclusion

In this report, we successfully fabricated the temperature-responsive CC film of silica micro-particles with VCL hydrogel by filling the void space of CC film with VCL precursor. After exchanging from air to VCL hydrogel in the void space, the Bragg reflection peak was red-shifted from 475 nm to 640 nm by changes in the refractive index contrast as well as increase of lattice constant, as supported by the theoretical calculation combined with swelling degree of VCL hydrogel.

Furthermore, we demonstrated the changes in reflection color of CC VCL gel film between red and green induced by temperature. The reflection color change from red to green happened from the decrease of lattice spacing of colloidal particles in CC simultaneously with shrinking behavior of VCL hydrogel film. As the future outlook, we will attempt the fabrication of VCL gel films with the drastic changes of reflection peak in the wide visible wavelength range. The present report provides promising clues to fabricate the CC films with the temperature-responsive biocompatible hydrogel of VCL from the environmental viewpoint. Moreover, as the light-emitting dyes are embedded in the CC VCL gel films, we anticipate that the low threshold laser action is generated by optical excitation, arising from the effect of photonic band gaps of CC structures [26-28].

Acknowledgements

All of the authors express sincere thanks to Messrs. Y. Shibata and T Kawa and Mses. K. Tokuhiro and M. Obara for his helpful supports concerning the experiments and discussions. One of the authors (S.F.) would like to acknowledge the financial supports from the Grant-in-Aid for Scientific Research (B) (No. 17H03848 and No. 21H02261) of the Ministry of Education, Science, Sports and Culture (MEXT) of Japan and NEXCO Group Companies' Support Fund to Disaster Prevention Measures on Expressways.

References

1. P. Pieranski, *Contemp. Phys.*, **24** (1983) 25.
2. O. D. Velev and E. W. Kaler, *Adv. Mater.*, **12** (2000) 531.
3. A. Stein, B. E. Wilson, and S. G. Rudisill, *Chem. Soc. Rev.*, **42** (2013) 2763.
4. H. Fudouzi and Y. Xia, *Langmuir*, **19** (2003) 9653.
5. S. Furumi, H. Fudouzi, and T. Sawada, *Laser & Photon. Rev.*, **4** (2010) 205.
6. Y. Seki, Y. Shibata, and S. Furumi, *J. Photopolym. Sci. Technol.*, **33** (2020) 473.
7. E. Yablonovitch, *Phys. Rev. Lett.*, **58** (1987) 2059.
8. J. D. Joannopoulos, P. R. Villeneuve, and S. Fan, *Nature*, **386** (1997) 143.
9. A. Richel, N. P. Johnson, and D. W. McComb, *Appl. Phys. Lett.*, **76** (2000) 1816.
10. P. A. Rundquist, P. Photinos, S. Jagannathan, and S. A. Asher, *J. Chem. Phys.*, **91** (1989) 4932.
11. J. H. Holtz and S. A. Asher, *Nature*, **389** (1997) 829.
12. D. Nakayama, Y. Takeoka, M. Watanabe, and K. Kataoka, *Angew. Chem. Int. Ed.*, **42** (2003) 4197.
13. K. Matsubara, M. Watanabe, and Y. Takeoka, *Angew. Chem. Int. Ed.*, **46** (2007) 1688.
14. J. M. Weissman, H. B. Sunkara, A. S. Tse, and S. A. Asher, *Science*, **274** (1996) 959.
15. T. Kanai, D. Lee, H. C. Shum, and D. A. Weitz, *Small*, **6** (2010) 807.
16. A. B. Imran, K. Esaki, H. Gotoh, T. Seki, K. Ito, Y. Sakai, and Y. Takeoka, *Nat. Commun.*, **5** (2014) 5124.
17. M. Prabaharan, J. J. Grailer, D. A. Steeber, and S. Gong, *Macromol. Biosci.*, **8** (2008) 843.
18. J. Liu, A. Debuigne, C. Detrembleur, and C. Jérôme, *Adv. Healthcare Mater.*, **3** (2014) 1941.

19. A. Imaz and J. Forcada *J. Polym. Sci. Part A*: *Polym. Chem.*, **48** (2010) 1173.
20. V. Kozlovskaya and E. Kharlampieva, *ACS Appl. Polym. Mater.*, **2** (2020) 26.
21. K. M. Rao, K. S. V. K. Rao, and C.-S. Ha, *Gels*, **6** (2016) 2.
22. S. Kozanoğlu, T, Özdemir, and A, Usanmaz, *J. Macromol. Sci. Part A-Pure Appl. Chem.*, **48** (2011) 467.
23. A. C. W. Lau and C. Wu, *Macromolecules*, **32** (1999) 581.
24. E. E. Makhaeva, L. T. M. Thanh, S. G. Starodoubtsev, and A. R. Khokhlov, *Macromol. Chem. Phys.* **197** (1996) 1973.
25. M. Beija, J.-D. Marty, and M. Destarac, *Chem. Commun.*, **47** (2011) 2826.
26. S. Furumi, H. Fudouzi, H. T. Miyazaki, and Y. Sakka, *Adv. Mater.,* **19** (2007) 2067.
27. S. Furumi, T. Kanai, and T. Sawada, *Adv. Mater.,* **23** (2011) 3815.
28. S. Furumi, H. Fudouzi, and T. Sawada, *J. Mater. Chem.*, **22** (2012) 21519.

Communication

Journal of Photopolymer Science and Technology
Volume 34, Number 5 (2021) 549−554 ©2021SPST

Synthesis and Optical Properties of Completely Etherified Hydroxypropyl Cellulose Derivatives

Yo Baba[1], Seina Saito[2], Naoto Iwata[1,2], and Seiichi Furumi[1,2*]

[1] Department of Applied Chemistry, Faculty of Science,
[2] Department of Chemistry, Graduate School of Science, Tokyo University of Science,
1-3 Kagurazaka, Shinjuku, Tokyo 162-8601, Japan
**furumi@rs.tus.ac.jp*

Previously, we have reported on the preparation of hydroxypropyl cellulose (HPC) ether derivatives by the Williamson ether synthesis as S_N2 reaction. In this article, we carried out the optimization of synthesis conditions to obtain the completely etherified HPC derivatives tethering hexyl ethers in the side chains (HPC-HeEt). By adopting *N*-methyl-2-pyrrolidinone (NMP) as a reaction solvent, as-synthesized HPC-HeEt showed high substitution degree of hexyl ethers, probably arising from high solubility of NaOH in NMP. Moreover, this optimized reaction condition enabled to apply the synthesis of completely etherified HPC derivatives with different length of alkyl chains. These HPC ether derivatives showed thermotropic cholesteric liquid crystal (CLC) phase with visible Bragg reflection. As a result, their reflection properties would be stable against humidity due to the robust bonding of ether group rather than ester.

Keywords: Cellulose, Williamson ether synthesis, S_N2 reaction, Cholesteric liquid crystals, Bragg reflection

1. Introduction

Hydroxypropyl cellulose (HPC) prepared by etherifying hydroxy groups of pristine cellulose with propylene oxide, as shown Fig. 1. The HPC derivatives are known to exhibit cholesteric liquid crystal (CLC) phase in the thermotropic manner through the chemical modification with appropriate side chains [1-10]. The CLC molecules spontaneously form the periodic helicoidal assemblages of nematic liquid crystalline layers by the intrinsic twisting force of chiral molecules. One of the most unique optical properties of CLCs is the selective light reflection, which can be regarded as a kind of Bragg reflection [11-16]. The maximum wavelength (λ) and spectral bandwidth ($\Delta\lambda$) of reflection peak are numerically expressed by the following equations of (1) and (2), respectively:

$$\lambda = n \cdot p \qquad (1)$$

$$\Delta\lambda = \Delta n \cdot p \qquad (2)$$

where n is the average refractive index of CLC, p is the helical pitch length, and Δn is the optical anisotropy corresponding to the difference between extraordinary and ordinary refractive index [17].

Hitherto, numerous reports on the HPC ester derivatives have shown thermotropic CLC phase with visible reflection characteristic [18]. The reflection properties of HPC ester derivatives would be vulnerable under highly humid condition due to the hydrolysis of ester linkages with water. This is because the ester linkage is easily cleaved due to its lower interatomic binding energy. To overcome this drawback for the practical applications, we have reported on the preparation of HPC ether derivatives by Williamson ether synthesis [19]. Such stable ether linkage maintains their reflection properties of CLC phase. However, we have not yet succeeded

Received April 1, 2021
Accepted April 28, 2021

in the complete etherification of HPC with long alkyl chains. Moreover, the reflection peak wavelengths of HPC ester derivatives are remarkably affected by the degree of substitution, i.e. the amount of remaining hydroxyl groups of HPC ester derivatives [20]. This tendency might be also observed for the HPC ether derivatives. Therefore, it is necessary to optimize the synthetic conditions for the complete etherification of HPC with alkyl side chains.

In this report, we optimized the synthesis conditions to proceed the complete etherification of HPC with hexyl ether groups in the side chains (HPC-HeEt), as presented in Fig. 1. We found that the combination of *N*-methyl-2-pyrrolidinone (NMP) as a solvent and NaOH as a base ensures us to synthesize HPC ether derivatives with high substitution degree. Also, it was confirmed that this reaction condition can be applied to the synthesis of other HPC ether derivatives with different length of alkyl chains.

2. Experimental

2.1. Synthesis of HPC hexyl ether derivative (HPC-HeEt)

We used commercially available HPC (FUJIFILM Wako Pure Chemical Co.; Viscosity of 2.0 wt% aqueous solution, 2.0~2.9 mPa·s) as the starting material. HPC was dried in vacuo overnight prior to use. When we measured ^{1}H-NMR spectrum of this pristine HPC in $CDCl_3$, the molar amount of chemically combined propylene oxide per anhydroglucose unit, i.e., the molar substitution (*MS*), was found to be 3.98. The *MS* value denotes the sum of *x*, *y*, and *z* in the Fig. 1. Therefore, the average molecular weight per anhydroglucose unit can be calculated to be 394 in g/mol. Subsequently, we analyzed the changes in ^{1}H-NMR spectrum of HPC during titration with trichloroacetyl isocyanate. From the ^{1}H-NMR spectral changes, the number of hydroxy groups substituted per anhydroglucose unit, i.e., the degree of substitution (*DS*), was estimated to be 2.40 according to the previous report [21].

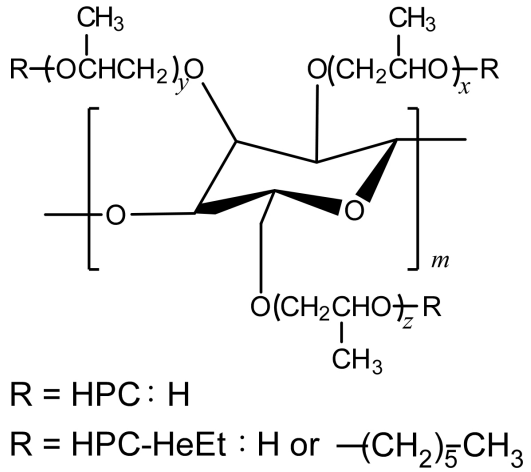

Fig. 1. Chemical structures of hydroxypropyl cellulose (HPC) and its derivative tethering hexyl ethers in the side chains.

We prepared HPC hexyl ether derivatives by the Williamson ether synthesis in different conditions, as compiled in Table 1. Here, the synthesis procedure of HPC-HeEt as an example is described as follows.

5.00 g of HPC was completely dissolved in 80.0 mL of dry *N,N*-dimethylformamide (DMF), and was subsequently added by 26.5 mL of 1-bromohexane (HeBr; 5.00 eq. to hydroxy groups of HPC). After stirring for 30 min at 65 ºC, 7.60 g of powdered NaOH (5.00 eq to hydroxy groups of HPC) and 1.58 g of KI (5.00 mol% to alkyl bromide) were added. After that, this reaction mixture was stirred at 65 ºC for 48 h [19]. Subsequently, the reaction mixture was concentrated by evaporating the solvent, and poured into an excess of water. The impurities such as NaBr, unreacted NaOH, and 1-bromohexane were removed through repeated cycles of reprecipitation from tetrahydrofuran to water. Finally, the product was dried in vacuo at room temperature overnight to obtain the purified HPC-HeEt.

2.2. Fabrication of CLC cells

To fabricate CLC cells, HPC derivatives were sandwiched between the pair of two glass substrates. The cell gap was adjusted by polytetrafluoro-ethylene film spacers of with the thickness of ca. 200 μm.

Table 1. Synthesis conditions of HPC ether derivatives and their etherification degrees.

Entry	Solvent	Base (Amount)	Alkyl bromide	Etherification degree
1	DMF	NaOH (5 eq.)	HeBr	1.85
2	DMF	K_2CO_3 (5 eq.)	HeBr	n.r.
3	DMF	NaH (3 eq.)	HeBr	n.r.
4	NMP	NaOH (5 eq.)	HeBr	2.84
5	DMSO	NaOH (5 eq.)	HeBr	2.32
6	NMP	K_2CO_3 (5 eq.)	HeBr	n.r.
7	NMP	NaH (3 eq.)	HeBr	n.r.
8	NMP	KOH (5 eq.)	HeBr	1.89
9	NMP	NaOH (3 eq.)	HeBr	2.28
10	NMP	NaOH (5 eq.)	PeBr	3.00
11	NMP	NaOH (5 eq.)	BuBr	3.00
12	NMP	NaOH (5 eq.)	PrBr	3.00

2.3. The measurement of transmission spectra of CLC cells

Transmission spectra of the CLC cell were acquired by a compact CCD spectrometer (Ocean Optics, USB2000+) equipped with a collimated white light from a halogen light source (Ocean Optics, HL-2000). To evaluate the temperature dependences of reflection peak wavelengths of HPC ether derivatives, the temperature of CLC cell was precisely controlled by a hot stage system (Mettler-Toledo, HS82 & HS1).

3. Results and discussion

3.1. Estimation procedure for the etherification degree of HPC- HeEt by ^{1}H-NMR spectrum

Figure 2 shows the representative experimental result of ^{1}H-NMR spectrum of HPC-HeEt. The proton peaks around 0.8 ppm is assigned as the signals "a" corresponding to the terminal methyl groups in the inset of Fig. 2. In this study, the etherification degree of hexyl groups *(Hee*) was expressed by the following equation:

$$Hee = \frac{A(7 + 6MS)}{3 - 13A} \qquad (3)$$

where *A* is the integrated value of the signal peak "a" and *W* is the sum of the integrated values of all of protons in HPC-HeEt. As mentioned in the Experimental Section, we adopted the *MS* value of 3.98. It should be noted that the maximum of *Hee* is three as HPC monomer unit has three hydroxyl groups in its side chains. Additionally, FT-IR spectrum measurements before and after the Williamson ether synthesis were conducted to confirm the etherification of hydroxyl groups of HPC by checking the peak intensity of a broad peak at approximately 3500 cm^{-1} assigned to the stretching vibration of hydroxyl groups of pristine HPC. For instance, when the hydroxyl groups of HPC were completely etherified with hexyl ether side chains, the peak around 3500 cm^{-1} by stretching vibration of hydroxyl group thoroughly disappeared.

3.2. Conventional synthesis of HPC hexyl ether derivative (HPC-HeEt)

As a conventional synthesis, the Williamson ether synthesis proceeded in DMF in the presence of NaOH (Entry 1 in Table 1). As the product was analyzed by ^{1}H-NMR spectrum, the etherification degree of hexyl groups (*Hee*) was calculated to be 1.85 according to Eq. (3). This *Hee* value means that only 61.7% (1.85/3.00) of hydroxyl groups of HPC were etherified with hexyl bromide after the synthesis of HPC-HeEt. To prepare the completely etherified HPC derivative, we attempted the optimization of synthesis conditions of HPC ether derivatives in the following section.

3.3. Optimization of synthesis conditions of HPC ether derivatives

We carried out the syntheses of HPC ether derivatives by changing the reaction conditions such as solvent or base, as listed in Table 1.

First, we synthesized the HPC ether derivatives using three kinds of bases such as K_2CO_3, NaOH, and NaH. Herein, all of the solvent was DMF (Entries 1~3 in Table 1). When K_2CO_3 was adopted as a base, specified product was not obtained. This can be ascribed to the low solubility of K_2CO_3 in DMF. When NaH was used, viscous product precipitated immediately as gentle adding NaH into the reaction solution. The viscous products can be considered as an ionic

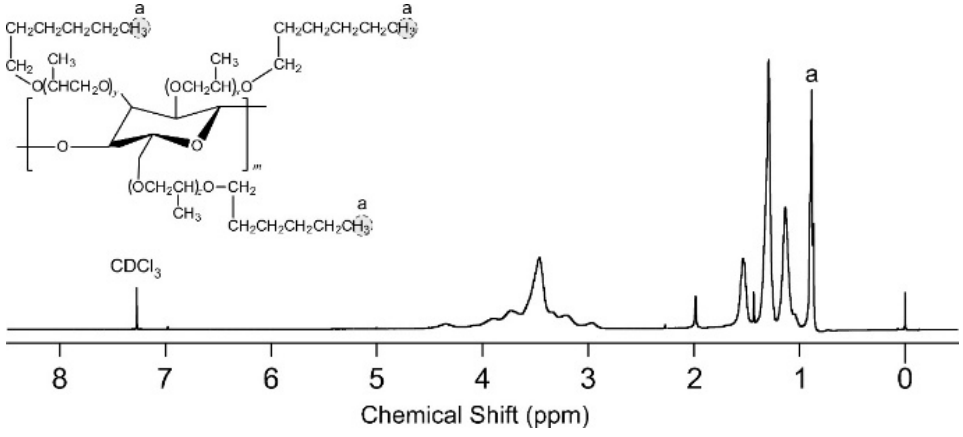

Fig. 2. ^{1}H-NMR spectrum of HPC-HeEt in $CDCl_3$ with tetramethylsilane as the internal standard. The inset shows the chemical structure of HPC-HeEt and its peak assignment in the NMR spectrum.

species formed by deprotonation of hydroxyl groups in HPC. Such ionic species cannot be dissolved in DMF. Therefore, the precipitations appeared in the reaction solution. From this result, we considered that the complete etherification of HPC is impeded by the precipitations of ionic species.

Secondly, we examined the effect of solvent on the etherification of HPC. Since the Williamson ether synthesis is regarded as the S_N2 reaction, the solvents with high polarity are known to promote the reaction. In this study, we used *N*-methyl-2-pyrrolidinone (NMP) and dimethylsulfoxide (DMSO) which would show higher solubility rather than DMF (Entries 4 and 5 in Table 1). In both cases, although we carried out the etherification of HPC in the same procedure, the reaction solutions were purified by the dialysis. When NMP was used, we obtained the product of HPC-HeEt whose *Hee* value was relatively high as 2.84. This *Hee* value was adequately high, as compared with that of synthesized using DMF as a solvent (*Hee*=1.85; Entry 1 in Table 1).

Figure 3 shows the comparison of FT-IR spectra of HPC-HeEt synthesized by using DMF and NMP as solvent. As is evident from this figure, there is difference in the peak intensity around 3500 cm^{-1}, which is assigned to the stretching vibration of hydroxyl groups, as mentioned above. This peak intensity was much smaller than that of synthesized using DMF, indicating that HPC-HeEt synthesized in NMP show higher *Hee* value rather than that synthesized in DMF. This result can be also explained from the difference of solubilities of NaOH. We confirmed that NMP can dissolve large amounts of NaOH while DMF cannot dissolve NaOH. Such a difference of solubility may enhance the reactivity as well as *Hee* value of HPC-HeEt. Additionally, when we used DMSO as a solvent, the solid product precipitated in the reaction solution and the *Hee* value was 2.32. This solid product can also be considered as an ionic species formed by deprotonation of hydroxyl groups in HPC, thereby impeding the complete etherification of HPC. From these results, we concluded that NMP is the most appropriate solvent for the etherification of HPC.

Thirdly, we changed the bases while using NMP as a solvent (Entries 6 and 7 in Table 1). Consequently, the same results were obtained when we used K_2CO_3 and NaH in DMF. Accordingly, the synthesis condition with combination of NMP and NaOH would be the best for synthesized HPC-HeEt with high *Hee* values.

Finally, we attempted to further optimize the reaction condition to synthesize HPC-HeEt (Entries 8 and 9 in Table 1). When we used KOH as a base, *Hee* value of product was estimated to be 1.89. It can be ascribed that deprotonation of hydroxyl groups in HPC is prevented by common ion effect caused by the addition of KI. When we decreased the amount of NaOH from 5.0 eq. to 3.0 eq., *Hee* value also decreased from 2.84 to 2.28 (Entries 4 and 9, Table 1). This is also attributed to the lower deprotonation speed by reducing the amount of base. Consequently, it was concluded that the synthesis using NMP and 5.0 eq. of NaOH was an ideal condition for synthesizing HPC-HeEt with high *Hee* values.

To show the versatility of this reaction condition, we synthesized a series of HPC ether derivatives with pentyl (HPC-PeEt), butyl (HPC-BuEt), and propyl ether side chains (HPC-PrEt) on the same conditions (Entries 10, 11, and 12 in Table 1). As a result, we successfully synthesized the completely etherified HPC derivatives. In all the cases, we confirmed that the *Hee* values reach 3.00 at the maximum estimated from ^{1}H-NMR spectra.

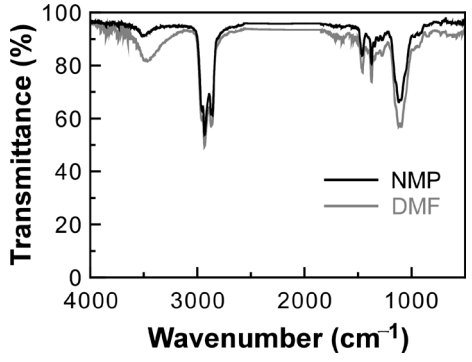

Fig. 3. Comparison of FT-IR spectra of HPC-HeEt synthesized by using DMF (Gray curve) and NMP (Black curve) as a reaction solvent.

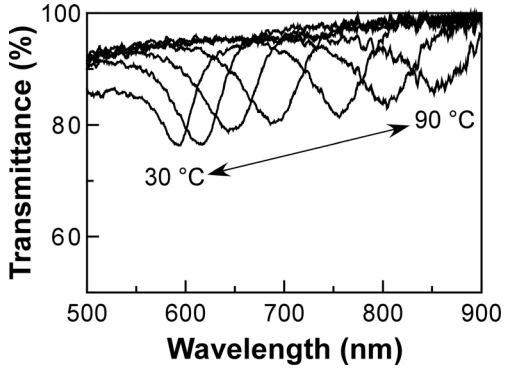

Fig. 4. Transmission spectral changes of the CLC cell of HPC-HeEt with *Hee* value of 2.84 as a function of temperature from 30 ºC to 90 ºC.

Furthermore, the complete etherification of HPC is supported by the disappearance of peak at approximately 3500 cm^{-1} in the FT-IR spectra.

3.4. Reflection properties of thermotropic CLCs of HPC ether derivatives

Figure 4 shows the changes in transmission spectrum of a CLC cell of HPC-HeEt with the *Hee* value of 2.84 upon heating process. At 30 ºC, a reflection peak around 590 nm was confirmed as red reflection color. When this CLC cell was heated from 30 ºC in stepwise manner, the reflection peak continuously shifted to longer wavelength, arising from the thermally induced expansion of the CLC helical pitch length. As heated at 90 ºC, the reflection peak reached 850 nm, corresponding to the near infrared wavelength range. In addition, when the CLC cell of HPC-HeEt was heated over 100 ºC, the reflection band thoroughly disappeared. To confirm the disappearance of reflection peak, we observed the optical texture of CLC cell of HPC-HeEt by using a polarized optical microscope upon heating process. As a result, we revealed the transition from CLC to isotropic phase heated around 105 ºC. This result implies that the disappearance of reflection peak is attributed to the thermally induced phase transition from CLC to isotropic phase.

Finally, we evaluated the temperature dependences of Bragg reflection wavelengths of HPC ether derivatives. Figure 5 compiles the Bragg reflection wavelengths plotted against the temperature for a series of HPC ether derivatives synthesized in this study, i.e., HPC-HeEt, HPC-PeEt, HPC-BuEt, and HPC-PrEt. In all HPC derivatives, the reflection peaks appeared at longer wavelengths at same temperature as the alkyl chain was longer. This is because the helical pitch of CLC phase is longer as alkyl groups are longer.

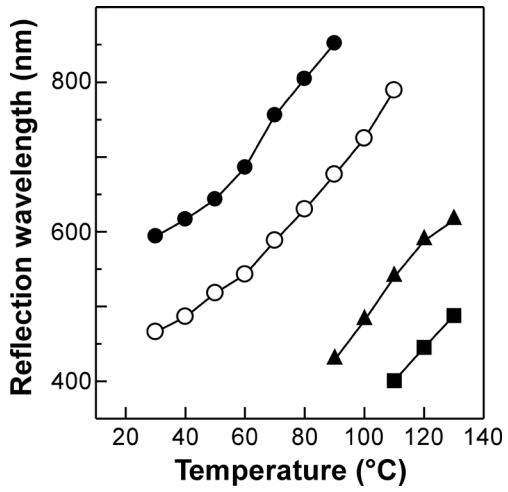

Fig. 5. Temperature dependences of Bragg reflection wavelengths observed from HPC ether derivatives of HPC-HeEt (Closed circles), HPC-PeEt (Open Circles), HPC-BuEt (Closed triangles), and HPC-PrEt (Closed squares).

4. Conclusion

In this study, we succeeded in the synthesis of HPC hexyl ether derivatives with a high substitution degree through the Williamson ether synthesis by using NMP which was higher solubility of NaOH than DMF. Moreover, by adopting NMP as a solvent, we prepared the completely etherified HPC derivatives with pentyl, butyl, and propyl ether groups in the side chains. Furthermore, we confirmed that such HPC derivatives show thermotropic CLC phase with visible reflection properties. We believe that the completely etherified HPC derivatives exhibit stable reflection properties because of chemical stability of ether linkage under highly humid condition, thereby leading to the technological applications to full color HPC materials.

Acknowledgements

We would like to express our deepest appreciation to Messrs. K. Hayata, Shimokawa, and Y. Ogiwara and Mses. R. Aoki, A. Kawaguchi, and Furukawa for their assistance concerning our experiments. One of the authors (S.F.) is indebted to the financial supports from the Grant-in-Aid for Scientific Research (B) (No. 17H03848 and No. 21H02261) of the Ministry of Education, Science, Sports and Culture (MEXT) of Japan and NEXCO Group Companies' Support Fund to Disaster Prevention Measures on Expressways.

References

1. H. Kosho, S. Hiramatsu, T. Nishi, Y. Tanaka, S. Kawauchi, and J. Watanabe, *High Perform. Polym.*, **11** (1999) 41.
2. T. A. Yamagishi, F. Guittard, M. H. Godinho, A. F. Martins, A. Cambon, and P. Sixou, *Polym. Bull.*, **32** (1994) 47.
3. P. Ohlendorf and A. Greiner, *Polym. Chem.*, **6** (2015) 2734.
4. J. Watanabe and T. Nagase, *Macromolecules*, **21** (1988) 171.
5. J. Watanabe, T. Nagase, H. Itoh, T. Ishii, and T. Satoh, *Mol. Cryst. Liq. Cryst.*, **164** (1988) 135.
6. F. Guittard, T. Yamagishi, A. Cambon, and P. Sixou, *Macromolecules*, **27** (1994) 6988.
7. I. Rusig, J. Dedier, C. Filliatre, M. H. Godhino, L. Varichon, and P. Sixou, *J. Polym. Sci. Part A Polym. Chem.*, **30** (1992) 895.

8. T. Yamagishi, T. Fukuda, T. Miyamoto, T. Ichizuka, and J. Watanabe, *Liq. Cryst.*, 7 (1990) 155.
9. B. Huang, J. J. Ge, and Y. Li, and H. Hou, *Polymer*, **48** (2007) 264.
10. K. Miyagi and Y. Teramoto, *Polymer*, **174** (2019) 150.
11. K. Hayata and S. Furumi, *Polymers*, **11** (2019) 1696.
12. H. de Vries, *Acta Crystallogr.*, **4** (1951) 219.
13. N. Tamaoki, *Adv. Mater.*, **13** (2001) 1135.
14. S. L. Tseng, G. V. Laivins, and D. G. Gray, *Macromolecules*, **15** (1982) 1262.
15. K. Akagi and T. Mori, *Chem. Rec.*, **8** (2008) 395.
16. D. W. Berreman and T. J. Scheffer, *phys. Rev. Lett.,* **25** (1969) 577.
17. S. Furumi, *Chem. Rec.*, **10** (2010) 394.
18. H. Ishii, K. Sugimura, and Y. Nishio, *Cellulose*, **26** (2019) 399.
19. S. Saito, K. Hayata, and S. Furumi, *J. Photopolym. Sci. Technol.*, **33** (2020) 461.
20. H. Hou, A. Reuning, J. H. Wendorff, and A. Greiner, *Macromol. Chem. Phys.*, **201** (2000) 2050.
21. F. F. L. Ho, R. R. Kohler, and G. A. Ward, *Anal. Chem.*, **44** (1972) 178.

Communication

Journal of Photopolymer Science and Technology
Volume 34, Number 5 (2021) 555−559 ©2021SPST

Suspensions of Polymer Hydrogel Microparticles with Highly Sensitive Detectability of Glucose

Tatsuya Kawa[1], Yosuke Shibata[2], Naoto Iwata[1], and Seiichi Furumi[1,2*]

[1] Department of Applied Chemistry, Faculty of Science,
[2] Department of Chemistry, Graduate School of Science,
Tokyo University of Science, 1-3 Kagurazaka, Shinjuku, Tokyo 162-8601, Japan
**furumi@rs.tus.ac.jp*

In this study, we synthesized the glucose-responsive hydrogel microparticles containing phenylboronic acid units by emulsion polymerization. The diameters of hydrogel microparticles could be controlled in the range between 133 nm and 199 nm by changing the surfactant concentration in emulsion polymerization. As-prepared hydrogel microparticles showed the coefficient of variation with approximately 10% in particle diameter regardless of the difference particle diameters, implying the relative monodispersity of microparticles. When glucose was added to the aqueous suspensions of hydrogel microparticles, the visible Bragg reflection visually appeared under alkaline conditions due to the formation of colloidal crystals caused by the increase of particle diameter triggered by the binding of glucose to the particles. Since the critical glucose concentrations to show a visible Bragg reflection were dependent on the concentration or diameter of microparticles, these hydrogel microparticles can be applied to the diabetic detectors and sugar sensors.

Keywords: Colloidal crystal, Bragg reflection, Hydrogel, Microparticle, Phenylboronic acid, Glucose

1. Introduction

Colloidal crystals (CCs) are three-dimensional periodic arrays of monodispersed particles [1-4]. Such CCs are regarded as one of the 3D photonic crystals, and exhibit the light reflection in accordance with Bragg's equation [5-6]. The wavelength of Bragg reflection peak (λ) is expressed by the following equation:

$$\lambda = 2nd \sin \theta \quad (1)$$

where n corresponds to the refractive index, d is the diameter of colloidal microparticles, and θ is the Bragg diffraction angle [7].

In general, the outermost surface of microparticles in CCs is negatively charged by dissociation of hydroxyl groups in water. Since the counterions are assembled on the surface and exist around microparticles, the negative and positive electron cloud is called the electric double-layer [2,8]. Electric repulsion is raised between

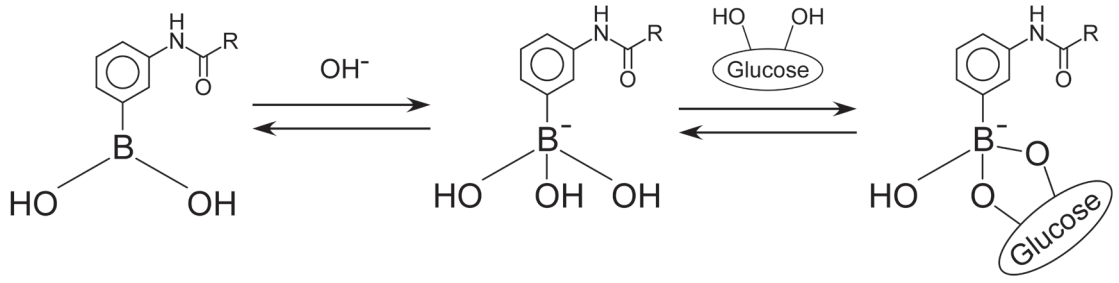

Fig. 1. Equilibrium reactions of a phenylboronic acid derivative under alkaline conditions.

Received March 30, 2021
Accepted April 28, 2021

the adjacent electric double-layers so that the microparticles can't move which enables the formation of CCs with a constant distance.

Recently, CCs which change their colors with external stimuli have been attracting great interests as their versatile applications to sensors, displays, and so forth. For example, thermosensitive microparticles can be used as temperature sensors [9], ion-responsive microparticles provide the applications to ion sensors [10], glucose-responsive microparticles give impetus to construct a self-regulating insulin-delivery system [11].

Especially, the development of glucose-responsive microparticles would give great impetus for the treatment of diabetes, a life-threatening disease showing nowadays an increased number of patients [11]. Previously, phenylboronic acid is one of the well-known compounds applied to glucose sensors [12-16]. As presented in Fig. 1, phenylboronic acid derivatives exist in equilibrium reactions between the uncharged and the charged forms in water [11,17,18]. However, the uncharged form with glucose is unstable in water because of its high susceptibility to hydrolysis [11]. On the other hand, when alkaline condition leads to the complex between charged phenylboronic acid and negatively charged glucose, the increase of glucose concentration can make stable the complex with glucose and phenylboronic acids through a reversible covalent bonding. The further addition of glucose induces a shift in the equilibrium to the direction of increasing the charged forms [19]. For instance, when such phenylboronic acid derivatives are chemically embedded in polymer hydrogels, the osmotic pressure is occurred by the increase of charged forms, resulting in the swelling of polymer hydrogels [11,13,18,19].

In this study, we synthesized the glucose-responsive swelling hydrogel microparticles which incorporate the phenylboronic acid units into poly(*N*-isopropylacrylamide) gel. The aqueous suspensions of microparticles formed the CCs with visible Bragg reflection in the presence of glucose. We found appropriate concentrations of hydrogel microparticles and glucose for the appearance of Bragg reflection. As a result, Bragg reflection emerged by the increase of glucose concentration.

2. Experimental

2.1. Materials

N-Isopropylacrylamide (NIPA), *N*,*N*'-methylenebisacrylamide (BIS), sodium dodecyl sulfate (SDS), potassium peroxodisulfate (KPS), and α-glucose were purchased from FUJIFILM Wako Pure Chemical Co., and *N*-cyclohexylamino-ethanesulfonic acid (CHES) was obtained from Tokyo Chemical Industry Co. Ltd. 3-Acrylamido-phenylboronic acid (AAPBA) was supplied from either Tokyo Chemical Industry Co. Ltd. or Combi-Blocks, Inc.

2.2. Synthesis of NIPA-AAPBA hydrogel microparticles

Aqueous suspensions of NIPA-AAPBA hydrogel microparticles were synthesized by emulsion polymerization of NIPA, AAPBA and BIS as hydrogel precursors, KPS as a thermal polymerization initiator, and SDS as a surfactant. The diameters of microparticles were controlled by changing the SDS concentrations, as shown in Table 1. For example, the suspension of hydrogel microparticles with the diameter of 133 nm were synthesized as follows.

AAPBA (0.58 g, 4.7 mmol), NIPA (3.1 g, 27 mmol), BIS (0.23 g, 1.5 mmol), and SDS (0.15 g, 0.52 mmol) were dissolved in ultrapure water (200 mL) in a 300 mL three-neck separable flask. This solution was mixed for 30 min and purged with nitrogen gas to exclude oxygen. Subsequently, the mixture was heated to 70 °C and stirred for additional 30 min. After that, a solution of KPS (63 mg; 0.23 mmol) in ultrapure water (6.2 mL) was added into the mixture with a syringe pump. The emulsion polymerization proceeded for 4 h [20]. Finally, the polymerization was stopped by exposing the mixture to the air and gentle cooling to room temperature.

The aqueous suspensions of hydrogel microparticles were obtained by two cycles of filtration through membrane filters with the pore sizes of 1.0 μm and 0.45 μm, and three cycles of centrifugation with 4.0×10^5 rpm for 30 min. After dispersing in ultrapure water again, the suspensions were deionized by stirring for overnight in the presence of 10 wt% of ion exchange resin beads to remove the remaining ionic species.

2.3. Measurement of diameter of hydrogel microparticles

The diameter and coefficient of variation (CV) value of hydrogel microparticles at 25 °C were determined by the particle size analytic technique with dynamic light scattering (DLS) (Nanotrac UPA, Microtrac). Here, the CV value was defined as the ratio of the standard deviation of particle diameters to the average particle diameter. To adjust pH of

aqueous suspension, a solution of CHES was used as a buffer.

2.4. Reflection spectral measurement of hydrogel microparticles

The reflection spectra were measured using a CCD spectrometer (USB2000+, Ocean Optics) equipped with a halogen light source (HL-2000, Ocean Optics) as the probing white light.

3. Results and discussion

3.1. Synthesis of NIPA-AAPBA hydrogel microparticles

The NIPA-AAPBA hydrogel microparticles with different diameters were prepared by the emulsion polymerization. The diameter of hydrogel microparticles was controllable by changing the amounts of SDS and average diameters of microparticles are shown in the left-side and middle columns of Table 1, respectively. The CV values of microparticles are also summarized in the right-side column of Table 1.

The average diameter of hydrogel microparticles was 133 nm when synthesized with 0.15 g of SDS. With decreasing the amount of SDS to 0.08 g and to 0.04 g, the average diameters increased to 170 nm and 199 nm, respectively. The decrease of particle diameter can be explained from the decrease of micelle diameter in emulsion polymerization process caused by the increase of the number of micelles triggered by the increase of SDS concentration.

The CV value of each hydrogel microparticles was approximately 10% regardless of diameter, indicative of the successful preparation of relative monodispersity of microparticles. It can be assumed that such a monodispersity of hydrogel microparticle enables the formation of well-ordered CC structures with Bragg reflection.

Table 1. Average diameters and CV values of NIPA-AAPBA hydrogel microparticles by the amounts of SDS used in emulsion polymerization.

SDS (g)	Average diameter (nm)	CV in diameter (%)
0.15	133	10.2
0.08	170	11.3
0.04	199	10.3

3.2. Measurement of swelling degree of hydrogel microparticles

Swelling degree of hydrogel microparticles was dependent on pH in the aqueous suspension. In this time, the swelling degree was defined as the ratio of hydrogel microparticle diameter at specific pH to that of at pH 7.5, as shown in Fig. 2 (A). The swelling degree of hydrogel microparticles was constant at 1.0 in the pH range of 7.5 to 8.0. However, in the pH range of 8.0 to 9.0, the swelling degree of hydrogel microparticles immediately increased to approximately 1.4. This swelling degree was maintained at 1.4 over pH values of 9.0. Such an increase of swelling degree can be explained as follows. Since the hydrogel microparticles are negatively charged under alkaline conditions, the electrostatic repulsion force makes the polymer network in the hydrogel microparticles to expand. The swelling of hydrogel microparticles occurs to balance the osmotic pressure caused by the expansion of polymer network. From the results, we carried out the following experiments of suspension prepared at pH of 9.0.

Next, the dependance of swelling degree of hydrogel microparticles and glucose concentration were evaluated, as shown in Fig. 2 (B). With the increase of glucose concentration, the swelling degree of hydrogel microparticles continued to

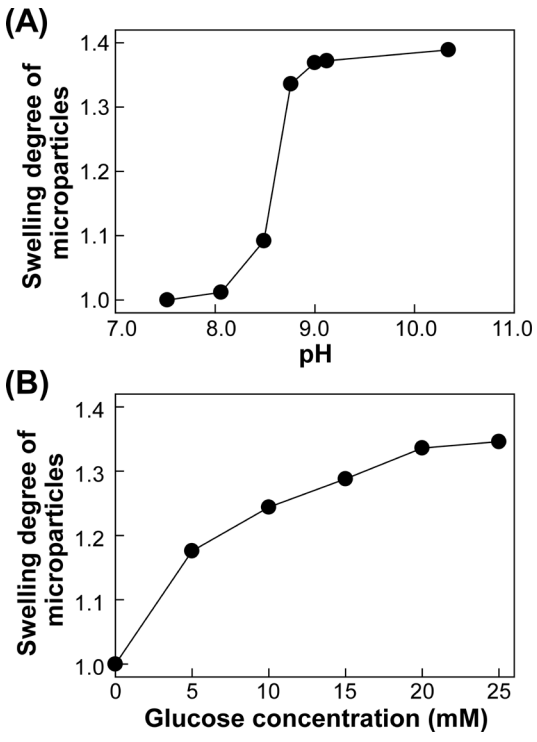

Fig. 2. (A) Changes in the swelling degree of 133 nm-diameter hydrogel microparticles tethering phenylboronic acid units as a function of pH value. The glucose concentration was fixed at 25 mM. (B) Changes in the swelling degree of 133 nm-diameter hydrogel microparticles tethering phenylboronic acid units at pH value of 9.0 under various glucose concentration.

increase due to the binding of glucose. On the other hand, the swelling degree became constant at approximately 1.3 when the glucose concentration was higher than 20 mM, suggesting the existence of an equilibrium. This is reasonable since the equilibrium moves to the direction of increasing the proportion of hydrogel microparticles without glucose as increasing the concentration of glucose.

3.3. Emergence of Bragg reflection of hydrogel microparticle suspensions

Figure 3 shows the changes in reflection spectrum of aqueous suspensions of hydrogel microparticles with the diameter of 133 nm as a function of the glucose concentration of 0 mM, 1.0 mM, and 2.0 mM. We could not observe Bragg reflection when the suspension containing the glucose concentration with 1.0 mM or in the absence of glucose. This can be attributed to the overlapping of electric double layers, which prevent the CC formation in suspension caused by the relatively small diameter of microparticles, accompanied by the increase of particle distance. However, Bragg reflection appeared by addition of glucose with the concentration of 2.0 mM. It can be assumed that hydrogel microparticles swell under relatively high concentrations of glucose. Consequently, the increase of microparticle diameter leads to the formation of CC structures with visible Bragg reflection. Taking these experimental results in account, the hydrogel microparticles can form the CCs with visible Bragg reflection depending on the glucose concentration.

Finally, we evaluated the appropriate concentrations of hydrogel microparticles with various diameters for the detection of glucose concentrations visualized by the emergence of Bragg reflection. The experimental results by using microparticles with the diameters of 133 nm, 170 nm and 199 nm are compiled in Fig. 4. The emergence of Bragg reflection was dependent on the concentrations and dimeter of hydrogel microparticles.

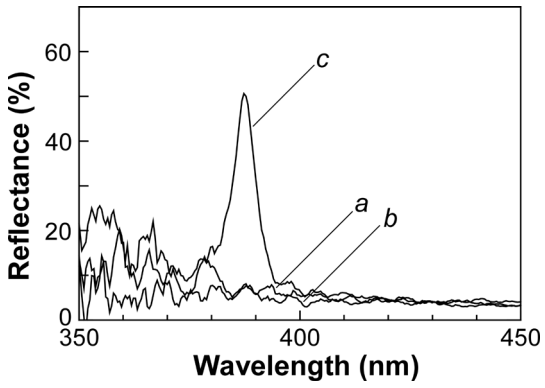

Fig. 3. Reflection spectra of the aqueous suspension of hydrogel microparticle with the diameter of 133 nm at the glucose concentrations of 0 mM (Spectrum *a*), 1.0 mM (Spectrum *b*), and 2.0 mM (Spectrum *c*).

First, we pursued the concentration of hydrogel microparticles for the glucose detection. As used the hydrogel microparticles with diameter of 133 nm, the maximum microparticle concentration where Bragg reflection emerged was 8 wt%. As increasing the diameters of hydrogel microparticles to 170 nm and 199 nm, the maximum microparticle concentrations for the emergence of Bragg reflection were increased to 9 wt% and 11 wt%, respectively. This can be ascribed to the overlapping of electric double layers caused by the increase of microparticle diameter, which enabled the formation of CCs with Bragg reflection.

Next, the emergence of Bragg reflection under various concentrations of hydrogel microparticles was investigated. In the case of the microparticles with diameter of 133 nm, when the microparticle concentration was decreased from 8 wt% to 6 wt%, the glucose concentration needed to emerge Bragg reflection was increased from 0 wt% to 8 wt%. This tendency was consistent with two other hydrogel microparticle systems with different diameters such as 170 nm and 199 nm. These results suggest that the microparticle distance becomes short when the concentration of hydrogel microparticles is increased. In this way, low concentration of glucose can be visually detected by the emergence of Bragg reflection.

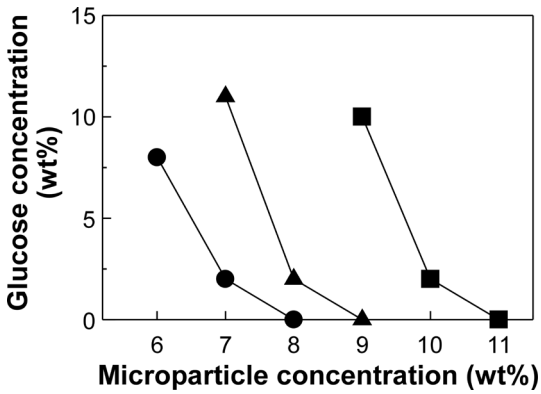

Fig. 4. Concentrations and diameters of hydrogel microparticles for the detection of glucose concentrations visualized by the emergence of Bragg reflection. In this study, three kinds of the suspensions of microparticles with the diameters of 133 nm (Circles), 170 nm (Triangles), and 199 nm (Squares) were used.

4. Conclusions

In this study, we have developed the microparticles of NIPA-AAPBA hydrogel with the diameters of 133 nm, 170 nm, and 199 nm. In the aqueous suspensions, the swelling degree of hydrogel microparticles is governed by not only pH value, but also glucose concentration. As adjusting the pH value over 9.0, Bragg reflection emerged by the increase of glucose concentration. Furthermore, the critical glucose concentration for the emergence of Bragg reflection can be controlled by changing the microparticle concentration or diameter. The present report provides novel guideline to fabricate the diabetic detectors and sugar sensors.

Acknowledgements

This research was financially supported in part by the Ministry of Education, Science, Sports and Culture of Japan under the Grant-in-Aid for Scientific Research (B) (No. 17H03848 and No. 21H02261) and NEXCO Group Companies' Support Fund to Disaster Prevention Measures on Expressways.

References

1. P. Pawel, *Contemp. Phys*, **24** (1983) 25.
2. Y. Xia, B. Gates, Y. Yin, and Y. Lu, *Adv. Mater*, **12** (2000) 693.
3. A. Docoslis and P. Alexandridis, *Electrophoresis*, **23** (2002) 2174.
4. Y. Ofir, I. W. Moran, C. Subramani, Kenneth R. Carter, and V. M. Rotello, *Adv. Mater*, **22** (2010) 3608.
5. S. Furumi, H. Fudouzi, and T. Sawada, *Laser & Photon. Rev.*, **4** (2010) 205.
6. A. P. Bartlett, A. K. Agarwal, and A. Yethiraj, *Langmuir*, **27** (2011) 4313.
7. M. Kumoda, M. Watanabe, and Y. Takeoka, *Langmuir*, **22** (2006) 440.
8. H. Ohshima, *Sikizaikyoukaishi*, **77** (2004) 328 (in Japanese).
9. M. Lutecki, B.Strachotova, M. Uchman, J. Brus, J. Plestil, M. Slouf, A. Strachota, and L. Matejka, *Polym. J.*, **38** (2006) 527.
10. J. H. Holtz, J. S. W. Holtz, C. H. Munro, and S. A. Asher, *Anal. Chem*., **70** (1998) 780.
11. K. Kataoka, H. Miyazaki, M. Bunya, T. Okano, and Y. Sakurai, *J. Am. Chem. Soc.*, **120** (1998) 12694.
12. S. A. Asher, V. L. Alexeev, A. V. Goponenko, A. C. Sharma, I. K. Lednev, C. S. Wilcox, and D. N. Finegold, *J. Am. Chem. Soc*, **125** (2003) 3322.
13. M. Honda, K. Kataoka, T. Seki, and Y. Takeoka, *Langmuir*, **25** (2009) 8349.
14. Q. Luo, P. Liu, Y. Guan, and Y. Zhang, *ACS Appl. Mater. Interfaces*, **2** (2010) 760.
15. S. Xing, Y. Guan, and Y. Zhang, *Macromolecules*, **44** (2011) 4479.
16. P.-C. Chen, L.-S. Wan, B.-B. Ke, and Z.-K. Xu, *Langmuir*, **27** (2011) 12597.
17. D. Nakayama, Y. Takeoka, M. Watanabe, and K. Kataoka, *Angew. Chem. Int. Ed.*, **115** (2003) 4197.
18. A. Kikuchi, K. Suzuki, O. Okabayashi, H. Hoshino, K. Kataoka, Y. Sakurai, and T. Okano, *Anal. Chem*, **68** (1996) 823.
19. A. Matsumoto, T. Kurata, D. Shiino, and K. Kataoka, *Macromolecules*, **37** (2004) 1502.
20. T. Still, K. Chen, A. M. Alsayed, K. B. Aptowicz, and A. G. Yodh, *J. Colloid Interface Sci.*, **405** (2013) 96.

Journal of Photopolymer Science and Technology
Volume 34, Number 5 (2021) 561−564 ©2021SPST

Protrusion Formation of Polymer Surface by Atomic Hydrogen Annealing

Akira Heya[1*] and Koji Sumitomo[1]

[1] *Department of Materials and Synchrotron Radiation Engineering, University of Hyogo, 2167 Shosha, Himeji, Hyogo 671-2280, Japan*
**heya@eng.u-hyogo.ac.jp*

The reaction of atomic hydrogen with polymer materials was investigated from the change in the surface morphology of various plastic substrates. The atomic hydrogens were genareted by decomposition of H_2 gas on a heated tungsten mesh. We call the surface-tretament as atomic hydrogen annealing (AHA). The surface morphology was changed by chemical reaction of atomic hydrogen and thermal effect. As the AHA treatment time was incresed, the surface projection was became larger. It is considered that the surface projection formation occurred by the enhancement of etching and shrinkage effects due to local heating.
Keywords: Atomic hydrogen annealing, Surface modification, Plastic substrate

1. Introduction

Polymer materials are cheap, light and flexible. Such materials are expected for use as substrates for flexible sensors. In addition, to improve the surface property of polymer materials, namely, adhesion, wettability, the surface modification has been investigated by various surface treatment. On the other hand, it is necessary to clarify the interaction between polymer material and hydrogen for realization of hydrogen society. The clarification of the reaction between hydrogen and polymer materials is an important issue for sustainable society using hydrogen energy and sensing network system.

Atomic hydrogens, in other words, hydrogen radicals, are generated by catalytic cracking reaction on a heated catalyst [1,2]. We proposed a surface treatment method using the atomic hydrogen, named as the atomic hydrogen annealing (AHA) [3-11]. In AHA, the hydrogen molecules are decomposed by the catalytic cracking reactions on the heated tungsten (W) catalyst placed near the sample. The decomposition efficiency of H_2 is much higher on heated catalyst surface than in gas phase such as plasma process [12]. The AHA method can treat on a large area sample simply by spreading the catalyst widely without plasma damage.

The technique can be applied to the low-temperature crystallization of a-Si [3], dry etching of crystalline silicon [13], vacuum chamber cleaning and photoresist removal [14-17].

The surface modifications of plastic substrates, namely, polyvinyl chloride (PVC) [4], polyethylene (PE) [4], polypropylene (PP) [4], polyethylene naphtahalate (PEN) [6], and poly methyl methacrylate (PMMA) [18] have been investigated for controlling the surface properties.

In this study, the reaction between polymer materials and atomic hydrogen was investigated from the change in the surface morphology of various plastic substrates.

2. Experimental

The AHA apparatus used in this study and the concept of AHA are shown in Fig. 1. In AHA, the hydrogen molecules are decomposed on the heated catalyst (W mesh). The atomic hydrogens arrive on the sample surface and diffuse into the sample. The chemical reactions such as hydrogenation and reduction occur on the surface and the interior of sample. In addition, the sample surface is locally heated by the energy of recombination reaction.

A 55×55 mm^2 W mesh with a wire diameter of 0.03 mm and having 50 holes/inch was heated to 1600 and 1700 °C by electrical heating in H_2 atmosphere. The applied voltages and currents of W

Received March 31, 2021
Accepted April 27, 2021

mesh were 10.5 V and 23.8 A for a mesh temperature (T_{mesh}) of 1600 °C and 14.0 V and 28.8 A for a T_{mesh} of 1700 °C, respectively. The flow rate of H_2 and gas pressure were 100 sccm and 30 Pa, respectively. The distance between the W mesh and the sample was 80 mm.

The temperature of sample surface was measured by a K-type thermocouple (TC) attached on a PET by a polyimide tape. The optical image of polyethylene terephthalate (PET) and TC on the sample holder is inserted in Fig. 2.

The PET (Lumirror S10, Toray Industries, Inc.), PEN (Teonex, Teijin Ltd.), PP (6-607-02, As One) and PVC (61-7474-17, As One) were subjected to AHA. The samples (plastic substrate of 40 × 40 mm^2 or 40 × 80 mm^2 in size and 0.2 mm in thickness) were fixed at the sample holder (stainless steel plate, 130 × 130 mm^2 in size and 10 mm in thickness) by a polyimide tape. The T_{mesh} was fixed at 1700 °C for the surface modification of plastic substrate. The AHA treatment times (t_{AHA}) were 600 and 3600 s. The surface morphology was observed by field emission scanning electron microscope (FE-SEM, Regulus8220, Hitachi High-Tech Corp.). To suppress charge up, Os film was coated on the polymer substrate before SEM observation. The SEM images were obtained at an applied voltage of 5 kV, an emission current of 10 μA.

3. Results and discussion

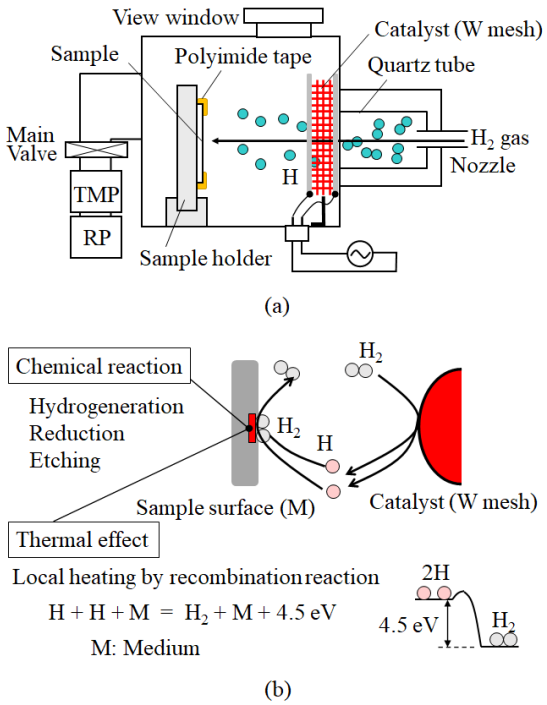

Fig. 1. (a) Schematic diagram of the AHA apparatus. (b) Concept of AHA.

3.1. Surface temperature of PET during AHA

The surface temperature of PET is shown in Fig. 2. The temperature of PET was increased to 113 °C for 600 s and 172 °C for 3600 s, respectively. In this apparatus, the sample temperature was not controlled by a heater and/or a cooling system. Therefore, the sample temperature was automatically increased by thermal radiation from the heated W mesh. At a T_{mesh} of 1600 °C compared to 1700 °C, the surface temperature of PET was reduced by 40 °C for 600 s. It was shown that the temperature of plastic substrate is reduced by decreasing T_{mesh}. In addition, it has been confirmed that the surface temperature of plastic film (thickness of 0.1 mm) can be maintained at a low temperature by improving the adhesion between the plastic film and cooled metal drum in roll-to-roll system [19]. It is expected that the surface temperature could be reduced by decrease in T_{mesh} or by using the cooling system for polymers with low heat resistance.

3.2. Surface modification of plastic substrate

SEM images of the various plastic substrates before and after AHA are shown in Fig. 3. The oblique angle view (60 degrees) of the SEM images for the plastic substrates at a T_{mesh} of 1700 °C for a t_{AHA} of 3600 s are shown in Fig. 4. As the t_{AHA} was increased, the surface roughness of the PET, PEN, and PVC was increased. In the PET and PEN, the concavo-convex surface was formed at a t_{AHA} of 600 s. The protrusion with circle and oval shapes were observed at a t_{AHA} of 3600 s. The width of white-contrast oval was almost constant at 30 nm. On the other hand, the length of white-contrast oval was varied from 30 to 200 nm. From the oblique angle view, the protrusions were connected to each other on the polymer surface. In addition, the surface

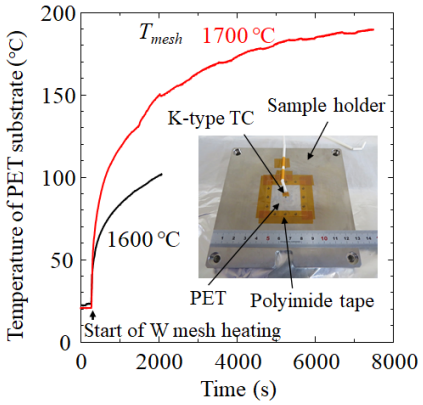

Fig. 2. Temperature of PET substrate as a function of treatment time.

morphology of PVC was changed by AHA. However, the surface morphology of PVC after AHA was different from PET and PEN. It is considered that the protrusion was generated via cracking of top surface of PVC. On the other hand, the change in surface morphology of PP was small. However, small dents were observed. It was found that the surface morphology was depended on the thermal property and chemical composition of polymer material.

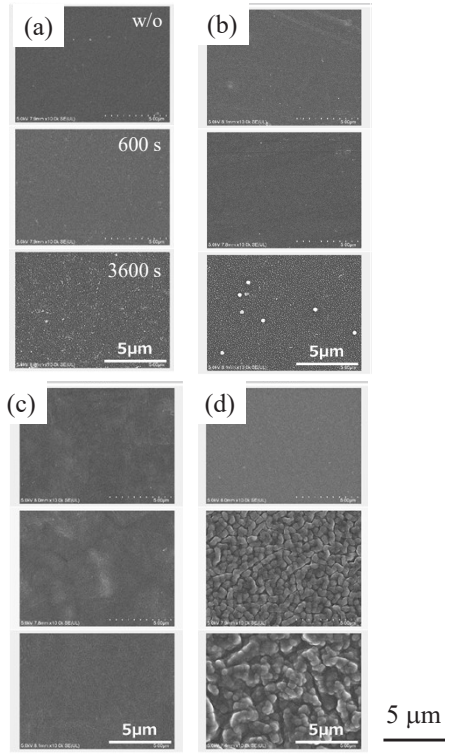

Fig. 3. SEM images of plastic substrates before and after AHA. (a) PET. (b) PEN. (c) PP. (d) PVC. The conditions of the upper, middle, and lower images are w/o, 600, and 3600 s.

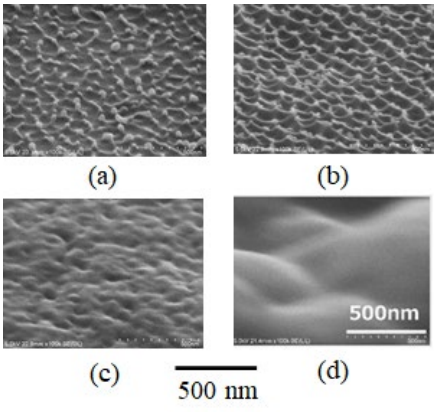

Fig. 4. Oblique angle view (60 degrees) of SEM images for the plastic substrates after AHA. (a) PET. (b) PEN. (c) PP. (d) PVC. The t_{AHA} was 3600 s.

It was reported that crosslinking or degradation is produced by irradiation of electron with high energy of 800 kV [20, 21]. For the SEM observation in this study, however, the influence of electron irradiation was negligible because of low current and low applied voltage, and Os coating.

3.3. Formation mechanism of surface protrusion on plastic substrate by AHA

The formation mechanism of the surface protrusion on the plastic substrate by AHA is discussed by thermal property of plastic substrate and behavior of atomic hydrogen. The thermal properties of plastic substrate are summarized in Table 1. These values are referred as typical property.

To clear the origin of the surface modification, the treatment time to exceed the glass transition temperature (T_g) are shown in Fig. 5. In this figure, the temperature of PET was used. Although the temperature of the other plastic substrates, namely PEN, PP, and PVC, might be different with PET, the T_g of the other substrates are indicated and are also discussed. In the PET, the temperature reached T_g (69 °C) for 100 s. Therefore, the surface modification is discussed based on treatment time beyond T_g. Below the melting point (T_m), the polymer in amorphous region only behaves like rubber and does not deform unless an external force is applied. The increment of surface roughness by increasing t_{AHA} is not explained only by thermal deformation. In the case of PEN, the surface temperature was below T_g for a t_{AHA} of 600 s, and that was above T_g for a t_{AHA} of 3600 s. However, the surface morphologies of PEN after AHA for 600 and 3600 s were similar to PET. This indicates that the surface modification of PET and PEN did not depend on only T_g. The T_g of PP was low as 0 °C and the surface temperature during AHA was above T_m of 168 °C. The change in surface morphology of PP was small. The T_m was not important for protrusion formation of PP. This indicates that the protrusion formation of polymer surface by AHA was not only depended on the thermal effect.

It was reported that the surface modification occurred above T_g [22]. It was known that the surface modification occurred not only thermal effect but also atomic hydrogen effect because the surface morphology was not changed by He treatment [4]. Therefore, it was considered that the formation mechanism of surface protrusion is related to reaction of atomic hydrogen with polymer above T_g. In addition, it implies that the protrusion

formation due to shrinkage was enhanced by the reaction of atomic hydrogen such as decomposition and etching of plastic substrate.

The formation mechanism of protrusion in the PVC was differed with the PET and PEN because the surface morphology was differed with the PET and PEN. From the previous study, the halogen and

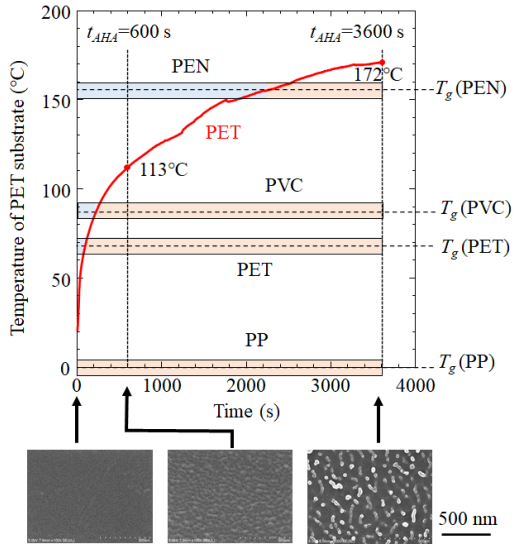

Fig. 5. Temperature of the PET substrate as a function of AHA treatment time. The values of T_g for plastic substrates are shown. The light orange bars indicate the treatment region above T_g. The SEM images of PET at 0, 600, and 3600 s are shown at the bottom.

oxygen atoms are preferentially removed by AHA [4]. Therefore, the shrink of PVC occurred by the removal of halogen atoms. It implies that the surface protrusion of PVC was formed by shrinkage due to elimination of Cl atoms.

4. Conclusion

The surface modification depended on the constituent elements (halogen and oxygen atoms) of the polymer. As the t_{AHA} was incresed, the surface protrusion became larger. It is considered that the surface protrusion formation was realized by combination of the chemical reaction of atomic hydrogen (substraction of oxigen and halogen atom and/or decomposition of main chain) and the enhancement of etching effect due to local heating.

Acknowledgements

This work was supported in part by the Tanikawa Foundation for the Promotion of Thermal Technology and Himeji City Academic-Industry Cooperation Grant.

References

1. I. Langmuir, *J. Am. Chem. Soc.* **34** (1912) 1310.
2. I. Langmuir and G.M.J. Mackay, *J. Am. Chem. Soc.* **36** (1914) 1708.
3. A. Heya, A. Masuda, and H. Matsumura, *Appl. Phys. Lett.*, **74** (1999) 2143.
4. A. Heya and N. Matsuo, *Jpn. J. Appl. Phys.*, **46** (2007) 3545.
5. A. Heya and N. Matsuo, *Jpn. J. Appl. Phys.*, **46** (2007) L709.
6. A. Heya and N. Matsuo, *Jpn. J. Appl. Phys.*, **47** (2008) 266.
7. A. Heya and N. Matsuo, *IEICE Trans. Electron*, **E93-C** (2010) 1516.
8. A. Heya and N. Matsuo, *Jpn. J. Appl. Phys.*, **53** (2014) 058002.
9. A. Heya and N. Matsuo, *Thin Solid Films*, **625** (2017) 93.
10. A. Heya, S. Hirano, and N. Matsuo, *Jpn. J. Appl. Phys.*, **58** (2019) 068006.
11. A. Heya, T. Harada, M. Niibe, K. Sumitomo, T. Watanabe, *J. Photopolym. Sci. Technol.*, **33** (2020) 419.
12. H. Umemoto, K. Ohara, D. Morita, Y. Nozaki, A. Masuda and H. Matsumura, *J. Appl. Phys.*, **91** (2002) 1650.
13. K. Uchida, S. Hashioka, A. Izumi, and H. Matsumura, *2000 Dry Process Symp.*, 2000, p.231.
14. A. Izumi and H. Matsumura, *Jpn. J. Appl. Phys.* **41** (2002) 4639.
15. M. Yamamoto, H. Umemoto, K. Ohdaira, S. Nagaoka, T. Shikama, T. Nishiyama, H. Horibe, *J. Photopolym. Sci. Technol.*, **28** (2015) 303.
16. T. Maruoka, Yousuke Goto, Masashi Yamamoto, Hideo Horibe, Eiji Kusano, Kazuhisa Takao, Seiichi Tagawa, *J. Photopolym. Sci. Technol.*, **22** (2009) 325.
17. M. Yamamoto, H. Horibe, H. Umemoto, K. Takao, E. Kusano, M. Kase, and S. Tagawa, *Jpn. J. Appl. Phys.*, **48** (2009) 026503.
18. A. Matsuo, S. Takagi, T. Nishiyama, M. Yamamoto, E. Sato, and H. Horibe, *J. Photopolym. Sci. Technol.*, **31** (2018) 369.
19. A. Heya, T. Minamikawa, T. Niki, S. Minami, A. Masuda, H. Umemoto, N. Matsuo, and H. Matsumura, *Thin Solid Films*, **516** (2008), 553.
20. E.J. Lawton, A.M. Bueche, and J.S. Balwit, *Nature*, **172** (1953) 76.
21. A.A. Miller, E.J. Lawton, and J.S. Balwit, *J. Polym. Sci.*, **14** (1954) 503.
22. D. Kawakami, S. Ran, C. Burger, C. Avila-Orta, I. Sics, B. Chu, B.S. Hsiao, and T. Kikutani, *Macromolecules*, **39** (2006) 2909.

JOURNAL OF PHOTOPOLYMER SCIENCE AND TECHNOLOGY
Volume 34, Number 5, 2021